

**Application of a pixellated  
detector to energy dispersive  
x-ray diffraction, and  
investigation of materials for  
breast tissue diffraction  
evaluation.**

Christiana Christodoulou

University College London

Submitted for the Degree of Doctor of Philosophy

2015

I, Christiana Christodoulou confirm that the work presented in this thesis is my own. Where information has been derived from other sources, I confirm that this has been indicated in the thesis.

## Abstract

Two pixellated application specific integrated circuits (ASICs) bump bonded to 1 mm thick Cadmium Telluride sensors were characterised and compared for the purpose of application in a combined energy dispersive and angular dispersive x-ray diffraction system. The energy resolution of the ASICs, the energy detection efficiency at 60 keV, the radiation responses, the number of dead pixels, and the charge sharing effects on the detection efficiency and energy resolution were considered. The parameters of the field programmable array (FPGA) used to acquire the data were also explored based on the number of frames detected, and the counting efficiency of the ASIC, which is not optimised to photon count, but to energy resolve for spectroscopic applications using a peak hold read-out. The selected ASIC was incorporated into a diffraction system which included a micro-focal source. This system was characterised for comparison with other future systems, as well as to establish important parameters such as the divergence of the system and the size of the beam at the sample, as this was necessary to define the voxel of the sample being considered in diffraction scanning.

The obtained data from the 2D array were investigated, in terms of utilising the detector array as a whole, i.e. all energies and detection angles, compared to only selecting angles and energies of interest. The obtained diffraction signals for caffeine, lard and Poly(methyl methacrylate) (PMMA) were investigated with respect to the sample thickness. Parameters utilised in the literature in diffrac-

tion studies, including the intensity of the diffraction peak, the full width half maximum (FWHM) of the peak and their ratios with respect to the area of the diffraction peak were also considered. These signals were shown to vary with the sample thickness, however this relationship was affected by the post-processing method used.

A High Purity Germanium system (HpGe) Energy Dispersive X-ray Diffraction (EDXRD) system was used to acquire diffraction spectra for a materials library and to establish potential materials for the design of anthropomorphic phantoms for breast tissue diffraction studies. In order to obtain a phantom with a realistic shape, materials could be melted and set into a tumour shape. Materials included plastics, such as polymorph, and biodegradable materials such as gelatine and agar. Polymorph, agar and gelatine showed, in terms of their diffraction spectra, density and their attenuation coefficients, the potential to be used in phantoms as breast tissue equivalent materials.

The diffraction system was used to scan a PMMA phantom created using a laser etching method. The phantom creation method was developed in this research and is characterised using transmission imaging to establish the relationship of the speed setting of the laser etching system, the greyscale value obtained from the images, and the etch depths of the laser system. This method of characterisation leads to recreation of the phantom based on the etch depths. The phantoms area created from an 8-bit image of a tumour. The phantom was scanned in the system both as is and also with water as an infilling material.

## Acknowledgements

I would like to thank my supervisors Prof. Robert Speller and Prof. Gary Royle for guiding me and supporting me throughout this research. I'd like to thank the Department of Medical Physics and Biomedical Engineering at UCL, Jem Hebden and EPSRC for funding this project. I am grateful for the opportunity provided by the Science and Technology Facilities Council (STFC) for using their detector within my work and also for scientific support and discussions regarding the system. In particular I'd like to give thanks to Matt Wilson, Matt Veale and Paul Seller.

I'd like to thank Caroline Reid, Dan O'Flynn, and Kate Rickets for all of their work discussions regarding the detector and diffraction systems, as well as Jenny Griffiths, Essam Baniqtah, Tasos Konstantindis, Nik Vijita, Nick Everdell and Yi Zheng for their support, scientifically and otherwise. Special thanks go to Mike Luk for reading my work despite our time difference issues. A special thanks goes also to Tang Chii Shuh for helping with the materials library work.

Special thanks go to my best friend Meera Taank and the rest of the Woodford County High School crew, Chiaki 'Chan' Crewes, and all those in the Radiation Physics group who helped me solve a problem with a good chat and a cup of tea. I would not be able to have continued with my research without the help of my parents, Andreas and Androulla Christodoulou, my sister Susie, and especially my loving partner Andrew Liew.

# Contents

|          |  |           |
|----------|--|-----------|
| <b>1</b> | <b>Introduction</b>  | <b>20</b> |
| 1.1      | Background . . . . .                                       | 20        |
| 1.2      | Photon interactions with matter . . . . .                  | 21        |
| 1.2.1    | Photoelectric absorption . . . . .                         | 21        |
| 1.2.2    | Incoherent scatter . . . . .                               | 22        |
| 1.2.3    | Coherent Scatter . . . . .                                 | 24        |
| 1.2.4    | X-ray semiconductor detectors . . . . .                    | 28        |
| 1.2.4.1  | Charge carrier transport . . . . .                         | 29        |
| 1.3      | Diffraction and breast tissue . . . . .                    | 35        |
| 1.3.1    | Imaging . . . . .  | 38        |
| 1.3.2    | Multivariate analysis studies . . . . .                    | 39        |
| 1.4      | Tissue equivalent materials . . . . .                      | 41        |
| 1.5      | Cadmium (Zinc) Telluride sensors and EDXRD . . . . .       | 47        |
| 1.6      | Thesis layout . . . . .                                    | 51        |
| <b>2</b> | <b>Characterisation of two 80×80 ASICs</b>                 | <b>54</b> |
| 2.1      | Description of the pixellated ASIC CdTe detector . . . . . | 54        |
| 2.1.0.1  | Charge sharing . . . . .                                   | 60        |
| 2.1.0.2  | Temperature control . . . . .                              | 64        |
| 2.1.0.3  | Humidity control . . . . .                                 | 68        |
| 2.1.0.4  | Detector software . . . . .                                | 69        |

|  |            |
|--|------------|
| <i>CONTENTS</i>  | 5          |
| 2.1.1 Other comparable detectors . . . . .                                   | 71         |
| 2.1.2 Specific information on the detector system used . . . . .             | 74         |
| 2.2 Properties required for EDXRD . . . . .                                  | 76         |
| 2.3 Objectives . . . . .   | 78         |
| 2.4 Method for energy resolution and energy efficiency . . . . .             | 80         |
| 2.5 Results: Energy resolution excluding charge sharing events . . . . .     | 81         |
| 2.6 Results: Efficiency excluding charge sharing events. . . . .             | 89         |
| 2.7 Charge sharing considerations . . . . .                                  | 91         |
| 2.7.1 Energy resolution and efficiency with charge sharing events            | 92         |
| 2.8 Investigation of Row- $S_1$ parameter and stability for ASIC A . . . . . | 95         |
| 2.8.1 Method . . . . .   | 96         |
| 2.8.2 Results for Row- $S_1$ investigation . . . . .                         | 97         |
| 2.8.3 System stability results . . . . .                                     | 103        |
| 2.9 Discussion . . . . .   | 104        |
| 2.10 Conclusions . . . . .   | 110        |
| <b>3 Diffraction system</b>  | <b>112</b> |
| 3.1 Introduction . . . . .   | 112        |
| 3.2 Objectives . . . . .   | 114        |
| 3.3 System considerations . . . . .  | 115        |
| 3.4 X-ray spectrum . . . . .   | 119        |
| 3.4.1 Introduction . . . . .   | 119        |
| 3.4.2 Half value layer theory . . . . .                                      | 120        |
| 3.4.3 Experimental method . . . . .  | 121        |
| 3.4.4 Results . . . . .  | 122        |
| 3.4.5 Determination of x-ray spectrum . . . . .                              | 124        |
| 3.5 X-ray focal spot . . . . .   | 125        |
| 3.5.1 Introduction . . . . .   | 125        |

|          |   |            |
|----------|---|------------|
| 3.5.2    | Theory of focal spot calculation . . . . .  | 126        |
| 3.5.3    | Experimental system . . . . .   | 131        |
| 3.5.4    | Image processing and results . . . . .  | 132        |
| 3.6      | Calculation of beam divergence and beam height . . . . .  | 136        |
| 3.6.1    | Geometrical definitions . . . . .   | 136        |
| 3.6.2    | Beam height and beam divergence . . . . .   | 137        |
| 3.7      | Detector placement . . . . .  | 138        |
| 3.7.1    | XRF and background signal . . . . .   | 142        |
| 3.8      | System automation . . . . .   | 144        |
| 3.9      | Diffraction signal and material thickness . . . . .   | 147        |
| 3.9.1    | Introduction . . . . .  | 147        |
| 3.9.2    | Theoretical thickness considerations in diffraction systems                                       | 148        |
| 3.9.3    | Experimental design . . . . .   | 151        |
| 3.9.4    | Results: Creation of diffraction profiles . . . . .   | 153        |
| 3.9.5    | Results: Effects and exclusion of fixed energy signals. . . .                                     | 160        |
| 3.9.5.1  | Simulation of XRF effects on the diffraction profiles   | 160        |
| 3.9.5.2  | Backscatter events . . . . .  | 162        |
| 3.9.5.3  | Summary . . . . .   | 164        |
| 3.9.6    | Results: Investigation of diffraction parameters with se-<br>lected angles and energies . . . . . | 165        |
| 3.10     | Discussion . . . . .  | 182        |
| 3.11     | Conclusions . . . . .   | 187        |
| <b>4</b> | <b>Materials Library</b>  | <b>188</b> |
| 4.1      | Introduction . . . . .  | 188        |
| 4.2      | Objectives . . . . .  | 194        |
| 4.3      | Method . . . . .  | 195        |
| 4.3.1    | Materials and their preparation . . . . .   | 195        |

|          |  |            |
|----------|--|------------|
| 4.3.2    | Diffraction profiles data collection . . . . .                                 | 198        |
| 4.4      | Results . . . . .  | 200        |
| 4.5      | Discussion . . . . .   | 208        |
| 4.6      | Conclusions . . . . .  | 210        |
| <b>5</b> | <b>Laser etched phantoms for EDXRD studies</b>                                 | <b>212</b> |
| 5.1      | Introduction . . . . .   | 212        |
| 5.2      | Objectives . . . . .   | 219        |
| 5.3      | Laser system . . . . .   | 221        |
| 5.3.1    | Details of the VLS CO <sub>2</sub> Laser system . . . . .                      | 221        |
| 5.3.2    | Laser system settings . . . . .  | 223        |
| 5.4      | Classification of the laser system . . . . .                                   | 225        |
| 5.5      | Method for the calibration of the phantoms . . . . .                           | 227        |
| 5.6      | Method for establishing the intensity–PMMA thickness relationship              | 230        |
| 5.7      | Analysis . . . . .   | 230        |
| 5.8      | Discussion . . . . .   | 236        |
| 5.9      | Creation of a diffraction test phantom . . . . .                               | 238        |
| 5.9.1    | Context of this section . . . . .  | 242        |
| 5.9.2    | Experimental method for diffraction test phantom imaging                       | 242        |
| 5.9.3    | Results: Production of diffraction images of the unfilled<br>phantom. . . . .  | 244        |
| 5.9.4    | Results: Production of diffraction images of the in-filled<br>phantom. . . . . | 248        |
| 5.9.4.1  | Relative intensity image . . . . .   | 255        |
| 5.9.5    | Discussion: Creation of a diffraction test phantom . . . . .                   | 257        |
| 5.10     | Conclusions . . . . .  | 261        |
| <b>6</b> | <b>Future work</b>   | <b>263</b> |

*CONTENTS*

8

**7 Publications**

**288**

# List of Figures

|       |  |    |
|-------|--|----|
| 1.2.1 | A diagram of the principles behind Bragg's Law. . . . .  | 25 |
| 1.2.2 | p-n junction charge transport. . . . .   | 30 |
| 1.2.3 | The depletion region is filled with negative or positive ions. . . .   | 31 |
| 1.2.4 | The effects of the application of forward or reverse bias. . . . .   | 32 |
| 1.2.5 | Determining the efficiency of 1 mm thick CdTe. . . . .   | 34 |
| 1.3.1 | Attenuation coefficients of three main tissue types presented in<br>Johns and Yaffe (1987) . . . . .   | 36 |
| 1.3.2 | Figure taken from Kidane et al. (1999) which shows the differences<br>in the diffraction signal between adipose and carcinoma. . . . .       | 38 |
| 1.5.1 | Typical EDXRD system. The detector is traditionally placed per-<br>pendicular to the selected angle of the diffraction measurements. . . . . | 50 |
| 2.1.1 | Schematic of the CdTe sensor and electrodes. . . . .   | 55 |
| 2.1.2 | Diagram of read-out process. . . . .   | 56 |
| 2.1.3 | User interface to control the FPGA. . . . .  | 57 |
| 2.1.4 | Schematic of the ASIC frame read-out, taken from Jones et al.<br>(2009) . . . . .  | 58 |
| 2.1.5 | Definition of terms used in the data acquisition GUI. . . . .  | 59 |
| 2.1.6 | Diagram of charge cloud expanding across two pixels . . . . .  | 61 |
| 2.1.7 | Diagram of example charge sharing events detected by the sensor. . . . .   | 63 |

|        |  |    |
|--------|--|----|
| 2.1.8  | Detector housing unit with a Peltier cooling system, fan, and data acquisition electronics. An example 80×80 ASIC is also shown. . . . .   | 66 |
| 2.1.9  | The temperature of the copper block is set using this GUI. . . . .   | 67 |
| 2.1.10 | Measured temperature variations. The linear best fit was found to be $y=0.84x + 13.8$ , where $y$ is the temperature at the back of the ASIC and $x$ is the temperature set at the copper block. . . . . | 68 |
| 2.4.1  | Schematic of system set-up. . . . .  | 80 |
| 2.5.1  | Example of a good pixel spectrum from pixel(33,80) in ASIC A. . . . .  | 82 |
| 2.5.2  | Example of a bad pixel spectrum from pixel(53,33) in ASIC A. . . . .   | 83 |
| 2.5.3  | Example of a Gaussian curve fit to exclude the charge trapping tail of a photopeak of 60 keV . . . . .   | 84 |
| 2.5.4  | ASIC A 59.5 keV energy resolution distribution. . . . .  | 85 |
| 2.5.5  | ASIC B 59.5 keV energy resolution distribution. . . . .  | 85 |
| 2.5.6  | ASIC A 18 keV energy resolution distribution. . . . .  | 87 |
| 2.5.7  | ASIC B 18 keV energy resolution distribution. . . . .  | 87 |
| 2.5.8  | ASIC A 14 keV energy resolution distribution. . . . .  | 88 |
| 2.5.9  | ASIC B 14 keV energy resolution distribution. . . . .  | 88 |
| 2.7.1  | Example spectrum including charge sharing events from ASIC A at pixel (33,78). . . . .   | 92 |
| 2.7.2  | Energy resolution distribution with charge sharing events included for both ASICs A and B at 14 keV. . . . .   | 93 |
| 2.7.3  | Charge sharing energy resolution distribution for both ASICs A and B at 18 keV . . . . .   | 93 |
| 2.7.4  | Charge sharing energy resolution distribution for both ASICs A and B at 59.5 keV. . . . .  | 94 |
| 2.8.1  | Spectral shape for the frame rate tests. . . . .   | 96 |
| 2.8.2  | Detected number of frames compared to the theoretical expected number of frames with standard deviation. . . . .   | 99 |

|       |   |     |
|-------|---|-----|
| 2.8.3 | Percentage number of single events detected. . . . .  | 100 |
| 2.8.4 | Percentage number of events detected. . . . .   | 100 |
| 2.8.5 | Mean single events detected. . . . .  | 101 |
| 2.8.6 | Example saturation point for the row value 100 . . . . .  | 102 |
| 3.4.1 | System for determining the HVL of the system. . . . .   | 121 |
| 3.4.2 | Output response to applied external filters. . . . .  | 123 |
| 3.4.3 | Output of the source compared to the prediction. Source fluctuations are accounted for the in the errors bars. . . . .            | 124 |
| 3.4.4 | Beam spectrum used for diffraction. . . . .   | 125 |
| 3.5.1 | A diagram of the principles behind focal spot blurring. . . . .   | 128 |
| 3.5.2 | Definitions for the calculation of geometric and focal spot blurring.   | 130 |
| 3.5.3 | Schematic of the focal spot measurement. . . . .  | 131 |
| 3.5.4 | Horizontally placed edge object. . . . .  | 133 |
| 3.5.5 | Determination of the oversampled ESF. . . . .   | 134 |
| 3.5.6 | The derivative of the oversampled ESF results in the LSF for the vertical edge. . . . .   | 135 |
| 3.6.1 | Schematic of the divergence geometry. . . . .   | 136 |
| 3.6.2 | Schematic of the beam height geometry. . . . .  | 137 |
| 3.7.1 | Detector displacement from the beam, as adapted from a diagram provided by Dan O'Flynn. . . . .                                   | 138 |
| 3.7.2 | Detector displacement from the beam. . . . .  | 139 |
| 3.7.3 | The angular distribution of the multi-angle diffraction system, based on the number of pixels at the corresponding angle. . . . . | 140 |
| 3.7.4 | Calculating a spectrum of the background signal which features the XRF signal of the detector. . . . .                            | 144 |
| 3.8.1 | Photo of the diffraction system which incorporates sample scanning and detector motion. . . . .                                   | 146 |

|        |  |     |
|--------|--|-----|
| 3.9.1  | Diagram of diffraction interaction for sample with thickness $t$ .<br>Adapted from Pani et al. (2009) . . . . .  | 148 |
| 3.9.2  | Geometrical representation of the diffraction system . . . . .   | 150 |
| 3.9.3  | The right hand side shows the 2D representation and the left hand<br>side shows the view from the top of the wedge. . . . .  | 151 |
| 3.9.4  | Calculation of the thickness, $t_x$ , of the sample at a position $l_x$<br>along the wedge. . . . .  | 151 |
| 3.9.5  | Diagram of the thickness tests experiments . . . . .   | 153 |
| 3.9.6  | Diffraction ring associated with the $0.8 \text{ nm}^{-1}$ peak of PMMA.<br>Sample thickness of 6 mm. Colourbar indicates the intensity de-<br>tected. . . . .                               | 154 |
| 3.9.7  | Diffraction ring associated with the $0.8 \text{ nm}^{-1}$ peak of PMMA.<br>Sample thickness of 11.4 mm. Colourbar indicates the intensity<br>detected. . . . .                              | 155 |
| 3.9.8  | Diffraction ring associated with the $0.8 \text{ nm}^{-1}$ peak of PMMA.<br>Sample thickness of 14.15 mm. Colourbar indicates the intensity<br>detected. . . . .                             | 155 |
| 3.9.9  | Diffraction rings associated with $0.68 \text{ nm}^{-1}$ and $1.4 \text{ nm}^{-1}$ peaks<br>of caffeine. Sample thickness of 6 mm. Colourbar indicates the<br>intensity detected. . . . .    | 156 |
| 3.9.10 | Diffraction rings associated with $0.68 \text{ nm}^{-1}$ and $1.4 \text{ nm}^{-1}$ peaks of<br>caffeine. Sample thickness of 11.3 mm. Colourbar indicates the<br>intensity detected. . . . . | 156 |
| 3.9.11 | Diffraction rings associated with $0.68 \text{ nm}^{-1}$ and $1.4 \text{ nm}^{-1}$ peaks of<br>caffeine. Sample thickness of 14.3 mm. Colourbar indicates the<br>intensity detected. . . . . | 157 |
| 3.9.12 | Example of an obtained diffraction spectrum of caffeine utilising<br>all of the obtained information. Sample thickness 14.3 mm . . . .   | 158 |

|        |   |     |
|--------|---|-----|
| 3.9.13 | Example of an obtained diffraction spectrum of caffeine utilising all of the obtained information. Sample thickness 7.5 mm . . . .  | 159 |
| 3.9.14 | Example of an obtained diffraction spectrum of caffeine utilising all of the obtained information. Sample thickness 14.3 mm . . . . | 159 |
| 3.9.15 | Apparent shift in momentum transfer signal due the geometry of the pixel. . . . .   | 161 |
| 3.9.16 | Demonstrating that a diffraction pattern can appear to be present due to a fixed energy signal. . . . .                             | 162 |
| 3.9.17 | Example background signal at $5^\circ$ , shows the broad signal at 40 keV–60 keV. . . . .   | 163 |
| 3.9.18 | Parameters of the considered diffraction signal with respect to sample thickness. . . . .   | 166 |
| 3.9.19 | Intensity signal variation for the $0.68 \text{ nm}^{-1}$ peak of caffeine. . . .   | 167 |
| 3.9.20 | FWHM variation for the $0.68 \text{ nm}^{-1}$ peak of caffeine. . . . .   | 167 |
| 3.9.21 | Intensity/Area variation for the $0.68 \text{ nm}^{-1}$ peak of caffeine. . . .   | 168 |
| 3.9.22 | FWHM/Area variation for the $0.68 \text{ nm}^{-1}$ peak of caffeine. . . . .  | 168 |
| 3.9.23 | Intensity signal variation for the $1.1 \text{ nm}^{-1}$ peak of lard. . . . .  | 169 |
| 3.9.24 | FWHM variation for the $1.1 \text{ nm}^{-1}$ peak of lard. . . . .  | 169 |
| 3.9.25 | Intensity/Area variation for the $1.1 \text{ nm}^{-1}$ peak of lard. . . . .  | 170 |
| 3.9.26 | FWHM/Area variation for the $1.1 \text{ nm}^{-1}$ peak of lard. . . . .   | 170 |
| 3.9.27 | Intensity signal variation for the $0.8 \text{ nm}^{-1}$ peak of PMMA. . . . .  | 171 |
| 3.9.28 | FWHM variation for the $0.8 \text{ nm}^{-1}$ peak of PMMA. . . . .  | 171 |
| 3.9.29 | Intensity/Area variation for the $0.8 \text{ nm}^{-1}$ peak of PMMA. . . . .  | 172 |
| 3.9.30 | FWHM/Area variation for the $0.8 \text{ nm}^{-1}$ peak of PMMA. . . . .   | 172 |
| 3.9.31 | Example caffeine diffraction rings only utilising energies of 15–20 keV. . . . .  | 174 |
| 3.9.32 | Example diffraction signal of caffeine utilising only energies of 15–20 keV . . . . .   | 174 |

|        |  |     |
|--------|--|-----|
| 3.9.33 | Example diffraction signal of PMMA utilising only energies of 15–20 keV. . . . .   | 175 |
| 3.9.34 | Relationship of peak intensity at $0.68 \text{ nm}^{-1}$ with thickness for caffeine. . . . .  | 175 |
| 3.9.35 | Relationship of FWHM at $0.68 \text{ nm}^{-1}$ with thickness for caffeine. .  | 176 |
| 3.9.36 | Relationship of FWHM/Area at $0.68 \text{ nm}^{-1}$ with thickness for caffeine. . . . .   | 176 |
| 3.9.37 | Relationship of Intensity/Area at $0.68 \text{ nm}^{-1}$ with thickness for caffeine. . . . .  | 177 |
| 3.9.38 | Relationship of peak intensity at $0.8 \text{ nm}^{-1}$ with thickness for PMMA.   | 178 |
| 3.9.39 | Relationship of FWHM at $0.8 \text{ nm}^{-1}$ with thickness for PMMA. .   | 178 |
| 3.9.40 | Relationship of FWHM/Intensity at $0.8 \text{ nm}^{-1}$ with thickness for PMMA. . . . .   | 179 |
| 3.9.41 | Relationship of Intensity/Area at $0.8 \text{ nm}^{-1}$ with thickness for PMMA.   | 179 |
| 3.9.42 | Relationship of intensity at $1.1 \text{ nm}^{-1}$ with thickness for lard. . . .  | 180 |
| 3.9.43 | Relationship of FWHM at $1.1 \text{ nm}^{-1}$ with thickness for lard. . . .   | 181 |
| 3.9.44 | Relationship of intensity/area at $1.1 \text{ nm}^{-1}$ with thickness for lard.   | 181 |
| 4.3.1  | Diffraction system used for the materials library . . . . .  | 199 |
| 4.4.1  | Obtained diffraction spectra. . . . .  | 202 |
| 4.4.2  | Obtained diffraction spectra for plastics and gels. . . . .  | 203 |
| 4.4.3  | Diffraction spectra obtained from the gel samples. . . . .   | 204 |
| 5.3.1  | Demonstration of the halftone dithering. . . . .   | 222 |
| 5.4.1  | Etching scale. The etch depth depends on several variables including the speed and power settings of the laser system. . . . .                       | 226 |
| 5.5.1  | The input vectorised image (l) consisting of varying greyscale blocks and the resulting etched PMMA piece with different speed settings (r). . . . . | 228 |

|       |  |     |
|-------|--|-----|
| 5.5.2 | Schematic of the system used for establishing response functions for the laser system. . . . .   | 229 |
| 5.7.1 | Flat field image at 22 kVp tube setting and no external PMMA filtration. The intensity values are shown in the colourbar. . . . .                                | 231 |
| 5.7.2 | Normalised intensity (digital number (dN)) filter response functions at different maximum tube settings. . . . .   | 232 |
| 5.7.3 | Speed calibration phantom. Image obtained at 18 kVp tube setting. The colourbar shows the intensity values. . . . .  | 233 |
| 5.7.4 | The final averaged response curve obtained for etching speed of 5%. 234  |     |
| 5.7.5 | Speed setting response of the laser system to the input greyscale values. The speed settings combinations are tabulated in Table 5.5.1 . . . . .                 | 235 |
| 5.7.6 | Change in the etch depth of the phantom with greyscale values. The changes can represent the changes in the presence of healthy and non-healthy tissues. . . . . | 236 |
| 5.9.1 | Original spiculated tumour ROI. The colourbar shows the corresponding greyscale values. . . . .  | 239 |
| 5.9.2 | Example transmission images for 15% then 15% (left) and 5% (right) . . . . .   | 240 |
| 5.9.3 | 3D representation of an etched tumour. . . . .   | 241 |
| 5.9.4 | A photo of the 6.5 cm thick PMMA and the spiculated tumour etched into the material using different speed settings. . . . .                                      | 241 |
| 5.9.5 | Schematic of phantom placement in the diffraction system. . . . .  | 242 |
| 5.9.6 | Primary region of interest and the copper marker placement. . . . .  | 243 |
| 5.9.7 | Relationship $PMMA_t(I_d)$ between the signal of diffraction of PMMA at $0.78 \text{ nm}^{-1}$ and the sample thickness. . . . .                                 | 245 |

- 5.9.8 Top left: The original transmission image of the infiltrating ductal carcinoma. The position of the scanned ROI is indicated by the black box. Top right: The original transmission image of the tumour re-binned such that the pixel size corresponds to the steps used in the scan, i.e.  $0.5\text{ mm}\times 0.5\text{ mm}$ . Bottom left: The intensity of the diffraction data at  $0.78\text{ nm}^{-1}$ . Bottom right: The thickness variation of the phantom in the region of interest. All images have the same contrast and the greyscale values correspond to the average thickness found at the corresponding scan position. . . . . 247
- 5.9.9 Images from the PMMA and water scan. Top left: The original transmission image of the infiltrating ductal carcinoma. The position of the scanned ROI is indicated by the black box. Top right: The original transmission image of the tumour re-binned such that the pixel size corresponds to the steps used in the scan, i.e.  $0.5\text{ mm}\times 0.5\text{ mm}$ . Bottom left: The intensity of the diffraction data at  $0.78\text{ nm}^{-1}$ . Bottom right: The thickness variation of the phantom in the region of interest. All images have the same contrast and the greyscale values correspond to the average thickness found at the corresponding scan position. . . . . 249
- 5.9.10 Top left: The original transmission image of the infiltrating ductal carcinoma. The position of the scanned ROI is indicated by the black box. Top right: The original transmission image of the tumour re-binned such that the pixel size corresponds to the steps used in the scan, i.e.  $0.5\text{ mm}\times 0.5\text{ mm}$ . Bottom left: The intensity of the diffraction data at  $1.6\text{ nm}^{-1}$ . Bottom right: The thickness variation of the phantom in the region of interest. All images have the same contrast and the greyscale values correspond to the average thickness found at the corresponding scan position. . . . . 251

|        |  |     |
|--------|--|-----|
| 5.9.11 | Top image: The intensity of the diffraction at $0.78 \text{ nm}^{-1}$ and the positioning of the corresponding sub ROIs. Bottom image: The original transmission image of the phantom with pixel size corresponding to that of the scan, i.e. $0.5 \text{ mm} \times 0.5 \text{ mm}$ . . . . . | 253 |
| 5.9.12 | Variation in the diffraction intensity contrast with varying diffraction window. . . . .   | 254 |
| 5.9.13 | Variation in the diffraction intensity contrast with varying diffraction window. . . . .   | 255 |
| 5.9.14 | Relative intensity images of the scanned phantom. From top left clockwise, the momentum transfer windows are $0.01 \text{ nm}^{-1}$ , $0.02 \text{ nm}^{-1}$ , $0.2 \text{ nm}^{-1}$ and $0.4 \text{ nm}^{-1}$ . The colorbar indicates the relative intensity. . . . .                        | 256 |
| 5.9.15 | Relationship between the contrast of the sub ROIs with respect to the momentum transfer window. . . . .  | 257 |

# List of Tables

|  |     |
|--|-----|
| 1.2.1 Semiconductor material properties. . . . .   | 29  |
| 1.4.1 Summary of diffraction parameters used in the literature. ✓ indicates<br>the parameter is used. . . . .  | 43  |
| 2.5.1 Detector average energy resolution values calculated from all pixel<br>values for ASIC A and ASIC B. . . . .   | 89  |
| 2.5.2 The percentage number of pixels not used for the energy resolution<br>analysis. . . . .  | 89  |
| 2.6.1 Calculated detector efficiency at 59.5 keV using the working areas<br>of the ASICs. . . . .  | 91  |
| 2.7.1 Detector average energy resolution values. . . . .   | 94  |
| 2.7.2 Detector efficiency calculation. . . . .   | 95  |
| 2.8.1 Frame rates and row values. . . . .  | 97  |
| 2.8.2 Detected frames compared to the number of written frames . . . .   | 98  |
| 2.8.3 Frame rate and row value. . . . .  | 103 |
| 2.8.4 System crashes experienced during frame rate acquisitions . . . .  | 103 |
| 3.4.1 Aluminium filter details. Using the density of aluminium at room<br>temperature, the value of the thickness can be calculated from the<br>different surface areas. . . . . | 122 |
| 3.5.1 X-ray source operational limits. . . . .   | 126 |

|  |     |
|--|-----|
| 3.7.1 The expected photon energies corresponding to the momentum transfer values of interest, based on the geometry of the system. . . | 141 |
| 3.7.2 X-ray Fluorescence lines of cadmium and tellurium given in keV. . .  | 142 |
| 3.9.1 Percentage of the total absorption through the processing of incoherent scatter. . . . .   | 163 |
| 4.3.1 Summary of the plastics used for the library . . . . .   | 196 |
| 4.3.2 Biodegradable gel samples . . . . .  | 198 |
| 4.4.1 Summary of peak positions and FWHM values. . . . .   | 205 |
| 4.4.2 Data from Poletti et al. (2002a) . . . . .   | 206 |
| 5.3.1 Colour functionality in the laser system software. . . . .   | 223 |
| 5.5.1 Speed combinations used for etching into 6.5 mm thick PMMA . .   | 227 |
| 5.5.2 Mean energy values of the spectra using a Mo target . . . . .  | 229 |
| 5.7.1 Details of the speed settings used and the corresponding maximum etch depth. . . . .   | 235 |

# Chapter 1

## Introduction

### 1.1 Background

X-ray diffraction can be used to explore the molecular structure of crystalline and amorphous materials. The technique is reliant on the experimental system and the utilised detector. The development of energy resolving semiconductor detectors has made it possible to explore x-ray diffraction in a laboratory setting using polychromatic sources, such as those found in hospitals or easily purchased varieties. The relationship between the molecular structure and the diffraction signature has made it possible to explore the differences in the diffraction signatures of, for example, carcinoma and adipose tissue for potential use in a clin-

ical environment for diagnosis and therapeutic techniques. Current diffraction systems are not necessarily clinically viable for imaging of the breast or biopsy samples, but the use of room temperature detectors and possible development of portable detector systems has made this more of a reality.

## 1.2 Photon interactions with matter

The following details the types of photon interactions relevant to the energies of interest for the diffraction conducted in this research, as well as theory relevant to photon detection in semiconductors.

### 1.2.1 Photoelectric absorption

Photoelectric absorption occurs when a photon interacts with an atom resulting in the ejection of an electron from its electron state, due to the transfer of photon energy to kinetic energy of the electron. The electron thus gains enough energy to be ejected from the atom and is known as ionisation. This can result in an electron from a higher electron state filling the vacated state, resulting in the emission of another photon. This process is called X-ray Fluorescence (XRF). The kinetic energy of the photoelectron is given by Eqn 1.2.1.

$$E_e = h\nu - E_b \quad (1.2.1)$$

Where  $E_e$  is the energy of the photoelectron,  $h$  is Plank's constant,  $\nu$  is defined as the photon frequency thus  $h\nu$  is the incident photon's energy and  $E_b$  is the binding energy of the electron. On ionising the atom it is left in an excited state, and to recover the lowest energy formation, an electron from an outer atomic orbit replaces the former, thereby releasing a photon of equivalent energy to the change in energy between energy states. These transition lines are based on a

material's electron state structures and are therefore known. Most ionisation occurs from the K-shell (the most tightly bound shell) in the atom.

The probability of interaction is complex as there is no analytical expression available, however, an approximate expression is available and is given by Eqn 1.2.2, where  $\tau$  is the probability of photonelectric interaction and  $n$  is an index value of between 3 and 4,  $Z$  is the atomic number and  $E_\gamma$  is the photon energy.

$$\tau \approx \frac{Z^n}{E_\gamma^3} \quad (1.2.2)$$

Once a photoelectron leaves the atom in an ionised state, it is possible for an electron from a higher energy state to fill the vacancy left by the photoelectron. Normally in this instance energy is lost from the electron as a photon, but it is also possible that this energy is transferred to another electron within the atom. In this case, another electron gains enough kinetic energy to leave its energy state and ionise the atom. This second electron is known as an Auger electron.

### 1.2.2 Incoherent scatter

Compton scatter, also known as incoherent scatter, is the interaction of a photon with an electron that is not tightly bound to the atom, and as such can be considered a free electron. This is due to the fact that the binding energy of these outer shell electrons is much lower than those of the inner shells. If the electron is considered to be at rest, the interaction results in the recoil of the electron and the scattering of the photon through angle  $\theta$ . The resultant energy of the photon,  $E_\gamma^1$ , is always less than the photon's initial energy,  $E_\gamma^o$ . The photon scatters through angle  $\theta$  and the electron recoils with angle  $\phi$ . From the principles of momentum conservation and conservation of energy, the energy of the photon after the interaction is given by Eqn 1.2.3,

$$E_\gamma^1 = \frac{E_\gamma^o m_e c^2}{m_e c^2 + E_\gamma^o (1 - \cos \theta)} \quad (1.2.3)$$

where  $m_e$  is the rest mass of the electron, and  $c$  is the speed of light through free space. Each successive interaction of this type will result in a photon with less energy and with a different direction of travel.

The total intensity,  $I_c(Z, q)$  attributed to Compton scatter emerging from a voxel (volume element) of the object can be, as presented in Harding (2004), written as

$$I_c(Z, q) = I_o(E_\gamma^o) A_p(E_\gamma^o) \frac{d\sigma_c(Z, q)}{d\Omega} N_a A_s(E_\gamma^1) \Delta\Omega + M_C \quad (1.2.4)$$

where  $I_o(E_\gamma^o)$  is the incidence intensity of photons with energy  $E_\gamma^o$  and  $A_p(E_\gamma^o)$  is the attenuation of the primary incident photons i.e. the attenuation of the photons that occurs between the source and the voxel. The other symbols include the atomic number  $Z$  of the material being irradiated,  $N_A$  for the surface density of atoms in the voxel (atoms  $\text{m}^{-2}$ ). In this equation, the cross section of incoherent scatter,  $\frac{d\sigma_c(Z, q)}{d\Omega}$ , has units of  $\text{m}^2 \text{atoms}^{-1} \text{sr}^{-1}$ .  $A_s(E_\gamma^1)$  is the attenuation of the secondary photon between voxel and detector,  $\Delta\Omega$  is the solid angle of the detector in steradians,  $M_C$  is the multiple scatter component. As defined by Hubbell et al. (1975),  $q$  is the momentum transferred to the atom, as shown in Eqn 1.2.5

$$q = 2k\hbar \sin\left(\frac{\theta}{2}\right) \frac{\sqrt{1 + (k^2 + 2k) \sin^2\left(\frac{\theta}{2}\right)}}{1 + 2k \sin^2\left(\frac{\theta}{2}\right)} \quad (1.2.5)$$

where  $\hbar$  is the reduced Planck's constant and  $k$  is the photon wave vector. In the case where  $\theta$  and  $k$  are small, this can be reduced to Eqn 1.2.6

$$q = 2k\hbar \sin\left(\frac{\theta}{2}\right) \quad (1.2.6)$$

The cross section of Compton interaction is based on the Klein–Nishina cross section  $d\sigma_k(Z, q)$  and the incoherent scatter function,  $S(Z, q)$

$$\frac{d\sigma_c(Z, q)}{d\Omega} = \frac{d\sigma_k(Z, q)}{d\Omega} S(Z, q) \quad (1.2.7)$$

$S(Z, q)$  takes into consideration the electron distribution and adjusts for atomic binding energies. These have been tabulated for all  $Z$  values of 1-100 by Hubbell et al. (1975).

### 1.2.3 Coherent Scatter

Rayleigh Scattering, also known as coherent scattering, is an elastic collision in which a photon interacts with a tightly bound electron, causing the electron to oscillate and emit radiation of the same wavelength as the incident photon, and so the photon energy remains unchanged after the interaction. When photons are considered as waves rather than particles, in materials with regularly spaced atomic structures, or lattices, the effect leads to constructive interference provided the condition for constructive interference is met. The condition requires that the additional path length travelled by a wave is equivalent to a whole wavelength. Figure 1.2.1 shows the principle behind x-ray diffraction.

$$n\lambda = 2d \sin \frac{\theta}{2} \quad (1.2.8)$$

Bragg's Law, as defined in Eqn 1.2.8, relates the photon wavelength  $\lambda$ , with the scatter angle  $\frac{\theta}{2}$  and the lattice planes spacing,  $d$ , and  $n$  is an integer to account for the fact that only path lengths equal to integer multiples of wavelengths will lead to constructive interference. In this case, the scatter angle is that between the atomic plane and the incident radiation.

The cross section of interaction,  $\frac{d\sigma_{coh}}{d\Omega}$ , for coherent scatter is given by Eqn 1.2.9

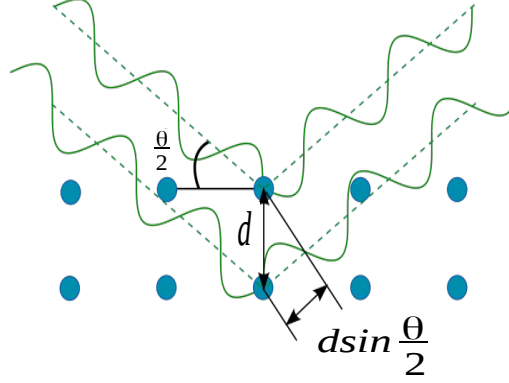


Figure 1.2.1: A diagram of the principles behind Bragg's Law.

$$\frac{d\sigma_{coh}}{d\Omega} = \sigma_{Th} F_{mol}^2(x, Z) \quad (1.2.9)$$

where  $\sigma_{Th}$  is the coherent cross-section for the elastic interaction of a photon with a free electron and is given by  $r_o^2/2(1 + \cos^2 \theta)$  in units of  $m^2sr^{-1}$ ,  $r_o$  is the classical electron radius.  $F_{mol}$  is the molecular structure function, also known as the molecular form factor. The complex function  $F_{mol}(x, Z)$  is related to the Fourier Transform of the charge distribution of electrons in the scattering atoms: it is therefore a property of only the material (Harding et al. (1987)). The transfer of momentum from the scattering structures to the photon causing it to deviate through scatter angle  $\theta$ , is represented by the momentum transfer function,  $\chi$ , where

$$\chi = \frac{\sin(\theta/2)}{\lambda} \quad (1.2.10)$$

The relationship between the momentum transfer and the  $d$  spacing is given in Eqn 1.2.11

$$\chi = \frac{1}{2d} \quad (1.2.11)$$

where the units for momentum transfer are given as  $\text{nm}^{-1}$  for materials with  $d$ -spacing values of the order of Angstroms ( $10^{-10}$  m)

From a mathematical standpoint,  $\chi$  is a function  $\chi(\theta, \lambda)$ , where  $\theta$  is the photon scatter angle and  $\lambda$  is the wavelength of the photon and there is an energy dependence on the momentum transfer. Therefore, when measuring the diffraction signal of a target, there are two possibilities; a variation of angle with a fixed  $\lambda$ , known as Angular Dispersive X-ray Diffraction (ADXRD), or the variation of  $\lambda$  and thus the energy of the incoming photons, known as Energy Dispersive X-ray Diffraction (EDXRD). In the case of ADXRD, an x-ray detector is placed at varying angles, whereas in EDXRD the detector remains in a fixed position and the energy of the x-rays is varied. This is typically done with a polychromatic source.

Powdered materials such as illicit drugs have a periodic electron distribution, and therefore Bragg's law is met and sharp diffraction peaks can be seen, depending on the spacing between the scattering planes. These materials have long range order due their periodicity. This is characterised by the unit cell which is replicated throughout the structure. In this case, coherent scatter can only take place over a limited Bragg angle. Amorphous materials like plastics and breast tissue however have short range order and therefore broader diffraction peaks. Short range order is related to first or second neighbour atoms and beyond this the positions of the atoms are not correlated, such is the case in a solid. Due to the lack of a repetitive structure, coherent scatter can occur in many directions leading to a wide range of possible Bragg angles. In this case, the expected intensity of the diffraction peak would be lower than that of a material with long range order.

The cross-section of interaction is dependent on the molecular form factor.

The molecular form factor  $F_{mol}$  is related to the molecular structure of the material, quantified by the electron density of the scattering atoms that form the molecule. In the case of elemental form factors, the form factor is the Fourier Transform of the electron charge density. The simplest model used to calculate the molecular form factors is the Independent Atomic Model (IAM), as in Eqn 1.2.12.

$$F_{mol}^2(x) = \sum_i f_i^2 a_i \quad (1.2.12)$$

where  $f_i$  is the elemental form factor and  $a_i$  is the atomic abundance. The IAM is also known as the free gas model, and assumes that each molecule will interact independently of the others. Additional complexity to the model can be provided by considering the correlation between the electrons of the different atoms in the same molecule. Further additions to the model can be made by considering the fact that there are interference effects due to the phase nature of waves, which leads to an angular-dependence structure, which is the diffraction pattern itself. In this case, the molecular form factor provides information about the material environment, as crystalline structure show sharp diffraction peaks due to the lattice order, while amorphous materials have broader diffraction peaks.

The measurement of the molecular form factors which determine the diffraction profiles of each material, is based on the electron distribution, as described in detail by Hubbell et al. (1975). Form factors of water have been determined by Morin (1982) and Latha et al. (2011), and agree with additional literature, such as Poletti et al. (2002a).

The mechanism of x-ray diffraction can be used to explore the material properties of the item for which x-ray photons interact. To then detect the photons which interact, it is necessary to have a detector capable of detecting x-rays. In addition to this, a detector which can measure the energy of a detected photon is also necessary for EDXRD methods. For this purpose, semiconductors are used.

### 1.2.4 X-ray semiconductor detectors

Regular structures within solids leads to established energy bands in which all electrons must reside, leading to the development of a valence band and a conductance band. The is the minimum energy separating the bands, and therefore the minimum energy required to excite an electron from the valence band to the conductance band. In the case of insulators, the band gap is high but in a semiconductor the band gap is at a level such that charge can be generated when a photon deposits its energy, but not so close such that charge can be generated through thermal combination. A band gap of between 1 eV and 5 eV defines a semiconductor.

The ionisation energy of semiconductors, or the  $W$ -value, is the value required to produce electron-hole pairs. The energy deposited by photons will lead to a number of electron-hole pairs being produced, based on the  $W$ -value. This means that the charge generated is proportional to the energy deposited by the photons. Common semiconductor materials used for x-ray imaging in medical, security, astronomy and other applications are shown in Table 1.2.1. These are Germanium (Ge), Silicon (Si), Cadmium Zinc Telluride (CdZnTe)-typically shortened to CZT, or Cadmium Telluride (CdTe).

When detecting photons, it is important that the detected charge and resulting pulse in the detector is genuinely a consequence of the interaction between photons and the material. The photoelectric absorption is the desired interaction, and the cross-section of interaction has a dependency on  $Z$ . From Table 1.2.1, it can be seen that the effective atomic number of CZT and CdTe are 49.1 and 50 respectively, making these semiconductor materials suitable for detection of higher energy photons, when compared to Ge and Si. The pair creation value ( $W$ -value) is the energy required to make an electron-hole pair (e-h). Therefore it would require a photon with energy of 44 eV to make 10 e-h pairs in Cadmium

| Material  | CdZnTe    | CdTe      | Ge          | Si          |
|---|-----------|-----------|-------------|-------------|
| Atomic number   | 49.1      | 50        | 32          | 14          |
| Density ( $\text{gcm}^{-3}$ )   | 5.78      | 5.85      | 5.33        | 2.33        |
| Band gap $E_{bg}$ (eV)  | 1.57      | 1.5       | 0.67        | 1.12        |
| Pair creation energy $W$ (eV)   | 4.6       | 4.4       | 3.0         | 3.6         |
| Resistivity $\rho$ ( $\Omega\text{cm}$ )                              | $10^{10}$ | $10^9$    | 50          | $< 10^4$    |
| Electron mobility $\mu_e$ ( $\text{cm}^2\text{V}^{-1}\text{s}^{-1}$ ) | 1000      | 1100      | 3900        | 1400        |
| Electron lifetime $\tau_e$ (s)  | $10^{-6}$ | $10^{-6}$ | $> 10^{-3}$ | $> 10^{-3}$ |
| Hole mobility $\mu_h$ ( $\text{cm}^2\text{V}^{-1}\text{s}^{-1}$ )     | 10 – 80   | 100       | 1900        | 480         |
| Hole lifetime $\tau_h$ (s)  | $10^{-6}$ | $10^{-6}$ | $10^{-3}$   | $10^{-3}$   |

Table 1.2.1: Semiconductor material properties.

Telluride. When the energy is of the order of keV, this would result in the order of 1000 e-h pairs. Therefore, one event is able to produce a large number of charge carriers, which in general means semiconductors have good energy resolution as well as a good signal to noise ratio. It is not possible to create charge at energies below the  $W$ -value as a result of photon energy deposition.

#### 1.2.4.1 Charge carrier transport

The most common form of semiconductor is known as a p-n junction, consisting of p-type and n-type materials that have been doped to either create more acceptor sites (holes) in the case of p-type materials, or have more donor electrons in the case of n-type materials. This affects the energy levels of the material.

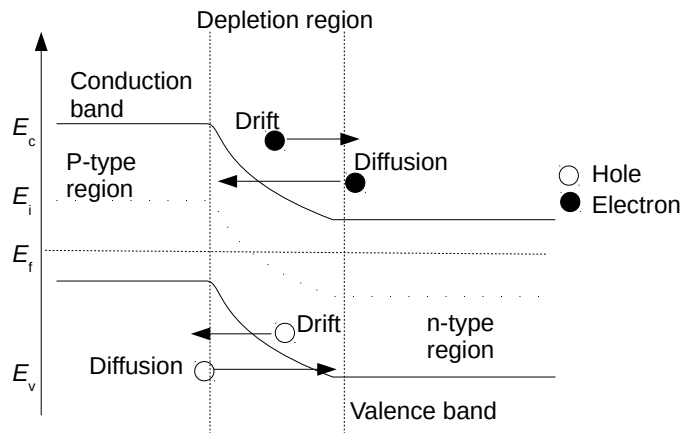


Figure 1.2.2: p-n junction charge transport.

When these materials are brought into close contact, diffusion can occur across the contact due to the difference in charge concentrations until equilibrium is reached. The transport of conduction electrons from the n-type to the p-type region leaves behind a positive charge in the donor impurity that is not free to migrate. In the case of the n-type material, holes diffuse across the junction to combine with an electron, which therefore leaves behind a fixed negative charge at an acceptor site in the p-type side. The diffusion effects lead to the build up of negative space charge on the p-type side and positive space charge on the n-type material. Figure 1.2.2 shows a p-n junction diagram.  $E_c$  is the energy level of the conductance band,  $E_f$  is the Fermi level,  $E_v$  is the energy of the valence band, and finally  $E_i$  is the built-in potential, and is equal to the difference between the Fermi levels of the two regions. For a system in thermal equilibrium, the Fermi level corresponds to the energy at which the probability of an electron occupying an energy state  $E_f$  is 50%.

The transport of the charge under equilibrium leads to an area called the depletion region- a region where there are no free charge carriers, as shown in

Figure 1.2.3. The space charge leads to a potential difference and therefore an electric field across the depletion region that prevents further diffusion taking place. This also defines the width of the diffusion region.

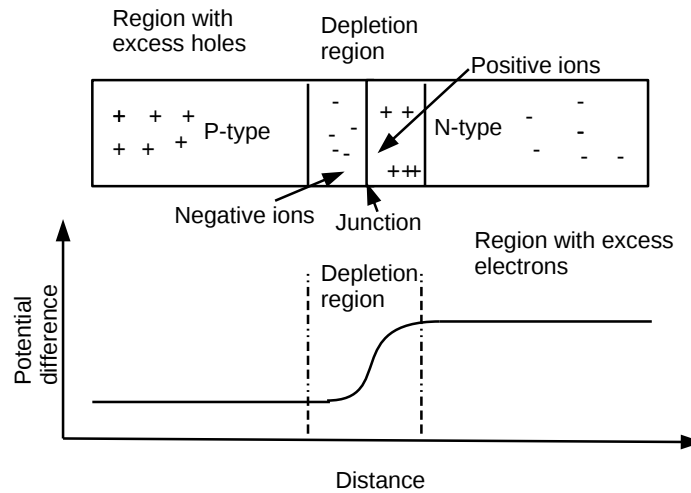


Figure 1.2.3: The depletion region is filled with negative or positive ions.

The depletion region width can be increased and decreased depending on the application of a forward or reverse bias to the two contacts, as shown in Figure 1.2.4. In the case of forward bias, the effect is to apply an electromagnetic force to the electrons in the n-type region, pushing them towards the junction, and in the case of holes, these are pushed from the p-type material. This therefore results in the transport of the majority charge carriers.

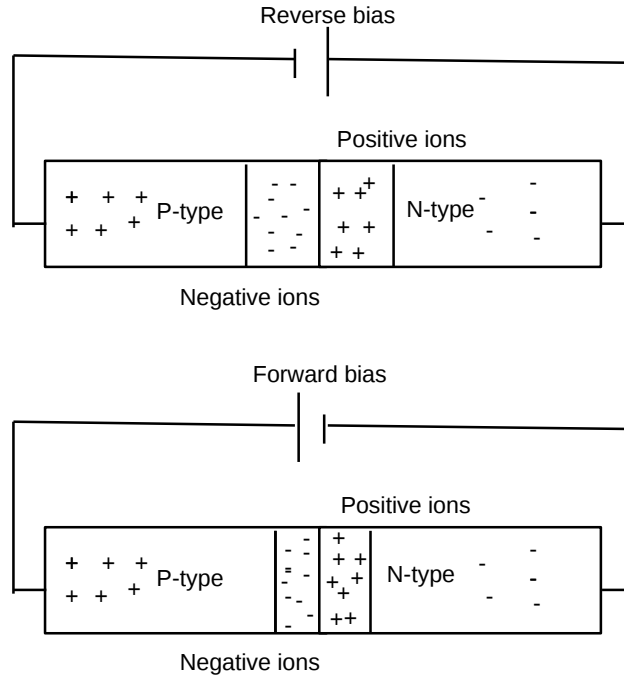


Figure 1.2.4: The effects of the application of forward or reverse bias.

Reverse biasing applies the negative terminal of a power supply to the p-type material and the positive to the n-type material. This leads to the conduction of minority carriers i.e. a flow of electrons in p-type material and flow of holes in n-type material. This therefore leads to the development of a diode whereby current easily flows in one direction but has high resistance in the opposite direction. A reverse bias increases the potential difference and therefore widens the depletion region.

The band gap of the material is important, as the probability per unit time of thermally generating an electron-hole pair in a semi-conductor is given by:

$$p(T) = CT^{\frac{3}{2}} e^{-\frac{E_g(T)}{2k_B T}} \tag{1.2.13}$$

where  $C$  is a constant which is dependent on the type of material,  $T$  is tem-

perature,  $E_g(T)$  is the band gap of the material and  $k_B$  is Boltzmann's constant.

Materials with a higher band gap value are less likely to have thermally generated e-h pairs than semiconductor materials with lower values, for a given temperature. A good photon detector should ideally be generating charge from the interaction of photons with the semiconductor material alone and not from thermal generation. It is therefore important that a detector has a low leakage current for use in photon detection systems. The higher band gap of CdTe (more than double that of Ge) is why the leakage current is low, making it attractive for potential room temperature portable systems. It is a requirement for detectors such as Ge and Si to be cooled, typically to liquid nitrogen temperatures to be used optimally and to reduce thermal charge generation. Due to their larger band gaps, CdTe and CZT do not require such cooling as they inherently have little to no thermal charge generation at room temperature, making them a viable option for room temperature based applications and portable systems as they would not need an accompanying cryogenic cooling system.

The charge transport properties of electrons in both CZT and CdTe is good with values of  $1000\text{--}1100\text{ cm}^2\text{V}^{-1}\text{s}^{-1}$  and with lifetimes of the order of microseconds. Hole mobilities, as detailed in Table 1.2.1, have been found to lie in the range  $10\text{--}100\text{ cm}^2\text{V}^{-1}\text{s}^{-1}$  and lifetimes are of the order  $10^{-6}\text{ s}$ . Cadmium Telluride detectors have poor charge collection efficiency due to the life times and mobilities of the charge carriers. This leads to the so called tailing associated with lower energies of a photopeak, caused by incomplete charge collection.

Any sensor material for use with x-rays needs to be able to absorb the photons to detect them in the first place. Figure 1.2.5 shows that from the interaction of photons with CdTe of 1 mm thickness, the materials efficiency at detecting photons is 80% at energies of 100 keV, and almost 100% at 60 keV.

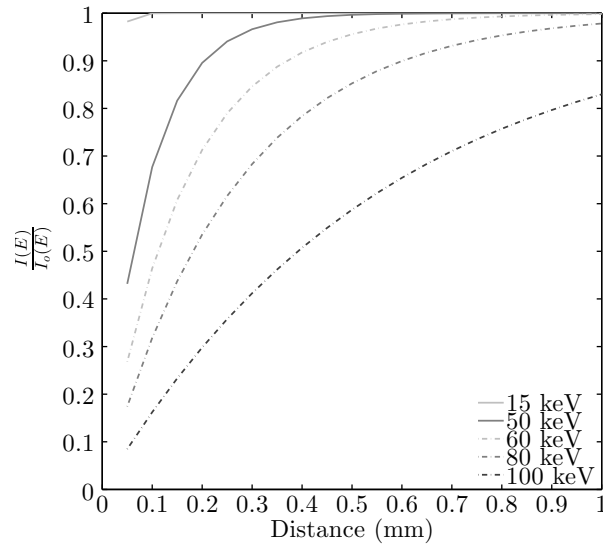


Figure 1.2.5: Determining the efficiency of 1 mm thick CdTe.

The efficiency was calculated based on the relationship in Eqn 1.2.14, known as the Beer–Lambert or Beer–Lambert–Bouger Law, which relates the attenuation of photons to the properties of the material through which the photons travel,

$$I(E) = I_o(E)e^{-\mu(E)x} \quad (1.2.14)$$

where  $I(E)$  is the intensity of photons with energy  $E$ , after travelling through material with thickness  $x$ ,  $I_o$  is the initial intensity of photons with energy  $E$ ,  $\mu$  is the linear attenuation coefficient, which is a property of the material itself, and is a function of photon energy. At 1.5 MeV, not shown on Figure 1.2.5 but determined from the NIST XCOM data, efficiency drops to less than 1% for 1 mm thickness material.

Previously, high purity germanium has been the detector of choice for lab based EDXRD applications due to its high energy resolution, stability and energy efficiency up to 100 keV.

### 1.3 Diffraction and breast tissue

Energy Dispersive X-ray Diffraction (EDXRD) and Angular Dispersive X-ray Diffraction (ADXRD) have both been used for medical purposes, security, material science and other fields. Scattering in medical terms was previously seen as a nuisance, contributing unwanted signal to images. Speller and Horrocks (1991), Speller (1999), and Royle et al. (1999) discuss the potential for using x-ray scatter information as a means to obtain further characteristics of normal tissues and disease states. Current diagnostic technologies such as mammography detect photons that have not had an interaction with the patient and therefore provide more information about what is not present in the patient than is present. In order for photons to scatter, either coherently or incoherently, there has to be an interaction with the matter that is present in the tissue. Therefore scattering signal can potentially provide information about unhealthy and healthy tissue types within the patient.

According to the World Health Organisation (WHO) (World Health Organisation (2012)), the total number of deaths caused by breast cancer in 2008 was 482,485 people, of which 154,507 (32%) were in Europe, with the majority of these female. The U.K runs a screening program for women over 50 years of age, performing mammography every 2-3 years for those eligible. The NHS Breast Screening programme in the U.K examined over two million women each year between 2009 and 2011 (NHS Cancer Screening Programmes (2012)). Mammography utilises the attenuation properties and density variations of tissue in the breast. Transmission imaging is reliant on the differences in the attenuation coefficients to distinguish different tissue types. Figure 1.3.1 shows that the linear attenuation coefficients are similar for the fibrous and infiltrating ductal carcinoma.

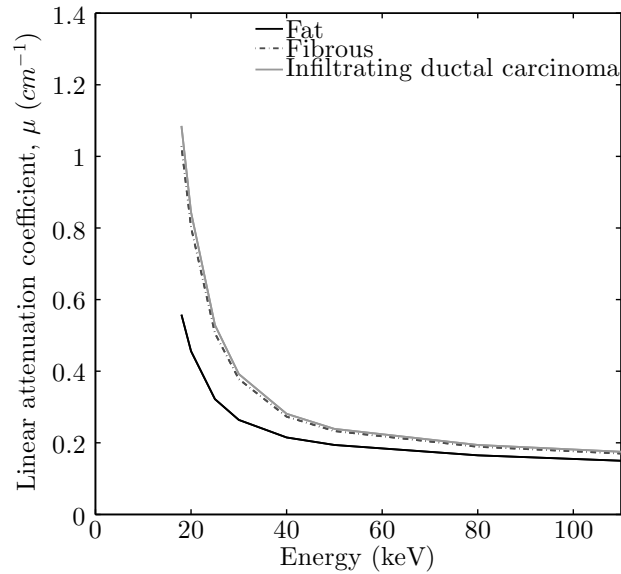


Figure 1.3.1: Attenuation coefficients of three main tissue types presented in Johns and Yaffe (1987)

The variations in the linear attenuation coefficients of major tissue types including, fat, fibrous and infiltrating ductal carcinoma, were measured by Johns and Yaffe (1987). Figure 1.3.1 shows that for a standard energy used in mammography, 18 keV, the maximum possible contrast between the fibrous tissue and infiltrating ductal carcinoma is only 5%. Therefore using the linear attenuation properties of the materials would make it difficult to separate the two tissue types in the materials at the energies used in mammography. Any distinction between the two tissue types is harder still in dense breasts, which contains a high proportion of fibroglandular tissue. Due to the similarity between fibroglandular tissue and carcinoma, it would also be difficult to distinguish between healthy and non-healthy tissue types. Fibroglandular and fat are considered to be healthy tissue types. The variation in signal between fat and fibroglandular would therefore look similar to signal variation between fat and infiltrating ductal carcinoma.

A suitable imaging technique must distinguish between the two or more tis-

sues being considered, such that there is high contrast between healthy and unhealthy tissues. X-ray diffraction is a potential technique that can be utilised to distinguish different tissue types. Several works have considered the coherent scatter signatures from healthy breast tissue and non-healthy tissues, considering their scatter profiles and establishing that adipose tissue has a diffraction peak at  $1.1 \text{ nm}^{-1}$ , while carcinoma has been shown to have a broader peak at  $1.6 \text{ nm}^{-1}$  (Kidane et al. (1999), Royle et al. (1999), Castro et al. (2004), Castro et al. (2005a)). In the work by Castro et al. (2005a), three excised breast tissue samples were scanned at the Brazilian Synchrotron Light Laboratory using photons of 11 keV. The scan sites were selected based on the visual inspection of a pathologist, selecting six sites based on the presence of healthy connective tissue, and adipose tissue and infiltrating carcinoma. Two scans were acquired, focussing on healthy regions from the tumour and the tumour itself. The samples had been fixed and had histopathological reference data. In Castro et al. (2004), tissue samples from breast, kidney and uterus were also scanned at the same synchrotron facility. The work by Kidane et al. (1999) utilised 100 samples obtained from women who underwent a mastectomy, lumpectomy or reduction mammoplasty procedures. The differences between normal tissue comprising of a mixture of adipose and fibroglandular tissue or neoplastic tissue which are carcinoma, benign, fibroadenoma and fibrocystic tissue, were considered. Fibroglandular tissue consists of equal amounts of fibrous or glandular tissue. When considering the literature, Kidane et al. (1999) has one of the largest tissue samples analysed that considered the difference between tissue types. It was shown that the diffraction signal of carcinoma had a weaker intensity signal at  $1.6 \text{ nm}^{-1}$  compared to the diffraction signal of adipose, which has a maximum diffraction signal at  $1.1 \text{ nm}^{-1}$ . It was also shown that the spectral shape of carcinoma was broader than that of the pure adipose tissue, as shown in Figure 1.3.2. Kidane et al. (1999) utilised a lab based system which included a polychromatic x-ray source.

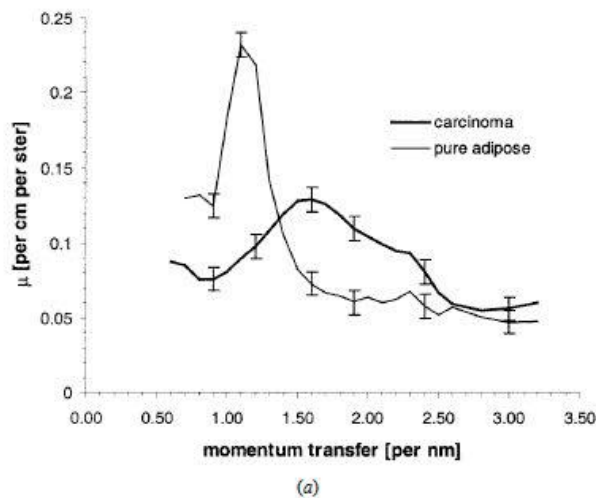


Figure 1.3.2: Figure taken from Kidane et al. (1999) which shows the differences in the diffraction signal between adipose and carcinoma.

The work conducted by Castro et al. (2005a) and by Poletti et al. (2002a) show agreement with the measured momentum transfer values of Kidane et al. (1999).

### 1.3.1 Imaging

The extension of using x-ray diffraction signatures of breast tissue to imaging has been conducted by Fernández et al. (2002) and Fernández et al. (2008) using a synchrotron facility, as well as Griffiths et al. (2004), Griffiths et al. (2008) and by Sidhu et al. (2009). Imaging in all cases involved scanning the sample and acquiring data at each location to build up a 2D image. Many research papers however are based on the use of synchrotron facilities to consider the differences between, for example, healthy and malignant tissue, or fibroglandular and benign tissue. In order to quantify diffraction spectra and identify the sample under consideration, diffraction peak positions are used to identify materials. In addition to the peak positions, other values from the spectra can be used to quantify diffraction spectra such as the intensity of the diffraction peaks, as

used by Griffiths et al. (2008), Castro et al. (2004), Kidane et al. (1999), and Evans et al. (1991), the peak area used by Ryan and Farquharson (2007a) and Theodorakou and Farquharson (2009), the full width half maximum of the peak as used by Poletti et al. (2004) and Elshemey et al. (2010), and the ratio of peaks heights, as utilised by Royle and Speller (1995) and Elshemey et al. (2010).

Due to its nature of being able to separate coherent scatter signal based on the molecular structure of materials, diffraction has been proposed as a means of intraoperatively testing surgical margins in works by for the purpose of aiding intraoperative surgical margin analysis (Farquharson et al. (2013), Mersov et al. (2014)), suggesting that x-ray diffraction could be used intraoperatively to reduce reoperative procedures, reducing distress to the patient and potentially saving time and money by preventing the need for staff and equipment being used at the second operation.

### 1.3.2 Multivariate analysis studies

Multivariate Analysis (MVA) has been the analysis method of choice in several publications for x-ray diffraction applied to security and medical applications. MVA is an umbrella term for the statistical analysis of more than one variable at a time, based on the observation of multiple variables. For the example of x-ray diffraction, once a spectrum has been obtained, the quantitative values of peak height, peak position, and peak width can all serve to be multiple variables from the same experiment. MVA can be used to not only classify a material type, such as healthy tissue from unhealthy tissue, but can also be used to identify the material itself. MVA is beneficial for applications with noisy data, such as in a medical or security setting where there is a potential need to get a quick response out of the system for identification purposes e.g. those with poor counting statistics and rapid scanning. Luggar et al. (1998) and Cook et al. (2009) are works which use MVA for the analysis of illicit materials in airport luggage

or postal packages. In these works, the primary method of MVA is partial least square (PLS) regression. PLS is a predictive method which utilises a training set of data from which a model can be obtained, from which a spectrum of an unknown sample can be compared and identified. If there is one dependent variable  $y$  then the linear regression model has the form  $y = Xb + f$  where  $y$  is a vector of dependent variables,  $X$  is a matrix of independent variables,  $b$  is a vector of regression coefficients and  $f$  is a vector of residuals. An example of  $y$  could be the amount of illicit material in a powdered sample, as has been considered by Cook et al. (2009) and Christodoulou et al. (2011), and the  $X$  matrix consists of the diffraction data acquired with that concentration value. If there is more than one dependent  $y$  variable then the equation may be written in the general form  $Y = XB + F$  where each component is a multi-dimensional matrix. A multivariate calibration process determines the regression coefficients  $B$  and the residuals  $F$ . This typically consists of a large data set of 'training' data where all elements are known, i.e. the  $y$  matrix and  $x$  matrix, this is in order to obtain information in the  $Y$  variables that cannot be explained by the  $X$  variables, which then produces a mathematical model that can be applied to independent unknown data. A full mathematical representation can be found in Esbensen et al. (2002). This is a method which creates principle components from the data to explain as much variation in the data as possible. The use of a model and training system allows for additional spectra of new materials to be added to the model, such that it can be updated. Farquarson et al. (1997) performed MVA on bone phantoms, Ryan and Farquharson (2007a) used multivariate analysis as a means of classifying breast tissues and Theodorakou and Farquharson (2009) used MVA for the classification of the secondary colorectal cancer. The benefits of using MVA is that it is, by its nature, able to reduce a problem with several variables into a problem with far fewer variables. The technique has been used for fluorescence and biological applications where there are several variables to

consider that are not easily measured, and thus is very useful for applications where it is easy to measure variables in the form of a spectrum but difficult to measure others-such as the percentage content of unknown drug samples or fat content of a sample.

## 1.4 Tissue equivalent materials

Obtaining breast tissue for the purposes of research can be difficult as it may require patient consent and licenses for the use and transportation of materials according to the Human Tissue Act (2006). When using breast tissue and relating the diffraction signal to the constituents of the tissue, it is necessary to know what the tissue comprises of. This requires a histopathological analysis or pathological analysis of the tissues to be performed.

To remove the need for breast tissue when performing breast tissue research with diffraction, other works have determined the molecular form factors of breast tissue and tissue equivalent materials such as polymethyl methacrylate (PMMA) and nylon, commercial materials such as CIRS: BR 70/30 and RMI 454 (Poletti et al. (2002a)), who used a monochromator and energy of 17.44 keV, the K-alpha line of molybdenum to obtain diffraction patterns. The angle variation was between  $1.3^{\circ}$ - $20^{\circ}$ , equivalent to momentum transfer range of  $0.2 \text{ nm}^{-1}$  to  $8.3 \text{ nm}^{-1}$ . Each sample considered was 5 mm thick to minimise the possibility of multi-scatter events and to limit the spectral data to single scatter events. Peplow and Verghese (1998) considered 16 samples including pork muscle, beef muscle and fat. Data were acquired using monoenergetic photons at varying angles of  $1^{\circ}$  to  $100^{\circ}$  in steps of  $0.25^{\circ}$ , using energies of 8 keV and 20 keV. Evans et al. (1991) considered the molecular form factors of water, olive oil, perspex (PMMA), and breast tissues including adipose tissue and carcinoma. The works compare the position of the maximum scatter peak, its corresponding FWHM, as well as the

normalised peak height. It was shown that the adipose tissue demonstrated similar peak positions to olive oil and perspex, and that fibroglandular tissue had similar positioning to that of water.

In all studies the method of comparison is a combination of both quantitative and qualitative reasoning. The use of quantitative measures such as the peak position, i.e. the position in terms of momentum transfer values at which the peak with maximum intensity occurs, the width of the peak, where commonly the most intense peak is considered, as well as the relative height, are all affected by the geometry and system used, as well as the corrections used on the data. For example, in the case of Poletti et al. (2002a), the data are adjusted for attenuation corrections, input spectra, and background scatter effects are removed. When considering the data to which they compare, it is stated that discrepancies between previous works' results and their own was due to potential variations of the samples, differences in the correction of spectra, influences due to the use of a monoenergetic source with a small bandwidth while other investigators used polychromatic sources to investigate tissue equivalent materials. The other influence is the effect of the variation in the momentum transfer resolution of the system which can affect the apparent width of the diffraction peak, when in fact it is a consequence of the system itself. Gonçalves et al. (1993) and Poletti et al. (2002b) describe that it is necessary to know the effects of the momentum transfer resolution to be able to directly compare to other materials for tissue equivalence.

Once the differences in tissue types for x-ray diffraction were established, several works have focussed on the exploitation of the differences and investigate quantitative methods for comparing healthy and non-healthy tissue types. This can also be applied to tissue equivalent materials and consideration for phantom designs. Table 1.4.1 summarises the various quantitative measures used so that benefits and disadvantages of these methods can be discussed.

| Study                        | Peak<br>position | Amplitude | FWHM | Area | MVA | Attenuation<br>correction |
|------------------------------|------------------|-----------|------|------|-----|---------------------------|
| Evans et al. (1991)          | ✓                | ✓         | ✓    | -    | -   | -                         |
| Kidane et al. (1999)         | ✓                | ✓         | -    | -    | ✓   |                           |
| Poletti et al. (2002a)       | ✓                | ✓         | ✓    | -    | -   | ✓                         |
| Poletti et al. (2004)        | ✓                | ✓         | -    | -    | -   | ✓                         |
| Ryan and Farquharson (2007a) | ✓                | ✓         | ✓    | ✓    | ✓   | ✓                         |
| Griffiths et al. (2004)      | ✓                | ✓         | -    | -    | -   | ✓                         |
| Griffiths et al. (2008)      | ✓                | ✓         | -    | -    | -   | -                         |
| Elshemey et al. (2010)       | ✓                | -         | ✓    | -    | -   | -                         |
| Elshemey et al. (2013)       | ✓                | -         | ✓    | -    | -   | -                         |
| Farquharson et al. (2013)    | ✓                | ✓         | ✓    | ✓    | ✓   | -                         |
| Conceição et al. (2009)      | ✓                | -         | -    | -    | ✓   | -                         |
| Conceição et al. (2011)      | ✓                | -         | -    | -    | ✓   | -                         |
| Konstantinidis et al. (2012) | ✓                | ✓         | -    | -    | -   | -                         |
| (Desouky et al., 2009)       | ✓                | -         | ✓    | ✓    | -   | ✓                         |

Table 1.4.1: Summary of diffraction parameters used in the literature. ✓ indicates the parameter is used.

The peak position is commonly used across all studies. The diffraction signal is a fundamental property of the sample type, where the coherent scatter leads to constructive interference and Bragg’s Law. The molecular structure is defined on the basis that the atomic spacings within the material have a defined value, and should not vary. Where the peak height is considered, this is at a peak position of interest, usually  $1.1 \text{ nm}^{-1}$  or  $1.6 \text{ nm}^{-1}$  for adipose or glandular tissue. This is conducted in particular for imaging studies, where a 2D image of intensity values at a momentum transfer of interest is displayed. This is the case for Griffiths et al. (2008) and Castro et al. (2005b). The peak height can be considered to be the intensity of the signal. However, unlike an intensity in mammography, the signal for x-ray diffraction is the result of photon interaction with the sample by

scattering. Therefore, the highest intensity of a diffraction peak corresponds to the interaction that is strongest within the sample.

The peak height is dependent upon the thickness of the sample and the energy of the interaction. The intensity of the peak position also depends on the number of photons for which the coherent scatter can occur in the first place. Also, any attenuation of the signal can affect the system. It is common for the samples to be attenuation corrected, as has been conducted by the majority of the works, with the exceptions of Elshemey et al. (2013) and Conceição et al. (2009), who did not perform attenuation correction on the data. Their data were then used for further analysis using MVA. Attenuation correction is suitable if it is desired to determine the 'true' intensity of diffraction i.e. the theoretical number of photons that interacted with the sample at position  $x$ , based on the detected number of photons at a particular energy for a specific geometry. However, the absolute position of the diffraction interaction is not known, and therefore the total path travelled by the photon is also not known. This leads to the assumptions for attenuation correction. In the case of polychromatic sources, the point of interaction is not necessarily the same for all photons with differing energies. In the imaging works of Griffiths et al. (2008), attenuation corrected diffraction images were compared with uncorrected diffraction images and it was found that there was no significant benefit to using the attenuation correction. It was also argued that attenuation correction could potentially lead to a deterioration of the image quality. It is possible to add noise to attenuated corrected data by over attenuation correcting. In the works by Kidane et al. (1999), attenuation correction of higher energies added noise to the spectra. It is possible to overcompensate for the loss of higher energy photons. This is due to the fact that the point of interaction is considered to be the same for all energies, and it would be expected that higher energy photons are less likely to interact, and if they do, would be more likely to interact deeper within the sample than a lower energy photon.

It could be argued that the attenuation correction is removing information from the system. The loss of signal at a particular momentum transfer is based on the interaction of the photons with the sample, so even the apparent loss of a signal can be considered to be information. This is in essence not a loss of signal, but rather it is not possible to record all of the true diffraction signal due to self-attenuation. It depends on the purpose of the study, if the attenuation correction is necessary or not. For comparison to equivalent materials, where it is important to establish materials which match the ideal signal of tissue, then attenuation correction is important. However in practice, the thickness of the sample may not be known, nor may it be possible to utilise transmission data for attenuation correction, which is the method performed by, Griffiths et al. (2008) and Ryan and Farquharson (2007a).

A limitation of the works using equivalent materials or real tissue is the thickness of the samples used for the diffraction studies. The majority of studies undertaken on breast tissue use thin biopsy samples. Kidane et al. (1999) used a cylindrical tube with cross-sectional area of  $25 \text{ mm}^2$ , corresponding to a thickness of approximately 2.8 mm. The study conducted by Pani et al. (2010) utilised a breast tissue biopsy of 6 mm. Synchrotron studies by Castro et al. (2004) and Castro et al. (2005b) used breast tissue of approximately 1 mm thickness, and the MVA study conducted by Conceição et al. (2011) used tissue of 3 mm thickness. It is desirable to have a thinner sample to reduce the effects of multiple scatter and to maximise the possibility of one interaction. The mean free path of the sample for a photon of a particular energy is given by  $\frac{1}{\mu}$ , where  $\mu$  is the linear attenuation coefficient.

The thickness of the sample is usually taken into consideration by performing attenuation corrections, and the sample thickness is set to a fixed value in individual studies for the purpose of signal comparisons and to keep multiple scatter effects low. In these circumstances, the thickness of a sample is known *a priori*

whereas in a real situation, for example where a biopsy sample is being analysed, the thickness of the sample and the constituents wouldn't necessarily be known without the aid of histopathological analysis. Rather than correcting for the thickness or using only samples of the same thickness, exploiting the variation in the thickness can be explored.

When comparing tissue equivalent materials it is also possible to consider the peak height, or the relative peak height of the main peak to the underlying background, or to compare it to another peak from the same data. This could be by considering the ratio of the diffraction peak at  $1.1 \text{ nm}^{-1}$  and at  $1.6 \text{ nm}^{-1}$ . This would be similar to introducing contrast to the system, which is based on the ratio of the intensity between the signals of, for example, carcinoma and healthy tissue types. For tissue equivalence, for the same system, adipose tissue and its equivalent would ideally have the same intensity, as the linear attenuation coefficients would be similar and so would the molecular structure. When comparing results from different systems, it would be expected that the relative peak heights would vary due to differences in the system, corrections, sample preparation, and sample thickness. Peak width is used to quantify the diffraction peak, commonly for the peak with the highest intensity, so for the case of tissues, this would be at  $1.1 \text{ nm}^{-1}$  for fat and  $1.6 \text{ nm}^{-1}$  for glandular tissue.

Not requiring breast tissue can make it easier for research groups to perform conceptual analysis techniques and scanning without procuring real tissue. For laboratory based x-ray diffraction work, phantoms and tissue equivalent materials can provide a substitute for healthy or unhealthy tissue, but do not require histopathological analysis nor do they require the use of fixing agents such as formaldehyde gas for fixing tissues in formalin (a solution of water and formaldehyde), they can be tailor-made for the purpose of the experiment and can be used multiple times, which makes it easier to analysis techniques to the ground truth provided by the phantom. Alkhateeb et al. (2012) used materials such as

wax, rubber and silicone, in addition to established materials such as nylon and PMMA to recreate contrast values calculated at the  $1.1 \text{ nm}^{-1}$  and  $1.6 \text{ nm}^{-1}$  peaks, when considering combinations of adipose, glandular, malignant and benign samples. The contrast values varied from 0.73 between adipose and benign tissue at  $1.1 \text{ nm}^{-1}$  to 0.08 between benign and malignant at  $1.6 \text{ nm}^{-1}$ . It was possible to recreate the contrast of the tissues using combinations of material such as nylon and silicone to represent adipose and benign tissues. It is primarily the contrast of the image that aids the identification of unhealthy tissue types.

## 1.5 Cadmium (Zinc) Telluride sensors and EDXRD

Laboratory based EDXRD methods do not need to use a monochromatic source from a synchrotron facility, monochromator, or by using characteristic lines of targets such as copper k-alpha, but are able to use polychromatic sources. An energy resolving detector is required for EDXRD systems due to the ability to differentiate between different photon energies. Typically, the ideal detector types have been High Purity Germanium (HPGe) for laboratory based systems. The intrinsic semiconductor material is a single pixel type detector with a large area (typically a few centimetres wide), 1 mm thickness and a typical resolution of 600 eV at 60 keV. However, the detector has to be cooled in order to reap the benefits of the material as it suffers from large leakage current at higher temperatures. The need for cooling, either through electronic cooling or with the use of liquid nitrogen and the size of the high purity germanium systems make them unsuitable for portable systems. Some applications prefer the option for portability, for example in a clinical environment where it might be necessary to move a detector around a room or a patient, or be carried easily from one place to another. The developments of CdTe and CZT growth have made it a viable commercial alternative to HpGe. In medical applications, photon counting CZT

detectors were investigated by Le et al. (2010) as an alternative to flat panel detectors in breast CT systems, and it was found that the dose to the patient was reduced by up to 52% when using a photon counting CZT detector system. CdTe has been used in a PET (Positron Emission Tomography) based system by Nakhostin et al. (2010) and Matsumoto et al. (2010) for investigating artefacts in a CT system because of its high energy efficiency, its comparable energy resolution to current detectors and its photon count ability. Beldjoudi et al. (2012) investigated CZT and CdTe for the possibility of using the material in photon counting detectors for homeland security. Enomoto et al. (2011) used a CdTe camera for exploring the use of CdTe for x-ray fluorescence with the application of cancer diagnosis. CdTe is also used for high gamma ray detection in space applications, Remoue (2009), Remoue et al. (2010), Hong et al. (2004) and Grindlay et al. (2010) all used CZT detectors for this very purpose. A review article on the development of CdTe and CZT for medical and astrophysics applications can be found in Del Sordo et al. (2010).

For x-ray diffraction specific research, Malden and Speller (2000) focussed on multi-arrays using CZT detectors with an energy resolution of 4 keV at 60 keV (Dedek et al. (2007), using multivariate analysis of energy-angle maps, which are also shown in the PhD thesis of Emily Cook for breast imaging (Cook (2008))). Other researchers have compared the two detector types to determine if CZT is able to provide similar results to those obtained with the standard HPGe detector. Studies include that of Pani et al. (2010), which considers the effects of the energy resolution difference between HPGe and a CZT detector on the effects on the diffraction pattern. Crespy et al. (2010) considered the effects of the resolution on a detection database for explosive materials being detected by diffraction. The study found that although the results for detection improved with the HPGe, a change in the geometry with the CZT could improve results. The growth of large CdTe crystals with a low defect density has led to the development of

pixellated, application specific integrated circuits (ASICs) using CdTe as a sensor when bonded onto the ASIC. This enables detectors to be designed with specific applications in mind. The pixellation means that not only is spectral information provided, but also spatial information, something that is not possible with single crystal detectors.

Several studies such as the research by Kidane et al. (1999), Royle and Speller (1995), Farquarson and Speller (1998), Li et al. (2010), Li et al. (2011), Sun et al. (2010) and O'Dwyer and Tickner (2008), used EDXRD for the investigation of amorphous and powdered materials. They have used a design similar to that shown in Figure 1.5.1. The system consists of an x-ray source, which is typically polychromatic, and a collimator fixed at a distance  $L_1$ . The x-ray source has a focal spot of size  $s$ . The sample is placed at a fixed distance from the primary collimator, which helps to define the dimensions of the beam at the sample and is referred to as the beam height. The secondary collimator is then used to select the required scatter angle, whilst limiting the detection of unwanted scatter events, such as those from other angles and background scatter.

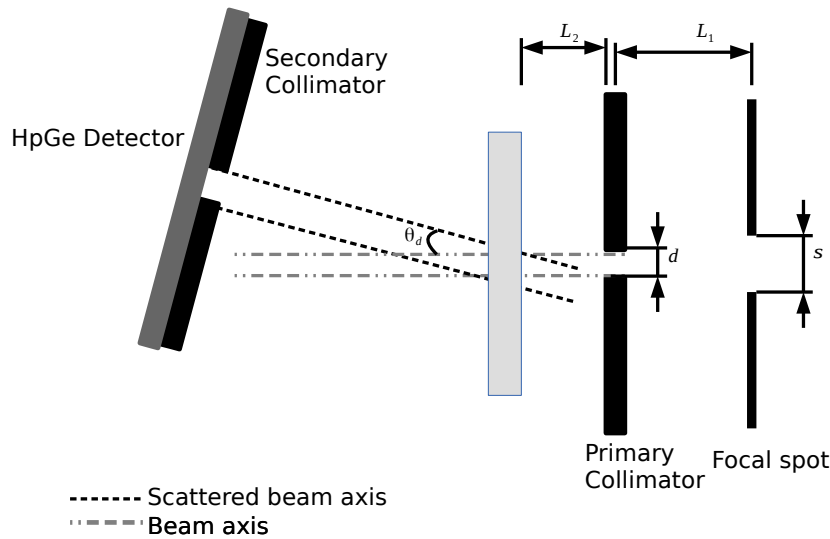


Figure 1.5.1: Typical EDXRD system. The detector is traditionally placed perpendicular to the selected angle of the diffraction measurements.

In terms of x-ray diffraction, some works have incorporated multiple detectors as part of their systems, such as Malden and Speller (2000), but otherwise typical EDXRD laboratory based systems do not utilise spatial information and energy resolution information in the same system. In the works of Malden and Speller (2000), the concept of an array of detectors is achieved through the use of single CdZnTe detector of crystal size  $5\text{ mm} \times 5\text{ mm} \times 2\text{ mm}$ , which was then moved to pre-selected positions. Fixed collimation was placed within the system, such that when the detector was moved using automated motion, the scatter angle was already selected by the collimation corresponding to that position. This style of system requires the use of a collimation system to be placed and aligned with respect the position of the sensor. Only then can diffraction spectra be achieved at differing angles. This type of scanning also requires multiple acquisitions utilising the same output beam, as the operational settings for the x-ray source was not

varied from the settings of 70 kVp and anode current of 20 mA.

A 2D detector array can allow for the simultaneous acquisition of diffraction data at multiple angles, as seen previously by Christodoulou et al. (2011), O’Flynn et al. (2012) and O’Flynn et al. (2013), using a 2D energy resolving detector for pixellated diffraction within an EDXRD. In the system created by Malden and Speller (2000), an element of ingenuity is required to manufacture the collimator for the system. With a pixellated detector, it is possible for a diffraction system to be self-collimating although this could have disadvantages as well. A secondary collimator means that any air scatter from the primary beam is detectable. A secondary collimator serves to define a scatter volume and to detect signal from a particular angle.

## 1.6 Thesis layout

A brief summary of each section in this Thesis is provided here.

The characterisation of the 2D pixellated detector system used in this research is presented in Chapter 2. Two previously uncharacterised ASICs (Application Specific Integrated Circuit) are presented in this Chapter, including details of the energy resolution, the energy detection efficiency at 60 keV, and the effects of charge sharing on both of these parameters. The application of the two ASICs to EDXRD are discussed in terms of practical requirements, and the best ASIC of the two is selected for further characterisation. A method for considering the linearity between the number of photons, for a specific integrated spectrum based on the photons used for x-ray diffraction, is presented here. This highlights the limit at which the number of photons detected is no longer directly proportional to the incoming number of photons and saturation begins to occur. The explores the detection limits of the detector due to the nature of the read out.

A diffraction system developed for the pixellated detector with the use of a micro-focal source and sample scanning is described in detail in Chapter 3, including the focal spot measurement, the beam output profile, as well as the effects of parameters such as the sample detected distance on the diffraction profiles themselves. A discussion on the system limitations and potential development of the system is provided. Exploration of the effects post processing of the diffraction data and sample thickness is also discussed in this section, with attention focussed on pork fat, PMMA, and caffeine as a comparative material. Imaging parameters such as the FWHM of the diffraction peak and intensity of the diffraction peak are used.

Chapter 4 discusses the possibility of using materials for diffraction phantoms for medical applications. This work utilises a high purity Germanium system to collect diffraction data of plastics based and gel materials. The materials' equivalence to breast tissue diffraction data is discussed in terms of the diffraction peak positions, the FWHM, density, and the linear attenuation coefficients of the materials. This is to expand on the current knowledge of equivalent materials with the aim of considering alternative materials that can be used in EDXRD phantoms.

The development of a novel phantom creation technique which uses an input image and a laser system to represent and excised tissue slice with both tumour and healthy tissue is presented in Chapter 5. The use of the laser cutting system is described in detail as well as the relationship between the input of the image to the software and the created hardware, including a method of characterisation of the phantoms developed by the author. Diffraction scanning results of a region of interest is shown as an example of diffraction imaging with the phantoms in the previously described system. Use of the phantom to explore contrast in diffraction

images and different post-processing has also been presented.

Finally, a discussion of potential future work is provided.

## Chapter 2

# Characterisation of two $80 \times 80$ ASICs

### 2.1 Description of the pixellated ASIC CdTe detector

The detector used in this project is a novel pixellated ASIC (Application Specific Integrated Circuit) designed primarily for CZT and CdTe (Jones et al. (2009), Wilson et al. (2010) and Seller et al. (2011)). The principle of the design is to be able to read out energy resolving spectra for each pixel, at the cost of processing time. The integrated circuit is therefore tailored for energy resolving capabilities,

with the principle application being x-ray spectroscopy. The sensor used consists of 1 mm thick CdTe bump bonded to the ASIC, which has  $80\times 80$  pixels with dimensions  $250\ \mu\text{m}\times 250\ \mu\text{m}$ . The sensor material consists of an M-pi-n (metal, slightly p-type, n-type) CdTe sensor, with indium at the cathode and aluminium at the anode which are of the order of micrometers thick. This in turn is gold bump bonded to the ASIC. Gold has high conductivity and is therefore ideal for transferring charge from the sensor to the ASIC. A schematic of the ASIC is shown in Figure 2.1.1.

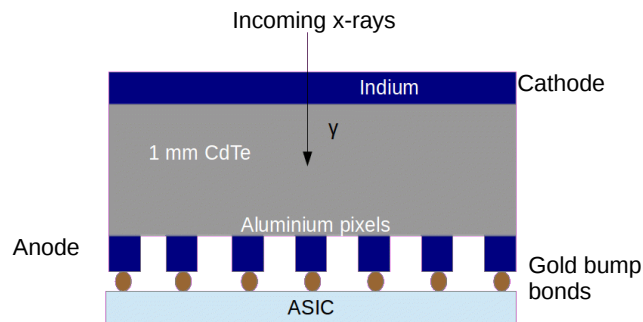


Figure 2.1.1: Schematic of the CdTe sensor and electrodes.

The sensor is illuminated from the cathode side, through the bulk material towards the anode. Therefore higher energy photons deposit energy closer to the anode, and low energy photons do so closer to the cathode. Each pixel in the ASIC has the following electronics for read-out shown in Figure 2.1.2.

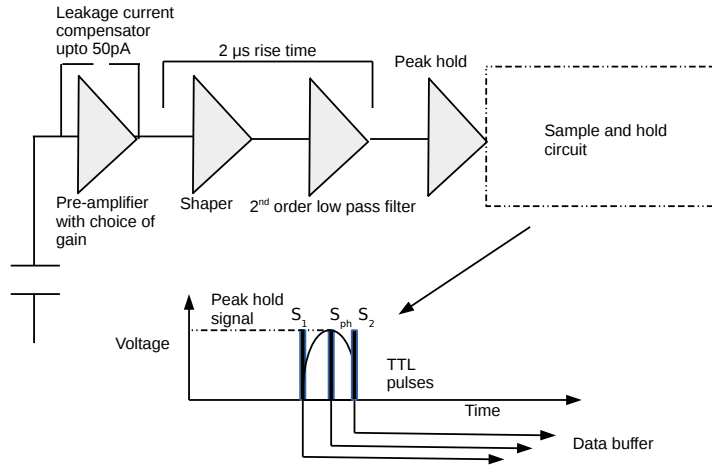


Figure 2.1.2: Diagram of read-out process.

Each pixel consists of a pre-amplifier, which can be set to high gain or low gain mode. The detector is optimised for usage at high gain, with a dynamic range of 5-150 keV as its primary energy range when used with 1 mm CdTe, but can also be used at lower gain at a dynamic range of 0.05-1.5 MeV. The detector is only used to detect photons within the energy range of 5-150 keV in this research, so therefore the high gain option is utilised.

The charge pulse is integrated to generate a voltage pulse which is then shaped for data sampling to take place. The ASIC utilises a peak hold event read-out (De Geronimo et al. (2001), De Geronimo et al. (2002)) and sequential rolling shutter data collection, the details of which can be found in Jones et al. (2009), which describes the prototype  $20 \times 20$  design. The rolling shutter data read-out is designed so that the 20 column outputs of each of the rows are sent sequentially to an analogue multiplexer for serial output to an off-chip 20 MHz 12 bit analogue to digital converter (ADC). The  $80 \times 80$  ASIC consists of four sections of 80 rows and 20 columns. Each section of 20 columns outputs each of the 80 rows sequentially to an analogue multiplexer (Seller et al. (2011)). The data are initially digitised locally by the field-programmable gate array (FPGA) which is then transferred

to the computer through a camera cable link base, designed for large data output and fast transfer of up to 200 Mbit/s.

The ASIC is designed to read out the highest energy event per pixel, and to do this, each pixel has a peak hold circuit as well as a select and hold circuit, or track and hold buffers, which are used to sample the shaper and peak hold voltages. To do this, global clocks are utilised that control the circuits in each pixel, the timings of which are based on the off-chip ADC frequency of 20 MHz. This is referred to as the global clock in the HEXITEC GUI (graphical user interface). The units of the additional timings are based on this global clock value. There are three parameters used to control the read-out of the ASIC:  $Row_s-S_1$ , which is denoted as Row-S1 in the GUI, shown in Figure 2.1.3, corresponds to the time between selecting a row and shaping the photon voltage signal.  $S_1-S_{ph}$  is the time between the shaper signal and the peak hold signal, and finally  $S_{ph}-S_2$  which is the second sample read-out time when the shaper signal is sampled a second time.

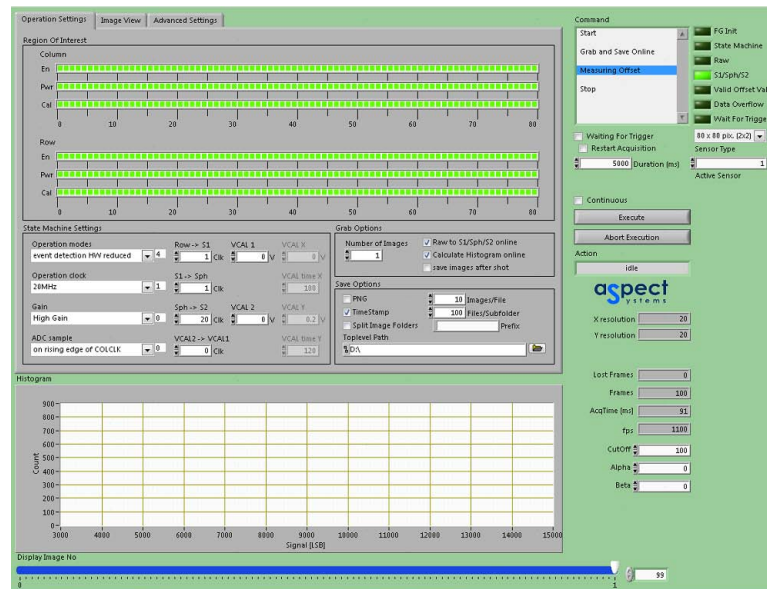


Figure 2.1.3: User interface to control the FPGA.

The purpose of  $S_1-S_{ph}$  and  $S_{ph}-S_2$  is to sample the filter twice, to determine when the peak hold signal has been sampled with respect to active signals of

the output. This then allows for any corrupted data to be recognised and not registered, to enable the sampling time to be completed and to sample the pulse shape.

Figure 2.1.4 provides a schematic of the detector read-out, as detailed by Jones et al. (2009). This uses the example of 5 rows and 5 columns selected for read out. First the row for read out is selected which is denoted as RowClk in the diagram. The Sclk is the global clock system for the  $S_1$ ,  $S_{ph}$  and  $S_2$  for signal sampling to establish the maximum signal per pixel. In this examples there are 5 instances of column read out for each row, as the example is for an example of  $5 \times 5$  pixels. When all rows and columns have been read out, the end of frame is indicated and the process begins again.

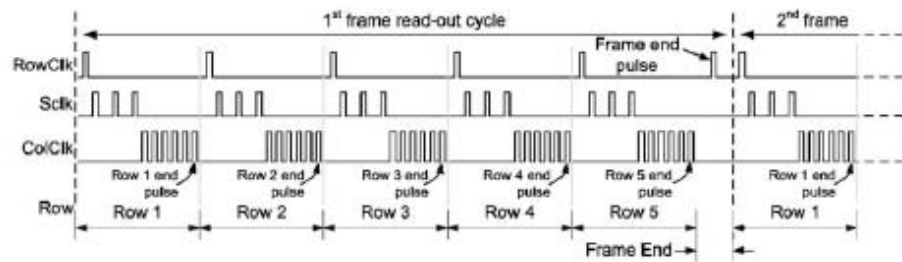


Figure 2.1.4: Schematic of the ASIC frame read-out, taken from Jones et al. (2009)

Figure 2.1.5 demonstrates the parameters used during the ASIC read-out in more detail.

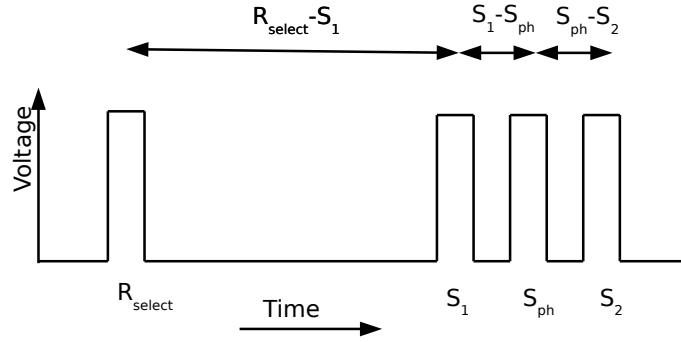


Figure 2.1.5: Definition of terms used in the data acquisition GUI.

The highest signal in each column for each row is read, i.e. each pixel in each row is read out sequentially, recording the highest measured signal for each pixel in that row, before moving on to the next row. The range of possible sampling times for the row select time and the first shaper time, is  $0.05 \mu\text{s}$ - $0.05 \text{s}$ , and the range of possible sampling times for both  $S_1$ - $S_{ph}$  and  $S_{ph}$ - $S_2$  are  $0.05 \mu\text{s}$ - $2 \mu\text{s}$ , as allowed by the GUI.

For this research, the global clock is set to 20 MHz and the  $S_1$ - $S_{ph}$  and  $S_{ph}$ - $S_2$  values are set to 1 and 40 respectively, thus allowing  $2.5 \mu\text{s}$  to sample the active signals. This then leaves the  $Row_s$ - $S_1$  time to be selected based on the application, as this is the active seeking time that the ASIC is exposed to photons for all pixels in a row. The row select time and the  $S_1$  time is the time between selecting the row and then sampling the peak hold signal. For a given number of photons, it would be expected that a longer  $Row$ - $S_1$  time would lead to a decrease in the number of photons detected. The timings of the peak hold and sample and hold circuits for data sampling affect the frame rate. The frame time,  $F_{time}$  of the detector is given by Eqn 2.1.1

$$F_{time} = (Row_s S_1 + S_1 S_{ph} + S_{ph} S_2 + N_{cols} + 1) \frac{N_{rows}}{\text{clk}} + \frac{1}{\text{clk}} \quad (2.1.1)$$

where  $\text{RowS}_1$  denotes  $\text{Row}_s-S_1$ ,  $S_1-S_{ph}$  is represented by  $S_1S_{ph}$ , and  $S_{ph}-S_2$  by  $S_{ph}S_2$  and have been previously defined,  $N_{cols}$  and  $N_{rows}$  are the number of columns and rows being read out, and  $\text{clk}$  is the global clock of the ASIC, which is 20 MHz. It takes 1  $\text{clk}$  value to select the rows and columns, therefore if 20 rows are selected, 20  $\text{clks}$  are required to select the 20 columns. Therefore the units of  $N_{cols}$  and  $N_{rows}$  are  $\text{clks}$  in this case.

This frame time relates to the total time taken for all pixels of the 2D-array to be read out. All pixels are actively seeking events, but the read-out is sequential across all rows.

The graphical user interface for the detector is designed by Aspect (Aspect Systems, Germany) and requires a LabView (National Instruments Cooperation) runtime license to work successfully.

### 2.1.0.1 Charge sharing

Due to the pixellation of the ASIC, it is possible for the detector to detect charge sharing events. Charge sharing is the phenomenon whereby charge from a single event is distributed in multiple pixels of the detector. It is caused by the diffusion of the charge cloud where electron-hole pairs undergo diffusion and repulsion due to Coulombic effects, as described by Ahmed (1997).

Once an electron-hole pair is generated from the deposition of energy from a photon, the charge carriers drift towards the electrodes with drift velocity  $v_{drift}$ , which is determined by their inherent mobility and their position within the bias induced electric field,  $E_f$ , as shown in Eqn 2.1.2 which uses the example of electrons.

$$v_{drift} = \pm\mu E_f(x) \quad (2.1.2)$$

where  $\mu$  is the mobility of the charge particle, corresponding to  $\mu_e$  for electron mobility and  $\mu_h$  for hole mobility, and where  $E_f(x)$ , is the electric field at position

*x*. The space distribution of the generated charge gradually increases due to diffusion effects. The resulting diffusion current density for electrons,  $J_{e,diff}$  is given by Eqn 2.1.3

$$J_{e,diff} = -D_e \nabla_e = \frac{-k_B T}{q_e} \quad (2.1.3)$$

where  $D_e$  is the diffusion constant for electrons, the electron concentration is given by  $\nabla_e$ ,  $q_e$  is the charge of the electron and all other parameters are as previously defined. The diffusion constant can also be written as Eqn 2.1.4

$$D_e = \mu_e \frac{k_B T}{q_e} \quad (2.1.4)$$

As the charge travels through the material, the diffusion and the drift motion causes the charge cloud, or charge distribution, to change. Figure 2.1.6, demonstrates an example of a charge cloud expanding over two pixels.

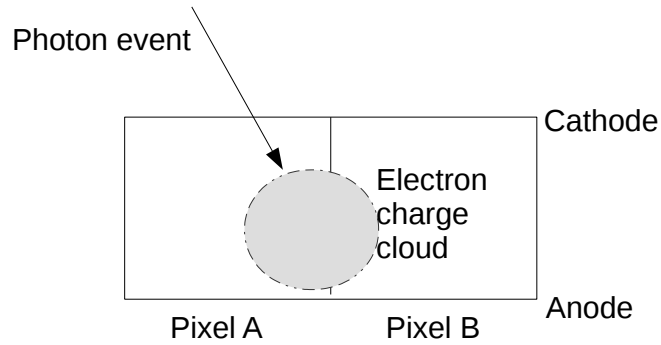


Figure 2.1.6: Diagram of charge cloud expanding across two pixels

It is possible to approximate the charge cloud distribution as a Gaussian, with a standard deviation  $\sigma_c$  as given in Eqn 2.1.5

$$\sigma_c = \sqrt{2D_e t_{drift}} \quad (2.1.5)$$

where  $t_e$  is the time elapsed since the creation of the charge cloud. By substituting Eqn 2.1.4 into Eqn 2.1.5, the following is obtained

$$\sigma_c = \sqrt{2\mu_e t_{drift} \frac{k_B T}{q_e}} \quad (2.1.6)$$

Rearranging Eqn 2.1.2 for electron mobility leads to Eqn 2.1.7

$$\mu_e = \frac{v_{drift}}{E_f(x)} \quad (2.1.7)$$

This leads to Eqn 2.1.8, when also considering that the electric field,  $E_f$  can be approximated as the detector voltage  $V$  divided by the detector thickness  $D_d$ . Based on the diffusion model, the standard deviation of the charge cloud is dependent on the temperature, the thickness of the material, the voltage applied and finally the distance travelled,  $d_d$ , by the charge particle in drift time  $t_{drift}$ .

$$\sigma_c = \sqrt{\frac{2k_B T D_d d_d}{qV}} \quad (2.1.8)$$

The total FWHM of this Gaussian distribution would give an approximation to the total spread of the electron cloud due to diffusion.

Therefore, the total spread  $s_c$  of the charge cloud is given as

$$s_c = 0.529 \sqrt{\frac{D_d d_d}{V}} \quad (2.1.9)$$

For the system used, the magnitude of the voltage applied is 400 V, the thickness of the CdTe sensor is 1 mm and the operation temperature is 287 K. Based on these values and using the diffusion model, the spread of the charge cloud from the cathode side to the anode is approximately 26.4  $\mu\text{m}$ . This does not however take into consideration the size of the charge cloud, which is considered to be a delta function in this model. The trenches between the pixels are of the order of 15  $\mu\text{m}$  (Seller et al. (2011)) and is therefore comparable to the spread of the

electron cloud, which could lead to a photon event being detected in neighbouring pixels.

This model does not consider the effects of repulsion, coherent scatter, or the initial number of electron-hole pairs initially created from the deposition of a photon. Several works have modelled the initial electron cloud size based on Monte Carlo simulations, including the works of Nilsson et al. (2007), Jae et al. (2009) and Iniewski et al. (2007). For photons with energy 100 keV, the initial charge cloud is approximately  $20\ \mu\text{m}$  for CZT (Jae et al. (2009)). The total width of a charge cloud after the deposition of 100 keV deposited at depth of 0.7 mm in the sensor would therefore be  $\sqrt{20^2 + 14.5^2}$ , which leads to a total spread of  $24.7\ \mu\text{m}$  at the anode.

The consequence of the charge sharing event is that one single photon event can be detected in multiple pixels. In the case of the pixellated ASIC used in this research, when two or more neighbouring pixels detect events above the threshold of 5 keV, these are considered to be charge sharing.

The following example in Figure 2.1.7 can be used to show how charge sharing events are recorded by the detector.

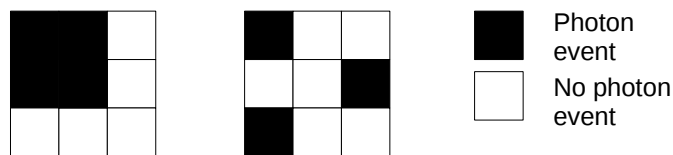


Figure 2.1.7: Diagram of example charge sharing events detected by the sensor.

In the case of the scenario on the left hand side of Figure 2.1.7, it appears as though four individual events have been detected when in fact this is a charge sharing event extending to three pixels, plus the original pixel in which the event

occurred. The scenario on the right hand side is considered to be three individual events as these pixels are not neighbours. If no charge sharing corrections are made all three pixels will register a charge pulse that is less than the original charge created from the deposition of a photon, and therefore the ASIC will record four lower energy events compared to the original event.

The detector system has a charge discrimination algorithm that will find instances where events have occurred in neighbouring pixels, such as in the scenario of the left hand side of Figure 2.1.7. In this case, all events are removed from the data, as the true energy deposited by a photon to create the charge sharing events is not known. Veale et al. (2012) investigated the effects of charge sharing in their detector system using monochromatic photons on 20 keV at a synchrotron facility. Scanning four pixels using a micro-beam of  $10\ \mu\text{m}\times 10\ \mu\text{m}$ , Veale et al. (2012) investigated the charge sharing events in terms of their location, based on intensity variations, as well as with respect to the raw data collected, the charge discrimination algorithm and a charge addition algorithm. The principle of charge addition is to identify the charge sharing events, to sum them and then allocate them to one pixel, which is the one with the highest detected charge. The charge sharing addition was not implemented in the software available for this research, and therefore the charge sharing discrimination which removes all charge sharing events was used.

### 2.1.0.2 Temperature control

The semiconducting material used in the detector is suitable for room temperature usage due to its low leakage current and band gap values as previously discussed in Section 1.2.4. The sensor is known as an M- $\pi$ -n type semiconductor, which relates to the contacts used, where M indicates the use of a metal substrate and  $\pi$ -n representative of a standard p-n semiconductor. This is also known as a Schottky diode semiconductor. The detector is reliant on minority carriers (electrons) for

charge collection. The metal contact fused in the detector is aluminium for the anode, which leads to a Schottky contact, and indium which acts as the cathode producing an Ohmic contact. The *polarisation effect* occurs when the bias is applied to the material and is associated with a decrease in counting efficiency. This is especially pronounced at lower energies as well as a decrease in pulse amplitude and poorer energy resolution with time. This affect is attributed to the shift and decrease in the electric field at the cathode Cola and Farella (2009), although the field across the whole sensor is affected. This is also seen detailed and explored by Bell et al. (1974), Malm and Martini (1974) and Sato et al. (2010). It has been shown that operating the detector at lower temperatures or applying a bias refresh method reduces this effect. This method involves periodically switching the bias off to reset induced polarisation (Bell et al. (1974), Nir, and Sato et al. (2010)). The effects caused by the bias refresh using a the ASIC bump bonded to 2 mm CdTe are detailed by Veale et al. (2011). It was found that the bias refreshing led to a slightly poorer energy resolution of 1.96 keV compared to 1.27 keV without. However it was found that the number of charge sharing events was 44% and remained stable over the course of 5 hours, whereas without bias refresh the charge sharing events increased from 46% to 75% in two hours.



Figure 2.1.8: Detector housing unit with a Peltier cooling system, fan, and data acquisition electronics. An example  $80\times 80$  ASIC is also shown.

To reduce any detector performance temporal variability a bias refresh method is used as well as cooling of the detector to both maintain the temperature at a constant level (with little fluctuation) and to reduce the effects of polarisation. The system is run with a Peltier cooling and both the hardware and software are designed by Aspect. The detector housing unit which incorporates a Peltier system, fan and the data acquisition electronics is shown in Figure 2.1.8. The ASIC is designed to sit on a copper block, which has been selected due to its high thermal conductivity of  $340 \text{ Wm}^{-1}\text{K}^{-1}$  (Haynes (2014)). The temperature of the copper block, on which the back of the sensor rests, can be set through a temperature GUI on the computer, as shown in Figure 2.1.9. To improve the heat conductance between the ASIC and the copper block, a small amount of Asaka AK-455 thermal compound is applied. The silver based compound has been designed specifically to transfer heat to a heat sink, which is equivalent to

the back of the ASIC and the cooler copper block. Silver has a slightly higher thermal conductivity value of  $429 \text{ Wm}^{-1}\text{K}^{-1}$  compared to that of copper. The temperature at the back of the ASIC is measured by another thermosensor. The GUI displays this temperature when requested by the user.

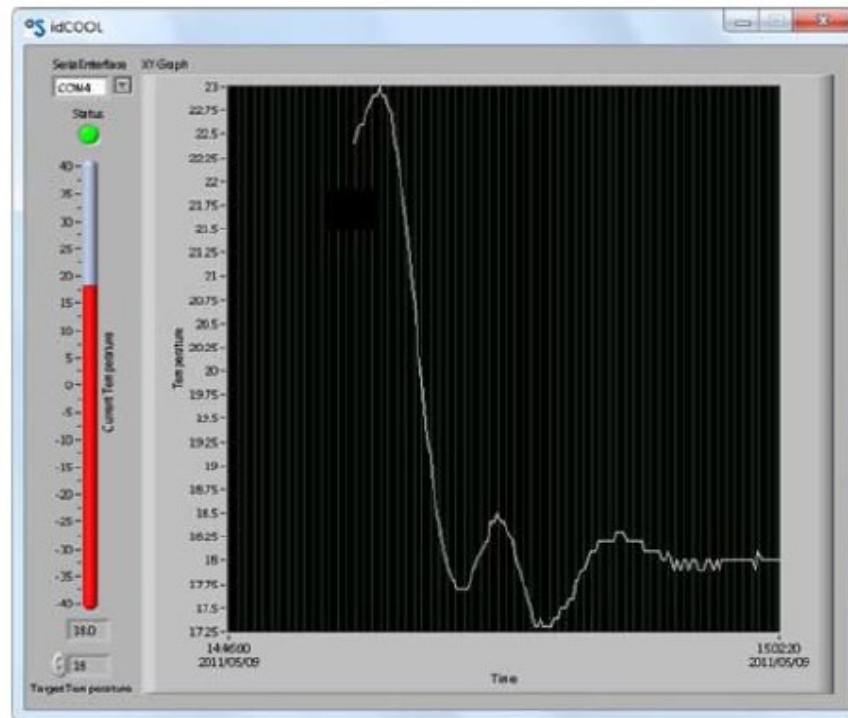


Figure 2.1.9: The temperature of the copper block is set using this GUI.

There is however a temperature gradient between the copper block and the back of the ASIC. On average, the temperature at the back of the sensor is measured  $14^\circ\text{C}$  more than that set in the GUI. Figure 2.1.10 shows the variation in the temperature set using the temperature GUI, and the temperature as read from the back of the ASIC. The data were obtained by setting the temperature of the copper block and allowing the temperature to stabilise. The measured temperature at the back of the ASIC was performed by obtaining five readings and calculating the mean. A linear regression was performed on the data, and it

was found that the linear fit for the temperature difference gave an  $R^2$  value of 0.99.

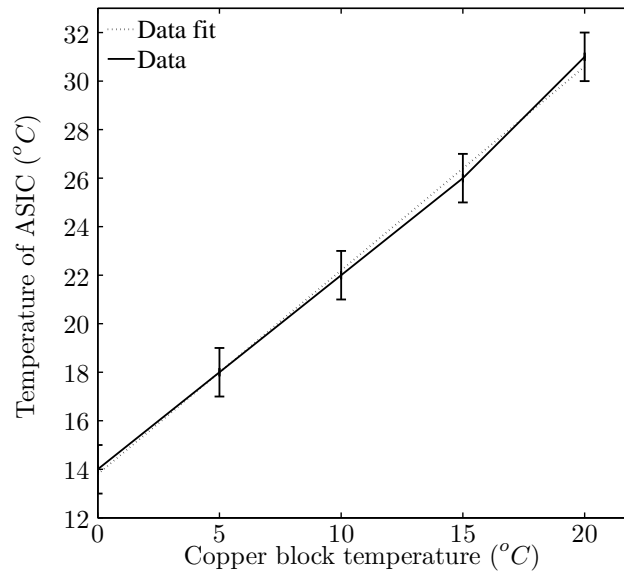


Figure 2.1.10: Measured temperature variations. The linear best fit was found to be  $y=0.84x + 13.8$ , where  $y$  is the temperature at the back of the ASIC and  $x$  is the temperature set at the copper block.

### 2.1.0.3 Humidity control

Moisture on the back of the sensor can lead to catastrophic results if the bias is applied to the detector, and can destroy the detector (Matt Wilson private communication, 2011). Corrosion of the surface of the CdTe was observed, and the tracks of the PCB (printed circuit board) were melted due to the increased current. Damage was also observed on the wire pads of the ASIC because of water on the power line of the ASIC. To prevent the risk of water damage and to use the detector in environments which are warm or cool, a humidity controller has been added to the system. The humidity sensor (SHT 1x/7x, Sensirion AG, Switzerland) is connected to the PC using a USB cable and it is possible to record

the output via the GUI provided for the sensor. The sensor itself is placed within the casing of the system such that it is able to record the ambient humidity around the ASIC. The system is able to measure and control the humidity, but this is independent of utilising the detector. The user has to ensure that the environmental conditions are suitable before operating the system.

The temperature of the copper block was set to 0°C , corresponding to a temperature of approximately 14°C at the back of the ASIC. The ambient humidity in the detector housing is first allowed to decrease, thus reducing the dew point temperature and then allowing the temperature to decrease. This prevents the risk of dew production on and within the detector. The detector is only used once the temperature is stabilised, and the bias voltage applied once the environment has no risk of producing dew.

The detector environmental control is self-contained, housed with the processing electronics of the detector. Although the ASIC is not necessarily run at room temperature, the detector system can still be considered suitable for applications that require portability in environments such as laboratories or hospitals.

#### **2.1.0.4 Detector software**

To use the detector, there are at least three different pieces of software to operate at the same time. The GUI must be open and used for communication with the detector. However, there is no humidity or temperature control from this software, nor is there a way to perform bias refresh from the GUI. The humidity monitor requires a piece of software, provided by Sensirion (Sensirion AG, Switzerland) which operates separately to all other software on the system. The software displays the humidity of the system on the screen, and can also be used to record the time variation of the humidity. The temperature control utilises software provided by Aspect (Aspect Systems, Germany) and again is a separate piece of software. This software is purely for monitoring purposes and it is not

possible to output temporal variation with temperature. The bias refresh, in the case of this work is conducted using MATLAB (Release 2012b, The MathWorks, Inc. Massachusetts, USA) and the instrumentation software, was provided by James Scuffman at the University of Surrey. The principle of the code is to pause the acquisition, the bias is refreshed i.e. the bias is set to 0 V and allowed to reach 0 V from the original -400 V. The bias is then increased after the user defined 'refresh time' and then allowed to settle within the settle time, a time also set by the user. All parameters can be set in the MATLAB code via a GUI developed by James Scuffman. The choice of these parameters are based on the recommendations of Matt Veale and Matt Wilson from the detector development group at the Rutherford Appleton Laboratory.

The data collected from the pixellated detector are encoded into DAT files. Details of the format and the encoding can be found in Sochi (2010). The data is stored using 16-bit values in a binary file. Each frame is separated by a counter, and each row and column within the frame that detected an event is recorded. Pixels that did not record an event in the frame are not recorded within the DAT files, helping to reduce processing time and data file size. The beginning of a frame is then marked with the sequence '255 255 255', followed by a 48-bit integer to mark the beginning of a frame, formed of three 16-bit values. Following this, every pixel that recorded an event is marked on a row-by-row basis. The row index is recorded using 8-bit values, followed by the magnitude of the event (16-bit) and the column in which the event occurred, recorded as an 8-bit value. All events detected in the same row are marked with a magnitude followed by the location. If additional rows acquire data, this is marked by the combination of '0 192', signifying a new row. If there are no other events in the frame, a new frame is recorded written as '255 255 255'.

For analysis of the data a HEXITECH executable has to be used on these .dat files. The HEXITECH executable was developed at the University of Manchester

by Simon Jacques. The HEXITECH executable is operated at the command line and returns the data as .hxt files. Running the executable and processing the data allows for data corrections to be applied, which includes end-of-frame corrections, incomplete data removal and charge sharing corrections, through the use of charge sharing discrimination. The details of the possible corrections to the data are provided by Wilson (2011). The charge sharing algorithm allows for the inclusion of all events in the data, whether they are charge sharing or not, or for the exclusion of charge sharing events from the final data. Each time the executable is used a text log file is generated. Recorded in these files is the number of frames measured, the number of frames written, the number of charge discrimination events, the number of events detected above a pre-defined ADU (analogue to digital unit) threshold value (set by the user), and the numbers of events detected. It is possible to set the ADU such that the lower noise edge described by Seller et al. (2011) is removed from the data.

The software used for viewing the .hxt files is 2Easy, developed by the University of Manchester and DSoFt (DSoFT Solutions Ltd, U.K.). However, it is possible to read the .hxt files in MATLAB for further analysis.

### 2.1.1 Other comparable detectors

There are several other detectors which either use Cd(Zn)Te as a sensor material, or which use 2D pixellated ASICs. The detectors have a different readout strategy and, in the case of the 2D pixellated ASICs, are not necessarily designed primarily for the use with CdZnTe.

Current 2D detectors include the Pilatus series (Kraft et al. (2009), Henrich et al. (2009)), which were primarily designed for  $320\ \mu\text{m}$  thick silicon, but are also characterised and bump bonded with  $450\ \mu\text{m}$  and  $1000\ \mu\text{m}$  silicon. The detectors are single photon counting detectors designed to measure high flux and which use an energy threshold. For each pixel, an energy threshold can be defined, for

example, 15 keV. All detected events are compared to the corresponding voltage generated within the detector: all those above this threshold are counted, and all those below are not. Threshold devices primarily incorporate a pre-amplifier and then a comparator voltage to check the generated voltage of the detected photon with the comparator of the desired energy. Each pixel has a binary counter that registers 0 for events detected below the threshold, and 1 for those above the energy threshold. The pixel size is  $172 \times 172 \mu\text{m}^2$ , with a counting rate of over  $2 \times 10^6$  x-rays per second per pixel. The quantum efficiency of the sensor depends on the thickness of the silicon used, as well as the energy. For the case of 5.4 keV photons, this is quoted as 93.4%, for the 320  $\mu\text{m}$  thick silicon and 93.9% for both 450  $\mu\text{m}$  and 1000  $\mu\text{m}$  thicknesses. The detectors are available with 1 mm CdTe, as described by the Dectris (Dectris AG, Switzerland) website (Dectris AG (2015)).

Also used with Si or CdTe are Medipix versions 1, 2 and 3, (Campbell (2011), Ballabriga et al. (2011), Pennicard and Graafsma (2011)) and MPEC (Fischer et al. (2001), Löcker et al. (2004)), which are also single photon counting detectors that use energy thresholds. In the case of MPEC, each pixel has two discriminators (i.e. two thresholds can be set) and two individual counters. The idea behind the design is to reduce the dose to the target through acquiring two images at different energies. If only one energy was used, two acquisitions would have to be performed with the use of different tube voltages. These detectors have low noise, reduced backgrounds, exclude low energy photons, have high frame rates, but have effects of pile-up. Medipix can also be configured to use two threshold levels and measure across an energy interval or window.

It is important to note that originally, Medipix and Pilatus were designed for synchrotron radiation applications, which are monochromatic and are high intensity when compared to lab based systems. Therefore the desire for high counting detectors is more significant and the need to energy resolve is less important. For example, in terms of ADXRD, this feature is not required, as the input energy

for the diffraction experiment would also be the recorded energy. For EDXRD, however, this is a required feature as a polychromatic source is used.

Different detectors experience and manage charge sharing in different ways. In the case of Medipix, there is a 'winner takes it all' mode, and rapid summation algorithm (Ballabriga et al. (2011)). The principle of the algorithm is to sum up the detector charge and assign the total measured charge to the pixel that recorded the highest amount of charge in the first place. In the case of the Pilatus ASIC, charge sharing is detailed in the paper by Bergamashi et al. (2010). Here it is found that setting the threshold at 50% of the energy of interest removes charge sharing events influencing the data, based on their model and experimental data.

Pixellation means it is possible to have spatial information from an acquisition and the larger the area the better. For example, in clinical applications, the larger the area, the greater the field of view. This would negate the need for any repeat acquisitions in order to image the whole region of interest, or tiling of images. In the case of EXDRD, large samples can be explored potentially, depending on the design of the system used. A large area pixellated detector offers the active area of interaction based on the area of the detector, but with the sensitivity based on the pixel size. Typically the smaller the pixel size the better. The pixel size for EDXRD influences the momentum transfer resolution but the whole sensor can be used to measure diffraction. For the HEXITECH, the pixel size is  $250\times 250\ \mu\text{m}$ , compared to  $55\ \mu\text{m}\times 55\ \mu\text{m}$  for Medipix, and  $172\ \mu\text{m}\times 172\ \mu\text{m}$  for Pilatus. Amptek (Redus et al. (2009)) have designed a single crystal detector and thus there is no spatial information available. The area of the Amptek crystal is  $5\ \text{mm}\times 5\ \text{mm}$ , with CdTe thickness of 0.75 mm. The Amptek detector does not experience charge sharing, as it is only a single crystal detector. This detector is able to energy resolve and record a spectrum.

### 2.1.2 Specific information on the detector system used

The detector has two key elements that contribute to its usage and design. The first aspect is the sensor. The sensor material is the material with which the photons interact and generate charge. In this research 1 mm CdTe, provided by Acrorad Ltd (Japan) is bump-bonded to the ASICs. CdTe of 1 mm is of use for high energy based applications due to the linear coefficient of absorption. This interaction efficiency relates to the percentage number of photons at a given energy that would be absorbed by the sensor material, and is independent of the efficiency of the readout. In the case of CdTe, absorption of photons up to 60 keV is almost 100%. In addition to the efficiency, CdTe offers more practical benefits to HPGe detectors typically used for diffraction, which do not offer the room temperature and portable capabilities that CdTe could provide.

The ASIC, unlike other 2D ASICs that are bump bonded with CdTe, records an energy spectrum for each working pixel utilising the peak hold read out method, as described by De Geronimo et al. (2001) and De Geronimo et al. (2002) and is specific to the detector. The emphasis on the readout is to be able to record photon energies at the expense of time Jones et al. (2009). Being able to energy resolve enables all energy information to be recorded and is therefore available for analysis; the whole spectrum can be considered.

It is important to note that the 'Front end' GUI of the detector is not user friendly-to be able to appreciate the values selected, it is necessary to understand the readout, as has been described in Section 2.1. Typically when setting up a detector for use, one speaks of frame rate- the time taken for a frame to read out, or instead the acquisition time, i.e. the time taken to record photons. In the case of the system used in this research, the frame rate is not set by the user, but rather the frame rate is calculated based on the read out parameters which have been previously described Section 2.1. Based on the read out method, the only

parameter considered in this work is Row-S1 parameter, as this is the parameter that influences the photon detector the most with regards to detecting photons in the pixel per frame. The other two parameters that the user can set in the GUI are to do with the peak hold and buffer read out. These parameters were selected based on the advice of Matt Wilson and Matt Veale (verbal conversation, 2011). There is however a limit on these parameters in that there must be at least a  $4\ \mu\text{s}$  separation for the sample time due to the rise time of the pulse shaping in the ASIC. Sampling the signals in less time would mean that the signal does not have time to shape properly and would therefore be incomplete. The focus of this work is to investigate the Row-S<sub>1</sub> time and how this parameter affects the number of photons detected for a selected spectrum.

It should be noted for this work that the system used, although an  $80\times 80$  pixellated system, is in fact a modified  $20\times 20$  pixel prototype system. The original  $20\times 20$  pixel system was described by Jones et al. (2009). Prior to this research, the  $20\times 20$  system and read out was modified by Aspect Systems in Germany such that the system could work with an  $80\times 80$  pixellated ASIC, rendering the previous  $20\times 20$  system obsolete. It is no longer possible to utilise a  $20\times 20$  ASIC in the system. The modification also meant that the software used was built upon the original software used in the system, including the LabView software and the 2Easy data viewer. The PC used with the detector is specific to the detector system used in this research, due to the camera cable link card and the software on the system used to read out the detector. The system uses two partitioned hard drives which are set-up in RAID (redundant array of independent disks) formation. In order to double the readout bandwidth, the data readout utilises a RAID 0, while the operating system uses a RAID 1 configuration. This means that the operating system is mirrored and there is redundancy in the system, should the system fail. However, in the case of RAID 0, the data are recorded between two hard drives which have been and there is no redun-

dancy; if the hard drives completely fail, all the data are lost unless they have been previously backed up onto a another hard drive.

## 2.2 Properties required for EDXRD

Properties that are desired for EDXRD for breast tissue include a good energy resolution, high counting efficiency, low noise and a linear response over the dynamic range of interest. The accurate identification of tissue types depends on the ability to detect and resolve the peaks present in the scatter profiles. Materials such as adipose or glandular tissue have broad diffraction peaks, as do short range ordered materials.

A high efficiency is desired as it would reduce the acquisition time of the system, which is especially important for high throughput systems and in a potential clinical environment and application where results need to be determined rapidly, and scan times have to be reasonable to obtain results. The intrinsic quantum efficiency of the sensors can be calculated based on the linear attenuation coefficient of photon interaction. For CdTe, it has already been shown that the detection efficiency of photons up to 60 keV is 100%. This is essentially an intrinsic interaction efficiency i.e. that 100% of photons with energy up 60 keV interact with the 1 mm CdTe. However, this does not consider the effects of the number of photons incident at the detector and the response due to the read out method of the ASIC and the system itself.

Linearity of the detector is important to ensure that the detector response itself is not responsible for causing changes in the relative peak intensities of the diffraction data. Relative diffraction peak heights have long been used as a means of characterising a diffraction spectrum. It is therefore desirable that the detector is linear over the dynamic range suitable for the application, or that the response of the detector is known and can be corrected for in the data. The energies of

the photons deposited are directly proportional to the charge generated in the detector, however not all of the charge is necessarily collected. The nature of the read-out, recording the highest energy photon in the pixel, would mean that not all photons are measured or recorded. This would mean that it is expected that the efficiency decreases for higher fluxes, due to the fact that the system is simply not designed to read every photon in the allocated time but to read out the highest energy in that time.

For systems where the flux at the detector is unknown, having a relationship between the flux at the detector, or dose, would also be useful. Knowing the relationship between the input flux and the measured output means one could retrospectively calculate the input flux (dose) on the system if the input spectrum was known.

Of importance for a diffraction system is that the majority of the pixels can be used. It is possible that some pixels are not bump bonded properly, and therefore that the readout in those pixels fails due to a short circuit or there is incomplete charge readout. In practical terms, this would mean that part of the  $2\text{ cm}\times 2\text{ cm}$  detector is not actually usable for recording spectra. It is possible to exclude these pixels in post-analysis, but ideally they would not be used at all in the acquisition to reduce the acquisition time and redundancy. It is possible to deselect pixels for readout in the GUI such that the deselected pixels are not readout, however this functionality failed after the upgrade of the system to an  $80\times 80$  system from the original  $20\times 20$ . This functionality can therefore not be used and any unusable pixels will have to be excluded during post-analysis. For acquisitions in a diffraction system it is also important to have system stability in terms of the operation of the system. If the system is not stable, this can prolong the total experimental time due to having to reacquire data (due to failed read out). During a software crash the acquisition has to be forced to stop and restarted, occasionally this would require that the whole P.C would need to be restarted.

This would practically influence the use of the detector in the long term with its current software and readout system. For systems that scan samples or perform 2D imaging such as that performed in Chapter 5, having a stable system is ideal to reduce acquisition time and to limit user influence in the system. Should the read out fail, repeat data would have to be taken at the last known successful read out point which would therefore prolong the scan time. For an end user, this would not be acceptable, as ideally the system should work automatically and without complication.

The detector housing which includes the data acquisition system and environmental control was the same for both ASICs, which will be referred to as ASIC A and ASIC B. The temperature of the copper block was set to  $0^{\circ}\text{C}$  for both ASICs, corresponding to a temperature at the back of each ASIC of  $13.8\pm 0.5^{\circ}\text{C}$ . The FPGA values were set-up with an active  $R_s-S_1$  of 100 clocks at 20 MHz, and included a bias refresh of 4 ms every 60 s (Matt Veale and Matt Wilson, private communication (2011)). This bias voltage was set to  $-400\text{ V}$ . All data collected by the detector system were initially processed in 2Easy software using the HEXITEC executable and then transferred to MATLAB (Release 2012b, The MathWorks, Inc. Massachusetts, USA) for further analysis. All code for analysis was developed by the author, but code for the energy calibration of the ASICs was developed by Matt Wilson.

## 2.3 Objectives

Two  $80\times 80$  ASICs bump-bonded with 1 mm CdTe are to be investigated in this Chapter to determine their suitability for EDXRD. The CdTe is produced by Acrorad (Acrorad Ltd, Japan) and each sensor has its own characteristics, as each has its own bump bonding, crystal defects, and electrical components used in the ASIC. The best performing ASIC, in terms of the energy resolution and

efficiency at 60 keV, will be selected for use in a diffraction system, which is described in Section 3. Also under consideration will be the number of usable pixels, which would affect the area of the sensor available to detect photons.

The work in this Chapter aims to consider the impact of the use of the charge sharing discrimination algorithm i.e. the effects of including all detected events or excluding those considered as charge sharing both on the energy resolution and detection efficiency based on Americium-241 spectra. An Americium-241 source with known output will be used during is used. In the literature, other detectors using CdTe and can energy resolve have also used the 59.5 keV line of Americium-241, including Redus et al. (2009) and Seller et al. (2011). Using Americium-241 allows for the direct comparison between other HEXITECH systems that have been investigated (Seller et al. (2011) and Veale et al. (2011)) and those that will be developed in the future. The energy resolution of the current standard detector for EDXRD, HPGe, is commonly quoted in the literature at 60 keV, and therefore using an Americium-241 source also allows for comparison to this value. A radioisotope also has a known output such that the number of photons incident at the detect can be easily determined.

To understand the effects of the parameter Row- $S_1$ , which is the allocated time to search for photons within each pixel in a row, as described in Section 2.1, this Chapter seeks to investigate the number of photons detected for an input spectrum with photon energies utilised in EDXRD. This work will focus on the selected ASIC. This is to investigate the performance limitations of the ASIC based on the number of photons incident at the sensor. The ASIC is inherently limited by the read out technique, i.e. that the highest energy photon is read out per pixel per frame. By considering different frame rates, this work aims to contribute to greater understanding of the value selection of the Row- $S_1$  parameter for EDXRD. This has not been previously performed with this system, the presented ASICs or with other existing systems.

This Chapter also considers the system stability to consider the practical implications of using the current detector and PC system for diffraction work. It should be expected that the system remains stable during acquisition, and if it is not, that the ideal operating parameters be found to limit any instability. For use in an automated EDXRD set-up, the detector system ideally will operate without user input once data acquisition begins.

Work from this chapter has in part been previously submitted as an abstract and presented by the author at the PG Biomed Conference 2013 at the University of Surrey (Christodoulou et al. (2013)).

## 2.4 Method for energy resolution and energy efficiency

An Americium-241 (Am-241) source of 359 kBq activity was placed at a distance of 19.5 cm from the detector, to ensure a uniform exposure, with an acquisition time of 14 hours, as shown in Figure 2.4.1.

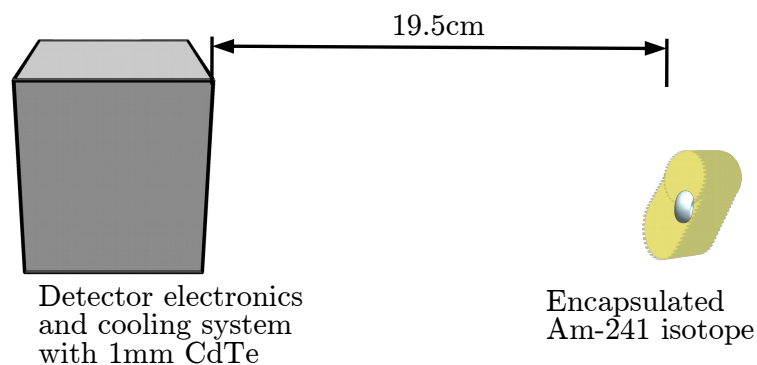


Figure 2.4.1: Schematic of system set-up.

Am-241 undergoes decay which produces photons at energies of 14 keV, 18 keV

and 60 keV, which covers the range of energies at which the detector would be used in a diffraction system. The energies of 14 keV and 18 keV are in fact L-lines of neptunium which occur at energies of 13.76 keV and 13.95 to make up the 14 keV line and 17.06 keV and 17.99 keV to make up the 18 keV lines, and are not resolvable by the detector. The bias voltage was -400 V, the bias refresh was set at 4 s with a 2 s recovery time.

## 2.5 Results: Energy resolution excluding charge sharing events

All data were processed using the HEXITECH.exe such that any charge sharing events and corrupted data were removed from the analysis, so that only single pixel events are included in the energy spectra. The spectra include a low energy noise edge at approximately 10 keV, the Am-241 lines at 13.9 keV, 17.8 keV and 59.5 keV, as well as characteristic lines of cadmium and tellurium at 23 keV and 36 keV. These have previously been observed by Redus et al. (2009) and Seller et al. (2011), both for CdTe sensors. The noise edge of the detector up to 10 keV is believed to be due to scattered events (Seller et al. (2011)). Photon energies below 10 keV are not used in the diffraction system, as detailed in Section 3.9.

Figures 2.5.1 and 2.5.2 show differences in spectral quality between two different pixels, one at pixel located(33,80) and the other from (53,33) in the 2D detector array. In the case of Figure 2.5.1 it is possible to see many features of the spectrum, which are annotated in the figure. In addition to features annotated, it is possible to detector the backscatter signal of 60 keV photons at 48 keV, a feature also observed by Redus et al. (2009) when characterising the Amptek detector with 1 mm CdTe sensor and an Am-241 source. It is not possible to distinguish these features in Figure 2.5.2. Each pixel was energy calibrated using the 14 keV, 18 keV and 59.5 keV lines of Am-241, using a linear relationship be-

tween the energy values and the energy bins of the pixels. The calibration code finds the ADC bin associated with Am-241. A linear regression fit is performed to find the relationship between the energy bins and the energy values of the photopeaks. The charge trapping tails of the photopeaks can also be seen.

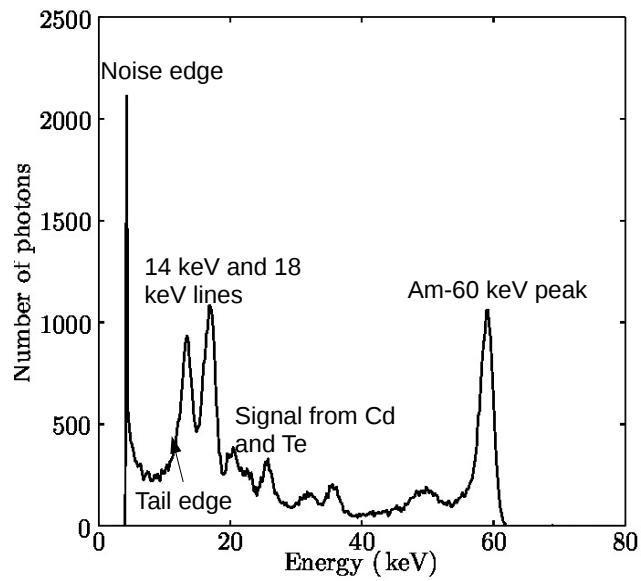


Figure 2.5.1: Example of a good pixel spectrum from pixel(33,80) in ASIC A.

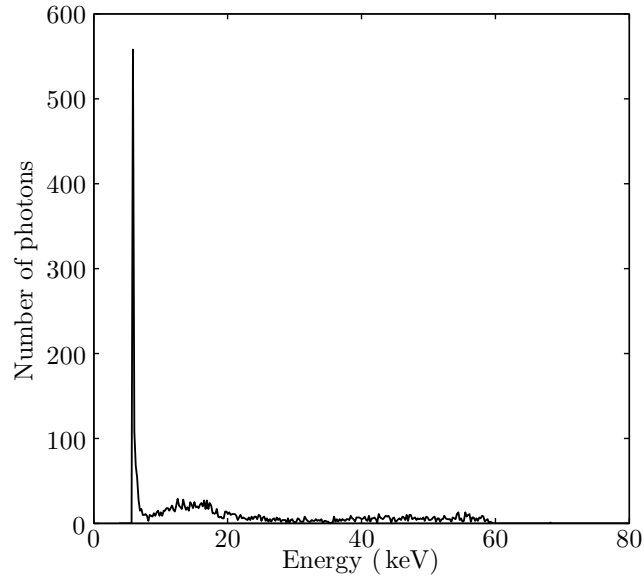


Figure 2.5.2: Example of a bad pixel spectrum from pixel(53,33) in ASIC A.

The energy spectrum per pixel was analysed in MATLAB using the inbuilt curve fitting functions and with code developed to find the FWHM of the Am-241 peak at 59.5 keV. For a Gaussian curve with mean value  $x_m$ , amplitude  $A_p$  and standard deviation of  $\sigma$ , the FWHM can be calculated using Eqn 2.5.1, based on the width of the Gaussian curve at an intensity value which is 50% of the amplitude.

$$\text{FWHM} = 2\sqrt{2\ln 2}\sigma \quad (2.5.1)$$

The Gaussian fit utilised the higher energy end of the curve to remove any effects caused by the charge trapping tail that can be associated with CdTe sensors. An example fit excluding the charge trapping tail is shown in Figure 2.5.3

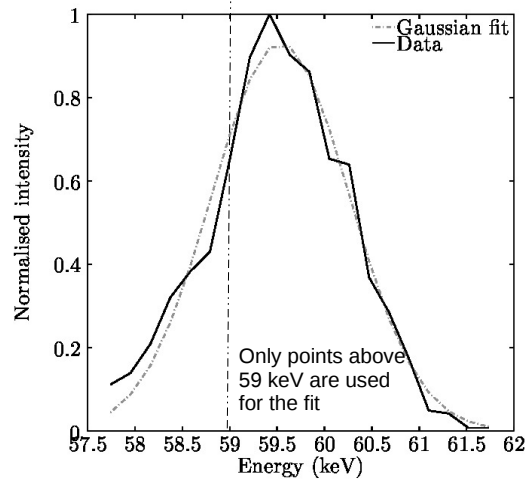


Figure 2.5.3: Example of a Gaussian curve fit to exclude the charge trapping tail of a photopeak of 60 keV

The algorithm for obtaining the fits involved finding the maximum peak value within a pre-defined window. A good pixel is considered to be one where the error in the integrated spectral counts is less than 5%. This was calculated by Eqn 2.5.2

$$\frac{\sum_i I_i}{\sqrt{\sum_i I_i}} \quad (2.5.2)$$

where  $I_i$  is the intensity value at the  $i$ th energy bin. Once all of the energy resolution values for each pixel were obtained, a histogram was produced for each energy for each ASIC, to consider the global distribution and variation in the energy resolution values across both ASICs. The histograms were obtained using 50 bins to assign the pixel energy resolutions from each ASIC, for energy values of 14 keV, 18 keV, and 60 keV.

Figures 2.5.4 and 2.5.5 show two histograms of the measured FWHM distri-

bution for the two ASICs at 59.5 keV. Pixels with noisy or no spectral response were not considered in the analysis. These pixels equated to 3.8% of ASIC A, and 18.5% of ASIC B.

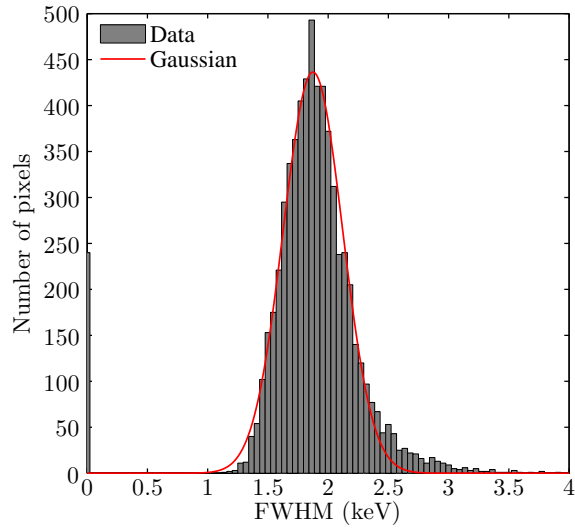


Figure 2.5.4: ASIC A 59.5 keV energy resolution distribution.

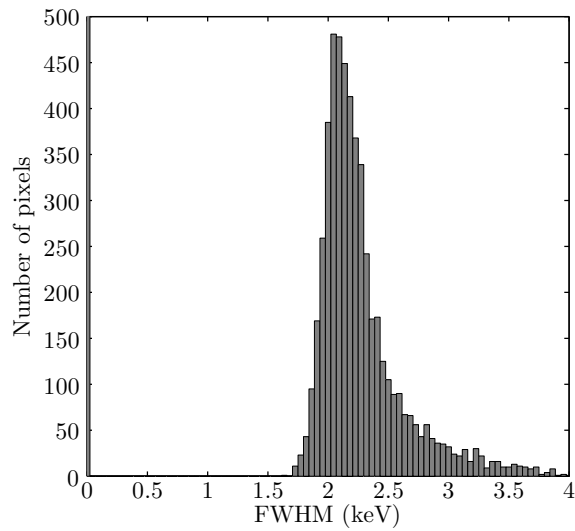


Figure 2.5.5: ASIC B 59.5 keV energy resolution distribution.

Considering the global energy resolution values, the mean value of energy

resolution was found to be  $1.9 \pm 0.3$  keV at 59.5 keV for ASIC A and  $2.3 \pm 0.4$  keV for ASIC B. A Gaussian distribution would be expected due to the primary sources of noise and randomisation in the system. Shot noise occurs due to the quantised nature of photons and photoelectrons within the detector, leading to a Poisson distribution over time. Thermal (also known as Johnson noise, Nyquist noise or Johnson-Nyquist noise) is generated by random thermal motion charge carriers within the detector. Finally, due to the randomisation of the number of photons incident at the detector, noise caused by variations in the photon rate follows the Poisson statistics. Extending the Poisson distribution to the limit of a large number of events, a continuous Gaussian distribution would be expected for the energy resolution of the system. A Gaussian fit for the histogram is used to demonstrate the deviation from a Gaussian-with the deviation primarily at the higher FWHM peak, which means that there is a widening of the photopeak for these pixels, due to the tail trapping influencing the Gaussian fit used for the energy resolution, or that energy resolution is generally speaking poorer in these pixels (no tail trapping influence). The fact that there is little to know deviation from the Gaussian histogram at lower FWHM values means that poor fitting due to the charge trapping tail is primarily responsible.

The deviation from the Gaussian is more pronounced in ASIC B. This ASIC has more pixels where spectra cannot be obtained or have poor statistics, namely those where the bonding has been unsuccessful, or the spectral quality is poor due to defects within the material. The energy resolution distribution for the 18 keV peak of Am-241 were also found, the FWHM distribution of which can be found in Figures 2.5.6 and 2.5.7.

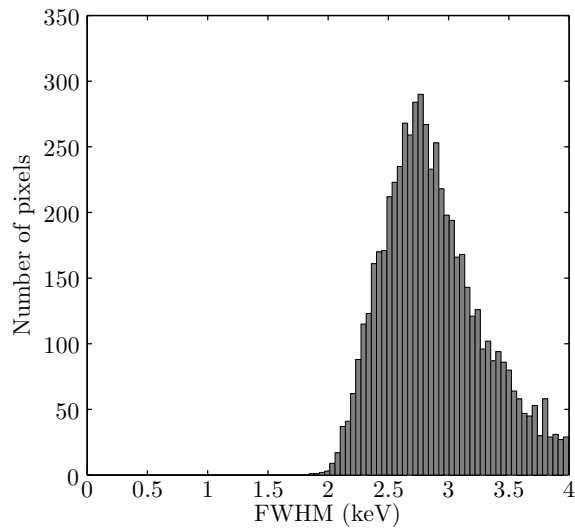


Figure 2.5.6: ASIC A 18 keV energy resolution distribution.

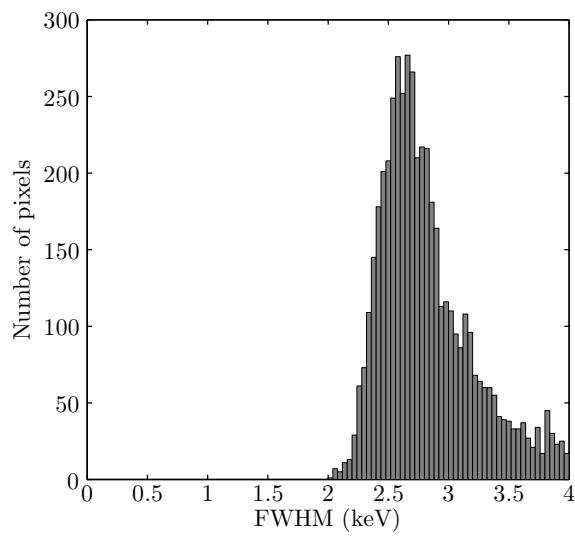


Figure 2.5.7: ASIC B 18 keV energy resolution distribution.

The energy resolution distributions for the 14 keV peak of Am-241 are shown in Figures 2.5.8 and 2.5.9.

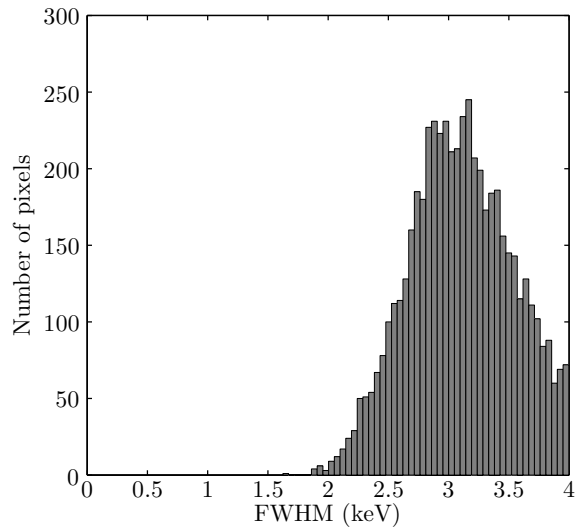


Figure 2.5.8: ASIC A 14 keV energy resolution distribution.

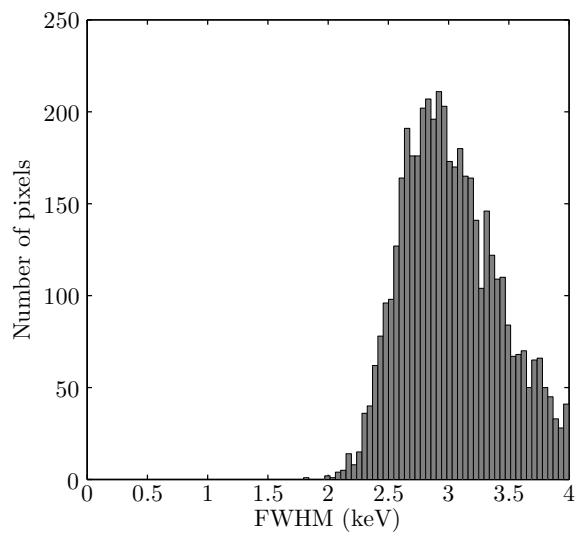


Figure 2.5.9: ASIC B 14 keV energy resolution distribution.

The mean energy resolution of all pixels, for energies 14 keV 18 keV and 59.5 keV for both ASICs was found, as well as the standard deviation of the distributions. These are summarised in Table 2.5.1

| Energy (keV) | 14             | 18             | 59.5           |
|--------------|----------------|----------------|----------------|
| ASIC A       | $3.13 \pm 0.4$ | $2.92 \pm 0.8$ | $1.94 \pm 0.3$ |
| ASIC B       | $3.05 \pm 0.4$ | $2.83 \pm 0.4$ | $2.31 \pm 0.4$ |

Table 2.5.1: Detector average energy resolution values calculated from all pixel values for ASIC A and ASIC B.

Excluded from this process were those pixels considered to have noisy or poor statistics. Any pixels that fell within the exclusion criterion were given a nominal FWHM value of 0 keV. These pixels were also excluded from the calculation of the global mean energy of the sensors. Table 2.5.2 summarises the percentage of poor pixels of each sensor used for the energy resolution calculations.

| Energy (keV) | 14   | 18   | 59.5 |
|--------------|------|------|------|
| ASIC A       | 15.2 | 8.2  | 3.8  |
| ASIC B       | 28.7 | 24.3 | 18.5 |

Table 2.5.2: The percentage number of pixels not used for the energy resolution analysis.

## 2.6 Results: Efficiency excluding charge sharing events.

The energy efficiency of the ASICs is explored in this section. The data previously used to determine the energy resolution distributions are used.

The number of photons expected to be at the detector area within the acquisition time was calculated and excluded the percentage of pixels not used in the energy resolution data, as found in Table 2.5.2. The yield of the 59.5 keV photon is 35.3% and therefore the number of photons within the acquisition time of 14

hours was calculated per ASIC, based on the active area of 3.65 cm<sup>2</sup> and 2.9 cm<sup>2</sup> for ASICs A and B respectively. The number of counts within the 59.5 keV peak within the FWHM was calculated per pixel and then summed over all used pixels to provide the total number of photons detected by the active area at 59.5 keV for each detector. The decay of Am-241 through alpha decay, leads to a daughter isotope of Neptunium-237, which leads to the further emissions of the 14 keV, 18 keV and 26 keV lines seen in a typical Am-241 spectrum. The 14 keV and 18 keV lines actually consist of several energy lines that are not resolvable by every pixel in the detector due to the energy resolution.

As quoted by Akovali (1994), the x-ray emissions from Neptunium-137 are a result from emission L-lines. There is a range of L-lines and the 14 keV line actually consists of photons of energies of 13.76-13.94 keV, a range of 180 eV, and the 18 keV line consists of energies of 17.5–18 keV, a range of 500 eV, which is not within the energy resolution limits of the sensors used in this work which are on average 3 keV. The percentage emissions at 14 keV, 18 keV and 59.5 keV of the source used are 13.5 %, 21 % and 35.5 %, respectively. Therefore, due to not being able to resolve the multiple energy lines, the energy efficiency was not calculated at 14 keV and 18 keV.

The total energy efficiency  $E_{Ef}$  of the ASICs for the 59.5 keV photons was determined using Eqn 2.6.1

$$E_{Ef} = \frac{I_{Am} Y a_{det} A_d T_a}{T_p} \quad (2.6.1)$$

where  $I_{Am}$  is the activity of the Americium source expected at the detector, taking into consideration the distance of the detector from the source,  $Y$  is the yield at the energy of interest, which is equal to 0.353 for the 59.5 keV gamma emission,  $T_a$  corresponds to the expected fraction of photons transmitted through the air,  $A_d$  is the expected fraction of photons absorbed in the detector material, and  $T_p$  is the total number of detected photons at 59.5 keV. Eqn 2.6.1 is the ratio

of the expected number of photons at the detector and the number of photons detected.

| ASIC | Expected photons | Detected photons | Measured efficiency (%) |
|------|------------------|------------------|-------------------------|
| A    | 4853281          | 2454900          | $50.6 \pm 0.2$          |
| B    | 4334711          | 2158189          | $49.8 \pm 0.2$          |

Table 2.6.1: Calculated detector efficiency at 59.5 keV using the working areas of the ASICs.

## 2.7 Charge sharing considerations

This section considers the same data but instead of removing charge sharing events, they are uncorrected and included in the spectra i.e. the charge sharing discrimination algorithm is not used. It would be expected that the counting efficiency at 59.5 keV increases but the corresponding energy resolution would decrease. This is due to the variation in the energy detected-the charge sharing events would always have a lower detected energy value than the true energy of the deposited photon energy, the energy resolution of the detector is expected to be poorer. Figure 2.7.1 shows the difference between an Am-241 spectrum which includes charge sharing events and that which uses the charge discrimination algorithm during post processing, taken from pixel (33,78) from ASIC A. It can be observed that there are more measured events when there is no charge sharing discrimination and is more pronounced at lower energies. Charge sharing events would be detected at lower energies than the original energy deposited.

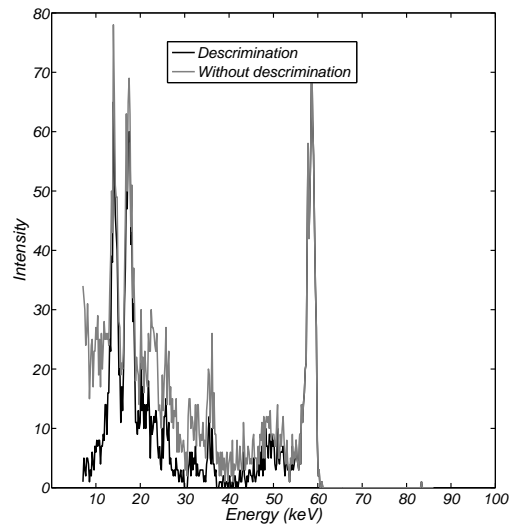


Figure 2.7.1: Example spectrum including charge sharing events from ASIC A at pixel (33,78).

The set up is exactly the same as previously described, but in this section the post processing has not performed charge sharing discrimination.

### 2.7.1 Energy resolution and efficiency with charge sharing events

Figures 2.7.2a and 2.7.2b show the distribution of the energy resolution when including charge sharing events for the 14 keV lines, Figures 2.7.3a and 2.7.3b show the distribution for the 18 keV peak and finally Figures 2.7.4a and 2.7.4b demonstrate the energy resolution distribution at 59.5 keV.

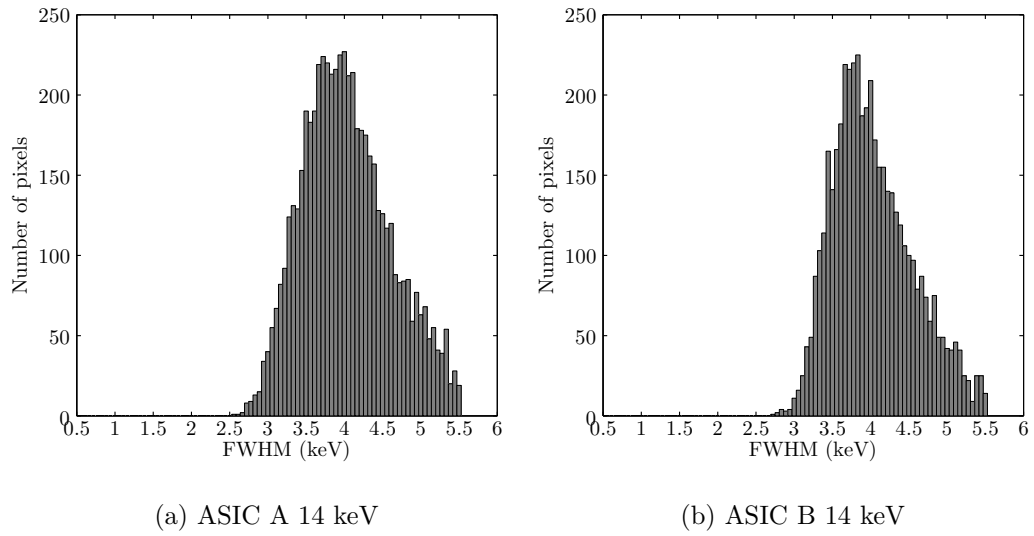


Figure 2.7.2: Energy resolution distribution with charge sharing events included for both ASICs A and B at 14 keV.

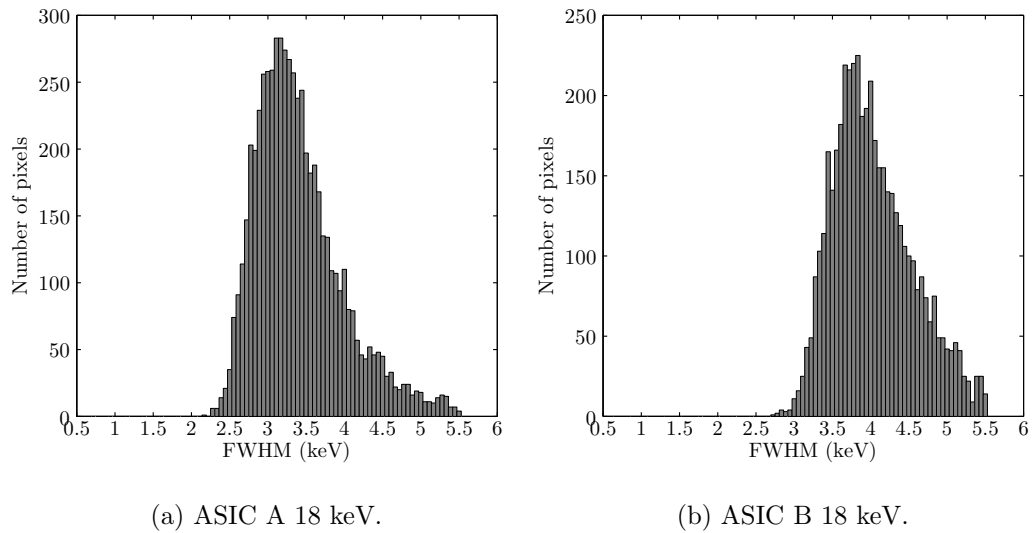


Figure 2.7.3: Charge sharing energy resolution distribution for both ASICs A and B at 18 keV

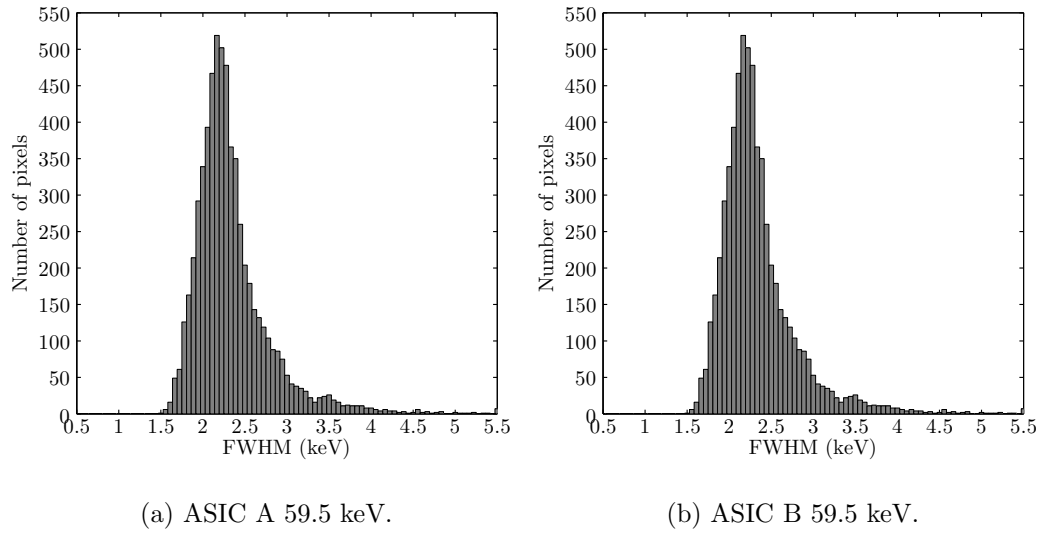


Figure 2.7.4: Charge sharing energy resolution distribution for both ASICs A and B at 59.5 keV.

The mean energy resolution, their standard deviations, and the energy efficiency at 59.6 keV line, are recorded for both detectors and summarised in Tables 2.7.1 and 2.7.2 respectively. For this research, due to the inclusion of a greater number of events, additional pixels were included in the analysis as the statistically usable area, i.e. those that fulfilled the criterion of having maximum 5% statistical error, were now included. This resulted in an area of  $3.78 \text{ cm}^2$  for ASIC A and  $3.26 \text{ cm}^2$  for ASIC B.

| Detector | 14 keV          | 18 keV          | 59.5 keV        |
|----------|-----------------|-----------------|-----------------|
| A        | $3.58 \pm 0.46$ | $3.23 \pm 0.37$ | $2.31 \pm 0.39$ |
| B        | $3.64 \pm 0.35$ | $3.15 \pm 0.33$ | $2.29 \pm 0.17$ |

Table 2.7.1: Detector average energy resolution values.

| Detector | Expected photons | Detected photons | Measured efficiency (%) |
|----------|------------------|------------------|-------------------------|
| A        | 5050212          | 3676200          | $73.2 \pm 0.1$          |
| B        | 3874501          | 2490300          | $64.6 \pm 0.1$          |

Table 2.7.2: Detector efficiency calculation.

When considering the charge sharing events at the 59.5 keV peak of Am-241 photopeak, the overall energy efficiency at 59.5 keV increases. In addition to this it can be shown that the overall energy resolution reduces due to the inclusion of these events. This results in the general broadening of the energy peaks per pixel. The number of expected photons at the sensors vary due to the number of 'dead' pixels present in each sensor is different.

## 2.8 Investigation of Row-S<sub>1</sub> parameter and stability for ASIC A

The following section details the operation settings of the detector, to determine the relationship between the row selection time and the number of photons incident at the detector. The row time was varied, resulting in a variation in the frame rate for a fixed integrated energy spectrum, and the output of the beam was varied in terms of its photon output rather than its energy spectrum by varying the current setting of the tube. Therefore, the integrated spectrum remained fixed, i.e. the accelerating potential of the x-ray source was kept constant, but the total number of photons incident at the detector was varied by varying the tube current.

During the acquisition of the data for the frame rate tests, the number of incidences of software crashes were observed and recorded in order to determine the stability of the detector system with respect to each Row-S1 and x-ray tube

current variation.

### 2.8.1 Method

The experimental set-up utilised was a micro focal x-ray source (X-tek, Tring, U.K), with a tungsten target, with inherent filtration of 0.175 mm aluminium. 15 mm was applied as external filtration close to the source and away from the detector to avoid scatter being detected by the sensor. This amount of filtration was used to reduce the number of photons to an order of magnitude suitable for the tests, and to limit the photon energies to 25–40 keV. Figure 2.8.1 shows the spectrum used for the tests, the shape of which was predicted by the SpekCalc software (Poludniowski and Evans (2007), Poludniowski (2007), Poludniowski et al. (2009)).

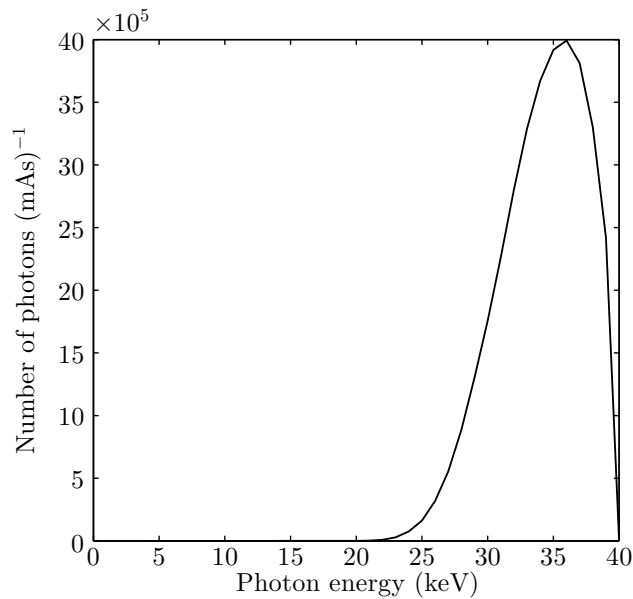


Figure 2.8.1: Spectral shape for the frame rate tests.

The detector was positioned at a distance of 23.5 cm away from the front of the x-ray source. The row select time was varied through 1, 10, 50, 100 and 500

clocks, as summarised in Table 2.8.1 and the tube current was varied between 0.1–1 mA.

| Row time (clk) | Frame time (ms) | Frame rate (s <sup>-1</sup> ) |
|----------------|-----------------|-------------------------------|
| 1              | 0.3             | 3900                          |
| 10             | 0.3             | 3400                          |
| 50             | 0.5             | 2200                          |
| 100            | 0.7             | 1500                          |
| 500            | 2.3             | 440                           |

Table 2.8.1: Frame rates and row values.

The detector was exposed for 60 s and the beam was set at a maximum potential of 40 kVp, but the tube itself is capable of reaching 125 kVp. The value was chosen with the given filtration, as preliminary experiments had shown that the detectors exposure to the unfiltered beam led to all results being interpreted as charge sharing events, even at the lowest operable tube current. The filtration also served to change the spectrum through beam hardening to limit the spectrum photons at energies of primary interest for x-ray diffraction.

## 2.8.2 Results for Row-S<sub>1</sub> investigation

The DAT file from each acquisition was processed using the data processing executable and the text log files were generated. To extract the information from the files, a script using the programming language Python (Python Software Foundation. Python Language Reference, Version 3.4. <http://www.python.org>) was developed by the author to read the output files and to extract the corresponding values from the data. The code searches for strings within the text files e.g. "Number of frames written" and records the corresponding number value following the parameter of interest, in this example, the number of frames written.

This process was repeated for each acquisition and the output parameter for each acquisition was recorded in another text file to be read into MATLAB for further processing.

The number of incident photons at the detector was calculated using the SpekCalc predictive software and inclusion of filtration values. The predicted number of photons per energy was calculated to adjust for the effects of the distance from the source to the detector, the detector area, and the current setting of the x-ray source. The total number of photons expected at the detector was calculated by integrating over the spectrum.

| Row time (clk) | Detected frames | Written frames |
|----------------|-----------------|----------------|
| 1              | $3612 \pm 181$  | $3612 \pm 181$ |
| 10             | $3241 \pm 1$    | $3241 \pm 1$   |
| 50             | $2134 \pm 1$    | $2134 \pm 1$   |
| 100            | $1612 \pm 435$  | $1612 \pm 435$ |
| 500            | $441 \pm 0$     | $441 \pm 0$    |

Table 2.8.2: Detected frames compared to the number of written frames

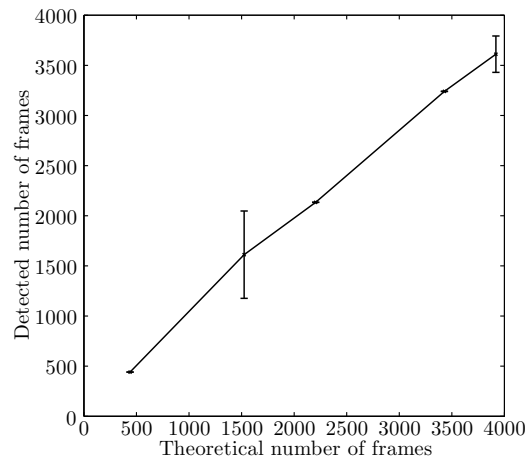


Figure 2.8.2: Detected number of frames compared to the theoretical expected number of frames with standard deviation.

The number of frames detected were exactly the same as the number of frames written which means that there were no frames removed due to incomplete frame data collection and is summarised in Table 2.8.2. There was also a good agreement between the number of frames detected and written, compared to the number of expected based on the theoretical calculations, as shown in Figure 2.8.2. However, as shown by the standard deviation in Figure 2.8.2, for row clk 1 and 100, there is a spread in the number of frames recorded during the acquisition. This is due to the read out of the detector which can be affected by the buffering and transfer of data to the PC i.e when data transfer is not at a rate fast enough for the DAQ. It was found that on occasion this would lead to software failure, and the detector system would require a restart.

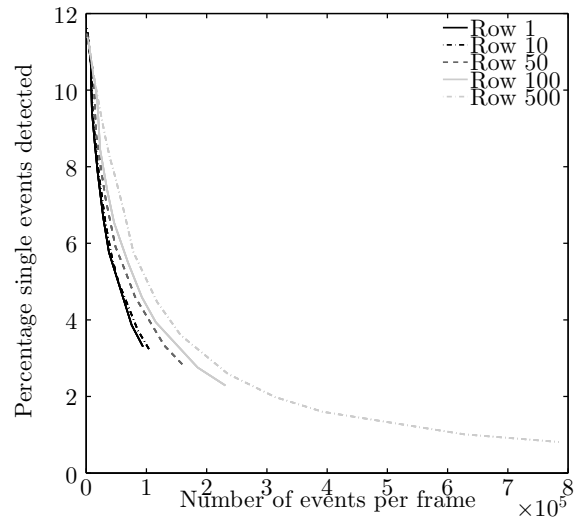


Figure 2.8.3: Percentage number of single events detected.

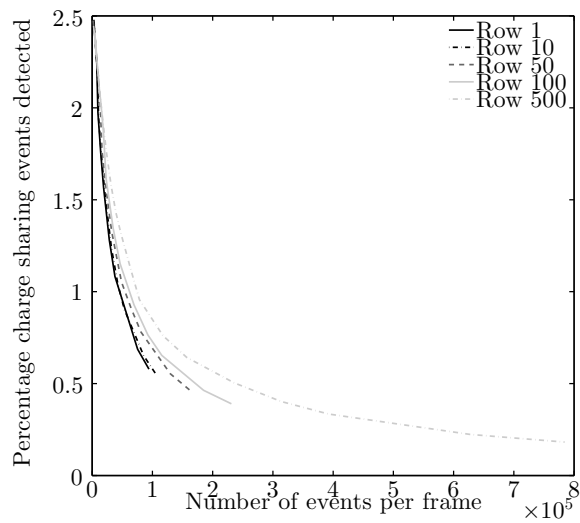


Figure 2.8.4: Percentage number of events detected.

Figure 2.8.4 shows the response for the total number of single events detected, i.e. no charge sharing events. These figures do not have error bars to show the plots clearly. A linear approximation for the region where fewer than  $10^5$  photons were expected per frame was found by fitting a first-order polynomial through the

data points using the MATLAB, and performing a least square fit, considering the errors as weights for the fit. The linear approximations were found with  $R^2$  values of 0.95. An example of the linear fitting is shown in Figure 2.8.5.

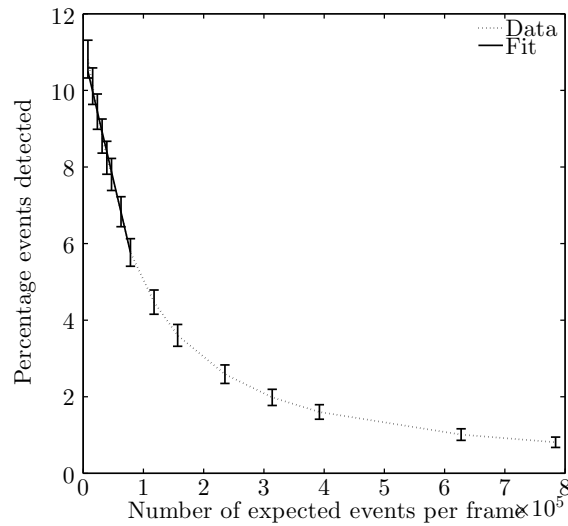


Figure 2.8.5: Mean single events detected.

Each threshold response was measured by interpolation of the data which was then extrapolated to higher fluxes as shown in Figure 2.8.6. The threshold limit and the linearity limit was found for each row setting. The linearity limit is found as this limit is where there is no-longer a directly proportional relationship between the number of expected events and the percentage events detected.

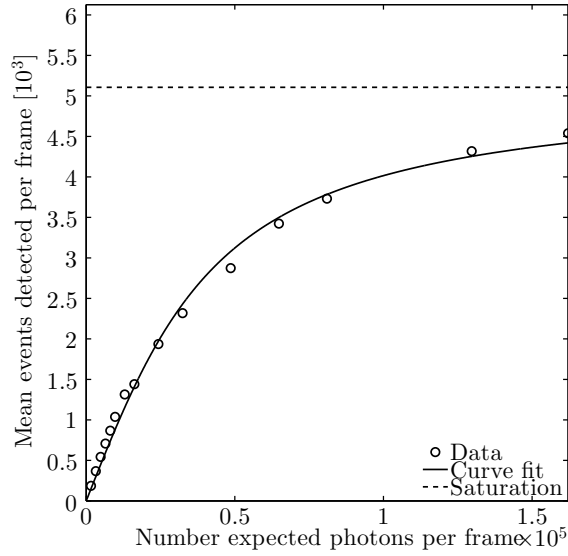


Figure 2.8.6: Example saturation point for the row value 100

Table 2.8.1 summarises the linear limit and the threshold limit for all row times and therefore for the frame rates used. The theoretical number of events per frame is 6400 which is equivalent to one event detected per pixel. For this ASIC this is found to be true for the row clock time of 500. The linear limit for all row clocks is similar, excluding that of 500. The limit of approximately 8% is consistent across all other row times. The maximum efficiency is 12%, found at the higher frame rates. This is to be expected, as increasing the frame rate would increase the efficiency, as the number of photons expected per frame would decrease, and therefore on average the pixels are able to detect at most one photon event during each frame.

| Row time (clk) | Linear limit    | Threshold limit |
|----------------|-----------------|-----------------|
| 1              | $7.87 \pm 0.42$ | $3129 \pm 55$   |
| 10             | $7.78 \pm 0.42$ | $3412 \pm 58$   |
| 50             | $7.97 \pm 0.42$ | $4563 \pm 68$   |
| 100            | $7.41 \pm 0.41$ | $5316 \pm 73$   |
| 500            | $5.77 \pm 0.36$ | $6420 \pm 81$   |

Table 2.8.3: Frame rate and row value.

It is seen from Table 2.8.3, that the limit for the row clock value is approximately 6400. Even as the number of photons increases, no more photons can be theoretically detected by the ASIC due to the nature of the read-out.

### 2.8.3 System stability results

The following table details the observed crashes during the data acquisition for Section 2.8.2.

| Tube current ( $\mu\text{A}$ ) | Row 1 | Row 10 | Row 50 | Row 100 |
|--------------------------------|-------|--------|--------|---------|
| 100                            | –     | crash  | crash  | –       |
| 150                            | –     | crash  | –      | –       |
| 200                            | –     | –      | crash  | crash   |
| 300                            | crash | crash  | –      | –       |
| 400                            | crash | –      | crash  | crash   |
| 500                            | crash | crash  | crash  | crash   |
| 600                            | crash | –      | crash  | –       |
| 800                            | crash | –      | crash  | –       |
| 1000                           | crash | crash  | crash  | –       |

Table 2.8.4: System crashes experienced during frame rate acquisitions

From Table 2.8.4 it can be seen that the system experienced many software failures during the acquisition of the data and no crashes experienced before  $100 \mu\text{A}$ . In each software crash situation, the acquisition had to be halted, and the GUI forced to shut down and then restarted. Occasionally it was necessary to shut down and restart the PC, which meant shutting down all other software, which would then have to be reloaded once the PC was switched on. This was both disruptive to the data collection process, and time consuming. Consistent crashes would reduce the possibility of using the detector in an automated diffraction system. It was therefore decided to operate the detector at a row clock time of 100, as this would be the fastest clock rate with the fewest number of system crashes. Based on the investigation of the number of photons detected for a given frame rate, the 100 clock level was found to not exceed the limit of more than one event detected per frame.

## 2.9 Discussion

The energy resolution of the ASICs has been shown to be approximately 2.3 keV at 59.5 keV. The quoted energy resolution for HPGe is given as 600 eV at 60 keV, although the HPGe planar sensor used in this research has a resolution of 440–480 keV. Although not as high as the HPGe, the value is better than previous Cd(Zn)Te type detectors used in diffraction (Malden and Speller (2000), Crespy et al. (2010)). These studies used Cd(Zn)Te detectors with energy resolution of 5% at 70 keV, 2 keV at 60 keV, respectively. In addition, the detector performs comparatively well to modern detectors which utilise the same sensor material, such as the values of the Amptek sensor which was found to be 0.6 keV at 60 keV (Remoue (2009)) and the Medipix sensor with a resolution of 3.36 keV at 60 keV (Greiffenberg et al. (2011)), both of which source their CdTe from Acrorad. The energy resolution at 59.5 keV for another ASIC bump bonded to 1 mm CdTe

was found to be 0.87 keV (Seller et al. (2011)). Any differences between systems would be caused by differences in processing (DAQ), system electronics (design and components used) and from variations in the sensor material itself.

The energy resolution histograms of each ASIC shows that there is a deviation from an ideal Gaussian distribution where the FWHM becomes systematically high for both ASIC A and ASIC B. This is suggestive of the poor fitting for the lower tail edge of the photo-peak. The fitting of the peak excludes, in principle, the lower energy tail by assuming that at 50% of the peak intensity the peak is behaving as a Gaussian. Where this assumption begins to fail, the fit would no-longer be suitable and the measured FWHM would be higher to take into the account the broadening of the peak. Although the fit is not necessarily suitable, this is still a means of quantifying the energy resolution of the 59.5 keV peak but without taking into account the lower tail edge. It is not uncommon practice to use the FWHM of the peaks, as has been performed by Veale et al. (2011). In order to be able to compare to previous systems, the photo peaks are assumed to be Gaussian.

Comparisons between the inclusion of charge sharing events or only including single detected effects showed that there was a slight deterioration of the energy resolution when using the charge sharing events within the spectra. These effects are more noticeable at the lower energies of 14 keV and 18 keV, as these energy bins have more charge sharing events recorded. It was decided that charge sharing would not benefit diffraction spectra, as the inclusion of charge sharing events would lead to an increase in the detection of apparent lower energy photons. This could serve to affect the measured intensity at these energies as well. In terms of diffraction for a fixed geometry, this would result in a greater number of photons apparently being detected at lower momentum transfer values which would therefore make a diffraction spectrum appear to have a stronger signal at lower momentum transfer values. This effect would be due to the detector itself,

rather than the photon interaction with the sample.

Research conducted by Veale et al. (2012) explores other algorithms such as charge sharing addition, so that these data are not removed, and therefore the detector efficiency would be expected to increase. This is however not implemented in this work as it was not available at the time. Future software updates will make this algorithm available for use in post-analysis of the data. Veale et al. (2012) only considered the use of a monochromatic x-ray source of 20 keV, and did not explore the effects of charge sharing with increasing energy. Based on the diffusion model, the effects of charge sharing is dependent on the photon energies involved (based on the depth of interaction). However, as the photon energy deposition increases, it is no-longer possible to consider the initial charge cloud as a delta function, as is the case in the diffusion model. If the detector were to be used at higher energies where the diffusion model can no-longer be justified i.e. the initial charge cloud size is significant, then this would also have to be explored, ideally as a function of photon energy to investigate how these algorithms respond to different energies.

The absorption of photons based on the linear attenuation coefficient of photons in 1 mm of CdTe means the sensor is suitable for diffraction with energies up to 60 keV, and therefore those typically used by x-ray diffraction studies when investigating tissue equivalent materials. For the momentum transfer values and probabilities of interaction of interest, the x-ray diffraction values would be detected, and is discussed further in Chapter 3. When considering the sensor and the readout, the detection efficiency increases from 40-50%, when excluding charge sharing events to values of 60-70% with the inclusion of charge sharing events. This is also to be expected as exclusion of the charge sharing events reduces the number of events detected in the same acquisition time. Removal of the events would serve to reduce the detection efficiency. This measured efficiency is based on the frame settings used, and the input to the detector utilised. The efficiency

is dependent on the input to the detector (number of photons and the energy of the photons), as well as the read-out parameters. The number of charge sharing events will also be affected by the spectrum used. This section of work focuses on the efficiency to highlight the effects of charge sharing on the spectra, and to also provide a means of quantifying the detector efficiency for the two ASICs in this research, which has never previously been performed.

Of the two ASICs, the effects of the charge sharing and changes in efficiency are mostly seen in ASIC A, which has a greater detection efficiency of 73.2% compared to that of 64.6% for ASIC B. However, the two ASICs perform similarly when considering only the single detection events with efficiency of  $50.6 \pm 0.2\%$  and  $49.8 \pm 0.2\%$ . The variation is caused by the fact that ASIC B has a greater number of unusable pixels caused by shortening in the ASIC or poor bonding. This would mean that there are fewer pixels to charge share with and also that for pixels where no charge was measured, it would appear as no split events were recorded. Comparison of the usable area of the ASICs show unusable areas of 3.8% and 18.5% for ASICs A and B, respectively. In terms of overall use, it is desirable to have as many working pixels in a detector system to obtain as much data as possible during an acquisition. The calculation of the energy efficiency of the system only includes the active area.

The investigation of the Row- $S_1$  parameter, and the stability was only considered for the selected ASIC A. Acquiring at higher frame rates leads to a higher percentage of photons being detected, at approximately 12%, with a linear response to a value of 7% counting efficiency over all photons. Presented here is therefore a method that would allow, for a determined input energy spectrum, the relationship between the incoming number of photons (and dose if the spectrum is known) and the point at which there is a linear relationship between these values. Where dose is important, e.g. in systems with real tissue, this method could be used to determining the input dose to the sensor when the output of the

detector is known. However, in this case the direct proportionality is observed up to 7% counting efficiency. Another method would be to use an Am-241 source or another source with a known output. However, the activity would affect the number of photons incident at the detector, and depending on the source type would only have peaks at selected energies rather than a continuous spectrum. It would not be possible to change the number of photons at the detector without adjusting the distance between the radioactive source and the sensor. Using an x-ray source for this experiment made it more practically relevant to any potential real sources, and the number of photons incident at the detector could be easily varied using the fact that there is a linear relationship between the x-ray source current and the number of photons incident at the sensor (for a fixed kilovolt potential). Adjusting a distance could lead to errors in the incident number of photons and therefore have a greater influence on the final calculated results. The primary source of uncertainty of the flux in the method presented here is due to the source.

Compared to detectors that are primarily photon counting and do not produce energy resolving spectra, the counting ability is comparatively low. For example, the Medipix 2 chip can count up to approximately 100,000 photons per pixel (Tlustos et al. (2006)), and each pixel has a pitch of  $55\ \mu\text{m}\times 55\ \mu\text{m}$ . The quoted counting ability of the Pilatus chip with 1 mm CdTe is  $5\times 10^6$  photons per second per pixel and each pixel is of size  $172\ \mu\text{m}\times 172\ \mu\text{m}$  (Dectris AG (2015)). However, the ability to energy resolve and have spatial resolution is of great advantage. Providing all energy information enables the user to be able to distinguish features that are of relevance to their measurements, and those that are not. For example, setting a threshold at 15 keV would mean all signals detected above that value would be counted and summed per pixel. It would not be possible to separate, for example, an XRF signal and a diffraction signal when a polychromatic source is used, as is conducted in Section 3. If used with a monochromatic source, such

as an ADXRD system, this does not become an issue. Having all the spectral information also allows for the investigation of the diffraction signal based on an energy value of energy range of choice, also conducted in 3.

The 2D pixellated ASIC is self-limiting due to the nature of the read-out i.e. each pixel measures the highest energy event detected in the user defined time. Therefore it is expected that not all events should be recorded as this is not the ASIC's primary design, but rather to be able to measure the photon energy and produce spectra for each pixel. This was a decision made at the design and implementation of the ASIC.

Post-analysis techniques in diffraction could potentially counteract any shortcomings in the global counting efficiency as MVA techniques have been developed specifically to deal with situations where detection statistics is low, such as in short acquisition times, so these techniques could be used with the detector if necessary. The efficiency is also dependent on the nature of the read out, and so it is difficult to directly compare different detector systems, especially when their ASICs are designed with a different emphasis. In the case of Medipix and Pilatus, this is to photon count above a specified energy threshold. With the detector system, the emphasis is to energy resolve, at the cost for acquisition time and detection rate (Jones et al. (2009)).

The stability of the system is greatly affected by the operating parameters, although there were system crashes throughout the stability experiment. System crashes prolong the experimental time and makes the detector system user unfriendly. The system crashes due to software conflict are not resolvable by the author as the source code was not provided by the company for further investigation. Generally speaking, the use of at least three pieces of software to operate the environmental controls and the detector itself is also user unfriendly. However, software development is currently in progress to make the software for the system more friendly, and to have it such that it is possible to control the temperature

and the humidity in the same user interface, as well as the bias refresh for the polarisation. Unfortunately, this software was not available for this work. Additionally, the fact that the readout parameters have to be input into the system is also user unfriendly, rather than having an 'acquisition time' or 'frame rate'. Future software will be designed to have the frame rate as an input parameter by the user (Matt Wilson, verbal communication, 2013)

## 2.10 Conclusions

Two ASICs were investigated in terms of their energy resolution, their energy efficiency at 59.5 keV, and the number of usable pixels. The effects of charge sharing on the spectra, quantified by the energy resolution and the energy efficiency including charge sharing events was also explored. The ASIC which was considered to be the best performing was then selected and investigated further. The operation of the detector system was explored in terms of the Row-S<sub>1</sub> time, and also in terms of the operational stability.

It was found that the mean value of energy resolution was found to be  $1.9 \pm 0.3$  keV at 59.5 keV for ASIC A and  $2.3 \pm 0.4$  keV for ASIC B. When charge sharing events were considered this was found to be  $2.31 \pm 0.39$  keV at 59.5 keV for ASIC A and  $2.29 \pm 0.17$  keV for ASIC B. However, for diffraction it would be better to not include charge sharing events due to the fact this would lead to an increase in the detection of apparent lower energy photons which would then appear that, for a fixed geometry, more events were detected at a lower momentum transfer value than was actually the case, due purely to the fact that charge sharing events lead to the detection of lower energy photons.

The percentage of unusable pixels for ASICs A and B was found to be 3.8% and 18.5%, respectively. This indicates that ASIC A has a greater usable area of 96.2%, which is more ideal for x-ray diffraction. A larger area sensor would allow

for a greater number of photons being detected, which would improve statistics of the diffraction profiles.

The ASIC performance based on their energy resolution values compared to previously used detectors and sensors makes it possible to use them for EDXRD experiments. Any potential issues with poor statistics data can be resolved by possibly using MVA techniques in future studies. Due to the higher usable sensor area, ASIC A is the ASIC used for the diffraction system developed in this work.

An experimental and analysis method for determining the linear response and saturation levels of a sensor are presented here. It was found that, for the input energy spectrum utilised, that there is a direct relationship between the number of photons incident at the detector and the number of measured photons. This limit of this relationship was found to be 7% for all Row-S<sub>1</sub>1 values except 500 clks. At this limit the detected input at the detector is no-longer directly proportional to the input spectrum, and therefore dose, at the sensor.

The system instability was also explored. The system experienced several crashes during operation. It was observed that there was the fewest number of crashes at 100 clks, and therefore this value is used for the future operation of the detector in this research.

# Chapter 3

## Diffraction system

### 3.1 Introduction

Previous works which have used the pixellated detector for x-ray diffraction include the works by O’Flynn et al. (2013), O’Flynn et al. (2012) and Christodoulou et al. (2011). The former two works utilised an  $80 \times 80$  system with no-secondary collimator, and the latter utilised a  $20 \times 20$  system with a secondary collimator for finer angle selection. The samples considered in O’Flynn et al. (2012) were explosives materials, such as Samtex and Hexamine. Christodoulou et al. (2011) utilises only powdered materials for the investigation of the multi-angle diffraction data for identification of illicit materials. These materials included caffeine

and crushed up tablets of paracetamol. Neither of the previous systems had automated sample stages, or the ability to move the sample such that diffraction imaging could be performed. In both cases, the thickness of the samples were standardised for the purpose of the investigations and to avoid variations in the thickness becoming a source of variation in the data. Excluding a secondary collimator makes the experimental set-up practically easier than aligning both a primary and secondary collimator.

Other investigations that explore the use of amorphous materials and in particular breast tissue in diffraction studies also have defined thickness throughout. As previously discussed in Section 1.3, several studies utilise standard thickness for their investigations. Kidane et al. (1999) used a cylindrical tube with cross-sectional area of  $25 \text{ mm}^2$ , corresponding to a thickness of approximately 2.8 mm. The samples were excised tissue from 100 women who had undergone mastectomy, lumpectomy or reduction mammoplasty procedures. In one of the thicker samples used in diffraction studies Pani et al. (2010) utilised a breast tissue biopsy of diameter of 6 mm. These samples were from surgically removed tissue of 11 women. Synchrotron studies by Castro et al. (2004) and Castro et al. (2005b) used breast tissue of approximately 1 mm thickness, which were excised breast tissues collected from the operating theatre and later fixed in formaline and the MVA study conducted by Conceição et al. (2011) used tissue standardised to 3 mm thickness. The 106 samples used in the study were also obtained from excised tissue during surgery. None of the studies explored the effects of thickness on their diffraction results, as this was not the primary focus of their studies. Pani et al. (2009) did consider the effects of sample thickness in their model, and how increases in thickness lead to poorer momentum transfer resolution, and therefore a deterioration in the diffraction data. This was conducted using both experimental data and a computer model, with the focus on crystalline structures rather than amorphous materials.

An example of researchers who have included scanning of samples in their systems include Pani et al. (2010), who performed EDXRD computed tomography (CT), by rotating breast tissue samples and reconstructing the images. Griffiths et al. (2008) investigated a microCT diffraction system at a synchrotron facility, considering breast tissue, reconstructing diffraction based images, as well as taking transmission images of the breast tissue. Castro et al. (2005a) also performed diffraction imaging at a synchrotron facility. Scanning of the sample allows for the reconstruction of 2D image of the sample. In the case of EDXRD there are several ways to obtain an image from the obtained spectra, but the most popular parameter is to consider the intensity of the diffraction peak at the momentum transfer value of interest in that study. When scanning a sample, it is possible to create an image by using a quantitative value from the spectra and display the amplitude of the parameter in each pixel, which corresponds to a position in the diffraction scan.

## 3.2 Objectives

This Chapter will detail the inclusion of the 2D detector array in a diffraction system that does not include a secondary collimator, and the effects of post-processing of the data with respect to sample thickness. Collimator design is not a focus of this work but rather to explore the possibility of utilising the detector with a micro-focal mammography source, which has not been presented in either O’Flynn et al. (2013), O’Flynn et al. (2012) or Christodoulou et al. (2011). The ability to image a sample is also presented in this system, which has not been performed before with this detector and diffraction system design.

For each pixel a spectrum is produced, resulting in theoretically 6400 diffraction spectra, assuming each pixel is usable. The aim of this work is to also consider how utilising the data affects the diffraction profile outputs with respect

to sample thickness, and to see how diffraction parameters used in imaging, summarised in Section 1.4, including the peak height, FWHM, and ratios between the peak height, FWHM and peak area are affected. More will be discussed in Section 3.9. The system will be focussed on biopsy samples, and is a choice by the author, based on the literature, which utilises mainly biopsy samples. The work aims to cover the range of biopsy sample thicknesses used within the literature to explore the thickness variation outputs for biopsy samples using the system presented. The behaviour of the diffraction signatures of breast tissue equivalent material of varying thickness in the system is unknown. For use in a clinical setting or where the input thickness is unknown, it would be ideal to be able to relate the output signal in the diffraction signal to the sample input, without knowing the constituents of the diffraction sample *a priori*. The thickness of a single material sample relates to the amount of a specific tissue present or tissue equivalent thickness in the sample.

The parameters of the diffraction system, such as the focal spot size, beam height and spectrum used are determined in order to be able to compare this prototype micro-focal with sample imaging system to any other future systems.

### 3.3 System considerations

When considering the peak positions of adipose tissue, glandular tissue, PMMA and nylon, which are used as tissue equivalent materials, the momentum transfer values of interest are  $0.78 \text{ nm}^{-1}$ ,  $1.1 \text{ nm}^{-1}$  and  $1.6 \text{ nm}^{-1}$ . No breast tissue is used in this work as it was not available for use in this research, instead the focus is on materials such as water and PMMA. It is therefore necessary to distinguish between the closest peaks of the materials, namely the  $0.78 \text{ nm}^{-1}$  and  $1.1 \text{ nm}^{-1}$  peaks of PMMA and lard respectively, which therefore requires a maximum momentum transfer resolution of  $0.3 \text{ nm}^{-1}$ . A diffraction system can

be characterised by its momentum transfer resolution and is based on Eqn 3.3.1, which can be considered as the fractional uncertainty of the energy value and angular value added in quadrature.

$$\frac{\Delta\chi}{\chi} = \sqrt{\left(\frac{\Delta\theta}{\theta}\right)^2 + \left(\frac{\Delta E}{E}\right)^2} \quad (3.3.1)$$

where  $\chi$ ,  $\theta$  and  $E$  are momentum transfer, diffraction angle and detected photon energy respectively and  $\Delta\chi$ ,  $\Delta\theta$  and  $\Delta E$  are equal to the difference between the maximum and minimum possible measured values at a given value, i.e.  $\Delta\theta$  is  $\theta_{max} - \theta_{min}$ ,  $\Delta E$  is  $E_{max} - E_{min}$  and finally  $\Delta\chi$  is  $\chi_{max} - \chi_{min}$ . Further definition of  $\Delta\theta$  for this system is provided in Section 3.9.2. The fraction  $\frac{\Delta E}{E}$  is equivalent to the energy resolution, which was previously calculated in Chapter 2. Based on this value, it is necessary to ensure that the geometry of the system is able to obtain a momentum transfer resolution of minimum value 0.3. This will be determined by the ability to measure the peak position of the two signals  $0.78 \text{ nm}^{-1}$  and  $1.1 \text{ nm}^{-1}$  i.e. that it is possible to record an intensity value at  $0.78 \text{ nm}^{-1}$  and  $1.1 \text{ nm}^{-1}$ . The effects of the energy resolution can be considered to be negligible as the fractional uncertainty in the energy is 0.04.

It should be noted that due to the angular dependency on the momentum transfer resolution, that each pixel would have its own momentum transfer resolution. As previously shown in Section 2.5, each pixel would also have its own energy resolution based on the spectral quality of that pixel. For this system, the momentum transfer resolution will be based on the global detector values. As will be seen later within this Chapter, the diffraction spectra of individual pixels are not considered, therefore using the sensor energy resolution, as determined from the histograms in Section 2.5, is the most appropriate option in this case.

The system presented is required to be automated as this allows for faster acquisitions as they do not require manual intervention. In particular for sample scanning where several 100 data points are taken, automation saves both time in

terms of the total acquisition time, and also intervention time of the user, who does not have to intervene in the acquisition in anyway, saving the individual time and effort. Although not a necessity, this is an attractive element of any potential clinical based diffraction system.

The x-ray source available for this research is a micro-focal tungsten target source from X-Tek (X-Tek, Nikon, Tring, U.K.). No fixed requirement is placed on the focal spot size, mainly due to the the fact that the focal spot size range is inherent to the x-ray source used, and its magnitude cannot be changed by the user. The system has a focal spot range between  $0.5 \mu\text{m}$  to  $40 \mu\text{m}$  depending on the demand on the accelerating potential (Ben Price, Nikon, private communication). Based on this, more emphasis was placed on selecting operation parameters, namely the kilovolt potential of the source and the tube current, and the focal spot size was measured based on these values. The focal spot size measurement becomes relevant when discussing the beam divergence and beam size at the sample, which will be discussed more in Section 3.6, and is found in order to determine these factors.

The energies used in the x-ray spectrum affect the available energies for x-ray diffraction in terms of both the energies of photons that interact with the 1 mm sensor material, and the photons which undergo coherent scatter leading to interference and diffraction. Therefore, it is a requirement that the spectrum should fall within the absorption efficiency of the 1 mm CdTe, such that this is 100% for most of the energies involved. Some studies have considered the best angles and energies to use for diffraction, in particular for water. These studies aim to minimise multi-scatter events and to encourage a stronger diffraction signal, rather than have a signal affected by incoherent scatter or multi-scatter events. Morin and Berroir (1983) considered the theoretical analysis of both coherent and incoherent scatter based on the works of Narten and Levy (1971), which considered the coherent scatter function for water, and the works of Hubbell et al. (1975),

which considers the incoherent scatter function of water. It was found that for photons with energies of 20 keV, 90% of photons were single scatter events. Later works by Taibi et al. (2000) investigated contributions of scatter signals on 5 cm breast tissue and Monte Carlo simulations. It was found that at  $9^\circ$ , coherent scatter events are 20 times that of incoherent scatter events. LeClair et al. (2006) found that 92% of photons exiting the sample at  $6^\circ$  is coherent signal. Johns et al. (2002) investigated medical imaging with scatter photons and for photon energies of 25 keV, it is found that over 55% of interactions within tissue is caused by scatter. Small angles are considered to be  $2^\circ$ - $12^\circ$  and specifically for water, a tissue equivalent material, at  $5^\circ$  no incoherent scatter from the sample is detected. At  $10^\circ$  and photon energy of 35 keV, there is four times as much coherent scatter signal than there is incoherent scatter. Ideally for a system the signals considered should be 'small', in the region of  $2^\circ$ - $12^\circ$  to detect coherent scatter. Following the literature investigations, energies of 20 keV to 35 keV is also ideal for these angle ranges. Therefore a spectrum that generates photons at these energies is ideal for use in x-ray diffraction, based on water and breast tissue results.

As stated the spectrum can affect the focal spot size which in turn affects the beam divergence and the beam size at the sample. The system requires that the beam height is less than 0.5 mm in both the x- and y- directions. This is a nominal value, but also means that finer structure could be investigated in diffraction studies. In general it is a balancing act, if the beam size is too small, the scatter volume is small and therefore the diffraction signal is low and would decrease the signal output. On the other hand, if the beam height is too large then finer structures cannot be investigated. For the purpose of this work it is important that the beam size is no more than 0.5 mm for the thickness studies, where the variation in the sample thickness is assumed to be negligible across the scatter volume. More will be discussed in Section 3.9.

All of these requirements have to be made based on the equipment available.

For example, there are geometrical limitations due to the finite size of the translation stages used for the automated system. This will also be discussed further in this Chapter. This system is not an optimised system but rather a prototype system of this nature that can be used as a comparison system for studies using the detector for breast tissue biopsies in the future.

## 3.4 X-ray spectrum

### 3.4.1 Introduction

The spectral shape, the range of energies generated and the intensity of the produced Bremsstrahlung output affects the counting time of diffraction acquisitions. The possible recordable momentum transfer values are also affected. This section details the determination of the inherent beam filtration and the spectral shape of the beam. In order to do this, a combination of measuring the half value layer (HVL) and an x-ray source output prediction software is utilised.

To predict the output of x-ray sources, Bremsstrahlung prediction software for tungsten anode targets utilise the probability of interaction of electrons with the target and the corresponding spatial distribution. Inputs to the software tend to be the radiation angle, the maximum kilovolt potential, and externally applied filtration in terms of common filters such as aluminium and molybdenum. From these factors the predicted Bremsstrahlung output and the HVL can be found from the theoretical output by varying the total filtration, keeping the external filtration as the value found from experimental data plus some unknown factor  $F_I$ . For this experiment the SpeckCalc 1.0 (Poludniowski and Evans (2007), Poludniowski (2007), and Poludniowski et al. (2009)) is used. The software was downloaded from the Institute of Cancer Research, and was free for research purposes. This software is chosen as it is specifically for use with

tungsten targets. Other available prediction methods include the Siemens website which has a toolbox for x-ray source prediction with a range of targets and energies (<https://w9.siemens.com/cms/oemproducts/Home/X-rayToolbox>). It is not possible to download the predicted spectrum from the website for analysis. Another possible predictor software is the MATLAB based Spektr (Siewerdsena et al. (2004)).

### 3.4.2 Half value layer theory

The Half Value Layer (HVL) is defined as the amount of external filtration of a radiation source that is required to be applied to reduce the original output of the source,  $I_o$ , to 50 % of the original output,  $I_{0.5}$ , when filtered externally by one type of material. This is based on the Beer–Lambert law, as given by Eqn 3.4.1,

$$I_{0.5}(E) = I_o(E)e^{-\mu_f(E)x_f} \quad (3.4.1)$$

where  $\mu_f$  is the linear attenuation coefficient of the filter material at energy  $E$ , and  $x_f$  is the thickness of the filter material. X-ray sources have internal windows added to filter the beam, and also the housing and tube itself can lead to attenuation. These combined effects are considered to be the inherent filtration  $x_i$  of the source. Therefore, the Beer–Lambert law can be written as Eqn 3.4.2.

$$I_{0.5}(E) = I_o(E)e^{-\mu_f(E)(x_f+x_i)} \quad (3.4.2)$$

assuming the inherent filtration is measured in terms of the same material as the external filtration. For sources such as those used in mammography, a HVL in terms of aluminium is often used as a reference. By applying external filters to the beam and measuring the output, a plot of output against external filtration can be obtained, a curve of best fit applied and then interpolated to find the  $I_{0.5}$  value. Once the HVL is known, it is possible to use Bremsstrahlung prediction

software to find the inherent filtration of the source by utilising the known value  $x_f$  to find the unknown value of  $x_i$ .

### 3.4.3 Experimental method

To measure the beam output a 15 cm<sup>3</sup> ion chamber with surface diameter of 3.96 cm (10100AT, Fluke Biomedical, Fluke Cooperation, USA) was placed 12 cm  $\pm$  0.3 cm from the x-ray source, such that the entire surface of the ion chamber area would be illuminated. The output of the x-ray source was measured with no external filtration based on the air kerma of the 15 cc of air in the ion chamber, using a Keithley 35050A electrometer. Aluminium filters (Goodfellows, USA) of fixed surface area of 4 cm<sup>2</sup> but differing thickness were then incrementally placed directly in front of the beam, so as to reduce scatter detection from the aluminium on the ion chamber. A schematic of the system set-up is given in Figure 3.4.1.

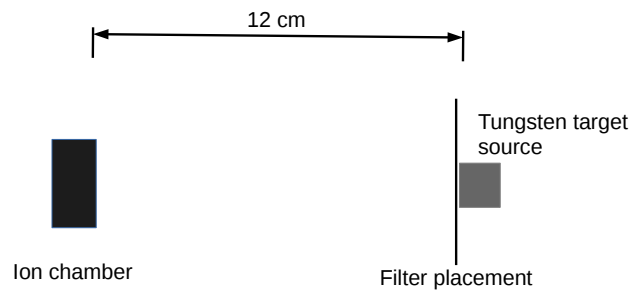


Figure 3.4.1: System for determining the HVL of the system.

The dosimeter was fixed to measure output in terms of the air kerma (mGy/s) and measurements were recorded when the readings had stabilised so as to ensure they were not obtained during periods of beam fluctuation. The aluminium filters, their surface density and equivalent thickness are detailed in Table 3.4.1.

| Aluminium filter combinations ( $\text{mgcm}^{-1}$ ) | Equivalent thickness (mm) |
|--|---------------------------|
| 0.00   | 0.00                      |
| 14.30  | 0.06                      |
| 16.50  | 0.07                      |
| 19.90  | 0.09                      |
| 21.80  | 0.10                      |
| 41.75  | 0.18                      |
| 51.10  | 0.22                      |
| 56.30  | 0.24                      |
| 58.25  | 0.25                      |

Table 3.4.1: Aluminium filter details. Using the density of aluminium at room temperature, the value of the thickness can be calculated from the different surface areas.

### 3.4.4 Results

To find the external filtration of aluminium required to reduce the initial output  $I_o$  to  $I_{0.5}$ , the output with respect to the applied external filter needs to be found. Code developed by the author in MATLAB was used to read in a Microsoft EXCEL (Microsoft Corporation) spreadsheet of data points, including measurements errors observed during the experiment, and to plot the measured output against the filtration of aluminium.

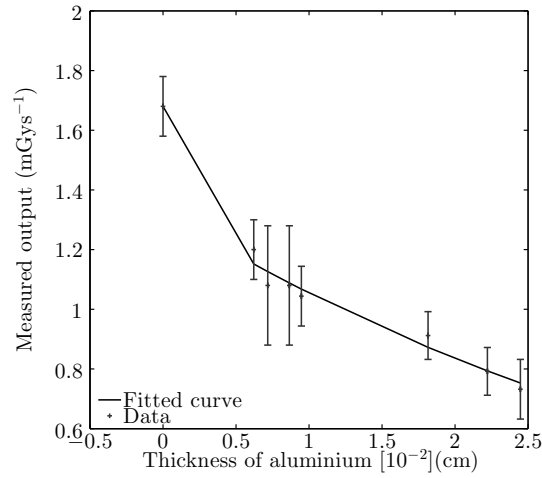


Figure 3.4.2: Output response to applied external filters.

The best fit curve shown in Figure 3.4.2 was found to be an exponential which is due to the exponential decay according to the Beer–Lambert Law as the filters attenuate the beam.

The interpolated HVL was found to be  $0.023 \text{ mm} \pm 0.004 \text{ mm}$ , i.e. the amount of filtration corresponding to  $I_{0.5}$ . This was performed using the `interp1` function in MATLAB. This HVL value can now be used as a reference value for x-ray source output prediction software. The SpekCalc software is able to predict the Bremsstrahlung output, including the corresponding HVL. All experimental values were entered into the prediction software, including the radiation angle of  $42^\circ$ , the maximum angle range at which photons are produced from the anode, and the kilovolt potential. By varying the total value of the filtration  $x_f + x_i$ , the predicted output of the source is found such that it matches the output recorded, as shown in Figure 3.4.3.

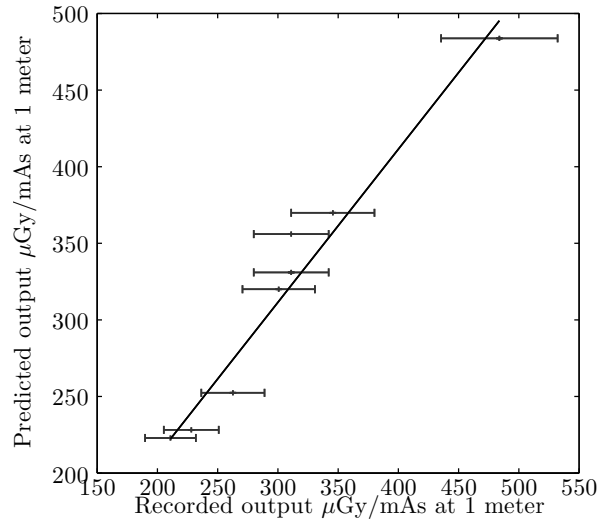


Figure 3.4.3: Output of the source compared to the prediction. Source fluctuations are accounted for in the error bars.

The corresponding internal filtration of the x-ray source was found to be  $0.175 \pm 0.2$  mm of aluminium. This is the value at which the output of the source and the predicted output as measured by the prediction software matched.

This result can now be used to determine the x-ray spectrum utilised through the use of x-ray source prediction software Spekcalc.

### 3.4.5 Determination of x-ray spectrum

When considering the inherent filtration of the x-ray source, the prediction software can be used to show the expected x-ray source spectrum. The output spectrum of the x-ray source with the limit of 70 kVp is shown in the Figure 3.4.4, where the mean energy of the x-ray spectrum is 26.4 keV. For the momentum transfer of interest and the geometry used, a large number of photons with energy of 20–40 keV is required for coherent interference to obtain diffraction peaks at the momentum transfer values under investigation.

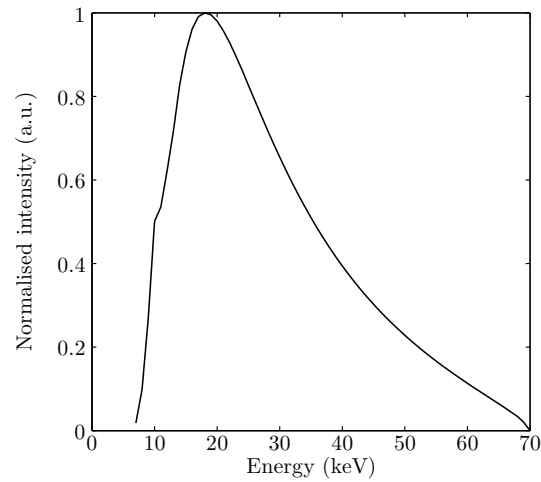


Figure 3.4.4: Beam spectrum used for diffraction.

## 3.5 X-ray focal spot

### 3.5.1 Introduction

Table 3.5.1 details the possible operational parameters of the source. These were determined from operating the source and finding the power limit, as the manual for the source did not explicitly state these values. This was also conducted to check the functionality of the source.

| Maximum potential (kV) | Maximum allowed current (mA) |
|------------------------|------------------------------|
| 65                     | 1.0                          |
| 70                     | 1.0                          |
| 75                     | 1.0                          |
| 80                     | 0.8                          |
| 90                     | 0.8                          |
| 100                    | 0.8                          |
| 110                    | 0.6                          |

Table 3.5.1: X-ray source operational limits.

To have the maximum output available for x-ray diffraction, it was decided to use a kilovolt potential of 70 kVp and current setting of 0.8 mA. The following focal spot measurements are based on these settings.

### 3.5.2 Theory of focal spot calculation

The blurriness of an image is quantified mathematically by the spatial resolution of the system, which relates to the ability to define boundaries within an image and to distinguish between them. In imaging terms, the spatial resolution is represented by the point spread function (PSF) in the spatial domain or the Modulation Transfer function (MTF) in the spatial frequency domain. Eqn 3.5.1 is the relationship between the two domains.

$$\text{MTF} = \text{F}(\text{PSF}) \quad (3.5.1)$$

In theory, the PSF is found by imaging an infinitesimally small object that can be expressed as a delta function in the  $(x;y)$  spatial domain i.e.  $(x, y) = \delta(x)\delta(y)$ . However in practical terms, it is not possible to acquire an image of an infinitesimally small object but only to approximate one. This can be done

using a small aperture in a material that is otherwise opaque to the photons used. This aperture has to be comparable to the expected spatial resolution of a system, and for systems with micrometer resolution it is not a trivial task to use an aperture of that magnitude and align it with the beam centre (Bushberg (2002)). A small aperture would also increase acquisition time and be difficult to manufacture in a radiopaque material such as lead due to its malleability. Other more practical methods can be used to measure the spatial resolution of the system such as measuring the line spread function (LSF). This considers a slit that theoretically extends infinitely in one dimension and is narrow in the other. The practical implications and limitations of this are similar to that of the point source. Instead, a more practical approach to measuring the spatial resolution of the system is used, namely the measurement of the Edge Spread Function (ESF).

The ESF is the integral of the line spread function, and therefore once the ESF is found from imaging the edge object, the derivative leads to the LSF, from which the spatial resolution of the system can be determined. Measuring the ESF as opposed to the LSF for measurements of focal spots were found to be as effective by Samei et al. (1998), Ardran and Crooks (1971) and Shuping and Judy (1978). It has been shown by Samei et al. (1998) and Samei et al. (2006) that the use of an edge object is not sensitive to any misalignment in the experimental system, nor is the measurement of the ESF sensitive to any scattered radiation. This makes it an attractive method due to simpler set-up.

Blurriness in an image can arise from four sources; 1) the focal spot and geometry, 2) the intrinsic resolution of the detector, 3) the motion of the sample, and 4) the analogue to digital conversion-which is applicable to digital detectors only (Webb (1988)). These sources of blurring can lead to a total blurring effect by the square summation, as shown in Eqn 3.5.2 (Wagner (1977) and Spiegler and Norman (1973)),

$$U_t = \sqrt{U_s^2 + U_d^2 + U_m^2 + U_a^2} \quad (3.5.2)$$

where  $U_t$  is the total blurring,  $U_s$  is blurring due to the focal spot and geometry,  $U_d$  is the blurring due to the intrinsic response of the detector,  $U_m$  is blurring due to motion, and  $U_a$  is signal blurring due to the analogue to digital conversion.

Blurring due to the motion of the imaging sensor or the sample leads to different projections of the objects at the plane of the detector. Geometric magnification arises due to the divergence of the x-rays from the source and the object itself. Due to this, the minimum geometric magnification factor is 1 or larger, hence the object at the image plane will be its normal size or a larger. The effect of the focal spot is to lead to an area behind the object which does not 'see' the focal spot at all. The object creates a shadow on the image plane and is referred to as the umbra, from the Latin for shade. At the edges of the object the shadowing effect becomes a partial effect as the x-rays from the source are able to be detected at the image plane. This leads to the penumbra, the partially shadowed area. These terms are defined in Figure 3.5.1.

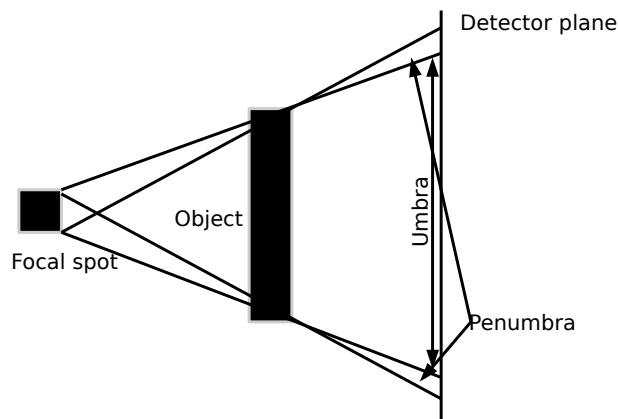


Figure 3.5.1: A diagram of the principles behind focal spot blurring.

The blurring due to the digital conversion arises from analogue to digital

conversion where the analogue signal is binned into digital bits, which can lead to the loss of some information from the signal (Yaffe and Rowlands (1997)).

To investigate the focal spot size for this system, the effects of  $U_d$ ,  $U_m$  and  $U_a$  have to be negligible or non-existent. There was no blurring in the system due to motion as both the detector and the sample were stationary. Any blurring due to analogue to digital conversion is ignored, as it is assumed that the 12-bit depth of the detector is sufficient to ensure no degradation of image quality when converting from analogue to digital signals. To record the effects of the focal spot, it is better to have the edge object positioned such that the geometric magnification and focal spot effect is large. Alternatively, to remove effects of the focal spot and the geometrical magnification, the test object would be placed on or very close to the detector, ideally on the surface of the detector itself. This is not required in this system as it is the effects of the focal spot that are being measured. The contributions due to geometric magnification and focal spot magnification are given in Eqn 3.5.3

$$U_s = \frac{sb}{a+w} = sm \quad (3.5.3)$$

where  $m$  is equal to the source–detector distance ratio and affects the blurring due to the focal spot,  $w$  is the distance between the focal spot and the x-ray source aperture,  $a$  is the distance between the x-ray source aperture and the object, such that the total source-object distance is  $a + w$ . Finally,  $b$  is the distance between the object and the detector. All terms are shown in Figure 3.5.2.

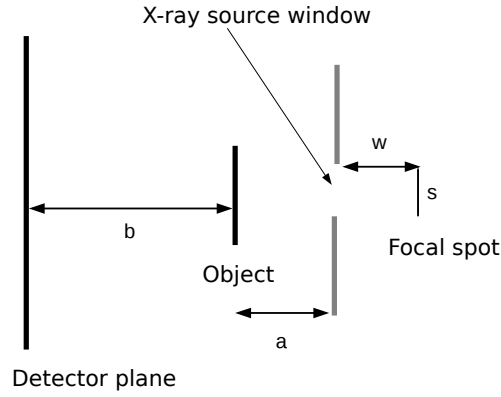


Figure 3.5.2: Definitions for the calculation of geometric and focal spot blurring.

The geometric magnification of the object on the detector is given by Eqn 3.5.4.

$$M = \frac{a + b + w}{a + w} \quad (3.5.4)$$

The total blurring,  $U_t$ , caused by the focal spot and the intrinsic detector response, ignoring terms  $U_m$  and  $U_a$  in Eqn 3.5.2, normalised by the magnification factor,  $M$ , is given by Eqn 3.5.5.

$$U_t = \sqrt{\left(\frac{s^2 m^2}{M^2}\right) + \left(\frac{D^2}{M^2}\right)} \quad (3.5.5)$$

An experimental set-up has been designed such that the dominant effect is that of the focal spot and geometry rather than the detector response, and so the detector response contribution is ignored in the post-analysis. It is therefore possible to use Eqn 3.5.5 to calculate the blurring due to the focal spot, such that the total blurring  $U_t$  from Eqn 3.5.2 is only caused by the focal spot and geometric blurring. This reduces the total blurring to the expression in Eqn 3.5.6

$$U_t = \frac{sm}{M} \quad (3.5.6)$$

### 3.5.3 Experimental system

The experimental set-up, shown in Figure 3.5.3 allows for the exclusion of the detector response term  $\frac{D^2}{M^2}$  from Eqn 3.5.5, such that Eqn 3.5.6 can be used to determine the focal spot size.

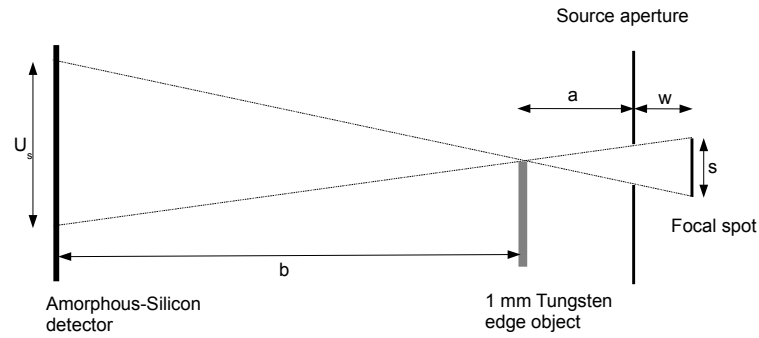


Figure 3.5.3: Schematic of the focal spot measurement.

The imaging detector used to determine the focal spot was a flat panel (PaxScan 4040R, Varian, U.S.) amorphous-silicon digital detector with a scintillating layer of Gadolinium Oxysulfide (Kodak Lanex Regular). The limiting resolution of which is given as  $2 \text{ lpmm}^{-1}$  at 70 kVp.

Given that the focal spot is the area of the anode struck by the electron beam in the x-ray source, it is necessary to quantify the focal spot size in both the horizontal and vertical directions. The 1 mm thick 99.95% pure tungsten (Alfa Aesar) edge was placed at fixed distances of 1.0 cm and 2.0 cm from the aperture

of the source in the vertical and horizontal configurations, and at a small angle of approximately  $3^\circ$ . The distance between the exit window and the focal spot was 6 mm (Ben Price, Nikon, email contact). This gave a total distance of 1.6 cm  $\pm$  0.2 mm from the edge object to the focal spot for the vertical orientation, and 2.6 cm  $\pm$  0.2 mm for the horizontal edge orientation. The differences in the placement of the edge arises due to practical limitations of placing the edge in the system without disturbing the collimator place holders that were previously set-up for another experiment. The combined distance  $a + b$  for both set-ups was 57.5 cm. Therefore, the distance  $b$  is given as 56.6 cm and 55.5 cm, leading to magnification values  $M$  of  $32 \pm 8$  and  $29 \pm 7$ , resulting in a sample distance ratio  $m$  of  $30.3 \pm 8$  and  $21.25 \pm 7$  for the vertical and horizontal orientations respectively. Ten images were acquired of each of the following; the image  $I(x, y)$  of the test object, dark field image  $I_d(x, y)$  and the flat field image  $I_f(x, y)$ , for both edge orientations.

### 3.5.4 Image processing and results

All ten edge images, dark field images, and flat field images were averaged to reduce contribution from random noise. From this, normalisation with the flat field image was performed to remove structural noise by correcting for gain and offset variations in the detector, using Eqn 3.5.7. This resulted in the corrected image  $\bar{I}_{cor}(x, y)$ .

$$\bar{I}_{cor}(x, y) = \frac{\bar{I}(x, y) - \bar{I}_d(x, y)}{\bar{I}_f(x, y) - \bar{I}_d(x, y)} [\bar{I}_f(x, y) - \bar{I}_d(x, y)] \quad (3.5.7)$$

A second order 2D polynomial fit correction was applied to the gain and offset corrected image, to remove any background signal effects arising from non-uniformity in the x-ray field. This was completed using the correction in Eqn 3.5.8

$$\bar{I}_{final}(x, y) = \frac{\bar{I}_{cor}(x, y)}{S(x, y)} S_{ave}(x, y) \quad (3.5.8)$$

where  $I_{final}$  is the final corrected image used to determine the ESF and the LSF of the system,  $S(x, y)$  is the second order polynomial fit to image  $\bar{I}_f(x, y)$  and  $S_{ave}(x, y)$  is the polynomial fit of the averaged flat-field image. This is done according to the international standards IEC 62220-1 and IEC 62220-1-2 and led to a final corrected edge test image, an example of which is shown in Figure 3.5.4.

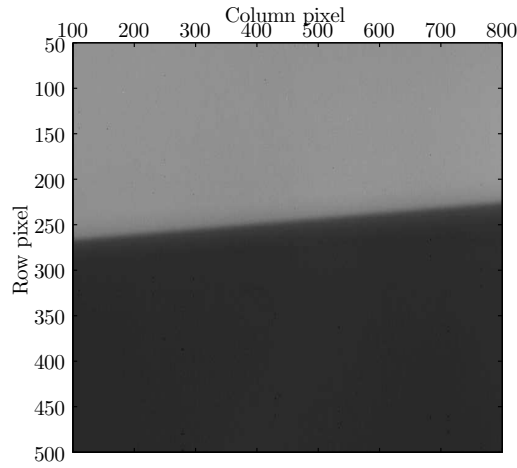


Figure 3.5.4: Horizontally placed edge object.

The angle of inclination was confirmed using a 1D first order polynomial fit of the greyscale values along the edge in the final corrected edge object i.e. intensity values along the  $y$  direction of the image using the method proposed by Price et al. (2008). The arctan of the gradient is equal to the angle of inclination. The  $N$  number of steps required to move the ESF across one pixel is given by  $N = \arctan(\alpha)$  where  $\alpha$  is the angle of inclination with respect to the horizontal or vertical axes. This sampling distance is assumed to be constant when calculating the ESF. Regions of interest with width of 20 by 250 pixels were generated, and shifted along the edge to obtain oversampled edge responses with the number of

steps required being the same value  $N$ . The averaged intensity profile from the regions of interest was calculated. The processing leads to the determination of the oversampled ESF.

Figure 3.5.5 shows the nine calculated ESFs, the ESF averaged from all oversampled ESFs, and finally the LSF for the vertically positioned edge object. The total blurring of the system was obtained by fitting a Gaussian curve to the LSF. It is important to note that the LSF has higher noise values at higher intensities as the noise is proportional to the square-root of the signal.

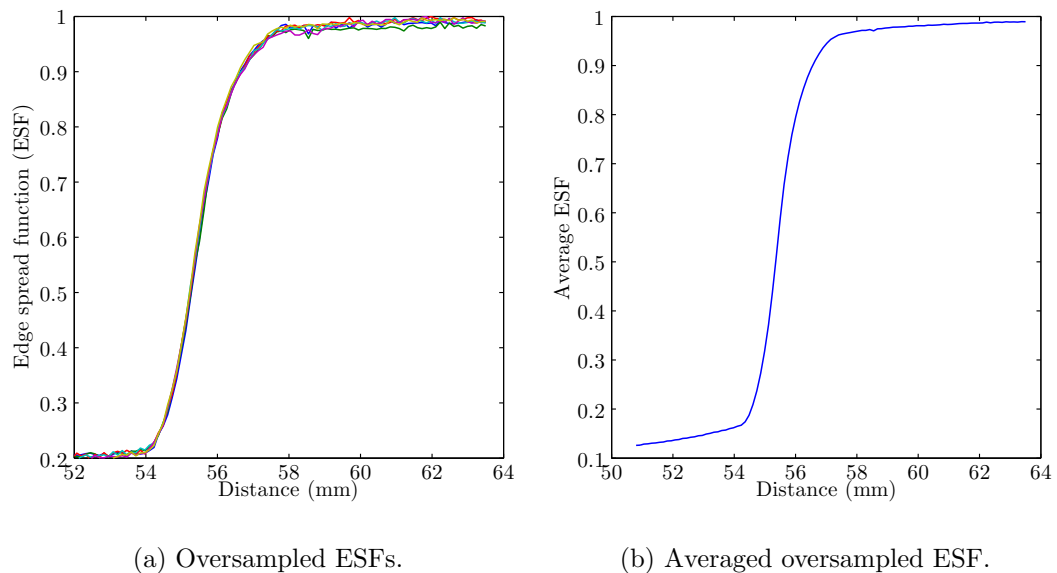


Figure 3.5.5: Determination of the oversampled ESF.

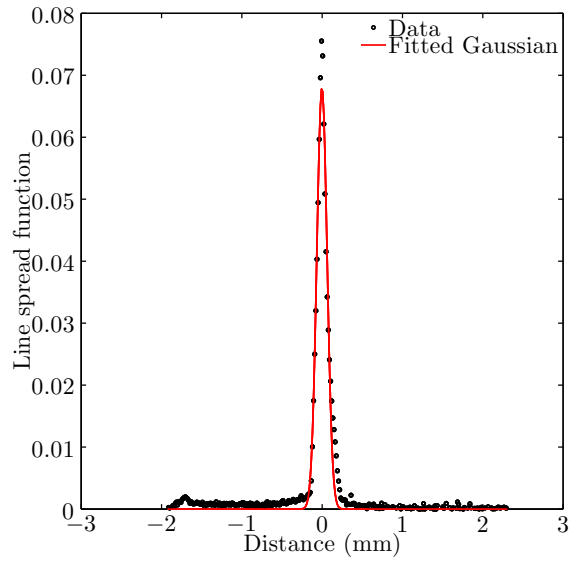


Figure 3.5.6: The derivative of the oversampled ESF results in the LSF for the vertical edge.

Figure 3.5.6 shows the zero-meaned LSF for the vertically orientated edge. As previously described in Eqn 3.5.6, the blurriness, as represented by the FWHM of the LSF function, is related to the focal spot size in the direction of interest. By fitting a Gaussian curve to the LSF, the FWHM was found to be  $0.21 \text{ mm} \pm 0.08 \text{ mm}$  for the vertical case and  $0.11 \text{ mm} \pm 0.04 \text{ mm}$  for the horizontal case. These values lead to an effective focal spot of  $6.8 \mu\text{m} \pm 1.1 \mu\text{m}$ . by  $5.0 \mu\text{m} \pm 1.7 \mu\text{m}$ .

Due to the small size of the focal spot and the errors in the measurements, the focal spot will be considered to have a circular area with diameter of  $6 \mu\text{m}$ , obtained from averaging the two values. The focal spot size can now be used in turn to calculate the height of the collimated beam at the sample, and therefore define the volume element in which diffraction can occur.

## 3.6 Calculation of beam divergence and beam height

The calculation of beam divergence and beam height is based on the focal spot size and the geometry of the system, as described below. Therefore no additional experimentation or data processing required for these calculation.

### 3.6.1 Geometrical definitions

Figure 3.6.1 shows a schematic of the beam divergence, where  $s$  is the focal spot size,  $d$  is the diameter of the collimator and  $L_1$  is the distance between the two.

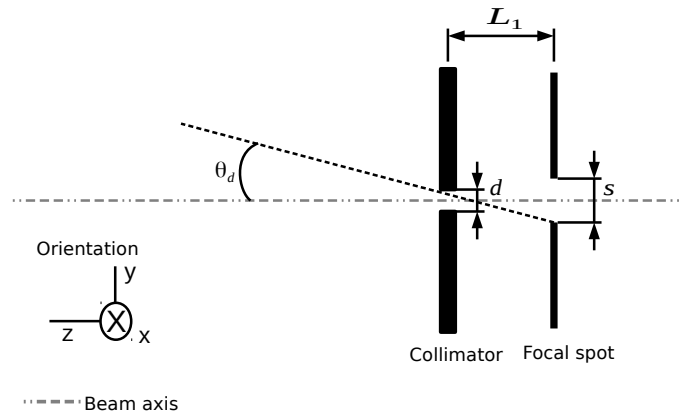


Figure 3.6.1: Schematic of the divergence geometry.

Eqn 3.6.1 relates the derived parameters to the divergence angle  $\theta_d$  by

$$\tan \theta_d = \frac{\frac{s}{2} + \frac{d}{2}}{L_1} \quad (3.6.1)$$

The divergence determines the beam width,  $h$ , in the  $(x,y)$  plane at the sample. The focal spot is considered to be a circular region with  $d$  of  $6 \mu\text{m}$ , as was previously found in Section 3.5. Figure 3.6.2 gives a schematic of the beam height

geometry with the previously defined symbols and also includes the collimator sample distance  $L_2$ .

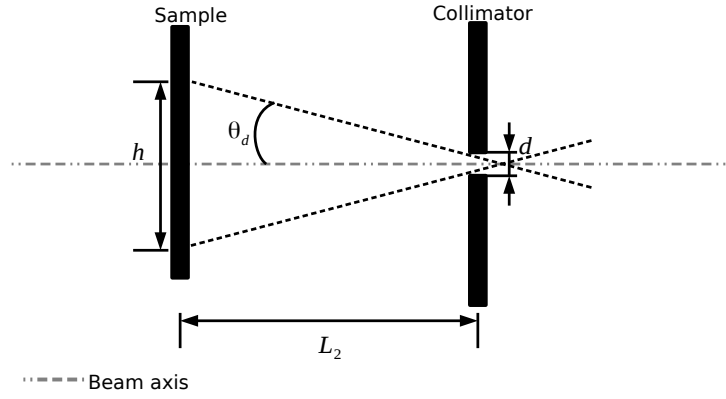


Figure 3.6.2: Schematic of the beam height geometry.

$$h = 2L_2 \tan \theta_d + d \quad (3.6.2)$$

It is possible to see from Eqns 3.6.1 and 3.6.2, that the divergence and beam height are dependent on the geometry of the system. A small collimator diameter is beneficial to image smaller objects but is detrimental to the counting statistics of the system. In this system a pinhole collimator of nominal diameter 0.5 mm was used.

### 3.6.2 Beam height and beam divergence

From these values the beam divergence angle  $\theta_d$  was calculated to be  $0.25 \pm 0.02^\circ$  and therefore the beam height,  $h$ , at the sample is approximately  $0.5 \pm 0.1$  mm. This therefore means that the divergence has a negligible effect on the beam height, and the collimator diameter is the dominant contribution.

### 3.7 Detector placement

Unlike a typical EDXRD system, where a detector is placed at a position to detect only one angle, it is possible to use a 2D array to detect multiple scatter angles in one acquisition. This utilises both its spatial properties and its energy resolving properties. The detection of multiple scatter angles has been previously demonstrated in the research by Christodoulou et al. (2011), O’Flynn et al. (2012) and O’Flynn et al. (2013). The method utilised in O’Flynn et al. (2013) is used in the current system, due to its ease of set up. To ensure the detector is sensitive to multiple scatter angles, the detector area is displaced from the beam axis as in Figure 3.7.1.

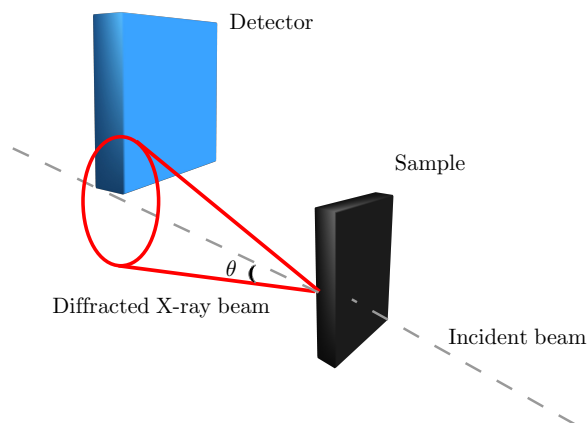


Figure 3.7.1: Detector displacement from the beam, as adapted from a diagram provided by Dan O’Flynn.

This diagram shows the collimated incident beam which, depending on the energy of interaction, will lead to the diffraction signal being detected at diffraction angle  $\theta$ . The 2D array is therefore able to detect multiple scatter angles. Figure 3.7.2 demonstrates, the calculation of the scatter angle a pixel is able to detect.

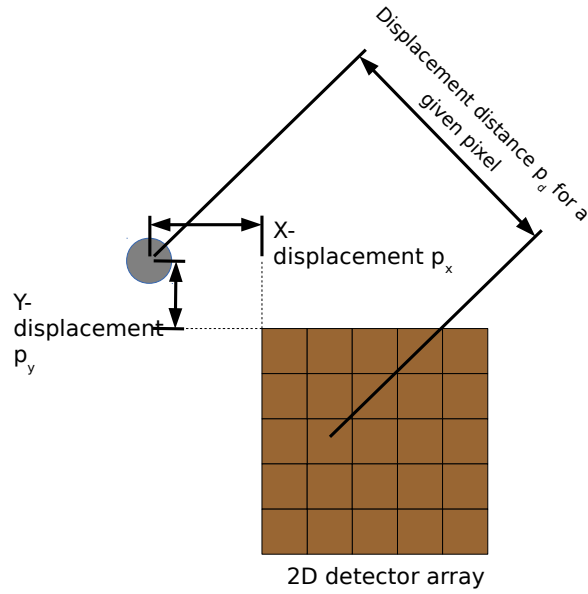


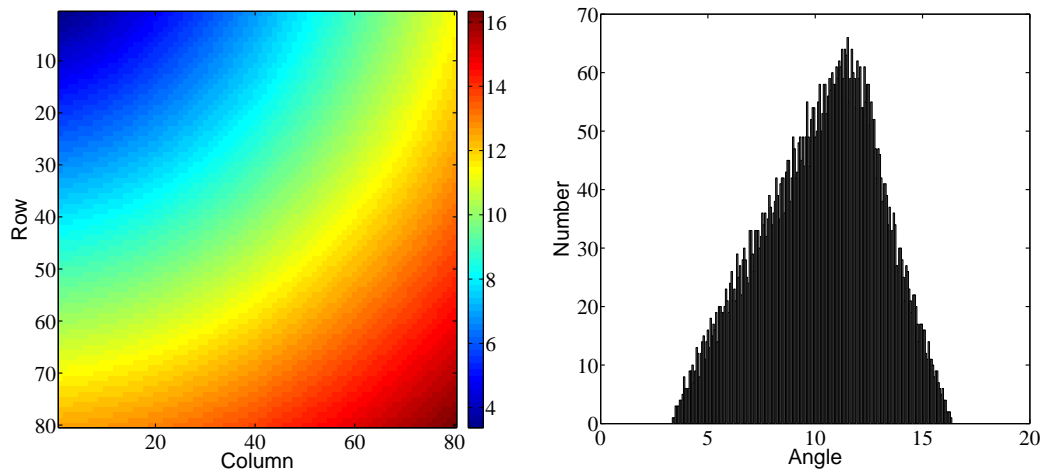
Figure 3.7.2: Detector displacement from the beam.

From the geometry presented in Figure 3.7.2, the displacement of an individual pixel  $p_d$  is given by 3.7.1

$$p_d = \sqrt{p_x^2 + p_y^2} \quad (3.7.1)$$

where  $p_x$  and  $p_y$  correspond to the displacement of the pixel in the  $x$  and  $y$  direction, respectively, and  $p_d$  is a hypotenuse distance.

For the geometry used in this system, the calculated angular distribution is presented in Figure 3.7.3a. Figure 3.7.3b also shows a histogram of the angular spread of the system.



(a) Colour map representation of the detected scatter angles across the 2D array, (b) Detector scatter angle distribution.

Figure 3.7.3: The angular distribution of the multi-angle diffraction system, based on the number of pixels at the corresponding angle.

| Scatter angle (°) | 0.8 nm <sup>-1</sup> | 1.1 nm <sup>-1</sup> | 1.6 nm <sup>-1</sup> | 2 nm <sup>-1</sup> | 3 nm <sup>-1</sup> | 4 nm <sup>-1</sup> |
|-------------------|----------------------|----------------------|----------------------|--------------------|--------------------|--------------------|
| 3                 | 38                   | 52                   | 76                   | 95                 | 142                | 190                |
| 4                 | 28                   | 39                   | 57                   | 71                 | 106                | 142                |
| 5                 | 22                   | 31                   | 46                   | 57                 | 86                 | 114                |
| 6                 | 19                   | 26                   | 38                   | 48                 | 71                 | 95                 |
| 7                 | 16                   | 22                   | 33                   | 41                 | 61                 | 81                 |
| 8                 | 14                   | 20                   | 29                   | 36                 | 53                 | 71                 |
| 9                 | 13                   | 17                   | 25                   | 32                 | 48                 | 63                 |
| 10                | 11                   | 16                   | 23                   | 29                 | 43                 | 57                 |
| 11                | 10                   | 14                   | 21                   | 26                 | 39                 | 52                 |
| 12                | 9.5                  | 13.                  | 19                   | 24                 | 36                 | 48                 |

Table 3.7.1: The expected photon energies corresponding to the momentum transfer values of interest, based on the geometry of the system.

The photon energies required to detect some selected momentum transfer values, such as 1.1 nm<sup>-1</sup> and 1.6 nm<sup>-1</sup>, are shown in Table 3.7.1. For some angles it is impossible to detect certain momentum transfer values due to the maximum photon energies available. The maximum energy limit of photons is 70 keV, therefore for the example of 3°, momentum transfer values of 0.8 nm<sup>-1</sup> and 1.1 nm<sup>-1</sup> are possible to detect. Similarly, for the example of 4 nm<sup>-1</sup>, only scatter angles of 9 degrees or higher will have the possibility of detecting coherently scattered photons with energies of less than 70 keV. This technique offers the possibility of covering a range of momentum transfer values, with each pixel being better suited to detect diffraction of certain momentum transfer signals than others.

In addition to this, in terms of visually viewing the diffraction rings, for an imaging system, this allows for the diffraction rings to be seen, as will be shown in Section 3 and already demonstrated by O’Flynn et al. (2013). For a system

with a potential clinical use, visualisation is a factor that would be of use for identification of disease. However, it may also be necessary to optimise the signal for diffraction, which at this stage has not been performed. It might be more ideal to have the detector at a narrower range of more useful angles, however in this case the diffraction signal in a visual sense would not be seen clearly. At the moment the use of the detector is not entirely optimised, as the measured diffraction signal is only apparent for those angles and energies where the diffraction signal is expected to be. At this stage, an exploration of the effects of this system and its uses are being considered.

### 3.7.1 XRF and background signal

High Z detectors such as Cd(Zn)Te have known issues with XRF from the sensor material itself. For photon interactions with matter, the photoelectric effect is dominant up to energies of 100 keV, which are used in this work. Photoelectric absorption can lead to the production of x-ray fluorescence, where the ionisation of the atom leads to an electron from a higher energy state falling to the lower and in doing so, emitting a photon equal to the differences in energies between the two shells. The XRF energies of cadmium and tellurium are summarised in Table 3.7.2.

| Element | $K\alpha_1$ | $K\alpha_2$ | $K\beta_1$ |
|---------|-------------|-------------|------------|
| Cd      | 23.2        | 23.0        | 26.1       |
| Te      | 27.5        | 27.2        | 31.0       |

Table 3.7.2: X-ray Fluorescence lines of cadmium and tellurium given in keV.

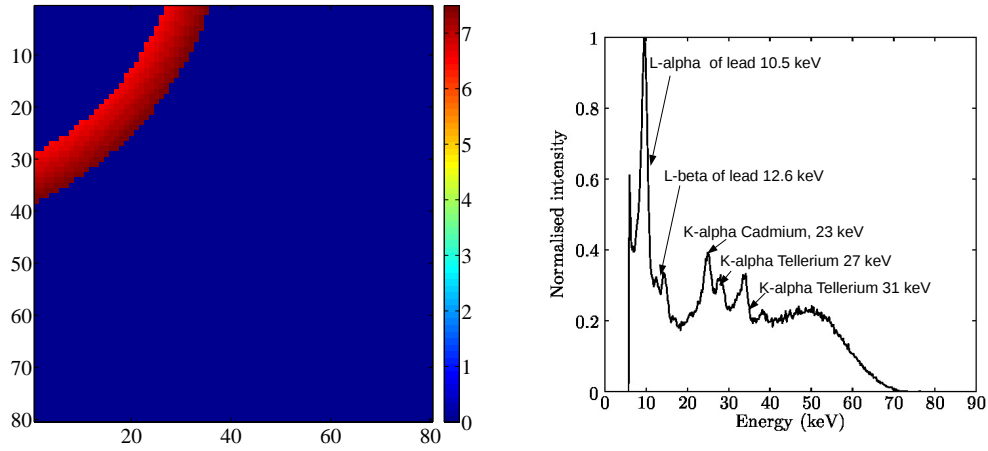
The energy of characteristic x-rays with the atomic number,  $Z$ . This is shown by Moseley's law, which determines the frequency of the K-alpha lines of a material. This is shown in Eqn 3.7.2, where  $f_r$  is frequency of the fluorescence photon,

$Z$  is the atomic number of the material, and  $k_1$  and  $k_2$  are constants that depend on the type of line being considered.

$$\sqrt{f_r} = k_1(Z - k_2) \quad (3.7.2)$$

This can lead to issues using high  $Z$ -value detectors. Also, the yield increases and in the case of the cadmium and tellurium, the yield of the k-alpha lines are 0.84 and 0.875, respectively. These XRF photons can themselves be detected by the material that caused them in the first place. CdTe absorbs 100% of these energy photons. The angular distribution of the fluorescence photons has a maximum normal to the incident radiation. What compounds this effect further is that photons which have fluoresced from a higher  $Z$  material, can cause fluorescence in another material with a lower  $Z$  value- depending on the absorption threshold of the k-alpha shell. Cadmium has an atomic number of 48, compared to tellurium which has an atomic number of 52. In this case, the XRF photons of tellurium which have values of 27.5–31 keV, are above the absorption threshold of cadmium, which is at 26.7 keV

Figure 3.7.4b is an example background signal obtained from a one minute acquisition. All pixels within angles of  $4.5^\circ$  to  $5.5^\circ$  were used to create this spectrum, by summing the signals from all pixels at these geometries, as shown in Figure 3.7.4a.



(a) Selected angles for chosen spectral profile. (b) Example spectrum obtained with no sample present. Acquisition time of one minute.

Figure 3.7.4: Calculating a spectrum of the background signal which features the XRF signal of the detector.

There are key features to note from Figure 3.7.4b. Lead is present within the system collimation as well as the surrounding shielding to reduce air scatter and background scattering within the system, and the XRF signal of lead can be seen at 10.5 keV and 12.6 keV. In addition there are the XRF lines of cadmium and tellurium at the pre-stated energy values, which are marked in Figure 3.7.4b. The L-alpha and K-alpha lines consist of at least two energies which are unresolvable by the detector. For example, in the case of cadmium, the energies of the  $K_{\alpha}$  lines are 22.984 keV and 23.173 keV for the  $K_{\alpha_1}$  and  $K_{\alpha_2}$ , respectively.

### 3.8 System automation

For the purposes of scanning a sample to obtain images, the system is automated using Newport translation stages (Newport Corporation, USA). The stages used were two ILS150PP models and one ILS100PP model, which correspond to auto-

mated motion across 150 mm and 100 mm, respectively. The ESP301 controller is used to connect the stages and the PC via a serial RS 232 port. Commands for the stages are based on the American Standard Code for Information Interchange (ASCII) character-encoding scheme. It is possible to use MATLAB for instrumentation control purposes to read and send ASCII based commands to the RS232 port, using the instrumentation control toolbox. Utilising code previously developed by James Scuffman at the University of Surrey, which coordinated the acquisition of the detector with the detector bias refresh i.e. that the bias refreshed occurred when the detector was not acquiring, the code was modified by the author to work with the translation stages in this system and the communication ports used. The code is able to move the sample stages to position ensuring that the motion of the stages occurs during the bias refresh of the detector i.e. when the detector is not acquiring. This is to ensure that there is minimal dead time during the acquisition. The translation stages are of finite size which sets a limitation of the minimum sample detected distance and collimator detected distance. The stages are 11 cm wide and any motion of the stages has to have a free passage with no items restricting any motion.

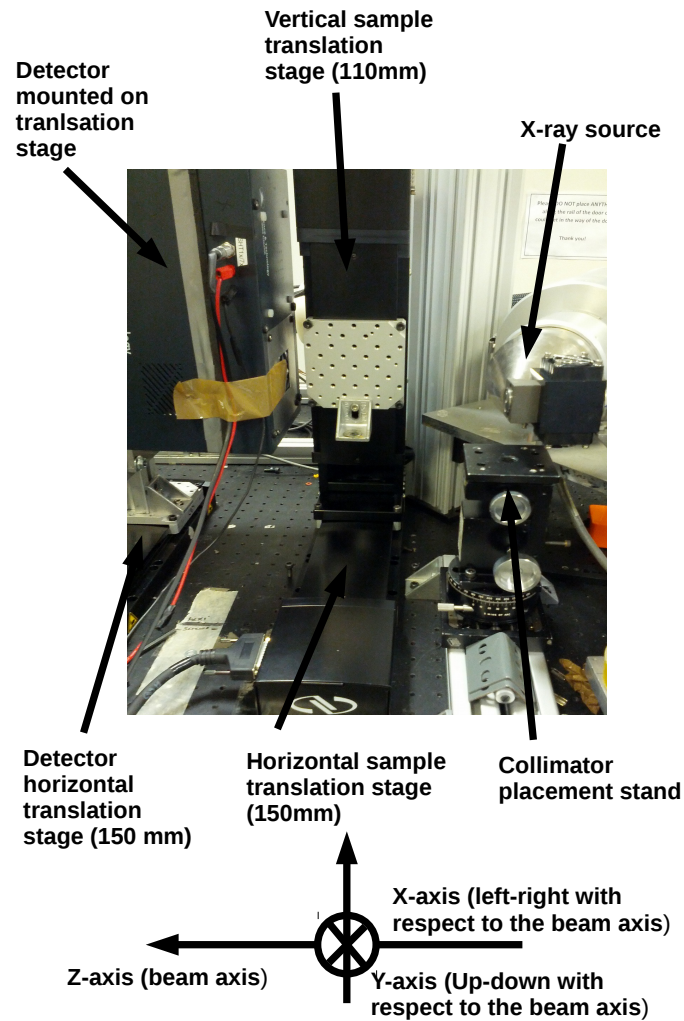


Figure 3.8.1: Photo of the diffraction system which incorporates sample scanning and detector motion.

As annotated in Figure 3.8.1, the detector is mounted on a translation stage of length 150 mm, the sample is able to move perpendicularly from left to right ( $x$ -axis) across the beam axis ( $z$ -axis) and vertically ( $y$ -axis). The horizontal movement of the sample stage is based on the motion of a 150 mm translation stage and the vertical motion uses a 100 mm stage.

## 3.9 Diffraction signal and material thickness

### 3.9.1 Introduction

The scatter volume of the interaction for the diffraction system is not fully defined. It is possible to detect scatter along a path subtended by the collimated beam, depending on the divergence angle of the system. The following experiments consider the effects of thickness on the change on the diffraction signal for PMMA, pork fat (lard) and caffeine, based on the parameters of interest utilised from within the diffraction literature, that could be of interest for displaying information for diffraction images. This also provides the opportunity to consider the effects of utilising the diffraction signal obtained from the detector in different ways. Currently, a range of angles are considered and therefore there may be, or would be expected to be, signals that are more useful than others, especially in light of the fact that not all pixels will detect diffraction. Therefore considering the detector signal as a whole may not be the best way to present the available data, but rather to use select information. This technique of having a wider range of angles will also depend on the user and the information they wish to obtain. In this case, as the system is being used to image phantoms, which will be described in Section 5, of importance is the ability to distinguish thickness variations in the diffraction system across the range of PMMA thickness used in the phantom development work, which is upto 6.5 mm. Therefore, the investigation will consider which data processing allows for greatest variability of the diffraction signal of PMMA across this range, primarily taking into consideration the maximum intensity of the  $0.8 \text{ nm}^{-1}$  peak of PMMA, as per the literature, which uses the intensity of the diffraction peaks of primary interest.

As no secondary collimator is used in the EDXRD experiment, the discussion is extended from the typical EDXRD case to the case of this system. The theory here expands on the theory presented by Pani et al. (2010), which utilises a

primary collimator. The theory is extended by the author to the case of a 2D detector array multi-angle technique and without the use of a secondary collimator.

### 3.9.2 Theoretical thickness considerations in diffraction systems

Considering the interaction of a photon in a sample with thickness,  $t$ , at position  $x$ , as shown in Figure 3.9.1.

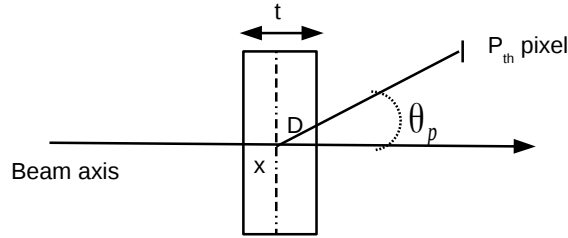


Figure 3.9.1: Diagram of diffraction interaction for sample with thickness  $t$ . Adapted from Pani et al. (2009)

The number of photons that scatter coherently at a generic point  $x$  in the sample is given by Eqn 3.9.1

$$dN(E) = N_x(E, x)\sigma_s(\chi, x)e^{-\int_D \mu^d \zeta} dx \quad (3.9.1)$$

where  $N_x$  is the number of photons with energy  $E$  at position  $x$  and  $\sigma_s$  is the linear differential scatter cross-section at a depth  $x$  in the sample. The exponential term takes into account the attenuation of the scatter photons within the rest of the sample to the detector, assuming that the attenuation between the sample and the detector is negligible.

The number of photons that reach a generic point  $x$  within the sample depends on the number of incident photons at the sample, with energy  $E$  and depends on

the attenuation in the sample until position  $x$  is reached.

This leads to Eqn 3.9.2

$$dN_x(E, x) = N_o(E)e^{-\int_x^0 \mu d\zeta} dx \quad (3.9.2)$$

The distance,  $D$ , travelled between the scattering point in the sample and the sensor can be written in terms of the scattering point,  $x$ , and the sample thickness,  $t$ , as in Eqn 3.9.3

$$D = (t - x) \cos \theta \quad (3.9.3)$$

Under the assumptions that the scatter angle and distance travelled is small, it is possible to approximate  $D \approx D \cos \theta$ , and also that the line integral of the linear attenuation along the path  $D$  can be approximated as  $x$  to  $t$ . When using this approximation and substituting Eqn 3.9.1 into Eqn 3.9.2, it is possible to write the total number of events detected at the detector from scatter point  $x$  as

$$dN(E) = N_o(E)\sigma_s(\chi, x)e^{-\int_o^t \mu d\zeta} dx \quad (3.9.4)$$

This demonstrates that the thickness affects the number of photons being detected at the detector. The thicker the material the greater the attenuation, and that it is possible to lose scattered photons (i.e. not detect them) as they are attenuated within the sample. In addition to this, the thicker the sample the fewer number of photons there are to be scattered at point  $x$  within the sample. The angular resolution is also dependent on the thickness  $t$ . The scatter angle is defined at the start of the sample, as shown in Figure 3.9.2.

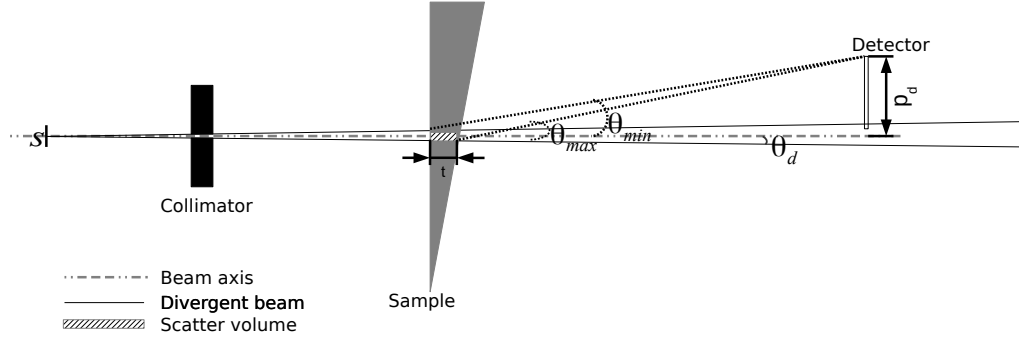


Figure 3.9.2: Geometrical representation of the diffraction system

The displacement distance from the collimated x-ray beam by hypotenuse distance  $p_d$  for a pixel, as previously defined in Section 3.7, and detector sample distance,  $L$ , defines the scatter angle for that pixel, such that

$$\tan(\theta) = \frac{p_d}{L} \quad (3.9.5)$$

The maximum possible detected scatter angle from sample can be written as

$$\tan(\theta_{max}) = \frac{p_d + \frac{\sqrt{2}}{2} D_p}{L - t} \quad (3.9.6)$$

where  $D_p$  is the length, and this case width, of a pixel, and for the smallest scatter angle

$$\tan(\theta_{min}) = \frac{p_d - \frac{\sqrt{2}}{2} D_p}{L} \quad (3.9.7)$$

Therefore the total angular resolution of the system, defined by Eqn 3.9.8

$$\frac{\theta_{max} - \theta_{min}}{\theta} \quad (3.9.8)$$

can be written as the following for this system.

$$\frac{\arctan\left(\frac{p_d + \frac{\sqrt{2} D_p}{2}}{L - t}\right) - \arctan\left(\frac{p_d - \frac{\sqrt{2} D_p}{2}}{L}\right)}{\arctan\left(\frac{p_d}{L}\right)} \quad (3.9.9)$$

Eqn. 3.9.9 shows that the angular resolution of the system is dependent on the positioning of the pixels, the scatter angle, and also the sample thickness.

### 3.9.3 Experimental design

To consider the effects of the thickness of a sample on the diffraction signal, a wedge shaped sample was designed. Figure 3.9.3 details the dimension of the wedge and the 2D representation.

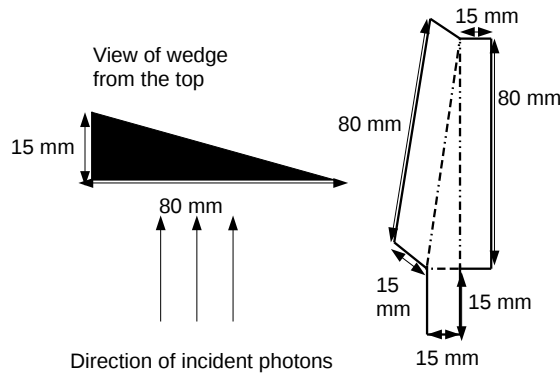


Figure 3.9.3: The right hand side shows the 2D representation and the left hand side shows the view from the top of the wedge.

It is possible to scan this design such that the sample thickness varies and it will do so based on the gradient of the wedge.

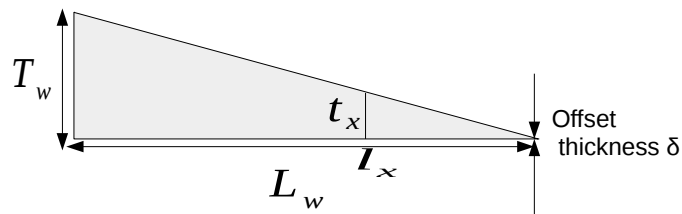


Figure 3.9.4: Calculation of the thickness,  $t_x$ , of the sample at a position  $l_x$  along the wedge.

Using the diagram in Figure 3.9.4, the thickness,  $t_x$ , of the wedge at a given point,  $l_x$ , can be calculated using the formula in Eqn 3.9.10

$$t_x = \frac{T_w}{L_w} l_x + \delta \quad (3.9.10)$$

where  $t_x$  and  $l_x$  are as previously defined,  $T_w$  is the total thickness of the wedge,  $L_w$  is the total length of the wedge, and  $\delta$  is an offset to take into consideration the finite thickness of the tip of the wedge.

It is assumed, as the beam height at the sample is 0.5 mm, that the variation of thickness across the scatter volume is negligible. The wedge design is useful for powdered materials such as caffeine, which do not hold their positioning well under gravity, and can be held within one container for the whole data acquisition rather than having to measure varying thicknesses of powdered material and pour it into individual sample holders. The wedge sample holder was made from enhanced cardboard of the order of 0.1 mm thick.

The samples investigated are caffeine, pork lard, and PMMA. Caffeine was considered as it has more order than materials such as PMMA and lard, and therefore could be used to compare. PMMA is explored due to its ease of use as well as the ability to use it in a potential phantom design, and cooking grade lard was used to represent adipose tissue.

One wedge was filled with lard and another was filled with caffeine. The top of the caffeine was secured with tape to prevent inhalation of the caffeine and any potential spillage of the caffeine across the work space. For PMMA, a slice was laser cut to the dimensions of the original design. However, at the thinner edge of the wedge the laser cutter burnt the material and therefore 4 mm from the narrow tip of the wedge was not usable.

The geometry of the system for the thickness test is shown in Figure 3.9.5.

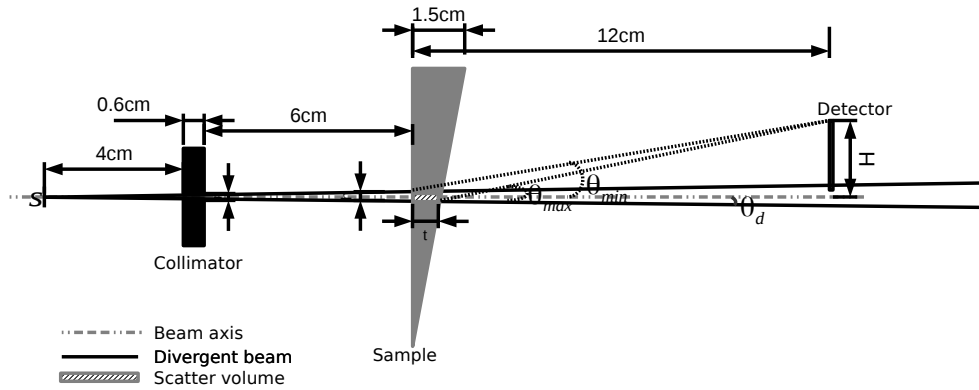


Figure 3.9.5: Diagram of the thickness tests experiments

Each sample was placed at a distance of 12 cm from the sensor. A perpendicular rule was used to make sure the edge of the sample was fixed perpendicular to the beam axis. The wedge sample was scanned every 2 mm using the automated acquisition system to move the sample perpendicular across the collimated beam. The total acquisition time for each position was set to 300 s and the bias refresh was applied for 4 ms. The bias voltage is held on for 60 s and then the refresh voltage applied. Therefore one 300 s acquisition would be the summation of five 60 s acquisitions at the same position. Background signals were acquired for the cases of no sample holder and the cardboard sample holder.

### 3.9.4 Results: Creation of diffraction profiles

All samples were post-processed using the Hexitech.exe executable such that .hxt files were created and then read into MATLAB. All data were background subtracted and time normalised. The intensity is in number of photons per minute.

As previously shown by O'Flynn et al. (2012) and O'Flynn et al. (2013), it is possible to view the diffraction rings of the sample-i.e. the higher intensity caused by the diffraction signal. Based on the geometry of the 2D-array, when the condition for diffraction is met, finding the intensity values of the pixels at

a particular energy should lead to a diffraction ring, which represents a peak in terms of momentum transfer. These are similar to the energy-angle maps produced by Malden and Speller (2000). Example figures are shown for the cases of PMMA at thicknesses of 6 mm, 11.4 mm and 14.15 mm.

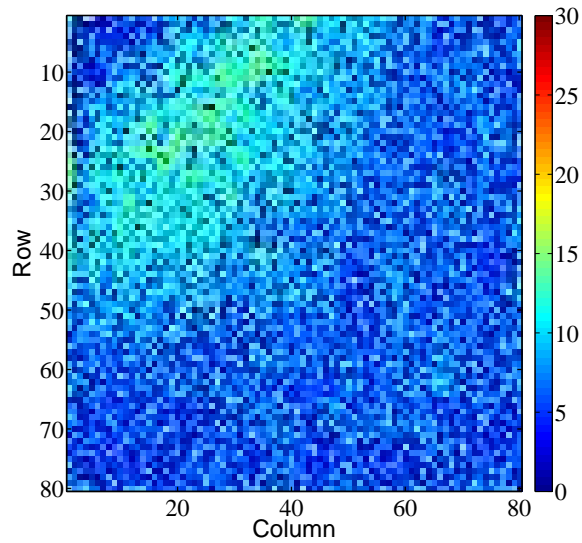


Figure 3.9.6: Diffraction ring associated with the  $0.8 \text{ nm}^{-1}$  peak of PMMA. Sample thickness of 6 mm. Colourbar indicates the intensity detected.

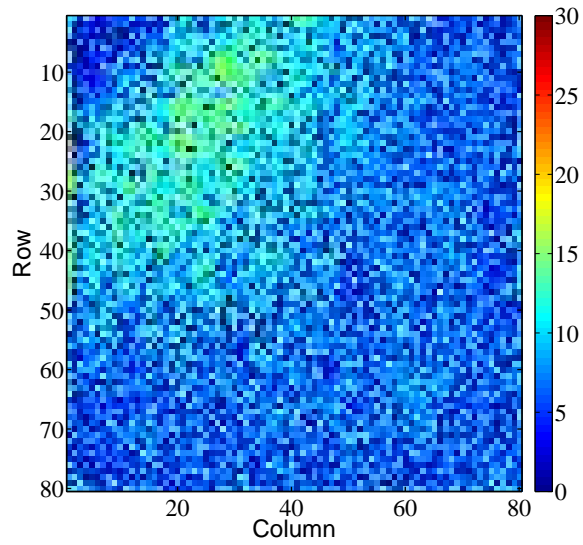


Figure 3.9.7: Diffraction ring associated with the  $0.8 \text{ nm}^{-1}$  peak of PMMA. Sample thickness of 11.4 mm. Colourbar indicates the intensity detected.

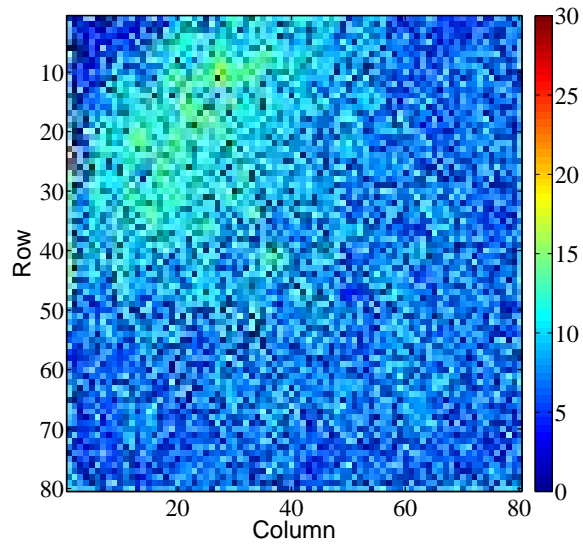


Figure 3.9.8: Diffraction ring associated with the  $0.8 \text{ nm}^{-1}$  peak of PMMA. Sample thickness of 14.15 mm. Colourbar indicates the intensity detected.

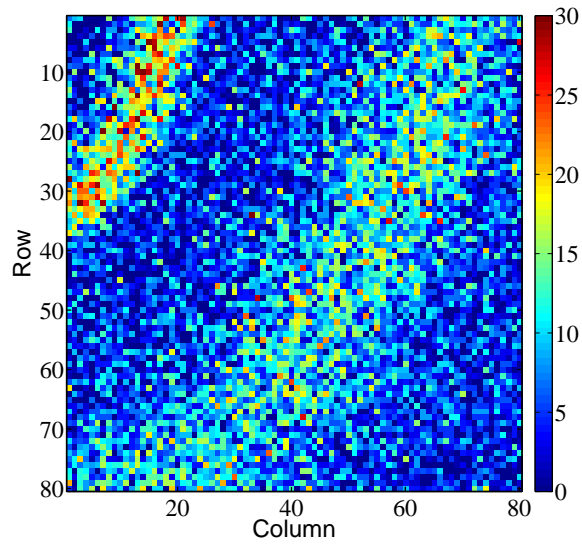


Figure 3.9.9: Diffraction rings associated with  $0.68 \text{ nm}^{-1}$  and  $1.4 \text{ nm}^{-1}$  peaks of caffeine. Sample thickness of 6 mm. Colourbar indicates the intensity detected.

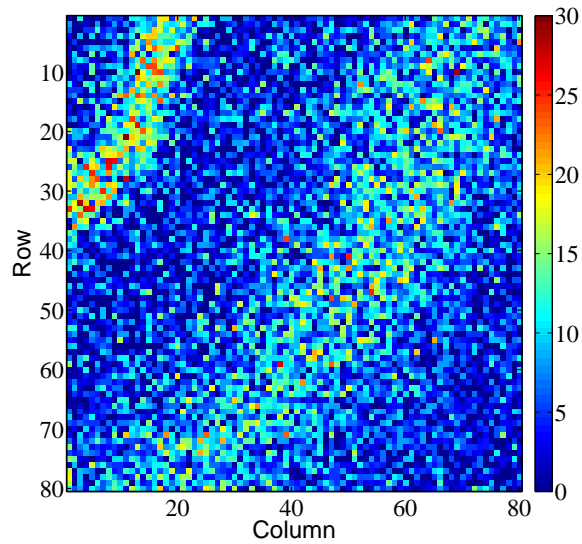


Figure 3.9.10: Diffraction rings associated with  $0.68 \text{ nm}^{-1}$  and  $1.4 \text{ nm}^{-1}$  peaks of caffeine. Sample thickness of 11.3 mm. Colourbar indicates the intensity detected.

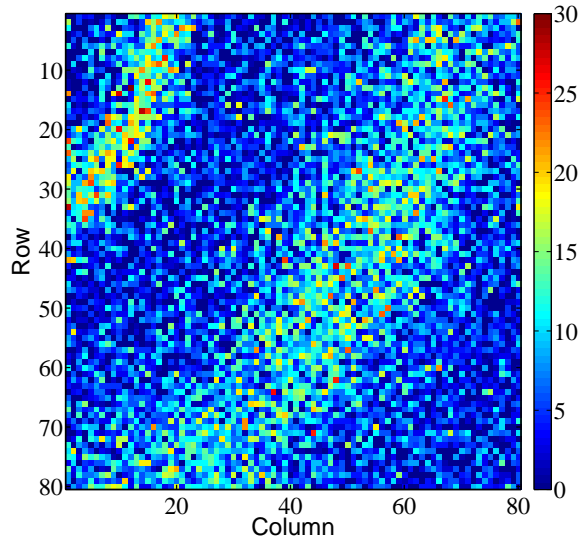


Figure 3.9.11: Diffraction rings associated with  $0.68 \text{ nm}^{-1}$  and  $1.4 \text{ nm}^{-1}$  peaks of caffeine. Sample thickness of  $14.3 \text{ mm}$ . Colourbar indicates the intensity detected.

There are several ways to process the data obtained from the 2D-detector array, which has 400 energy channels from the ADC. The data output is 3D data of dimensions  $80 \times 80 \times 400$ , with the ability to consider the energy spectrum as a whole i.e. utilising all measured energy values, to select energies of interest only, and to vary the geometrical angles used. As previously stated, not all angles will be able to detect diffraction signals for the momentum transfer values of interest due to the energies involved. Therefore they are not required for the analysis and could therefore be ignored for the post-processing as they would not contribute to a diffraction signal measurement. In addition, it is also necessary to consider the implications of any background signal within the system and any XRF signal originating from the detector itself, as these could potentially mask the true signal.

For all cases of post-processing-either using the 3D data as a whole or selecting information from the system, the principle of processing is the same.

Each  $p_{th}$  pixel has its own associated scatter angle  $\theta_p$  based on the system

geometry, and each pixel has 400 energy bins which have previously been calibrated such that every bin is associated with a photon energy. On a pixel by pixel basis, the detected intensity–energy background was subtracted from the detected intensity–energy diffraction signal. The  $i_{th}$  bin for every  $p_{th}$  pixel is converted to its momentum transfer value using the momentum transfer equation  $\chi = E_i 0.807 \sin(\frac{\theta_p}{2})$ , where momentum transfer is in units of  $\text{nm}^{-1}$ , and photon energy is in units of keV. The data is then interpolated to one common momentum transfer axis with bin spacing of  $0.005 \text{ nm}^{-1}$ . When selected energies or angles of interest are being considered, a mask can be applied to the data consisting of a value of 1 where information is desired and 0 where the information is not. All data were smoothed with the application of a Savitzky-Golay filter.

For the first example, all energies and all angles are processed and the energy axis per pixel were converted to momentum transfer from their pre-determined detection angle based on the geometry of the system. For the examples of caffeine and PMMA, the resulting diffraction spectrum which considers the sensor as a whole are shown in Figures 3.9.12–3.9.14.

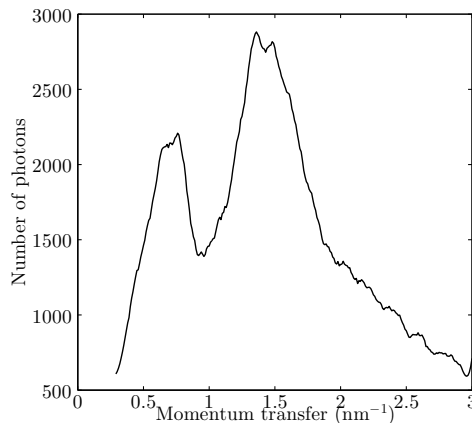


Figure 3.9.12: Example of an obtained diffraction spectrum of caffeine utilising all of the obtained information. Sample thickness 14.3 mm

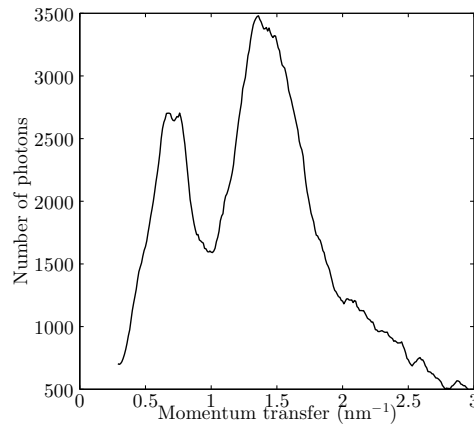


Figure 3.9.13: Example of an obtained diffraction spectrum of caffeine utilising all of the obtained information. Sample thickness 7.5 mm

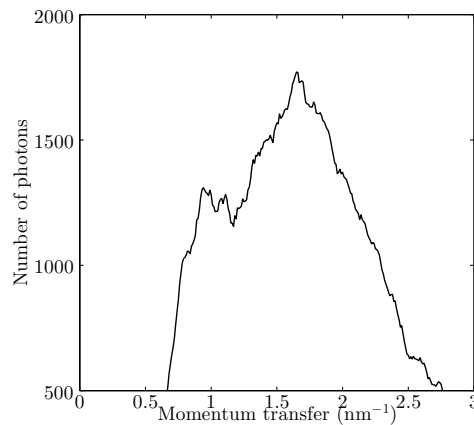


Figure 3.9.14: Example of an obtained diffraction spectrum of caffeine utilising all of the obtained information. Sample thickness 14.3 mm

These example spectra include all energies across all angles as well as signals of fixed energies, i.e. those from sources that are not dependent on the geometry of the signal, for example XRF signal. The effects of these signals on the diffraction output are considered in the next section.

### 3.9.5 Results: Effects and exclusion of fixed energy signals.

This section explores the effects of 'fixed energy signals' i.e those signals that do not vary with pixel geometry, using the obtained data. In the previous Section all pixels' spectra were summed together after being converted to a momentum transfer signal using the momentum transfer equation. Fixed signals could be expected from Compton back scatter in the detector itself which can be at fixed energy ranges, depending on the initial photon energies, as well as the XRF signal from the sensor material itself, i.e. from the cadmium and tellurium atoms.

Through the use of a simulation, the effects of including such signals are considered here, and spectra which exclude these signals are produced using the already obtained data.

#### 3.9.5.1 Simulation of XRF effects on the diffraction profiles

Each pixel of the 2D array is at a designated geometric detection angle based on the placement of the detector within the system. When converting each pixels' axis to momentum transfer, the momentum transfer equation is used. Therefore, any photo peak at a fluorescence energy would appear shifted in terms of a diffraction profile. If the K-alpha line of tellurium, which occurs at 27.5 keV, is detected within a pixel detecting scattered photons at  $8^\circ$ , any XRF photons at this energy would appear to have a momentum transfer value of  $1.54 \text{ nm}^{-1}$ . The apparent diffraction signal of the XRF peaks would vary depending on the angle of diffraction.

Simulation of a Gaussian signal with mean of 23 keV, corresponding to K-alpha of cadmium, with standard deviation of 0.5 keV was created within MATLAB using Eqn 3.9.11.

$$S_m = Ae^{-\frac{(E_x - \mu)^2}{2\sigma^2}} \quad (3.9.11)$$

where  $S_m$  is the simulated signal,  $A$  is the amplitude,  $E_x$  is the energy axis in keV,  $\mu$  is the mean energy in keV and  $\sigma$  is the standard deviation. Figure 3.9.15 shows for angles between 4–10 degrees the apparent momentum transfer increase of the energy peak observed at 23 keV.

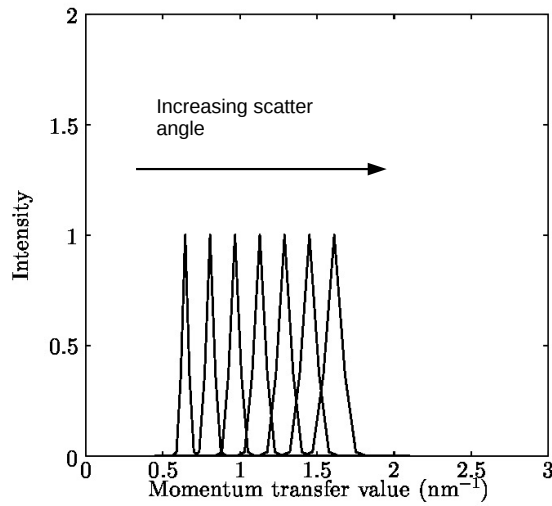


Figure 3.9.15: Apparent shift in momentum transfer signal due the geometry of the pixel.

A repeat simulation was conducted, this time randomising the intensity of the signal, to simulate variation in the detected signal within different pixels at different geometries. To do this the built in randomisation function `rand` in MATLAB was used, ensuring that the random intensity of the signal did not exceed a nominal value of 2, by limiting the amplitude of the random number generator. The new mathematical representation of the signal is as Eqn 3.9.12,

$$S_m = A_{rnd}e^{-\frac{(E_x - \mu)^2}{2\sigma^2}} \quad (3.9.12)$$

In this case, the simulated data were interpolated to the same momentum transfer axis, as is performed with the real data, and were summed up, again as is completed with the real data. The result, shown in Figure 3.9.16, demonstrates that apparent momentum transfer peaks can occur due to the shifting of the signal in momentum transfer, as well as summation of the signal to one momentum transfer axis.

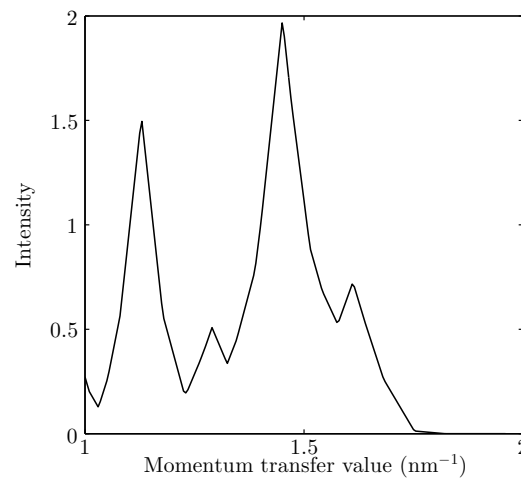


Figure 3.9.16: Demonstrating that a diffraction pattern can appear to be present due to a fixed energy signal.

Therefore the signal with possible XRF signal should be ignored, due to the possible influence to the final diffraction pattern.

### 3.9.5.2 Backscatter events

In addition, an apparent broad diffraction peak can be seen with an approximate value of  $1.6 \text{ nm}^{-1}$  in the summed spectra in Figures 3.9.12–3.9.14. As observed in the background scatter signal, a fixed broad peak is recorded between the energies of approximately 40–60 keV, as shown in 3.9.17. This can again be attributed to a feature of the sensor material and the detector itself.

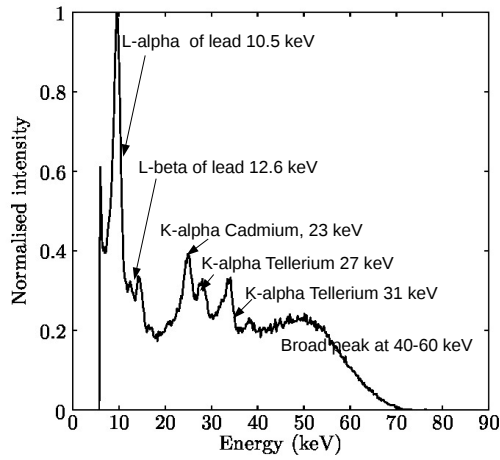


Figure 3.9.17: Example background signal at  $5^\circ$ , shows the broad signal at 40 keV–60 keV.

Such signals have previously been observed in Am-241 spectra with CdTe sensors, where 60 keV photons lead to a signal at 48 keV due to Compton backscatter. This has been observed in Redus et al. (2009) and is previously observed in Section 2.5. For photons of energies 50–70 keV, the percentage of Compton scatter based on NIST XCOM (Berger et al. (2010)) are shown in Table 3.9.1.

| Photon energy<br>(keV) | Total interaction as<br>incoherent (%) | Total photons<br>absorbed (%) |
|------------------------|--|-------------------------------|
| 50                     | 2.66                                   | 99.81                         |
| 60                     | 2.14                                   | 97.82                         |
| 70                     | 1.61                                   | 92.01                         |

Table 3.9.1: Percentage of the total absorption through the processing of incoherent scatter.

Therefore, on average, it is expected that 2.14% of photons with energies of

50–70 keV interact incoherently with the CdTe sensor. As the angle of interaction of Compton scatter approaches  $180^\circ$ , photons of 50–70 keV would lose 9–14 keV, thus leading to the detection of photons of 40–60 keV.

To avoid these features from contributing to the diffraction spectrum, energies of above 40 keV are ignored, as well as energies where the XRF signal can be detected. In order to remove non-diffraction signal further, only pixels in which diffraction signal is expected to be detected are included. This leads to the inclusion of photons with energies of 15–20 keV, and 33–40 keV, using angles of  $4^\circ$ – $8^\circ$ .

### 3.9.5.3 Summary

From observations made of the diffraction spectra and background spectra, fixed energy signals such as XRF signals and background scatter signals were found. In order to consider the effects of the inclusions of these signals on the diffraction spectra, a simulation was performed using 23 keV photons and demonstrating that for varying intensity signals at different geometries, an apparent diffraction pattern can appear, purely due to the effects of the conversion of the detected signal from energy to momentum transfer. Also highlighted in this Section is the detection of Compton backscatter events due to the interaction of 50 keV–70 keV photons, an effect also previously observed in the Am-241 spectra in Section 2.5. To prevent such signals from influencing the diffraction signals, these signals can be ignored through selected energies at which these signals are observed. Due to the energy resolving capabilities of the detector and the spatial resolving abilities, signals above 40 keV can be removed from the data, as well as the XRF signal.

### 3.9.6 Results: Investigation of diffraction parameters with selected angles and energies

Using the same experimental data obtained in Section 3.9.3 and excluding fixed energy signals as summarised in Section 3.9.5, the following parameters are considered and their variation with sample thickness is investigated. These include the intensity of the diffraction peak at the most intense diffraction peak, the FWHM of the peak, and the ratios of the intensity and the area of the peak, and the FWHM and the area. The intensity of the peak has been used extensively in the literature and is also primarily used to create diffraction intensity images in diffraction imaging studies. The FWHM is commonly used, and is an indicator of the changes in the diffraction peak as a consequence of the change in the thickness, and essentially the geometry of the system. The area under the curve is used to take into consideration the fact that a decrease in intensity associated with higher sample attenuation can be normalised by the area of the curve. Equally, the width of diffraction peak is expected to vary with thickness and the area would be expected to change. The parameters used are defined in Figure 3.9.18.

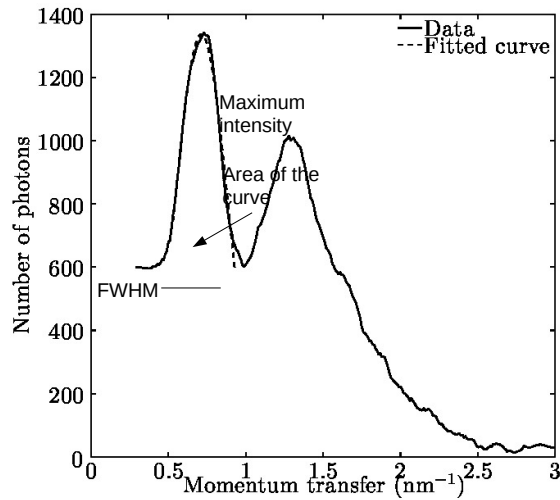


Figure 3.9.18: Parameters of the considered diffraction signal with respect to sample thickness.

In the first case all data which can be considered as fixed energy signals across all pixels i.e. the XRF and backscatter signals are excluded, this leads to photons of energies 15-20 keV and 33-40 keV at pixel angles of 4-8° being included. In addition to this, utilising only geometries that will detect diffraction at the energy ranges of interest are also considered. To exclude data, the post-analysis MATLAB code developed by the author utilised a data mask, which incorporated 0s at the sites of pixels and energy values not wanted in the post-analysis and 1s at the sites of pixels and energies that were included. These data were then converted to intensity momentum transfer signals and rebinned, as previously described in Section 3.9.4.

The following figures show the differing behaviour of the parameters for the three considered samples.

For each generated diffraction spectrum, for each sample and for each thickness for that sample, code was developed to find the FWHM, the area under the

diffraction peak, and the maximum intensity of the signal. From these values, the ratios were found for each thickness and for each sample.

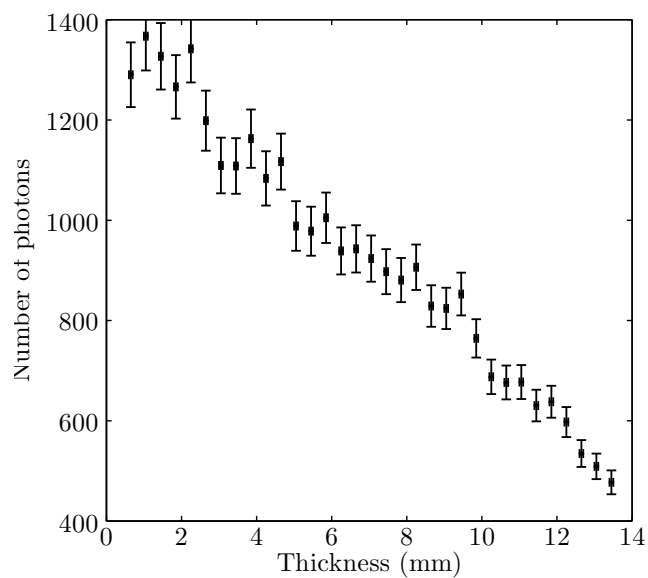


Figure 3.9.19: Intensity signal variation for the  $0.68 \text{ nm}^{-1}$  peak of caffeine.

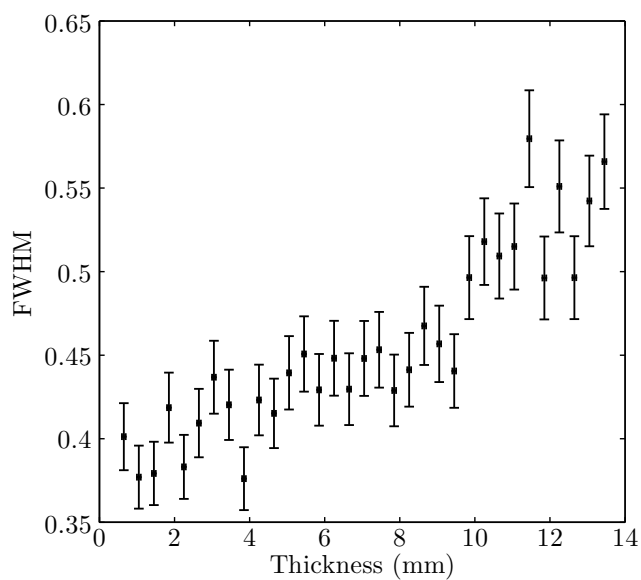


Figure 3.9.20: FWHM variation for the  $0.68 \text{ nm}^{-1}$  peak of caffeine.

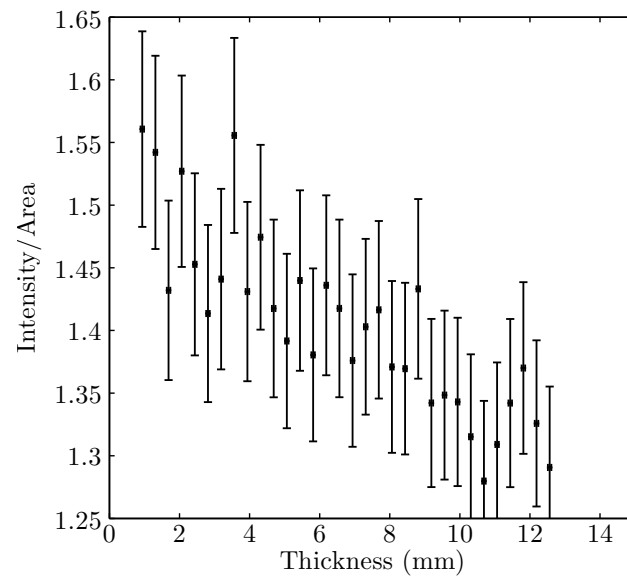


Figure 3.9.21: Intensity/Area variation for the 0.68 nm<sup>-1</sup> peak of caffeine.

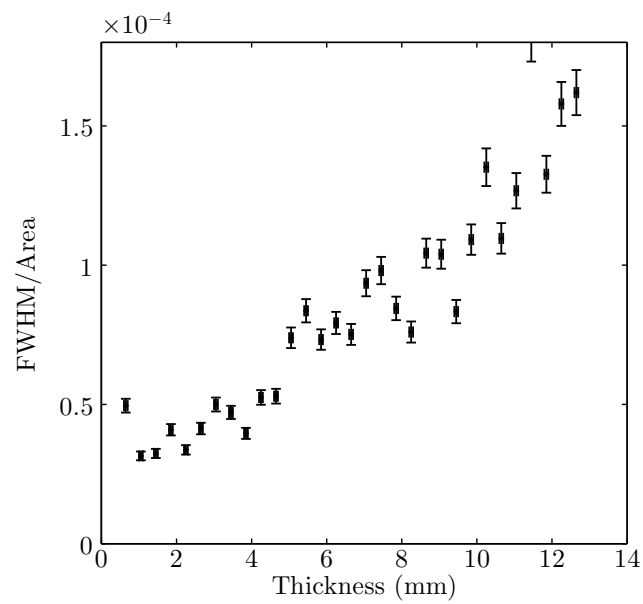


Figure 3.9.22: FWHM/Area variation for the 0.68 nm<sup>-1</sup> peak of caffeine.

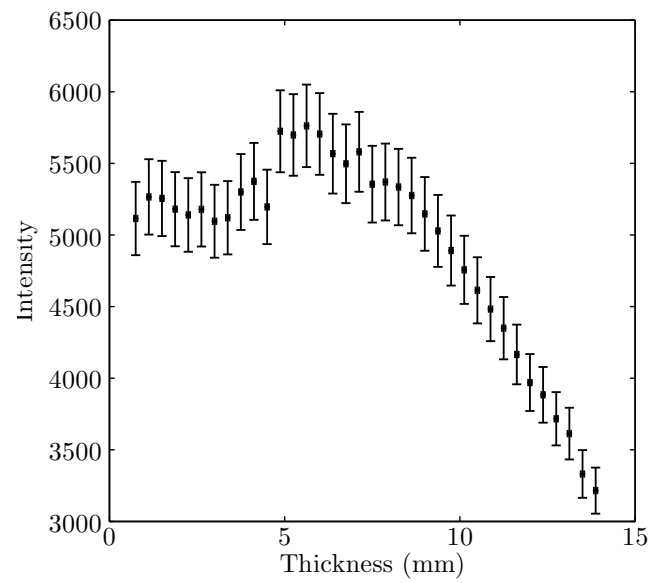


Figure 3.9.23: Intensity signal variation for the  $1.1 \text{ nm}^{-1}$  peak of lard.

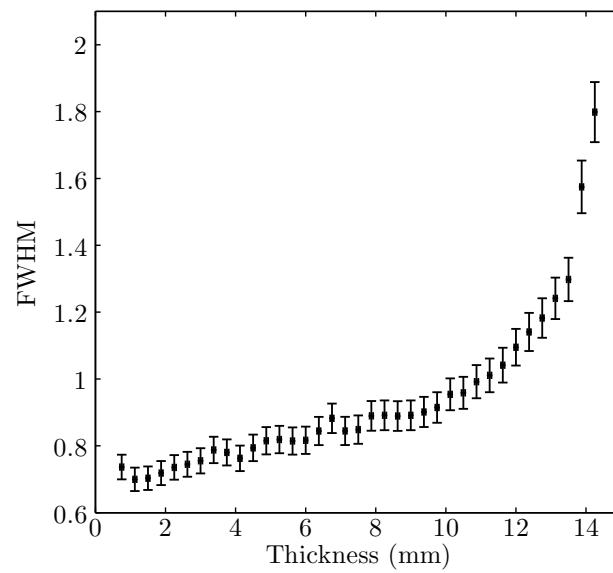


Figure 3.9.24: FWHM variation for the  $1.1 \text{ nm}^{-1}$  peak of lard.

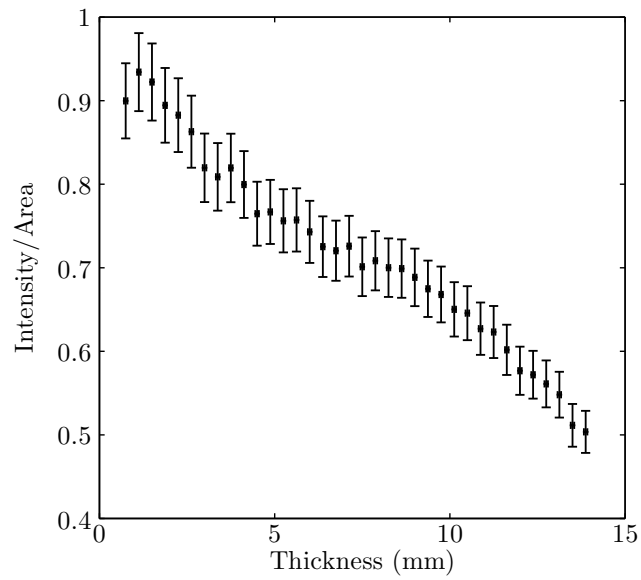


Figure 3.9.25: Intensity/Area variation for the  $1.1 \text{ nm}^{-1}$  peak of lard.

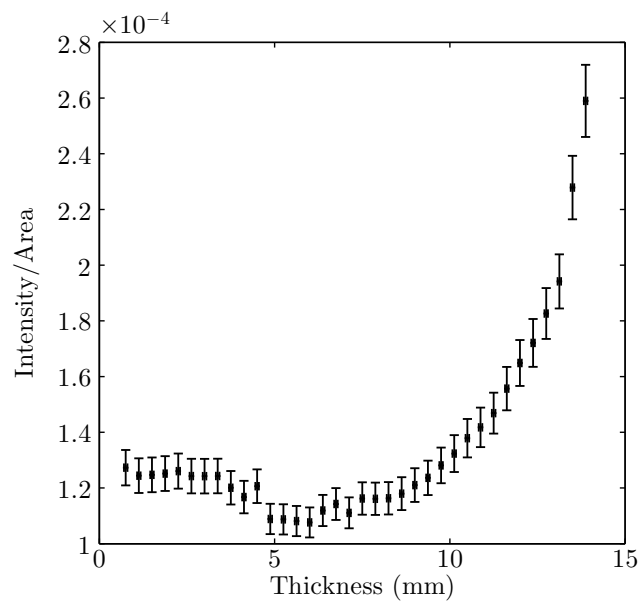


Figure 3.9.26: FWHM/Area variation for the  $1.1 \text{ nm}^{-1}$  peak of lard.

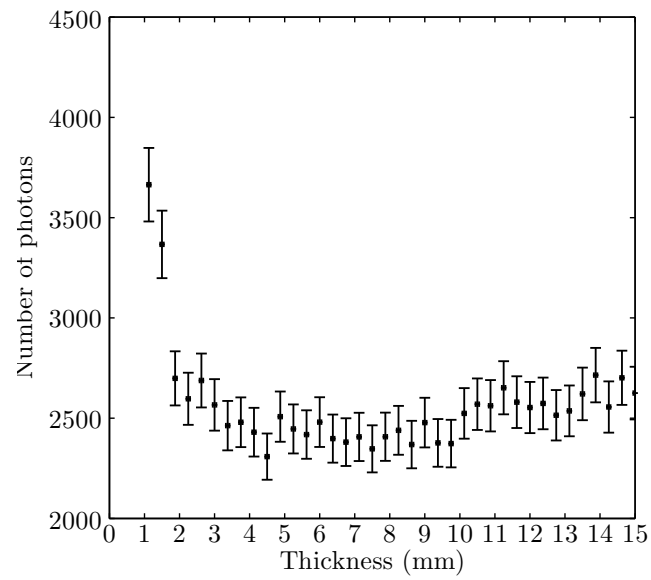


Figure 3.9.27: Intensity signal variation for the  $0.8 \text{ nm}^{-1}$  peak of PMMA.

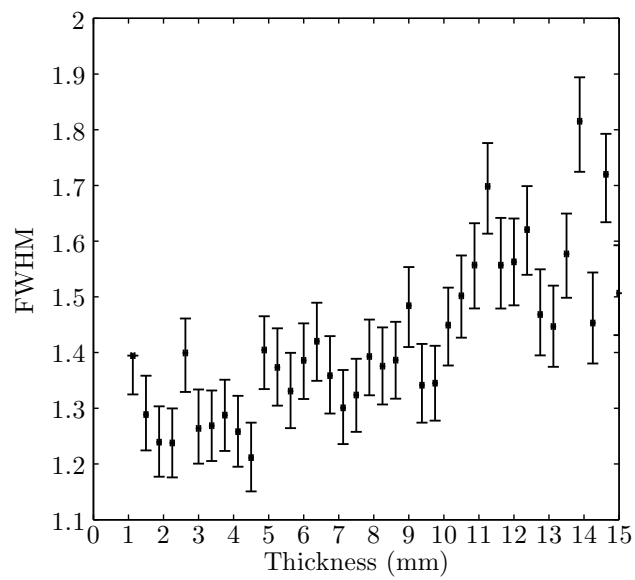


Figure 3.9.28: FWHM variation for the  $0.8 \text{ nm}^{-1}$  peak of PMMA.

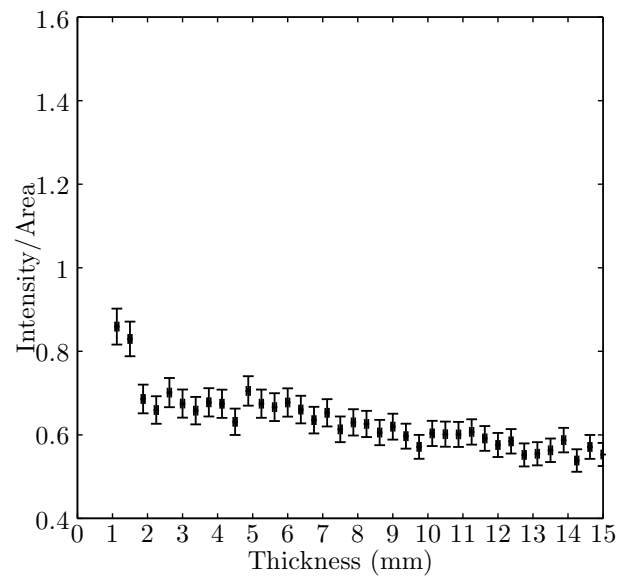


Figure 3.9.29: Intensity/Area variation for the  $0.8 \text{ nm}^{-1}$  peak of PMMA.

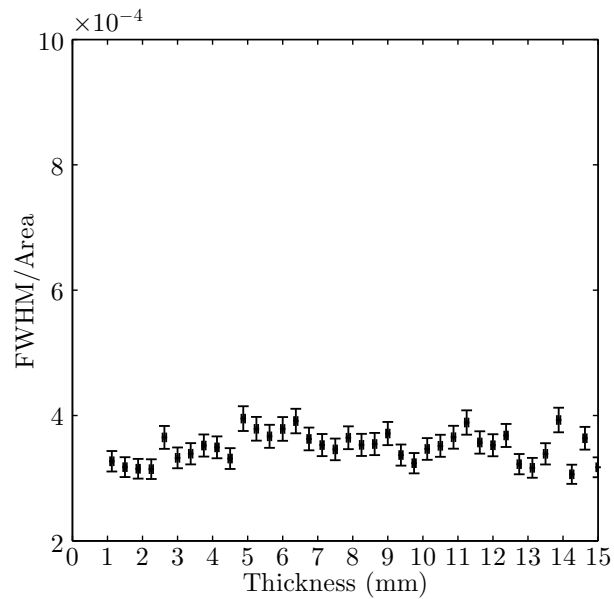


Figure 3.9.30: FWHM/Area variation for the  $0.8 \text{ nm}^{-1}$  peak of PMMA.

The general behaviour of the samples is the same—as the sample thickness increases, the diffraction peak after background subtraction decreases. Conversely,

if the thickness of the sample increases, the FWHM of the diffraction peak increases. Normalisation with the area of the curve leads to the same trends. As previously stated, the diffraction peak FWHM increases as the sample thickness increases, because the angles of diffraction being considered become less defined—the angular resolution of the system essentially begins to worsen and this signal from a larger angle range is being detected in a single pixel. All parameters show a trend associated with the thickness of the sample. However, for PMMA the broad peak of the diffraction signal leads to very little change with the thickness of the sample, suggesting that for broad peak materials, this system of self-collimation leads to little variation in terms of increasing the width of the diffraction peak. In addition, the signal for broad peaks are 'seen' by more pixels than sharper diffraction peaks, so the summation of the pixels could be contributing to this effect further. This is demonstrated by the examples in Figures 3.9.6 to 3.9.11.

The following data are processed as previously described, but this time a narrower range of angles were used i.e.  $6^{\circ}$ - $8^{\circ}$  instead  $4^{\circ}$ - $8^{\circ}$ , only photons of energies 15 keV-20 keV were used. This essentially makes the diffraction data more like ADXRD, where specific angles will detect photons at specific energies. Therefore rather than using the entire spectrum, a more select approach has been taken to refine the detected signal to only those of diffraction. The following are obtained examples for lard, PMMA, and caffeine.

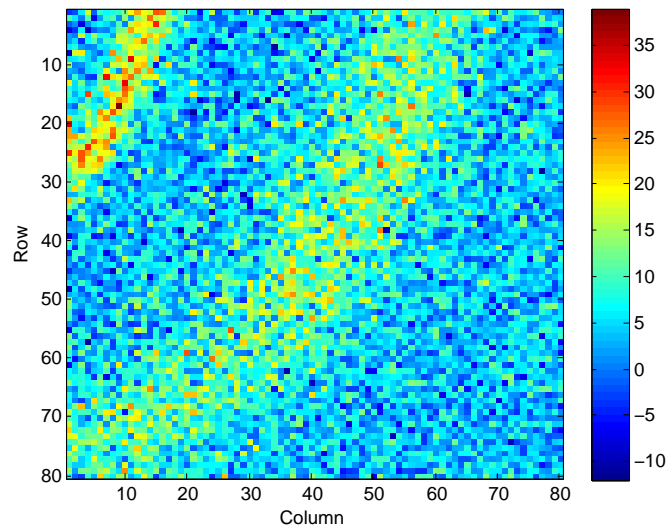


Figure 3.9.31: Example caffeine diffraction rings only utilising energies of 15–20 keV.

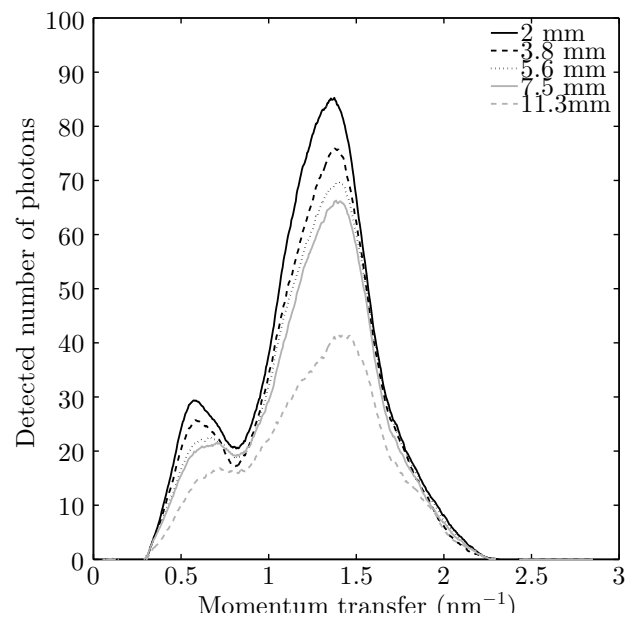


Figure 3.9.32: Example diffraction signal of caffeine utilising only energies of 15–20 keV

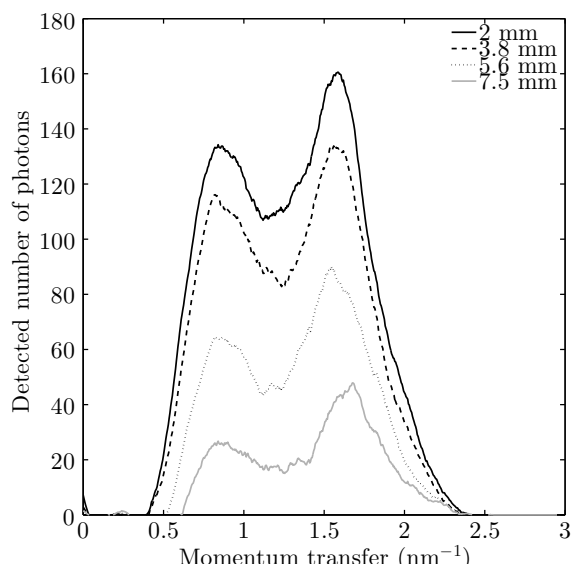


Figure 3.9.33: Example diffraction signal of PMMA utilising only energies of 15–20 keV.

The same parameters were considered for the peaks of the  $0.68 \text{ nm}^{-1}$ , the peak of  $0.8 \text{ nm}^{-1}$  of PMMA, and the  $1.1 \text{ nm}^{-1}$  of pork fat.

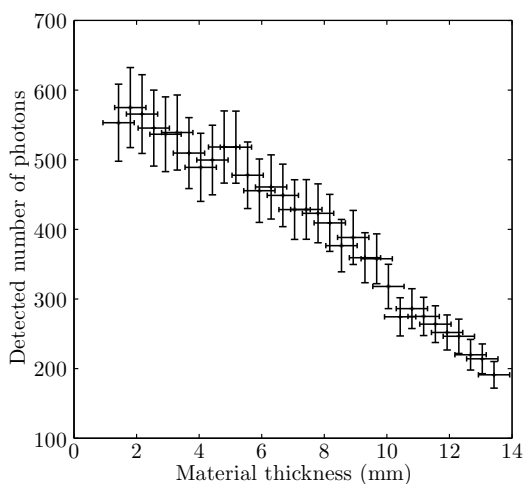


Figure 3.9.34: Relationship of peak intensity at  $0.68 \text{ nm}^{-1}$  with thickness for caffeine.

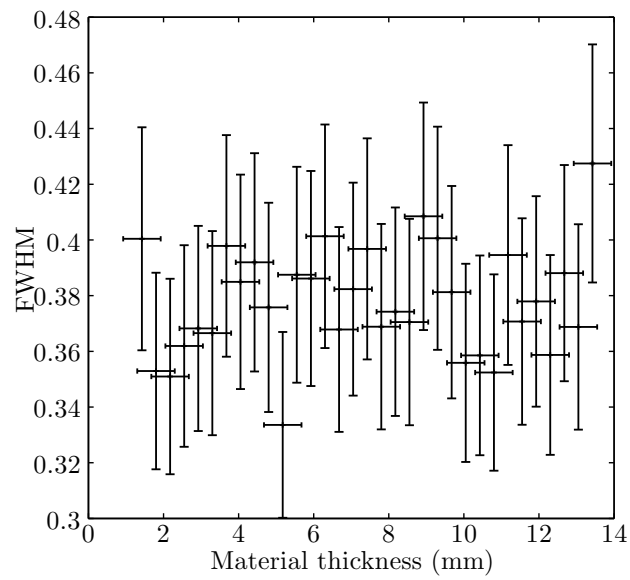


Figure 3.9.35: Relationship of FWHM at  $0.68 \text{ nm}^{-1}$  with thickness for caffeine.

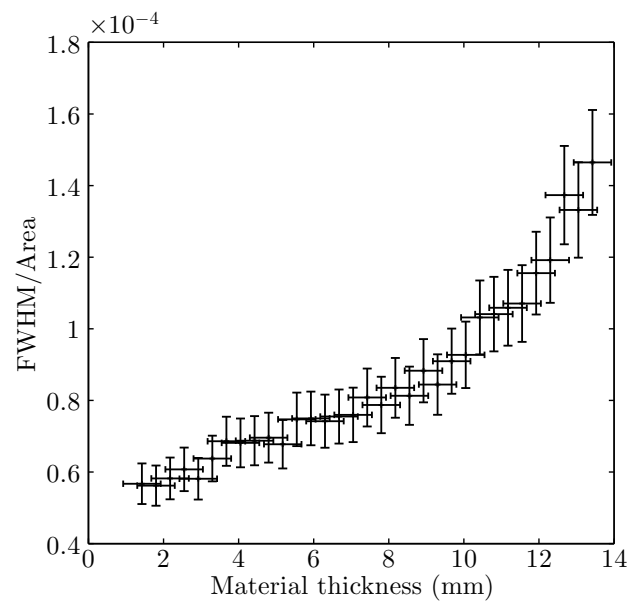


Figure 3.9.36: Relationship of FWHM/Area at  $0.68 \text{ nm}^{-1}$  with thickness for caffeine.

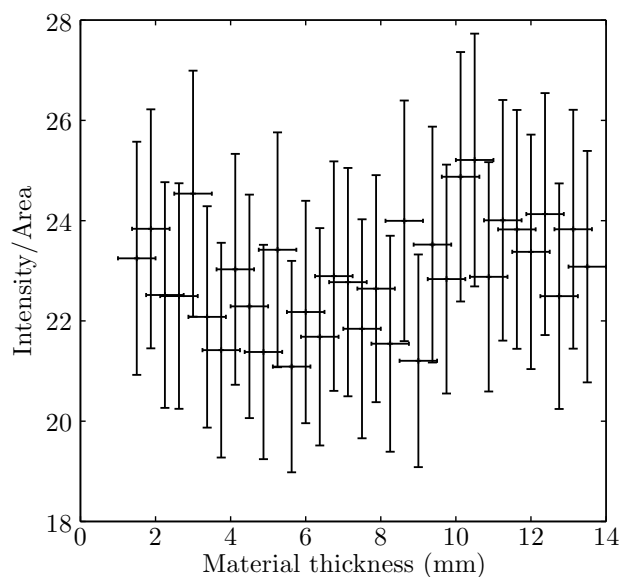


Figure 3.9.37: Relationship of Intensity/Area at  $0.68 \text{ nm}^{-1}$  with thickness for caffeine.

In this case the FWHM of caffeine can be interpreted as constant with sample thickness. The detection of diffraction over a narrower energy range and a narrower angle range would limit the number of photons being detected from other angles. This suggests that the FWHM of the peak doesn't change considerably when the 2D detector array is used in a similar manner to a standard ADXRD-i.e. limiting the angle choice and utilising a narrow band of energies. There is the suggestion of a slight increase which is to be expected. This is not as dramatic of an effect as seen previously when more energies and angles were utilised in the processing of the data.

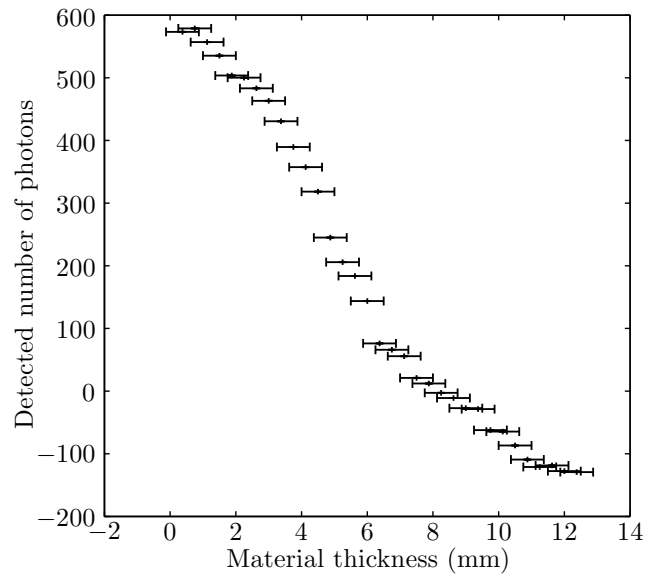


Figure 3.9.38: Relationship of peak intensity at  $0.8 \text{ nm}^{-1}$  with thickness for PMMA.

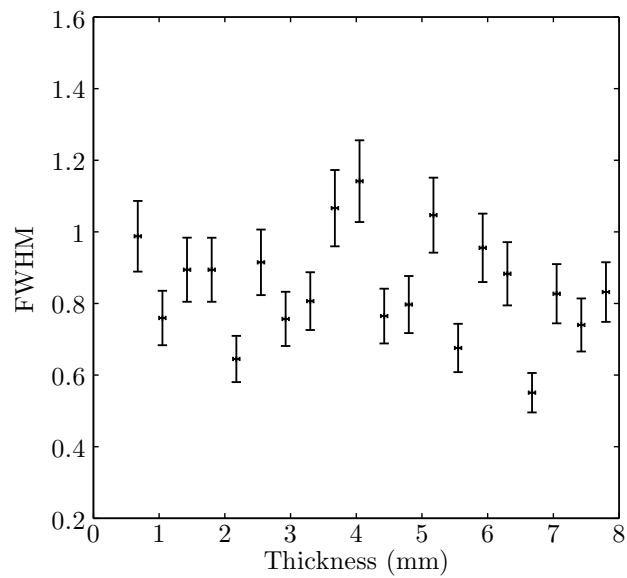


Figure 3.9.39: Relationship of FWHM at  $0.8 \text{ nm}^{-1}$  with thickness for PMMA.

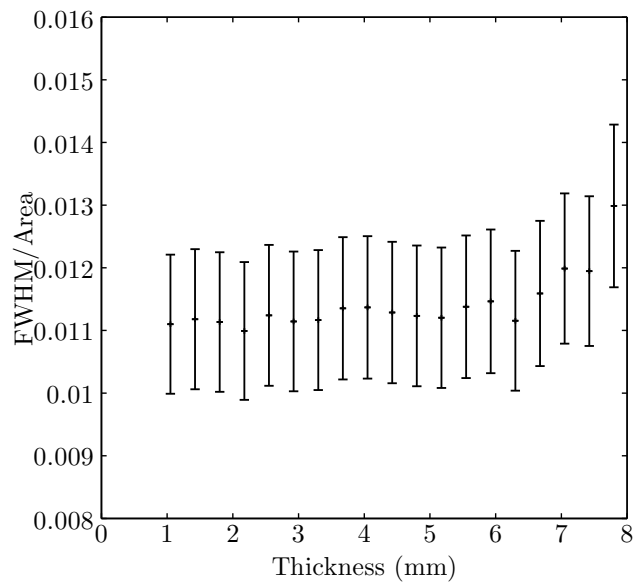


Figure 3.9.40: Relationship of FWHM/Intensity at  $0.8 \text{ nm}^{-1}$  with thickness for PMMA.

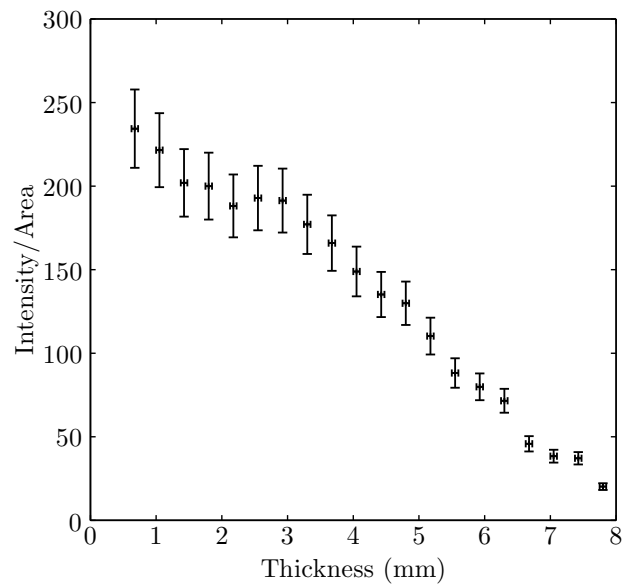


Figure 3.9.41: Relationship of Intensity/Area at  $0.8 \text{ nm}^{-1}$  with thickness for PMMA.

Again, in the case of PMMA, a variation with thickness can be seen in Figures 3.9.38–3.9.39. For intensity, the value becomes negative, indicating that the signal of the background at these energies exceeded the data from the sample signal. This could be due to attenuation effects of the sample. However, a variation of the signal is evident with the sample thickness and is more pronounced, utilising a narrower energy range and a range of angles when compared to Figures 3.9.27, 3.9.28 and 3.9.29.

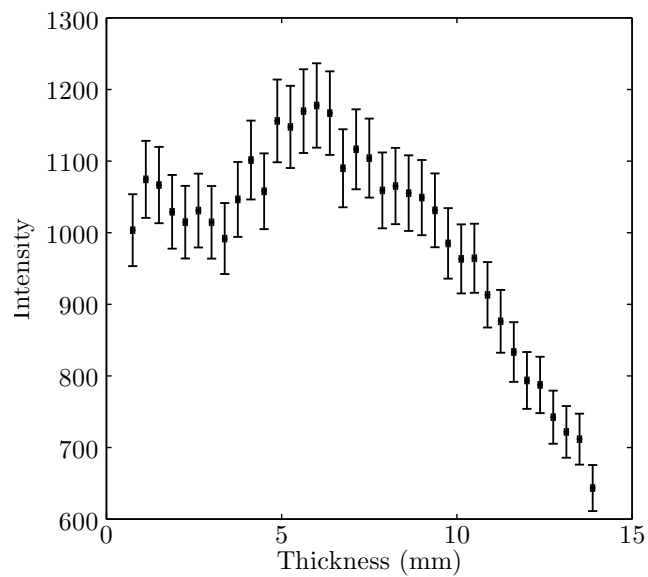


Figure 3.9.42: Relationship of intensity at  $1.1 \text{ nm}^{-1}$  with thickness for lard.

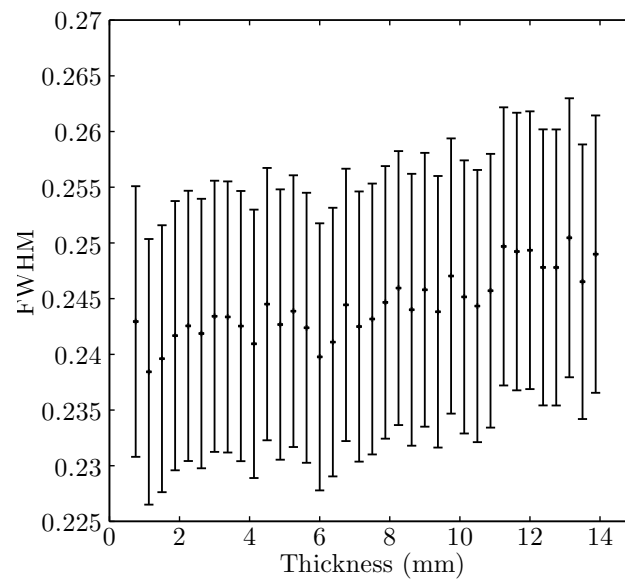


Figure 3.9.43: Relationship of FWHM at  $1.1 \text{ nm}^{-1}$  with thickness for lard.

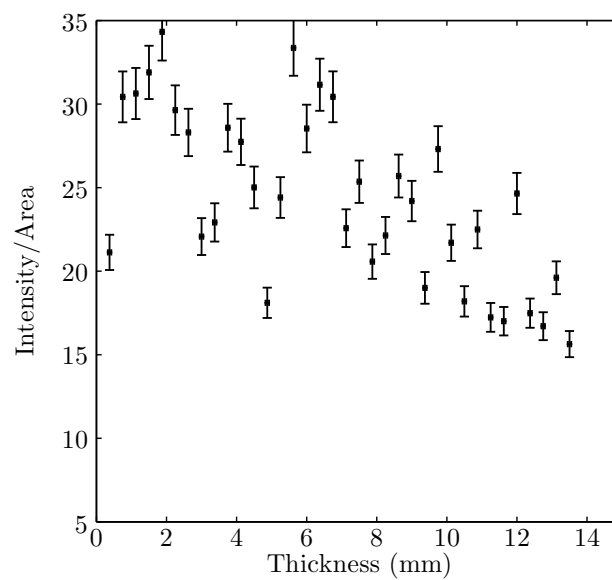


Figure 3.9.44: Relationship of intensity/area at  $1.1 \text{ nm}^{-1}$  with thickness for lard.

For lard a relationship between thickness and the intensity of the sample can be seen. The relationship between the ratios of the intensity and FWHM with

respect to area of the curve offer little in the way of variability with thickness, and the distribution of these can be explained as tending to a mean, as these values can be described as constant with respect to their errors.

### 3.10 Discussion

In this Chapter a prototype diffraction system that utilises a 2D detector multi-angle technique, which includes automated stages and a micro-focal source, has been described. The system has been used to explore how utilising the signal in different ways yields different relationships between imaging parameters and sample thickness, depending on the angles and energies used. This also demonstrates the ability to use the data extracted from the detector in multiple ways.

The focal spot size has been measured as  $6\ \mu\text{m}$ . This is within the expected operational range of the x-ray source, which is  $0.5\ \mu\text{m}$  to  $40\ \mu\text{m}$ . Due to the order of magnitude of the focal spot size the beam divergence is itself small, recorded as  $0.25 \pm 0.02$ , and the beam height at the sample is essentially the size of the nominal collimator diameter which in this case is  $0.5\ \text{mm} \pm 0.1\ \text{mm}$ . The HVL of the source was found to be  $0.175 \pm 0.2\ \text{mm}$  of aluminium with the kilovolt potential set at 70 kVp. Several other works exploring breast tissue or equivalent materials utilise tungsten target sources, however they do not all state the external or inherent filtration of the source, or produce the spectrum used. Bohndiek et al. (2009) utilised a tungsten target in their system, operating at 70 kVp but used filters such as gadolinium to reduce the width of the spectrum to tailor the spectrum to an ADXRD experiment. Kidane et al. (1999) utilised a tungsten target at 80 kVp with 2.5 mm aluminium and 2 mm beryllium, but do not produce the spectrum used. Pani et al. (2010) used 70 kVp and a focal spot of nominal size  $3\ \text{mm} \times 3\ \text{mm}$ . No external filtration is specified. Alkhateeb et al. (2012) also used a tungsten target with a focal spot of nominal size  $3\ \text{mm} \times 3\ \text{mm}$

with 0.8 mm filtration beryllium. Reproducing the spectrum here would enable future investigations to have a basis input for any simulations and comparisons to other spectra used in a similar diffraction system.

The system was physically limited by the inverse square law: It was decided to have the detector closer to reduce the acquisition time, especially in the case of imaging where 100s of points can be taken. Having the detector closer meant that a larger range of angles could be seen. Moving the detector back along the optical bench and the beam axis, as well as adjusting the beam displacement parameter, would mean that there would be a narrower range of angles. Moving the detector perpendicularly from the beam so as to adjust the beam-displacement parameter would lead to wider diffraction angles, which is not ideal for ensuring most events are coherent scatter events, rather than incoherent scatter events or multi-scatter events. To capture mostly coherent scatter events, it is ideal to use small angles over the range of  $2^\circ$ - $12^\circ$ . However, using small angles in this system means that the detector is more likely to detect the unscattered collimated beam which could dominate the signal at lower angles, and is not of interest. The smallest angle in this system was  $3^\circ$ . It should also be noted that at smaller diffraction angles, the expected scattered photon energies are higher. For example, to detect a signal at  $1.1 \text{ nm}^{-1}$ , at  $3^\circ$ , photons of energies 52 keV photons are required, which unfortunately fits within the backscatter peak of the sensor material. Incoherent scatter events interacting with the sensor material would be expected to increase with higher energies, and this would also need to be considered if higher energy photons are used for diffraction studies and 1 mm CdTe.

Future systems would have to consider which processing technique is ideal for the required application. Currently, there is no fixed post-analysis method of biopsy samples, rather that parameters of interest are used, but these vary within the literature. No MVA technique has been established as a standard post-analysis method. Any future systems would require an adjustment to the

geometry presented here, focussing on avoiding the escape peaks of the sensor by selecting geometries that would require photons at higher energies. However, this itself poses problems. Higher energy photons are less likely to coherently scatter with the sample, and it is more likely that incoherent scatter events would be detected as well. Some researchers utilise the incoherent scatter signals as well, including the works of Ryan and Farquharson (2007b), Sidhu et al. (2009) and Mersov et al. (2014), therefore this could be of interest for future systems and development. If a larger focal spot size, and therefore a larger output source was used, then the inverse square law and reduction of signal is less of an issue, and therefore the detector could have been placed at a distance further away from the sample. This could impact the choice of collimator size, and can be adapted on the rest of the geometry, depending on the careful selection of translation stages. The system here used what was available at the time.

In terms of visualising diffraction, the system is ideal as the diffraction rings appear clearly on the display. If a narrower angle range was used, this diffraction ring would not appear as clearly, as there would be a more uniform diffraction signal across the entire sensor. This poses a potential user problem. Being able to visualise the diffraction ring makes it possible to see that there is in fact diffraction being detected for the sample, which for potential clinical applications and biopsy samples, may be of use for end users.

Using the detected diffraction peaks of PMMA and lard, which had separable peaks measured at  $0.78 \text{ nm}^{-1}$  and  $1.1 \text{ nm}^{-1}$ , as well as the diffraction profile of caffeine, parameters of intensity at a selected momentum transfer value, the FWHM of the peak, the ratio of the intensity of the peak and the area under the curve, as well as the ratio of the FWHM and the area under the curve were presented. The general relationships with thickness varied depending on the post-analysis method used i.e. which energies and angles were used to produce the diffraction spectra. Caffeine, a more structured material had what could be described as

a linear relationship between the intensity of the diffraction peak and the sample thickness. The intensity is almost halved when only 15-20 keV and 33-40 keV photons are used and  $4^{\circ}$ - $8^{\circ}$  are considered. It is expected that the intensity would decrease if the number of pixels summed to produce a spectrum decreases. The FWHM of the peak of  $0.68 \text{ nm}^{-1}$  gets worse with thickness, this is to be expected due to the fact that the angular resolution of the system is less clearly defined. This is the case when considering 15-20 keV and 33-40 keV photons and  $4^{\circ}$ - $8^{\circ}$ . However, the FWHM becomes more stable as the angles and energies used are more limited, this would suggest that the angular resolution is not as affected over this range of thickness.

For PMMA the signal begins to decrease with signal, but more so when the more limited values of 15-20 keV photons and  $6^{\circ}$ - $8^{\circ}$  are used. PMMA is less crystalline than caffeine and therefore in the ideal ADXRD case, diffraction peaks would be expected to be broader in general. The PMMA peak at  $0.78 \text{ nm}^{-1}$  becomes more defined when utilising a narrower range, as shown by the intensity profiles, as well as the FWHM profiles. As previously stated, PMMA will be investigated in Section 5 to explore the variation of PMMA thickness for imaging purposes. The narrower range of 15-20 keV photons and  $6^{\circ}$ - $8^{\circ}$  will be used for this purpose.

Finally lard behaves similarly with regards to its intensity variation with thickness in both cases. The FWHM of the lard also remains relatively stable when a narrower range of settings is used, similar to PMMA.

In order to explore the reasons behind these results, further tests and analysis, such as simulations, could be used in the future. For the present work, of interest is how to best use the detector data to obtain useful information for later research presented in Section 5, to demonstrate that variations do occur when utilising different data from the multi-angle diffraction signal, and that any future system would have to take these factors into consideration when processing the data. It

could be that for different signals, i.e. different momentum transfer of interest, for a fixed geometry, that the diffraction signals can be used in a different way for each case. These results can be part of the basis of simulations of system geometry, including the x-ray spectrum used and the detector displacement, and how this influences the relationships between imaging parameters and sample thickness. This would be important to know for a clinical based system with thickness variation, as well as focussing on the best post-analysis for the signal of interest.

Future tests can consider thicker samples still, but in the event that, for example the system is used for breast tissue specifically, the geometry of the system will have to be optimised for such a case. Ideally it would be possible to utilise the detector array without having to remove data from the post-analysis due to the influence of the XRF and the detection of backscatter. For a particular signal, the parameters used to obtain greatest variability with thickness can be explored, as the behaviour of these parameters with thickness does not behave consistently when different energies and angles are used. The 2D detector array allows for the exploration of these parameters from one acquisition, potentially being able to optimise the parameters used for a specific system depending on the desired outcome. For example, in this work, it has been found the intensity variation has offered the most in terms of variability with sample thickness. In particular, when discussing PMMA, there is greater variability with the sample thickness and the intensity of the  $0.8 \text{ nm}^{-1}$  diffraction peak when using the narrower range of energies 15 keV–20 keV, and the angles of  $6^\circ$ – $8^\circ$ .

The exploration of collimators for the system could also be considered. The self-collimation method, where no secondary collimators are used, means the system is prone to detection of scatter events that are not necessarily from the samples themselves. As the sample thickness increases, it would be expected that multiple scatter events would be detected and the scatter angles of the system

would be less defined, as the scatter volume is no-longer clearly defined. Further work would have to be performed for such a system using thicker samples.

### 3.11 Conclusions

The system developed includes a micro-focal x-ray source with the ability to image samples using an automated data acquisition system with a 2D detector array. The focal spot size was measured as  $6\ \mu\text{m}$  and the HVL of the system was measured as  $0.175 \pm 0.2\ \text{mm}$ . The spectrum utilised was selected based on the ranges of energies that could be used for diffraction, as well as keeping in line with other studies that investigated EDXRD for breast tissue biopsy samples, with 70 kVp being selected for the x-ray source.

There are practical considerations relating to the use of the sensor material in a diffraction system, which include the avoidance of the escape peaks of the CdTe, as well as considering the potential backscatter signal as a result of higher energy photons interacting incoherently with the sensor material, and being detected as backscatter within the sensor. However, due to the fact the detector is designed to energy resolve and obtain information for each usable pixel, it is possible to avoid these problems by only utilising energies away from the fixed energy signals. For the detector system to be used in a clinical setting for breast tissue biopsy samples, it would be necessary to optimise the geometry for the desired signal, i.e. for the momentum transfer signals of interest.

It has been shown that it is possible to use the data obtained to select certain energies of interest, as well as to select angles. This has an effect on the relationship between imaging parameters, such as intensity and the FWHM of diffraction peaks of interest.

# Chapter 4

## Materials Library

### 4.1 Introduction

As discussed previously in Section 1.4, several works have investigated tissue equivalent materials for the use of diffraction studies. These materials have included, but are not limited to PMMA, nylon, water, olive oil and animal tissue, including pork fat. According to the International Commission on Radiological Protection (ICRP), adipose consists of 12% hydrogen, 64% carbon, 0.8% nitrogen and 23.3% of oxygen, with other elements such as calcium and chlorine also being present in small amounts (ICRU (1989)). According to the International Commission on Radiations Units and Measurements (ICRU), adipose tissue mainly

consists of 11% hydrogen, 60% carbon, 0.7% nitrogen and 28% of oxygen with other elements such as chlorine, calcium and sodium also being present in small amounts. The density of adipose tissue is given as  $0.95 \text{ gcm}^{-3}$ . Breast tissue has components of 11% hydrogen, 15% carbon, 3% nitrogen and 53% oxygen, with a density value of  $1.02 \text{ gcm}^{-3}$  (ICRU (1989)).

Plastics tend to be of interest as tissue equivalent materials due to their compositions of low  $Z$  materials, including oxygen, carbon, nitrogen and hydrogen, such as the monomer  $\text{C}_3\text{O}_2\text{H}_8$  of PMMA, and a composition of 8% hydrogen, 63% carbon and 32% oxygen with a density of  $1.19 \text{ gcm}^{-3}$ . The structure of a plastic is one of a repeated monomer, which is similar to considering a unit cell forming a lattice in crystalline materials. In the case of plastics, however, there is short range order, similar to that of human tissue, as opposed to long range order of crystalline materials, which leads to broader diffraction peaks. Plastics offer an amorphous type material with crystalline features which contain elements seen in human tissue. Human tissue does also contain other elements with higher atomic number  $Z$ , such as zinc, iron and calcium, which are primarily investigated in terms of their XRF signal, as seen in the works of Geraki et al. (2004a), Geraki et al. (2004b), Geraki et al. (2004c) and Farquharson et al. (2013).

Human breast tissue is complex in its structure, with many constituents. Broadly speaking within diffraction the primary discussion is focussed on adipose tissue, the fat storing tissue which includes water and adipocyte cells as part of its structure, as well as glandular tissue which make up the glands and duct structures. There is also the supportive connecting fibrous tissue. The works by Kidane et al. (1999) quantify the general component of the cells in order to classify the tissue types. Adipose tissue is the fat storing tissue which includes adipocytes as well as water. Epithelial cells are found in the glandular tissue. In the study, they consider that healthy tissue is a combination of adipose and fibroglandular tissue, which itself consists of fibrous and stroma tissue. Tissue that is predominantly

adipose is classified as adipose, and tissue that is predominantly fibroglandular is classed as fibroglandular. Tissues with notable changes in benign epithial content were noted, and carcinoma classified based on the malignant epithial content. It is noted that the sharper diffraction peak at  $1.1 \text{ nm}^{-1}$  is associated with the large number of fat cells, aligned such that a high level order order is seen. Tissues which have invading cancer cells lose the structure and order associated with fat, as these cells replace the fat content, leading to less order in these tissues, and thus a broader diffraction peak than associated with adipose tissue. Tissues such as carcinoma also have a high water content, which is why there are similarities between the signatures of water and carcinoma, as demonstrated by Evans et al. (1991). Water is therefore of great interest as a tissue equivalence substance.

Small angle x-ray scattering (SAXS) is an x-ray scattering technique that is able to detect structures of less than typically  $100 \text{ nm}^{-1}$  (Falzon et al. (2006)) and has been used to explore differences in malignant tissues and normal, healthy tissue. Several studies have used SAXS to explore the role of collagen and invasive cancers, of which a summary can be found in Theodorakou and Farquharson (2008), which also includes a description of the technique. Collagen is the collective name given to the most proteins in the body, of which there are over 20 types of collagen. Collagen is typically found in all connective tissues, as well as skin, bone, and cartilage. Collagen fibrils are minute fibres of collagen which, when combined, help form connective tissue. Collagen fibrils with diameter of order of  $65 \text{ nm}$  aggregate in healthy tissue. The degradation of the collagen structure is known to occur and be a feature with infiltrating cancer. Several studies have investigated the differences between the SAXS signals of collagen fibres in normal tissue types and malignant tissue. One study includes that of Fernández et al. (2002) which used excised tissues containing both healthy and unhealthy tissue types performed at the European Synchrotron Radiation Facility (ESRF). They scanned their excised tissue samples typically in steps of  $1 \text{ mm}$  but reduced the

step to 0.25 mm in areas of particular interest. It was found that areas imaged away from the unhealthy tissue the axial period of collagen fibrils was  $65 \pm 0.1$  nm whereas in unhealthy tissue this was found to be on average 0.3 nm larger. In general the findings, as stated in the study, found that ordered collagen is found in tissue far from the cancerous sites, and that the collagen order begins to break down in invaded tissue areas. This corresponds to an increase in the axial period of collagen. They also found that the scatter signal is stronger from the area invaded by cancer, corresponding to a large increase of the specific surface area of the scatterer. A further study by Fernández et al. (2008) explored samples including ductal carcinoma and ductal carcinoma *in situ* which included healthy collagen and invaded collagen confirmed these results. A SAXS experiment performed by Sidhu et al. (2009) investigated the axial d-spacing of excised breast tissue. Collagen modules packed laterally and bound with hydrogen are arranged longitudinally within the tissue. This structure is repeated axially along the structure, and therefore the axial d-spacing is used in this study to quantify the periodicity of these structures. It has been found that the d-spacing increased with malignancy, therefore implying that the collagen structure was degraded by the infiltrating disease.

Several studies have explored the collagen structure of gelatine and agarose, the principle component of agar which contributes to gel formation. Studies have long since established that the diffraction pattern of gelatine is virtually the same as that of collagen, as described in the review article by Clark (1931). More recent studies such as that of Perzon and Djabourov (1990) also highlight the similarities between collagen diffraction patterns and that of gelatine. Agarose has also been investigated, with the molecular structure of the produced gels depending on the method of preparation. Although agarose, as a part of agar, and gelatine both have similarities to collagen due to their structure, these features would not be seen in the diffraction system developed in this research, as there is no sensitivity

to momentum transfer values that correspond to that required to measured collagen type structures. An EDXRD system is designed to see structures of typically greater than 100 nm (Theodorakou and Farquharson (2008)). Momentum transfer values of less than  $0.4 \text{ nm}^{-1}$  cannot be detected within the system presented in this research, based on the detectable momentum transfer values.

Previous studies that have used phantoms have primarily consisted of PMMA phantoms, such as the works by Griffiths et al. (2008) utilised two phantoms for their study, one combining both thin tissue samples and PMMA, and the other utilising just PMMA. The test phantom of PMMA only was designed by the investigators for their study to test the spatial resolution of their system, which consisted of a 3 cm block of PMMA formed from the combination of three 1 cm slabs. Within these slabs, holes of range 1 mm to 8 mm were drilled in order to be imaged in their diffraction system. This phantom is not designed to be anthropomorphic, but was being used for the study to create images as a means of testing the spatial resolution in the system in a methodical way. The users used drilling bits and standing drill to create the phantom. This is not a standardised phantom, but one designed specifically for their spatial resolution study. The second phantom used in the study is designed to use real tissue, which were of the order 1.5 cm thick. These were then packed within slabs of 1 cm of PMMA and 1.5 cm of low density packing. This 4 cm thick phantom was itself contained in a thin walled air-tight PMMA container. In this case the tissues were unfixed tissue that had to be contained for imaging purposes, and also not come into contact with the user. The materials used include PMMA, an easily procured and cheap material commonly used in diffraction studies.

Where fixed tissues are available, these are preferentially used when considering the variations between healthy and unhealthy tissue types, including the works of Castro et al. (2004), Castro et al. (2005b), Kidane et al. (1999), Griffiths et al. (2004) and Pani et al. (2010). The clinical potential in diffraction for biopsy

samples, with thickness of less than 6 cm has been shown based on the literature. However there is no current approach to creating a phantom that could simulate a biopsy sample that could be used for system testing, or in situations where breast tissues are not available. Therefore, considering other materials could be useful for expanding the current used materials as well as consider their material properties for phantom creation.

In terms of the physical properties of a material for x-ray diffraction studies, the molecular structure has to be taken into account, such that the diffraction patterns would be similar to that of the tissue of interest, e.g. broad diffraction peaks in the case of carcinoma. This would mean having chemical composition with low  $Z$  elements such as carbon, hydrogen, nitrogen and oxygen. It also follows that the attenuation properties of the material should also be similar, as should its density to make it a more realistic representation of the tissue of interest. In terms of the diffraction signal the most common parameter considered for tissue equivalence is the position of the diffraction peaks and the comparison of intensities at these peaks, as shown in Section 1.4. Therefore, it would be desired for the positions of the peak intensities, as well as the relative intensities of these peaks, be the same as the tissue material. Another property consistently used is the FWHM of the diffraction peaks. However, this is geometry dependent, as the angular resolution of the system and also the thickness of the sample can affect the width of the diffraction peak. This is therefore an effect of the geometry as opposed to being purely an effect of the sample, although amorphous materials do generally speaking have wider diffraction peaks compared to crystalline structures.

In addition to the properties for making phantoms and for using a material, other things to consider would be the procurement of the items. Ideally they would be easily obtained and relatively cheap, or at least the cost known such that any users could make the choice of using that particular material or not.

The materials should not be harmful to the user (e.g. poisonous, carcinogenic etc), otherwise additional precautions would have to be made when using the materials, adding to cost and risk to the user. For anthropomorphic phantoms, a requirement would be that the materials could be processed in such a way that they could be shaped like the tissue of interest. In the case of geometric phantoms, there is less restriction, although it might be necessary to be able to carve or drill in to the material, as has been previously done for phantoms in studies such as in the works of Griffiths et al. (2008).

Imaging contrast of a anthropomorphic phantoms should match what is seen during real imaging of tissue. Currently there is no standardised contrast considered as acceptable for diffraction imaging studies, although a recent investigation by Alkhateeb et al. (2012) has investigated the combination of materials which lead to the best tissue contrast in relation to other studies. In this study, diffraction signatures of combinations of materials, for example, nylon and glue, and the contrast are compared to the contrast of combinations of tissue types, e.g. malignant and benign, as found in the literature. The study itself does not use any tissue samples.

The creation of a phantom is also ideally reproducible or has a life time such that the studies can be completed using the same phantom i.e. it is specific to a study. In this work, no restrictions are placed on the lifetime of the study. This would allow for researchers to use the materials investigated for their studies as they choose to.

## 4.2 Objectives

This Chapter aims to investigate plastics and gels for use as tissue equivalent materials for breast tissue x-ray diffraction by developing a materials library, consisting of diffraction spectra and the materials' properties. Gels such as gela-

tine and agar are colloid hydrophilic substances that form semi-solid gels when dissolved in hot water. They could therefore potentially be used in a diffraction phantom to hold water within the phantom, but have not yet been considered in the context of being an EDXRD tissue equivalent material within the literature, to the author's knowledge.

This Chapter aims to consider the materials in terms of their density, chemical composition, user-ability, linear attenuation coefficient at 17.44 keV (used as a reference energy based on previous works), as well as the melting point for practical implications. This Chapter aims to begin a materials library that considers the practical implications of materials for future diffraction works which require phantoms, as well as providing potential alternative materials to PMMA and water. These can serve as reference materials for the future. To this end comparisons would have to be made to the known diffraction spectra of adipose and glandular tissue from the literature. Since the momentum transfer peaks are of primary interest as a means of characterising spectra, materials previously presented in the literature, including caffeine, can be used as reference data to compare to previous results, acting as a means of validating the system.

## 4.3 Method

### 4.3.1 Materials and their preparation

A summary of the plastic based materials is provided in Table 4.3.1 and Table 4.3.2 summarises the gel type materials. The information was collated by the author based on the information sheets from the websites of the Plastic Shop ([www.theplasticshop.co.uk](http://www.theplasticshop.co.uk)) and Tiranti's Ltd ([www.tiranti.co.uk](http://www.tiranti.co.uk)). The Table details the commercial name as provided by the supplier website, as well as information from the respective data sheets. The density values are given at 23 °C

and the CAS number corresponds to the materials' Chemistry Abstract Service registry number. The chemical composition was found based on the CAS number if this was not provided in the data sheet of the material.

| Commercial name | Chemical Composition   | CAS number | Density ( $\text{gcm}^{-3}$ ) | Melting point ( $^{\circ}\text{C}$ ) |
|-----------------|--|------------|-------------------------------|--------------------------------------|
| Delrin          | $\text{CH}_2\text{O}$  | 9002-81-7  | 1.43                          | 175                                  |
| Ertalyte        | $\text{C}_{10}\text{H}_8\text{O}_4$ . Coat $\text{In}_2\text{O}_3\text{SnO}_2$ | 25038-59-9 | 1.39                          | 255                                  |
| Lexan 9030      | $\text{C}_6\text{H}_4\text{C}(\text{CH}_3)_2\text{C}_6\text{H}_4\text{OCO}_2$  | 24936-68-3 | 1.2                           | -                                    |
| Nylatron GSM    | $\text{NH}(\text{CH}_2)_5\text{CO}$  | 25038-54-4 | 1.16                          | 220                                  |
|                 | + $\text{MoS}_2$   | 1317-33-5  |                               |                                      |
| Ertalon 66-GF30 | $\text{CO}(\text{CH}_2)_4\text{CONH}(\text{CH}_2)_6\text{NH}$                  | 3213-17-2  | 1.29                          | 255                                  |
|                 | + $\text{CF}_2\text{CF}_2$   | 9002-84-0  |                               |                                      |
| Errtalon LFX    | $\text{NH}(\text{CH}_2)_5\text{CO}$  | 25038-54-4 | 1.2                           | 220                                  |
| Polyester resin | $\text{C}_8\text{H}_8\text{O}_2$   | 100-42-5   | 1.11                          | -                                    |
| Polymorph       | $\text{C}_6\text{H}_{10}\text{O}_2$  | 24980-41-4 | 1.15                          | 60                                   |
| PTFE            | $\text{C}_2\text{F}_4$   | 9002-84-0  | 2.17                          | 327                                  |

Table 4.3.1: Summary of the plastics used for the library

The commercial names are provided in order to more easily label the samples. Delrin, also known as Ertacetal H, is chemically known as Polyoxymethylene homopolymer. Ertalyte is better known as Polyethyleneterephthalate (PET), and Lexan 9030 is a polycarbonate with a main monomer of poly (bisphenol-A carbonate). Nylatron GSM consists of cast polyamide 6 (Nylon 6) and is filled with molybdenum. Ertalon 66-GF30 consists of Nylon 66 with 30% glass fibres. Ertalon LFX consists of the polyamide 6 (Nylon 6) with oil filling. Polymorph is also known as Polycaprolactam and finally PTFE is Polytetrafluoroethylene. In the case of the polyamide samples the addition of, for example, glass filling,

changes the properties when compared to the oil filled Nylon 6. Both the density and the melting point values are affected. The practical properties are affected, however the diffraction properties have not yet been investigated.

No melting point is provided for Lexan 9030 in Table 4.3.1 as it has been documented that there is no specific melting point but rather the material gradually softens over a range of temperatures (General Electric Company (1997)). Polyester resin is designed to be set at a particular temperature using a catalyst, such as the recommended Methyl ethyl ketone peroxide (MEKP) Butanox M50 (Alec Tiranti Ltd). With the exception of polymorph and resin, all other materials are classed as thermoplastics which are those that can be used under high temperature conditions. Polymorph was melted with 60 °C water and then placed in a premade mould 3 mm deep. Polymorph was then left to set before being removed from the mould.

All materials were either laser cut to 3 mm thickness or cut with a band saw to 3 mm thickness, with calliper measurements being taken to measure the thickness and any variation in the thickness. The gels were set to 3 mm using a mould made from enhanced cardboard that was folded into a rectangle of 4 cm × 2 cm and had thickness of  $3 \pm 0.3$  mm. 3 mm is used as a reference thickness in order to limit any multiple scatter events and to prevent the thickness affecting the diffraction signal, and is similar to the magnitude of thicknesses used in biopsy sample studies. Practically speaking, the samples of the procured plastics came at different thicknesses, with 3 mm being the smallest thickness. Therefore it was decided to reduce the thickness of the other materials to match the minimum possible thickness available.

| Sample name | Agar (%) | Gelatine (%) | Water (%) |
|-------------|----------|--------------|-----------|
| Agar 1      | 5        | -            | 95        |
| Agar 2      | 9        | -            | 91        |
| Gelatine 1  | -        | 5            | 95        |
| Gelatine 2  | -        | 9            | 91        |
| Gelatine 3  | -        | 17           | 83        |

Table 4.3.2: Biodegradable gel samples

Preparation of the agar and the gelatine were based on the instructions provided on the packaging. In the case of gelatine, sachets of 12 g of gelatine were mixed with 120 ml, 240 ml and 60 ml, in order to get different percentages of gelatine content. The contents were measured to confirm the amount was as stated in the sachets. The same was performed for the agar, measuring 12 g of powder and using the same amount of water. Once prepared, the gels were left to set in 3 mm thick pre-made trays. All gels remained set during the acquisition.

### 4.3.2 Diffraction profiles data collection

All items were analysed in an EDXRD diffractometer to obtain the materials' diffraction profiles. A diagram of the system is shown in Figure 4.3.1. The system was previously set-up in the Radiation Physics lab at UCL and redesigned by PhD student Chiaki Crewes.

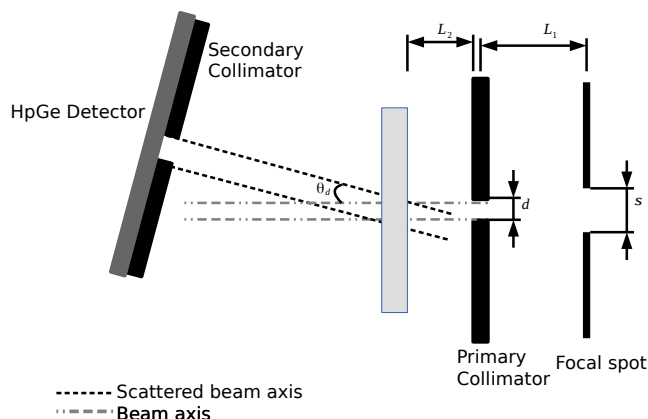


Figure 4.3.1: Diffractometer system used for the materials library

The system consists of a polychromatic tungsten target anode source and brass collimators of 2 cm thickness with a pinhole of 1 mm. The secondary collimator was placed at a nominal scatter angle of  $5.8^\circ$  and all samples were placed at a primary collimator to sample distance of 2 cm. The 2 cm distance was constant as a place-marker with fixed width of 2 cm was used to place the sample from the first collimator. The scattered photons were detected using a HPGc detector with diameter 26 mm and depth 10 mm (model GLP 3636013-P, EG&G Ortec, Oakridge, TN, USA). For the gel samples, these were placed in thin plastic bags of less than 0.1 mm thickness to prevent the gels from touching the equipment and also to mount the gel within the system. The detected spectra were analysed using a computer based multichannel analyser (MCA) card (DSpec JR, EG&G Ortec). The PC software (Maestro, EG & G Ortec) was used and the detected photons assigned to one of 2048 energy channels. All data acquired in the Maestro system were saved in the .Spe format which can then be easily read into MATLAB for analysis.

Each material was placed into the diffraction system for an acquisition time of 500 s. The background measurements were taken to ensure that the background

scatter signal was removed from the sample signal. The effects of the thin plastic bag were negligible.

## 4.4 Results

A function was written by the author to read in the collected diffraction data from .Spe format into MATLAB for post-processing and analysis. This resulted in  $1 \times 2048$  vector of intensity values produced from the data collection for each input sample, corresponding to the photon intensity for each energy bin. The HPGe was energy calibrated using previously obtained Am-241 data from Chiaki Crewes such that a photon-intensity spectra was obtained for each sample and background scan.

The spectra were all background corrected by subtracting the spectrum recorded with no sample present in the system, and were also attenuation corrected. The attenuation factors were found by the author by inputting the chemical composition into the NIST XCOM database (Berger et al. (2010)) using the data provided in each samples' data sheet. Where the composition of additional constituents was unknown, only the main material, considered to be the major component of the sample, was taken into consideration. These data were collated by the author by combining information from the data sheets and the CAS numbers and inputting the compound chemical equation in the NIST XCOM database. All the attenuation data for each sample were downloaded from the NIST XCOM website. Due to the unknown composition of agar and gelatine, pure water was used to approximate the attenuation coefficients for these samples. As the water content is the dominant content in the gels, it is considered that this assumption would be a fair one.

To compare to the normalised data from the literature, all data were time corrected such that the spectra were presented in number of detected photons

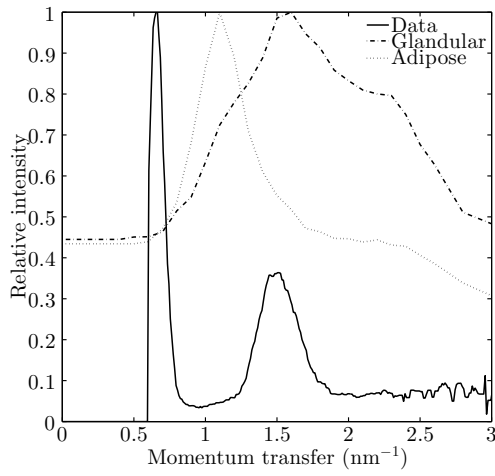
per second, and were then normalised to the maximum intensity of each spectrum. The data were compared to Poletti et al. (2002a), who also found results for momentum transfer peak position and linear attenuation coefficients corresponding with previous works. To do this, the tabular information of the scatter attenuation coefficient from Poletti et al. (2002a) was copied by the author into a text file which could then be read into MATLAB.

All attenuation coefficient data were interpolated in MATLAB using a linear interpolation method to find the attenuation coefficients at the energies corresponding to those of the energy axis of the HPGe detector. This energy axis was then converted to momentum transfer using the momentum transfer equation, such that the attenuation coefficients were a function of the momentum transfer values. This approach is similarly utilised by Pani et al. (2009). This is necessary in order to ensure the attenuation coefficient function for each material is a function of the energy axis of the HPGe, which in turn can be represented as momentum transfer using the conversion presented in Pani et al. (2009), as given in Eqn 4.4.1

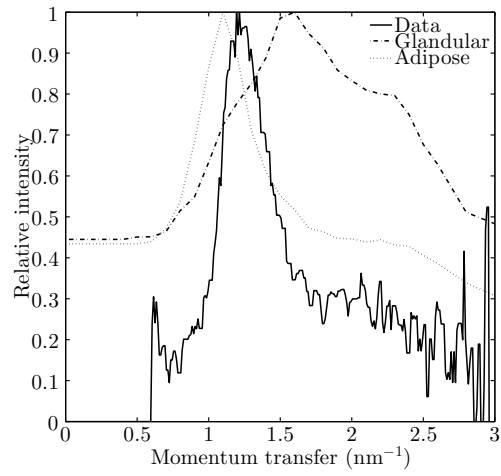
$$\chi(\text{nm}^{-1}) = 0.806E(\text{keV}) \sin\left(\frac{\theta}{2}\right) \quad (4.4.1)$$

where  $E$  is the energy of the detected photon in units of keV,  $\chi$  is calculated in units of  $\text{nm}^{-1}$  and  $\theta$  is the measured scatter angle, which in this case has a nominal value of  $5.8^\circ$ .

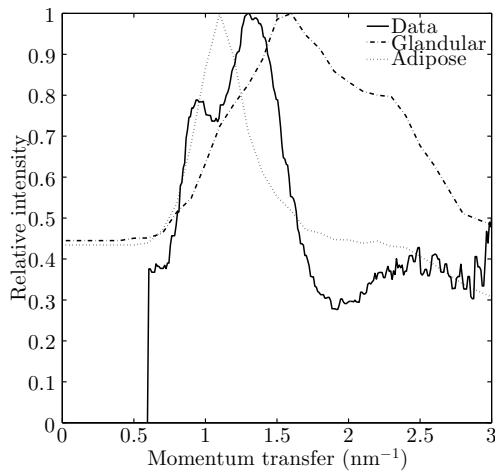
Figures 4.4.1, 4.4.2 and 4.4.3 shows the obtained diffraction spectra for the caffeine sample, plastics and gels. All data are plotted with the normalised adipose and glandular tissue signatures presented by Poletti et al. (2002a). This allows for visual comparisons of the samples to the two spectra of interest for breast tissue equivalent materials work, namely adipose and glandular tissues.



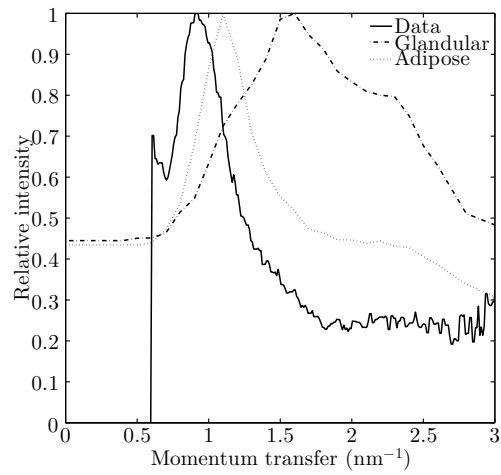
(a) Diffraction spectrum of 99.9% caffeine.



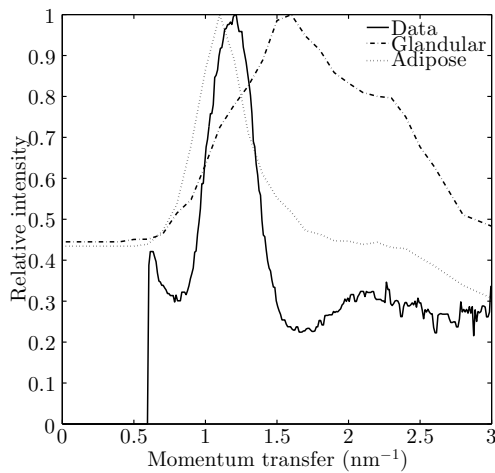
(b) Diffraction spectrum of Delrin.



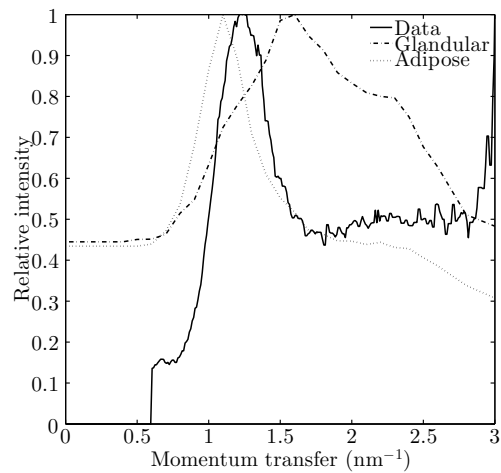
(c) Diffraction spectrum of Ertalyte.



(d) Diffraction spectrum of Lexan.

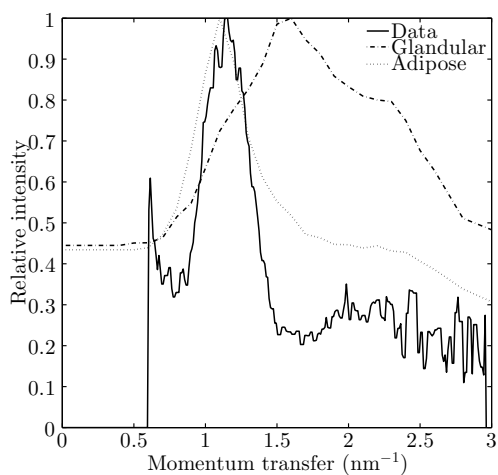


(e) Diffraction spectrum of Nylatron.

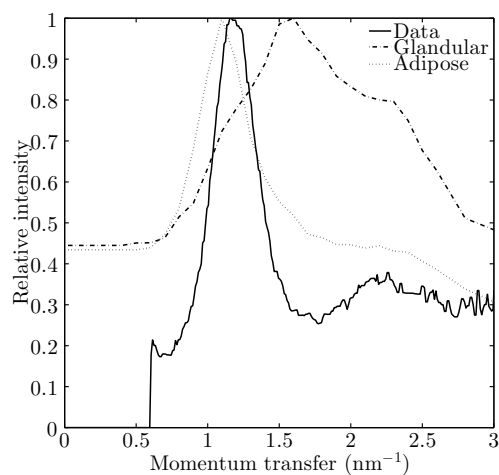


(f) Diffraction spectrum of Ertalon 66-GF30.

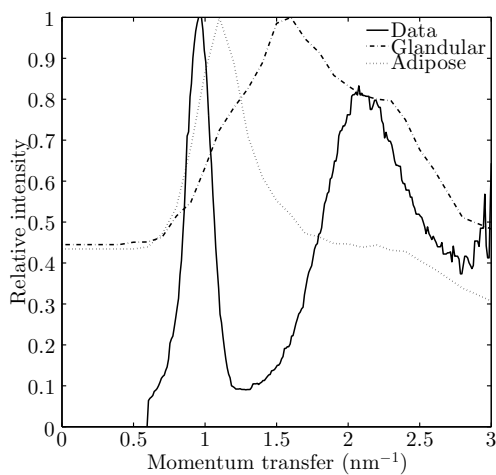
Figure 4.4.1: Obtained diffraction spectra.



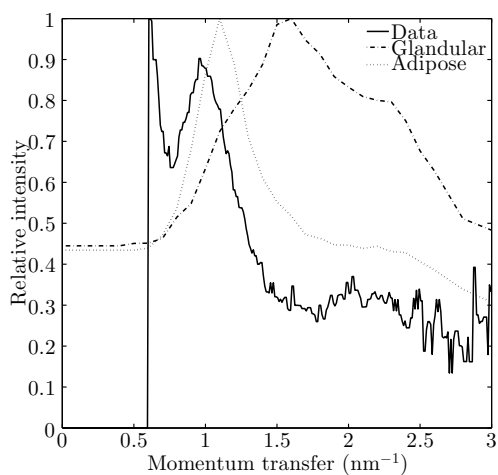
(a) Diffraction spectrum of Erlaton LFX.



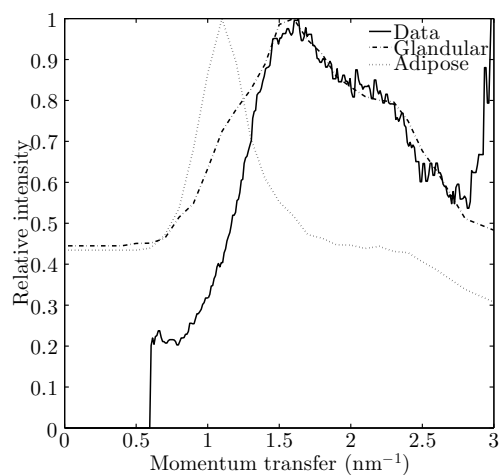
(b) Diffraction spectrum of Polymorph.



(c) Diffraction spectrum of PTFE.

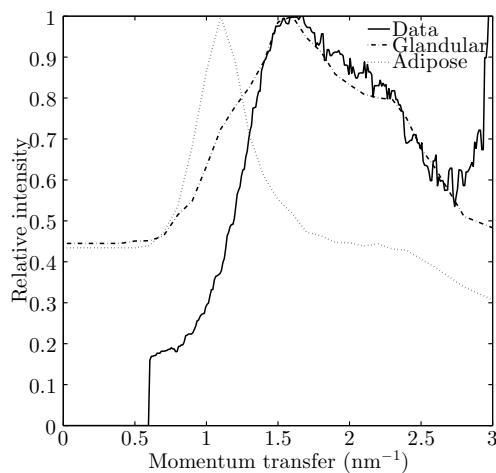


(d) Diffraction spectrum of polyester resin.

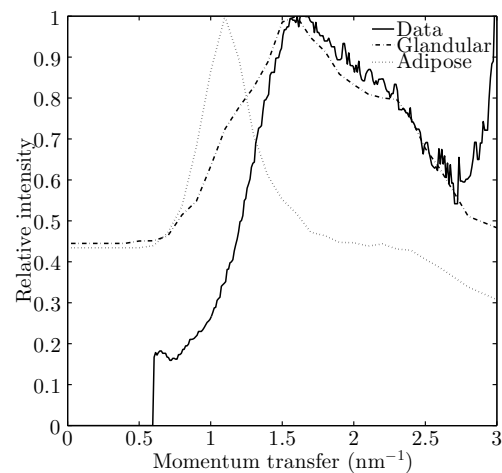


(e) Diffraction spectrum of Agar 10%.

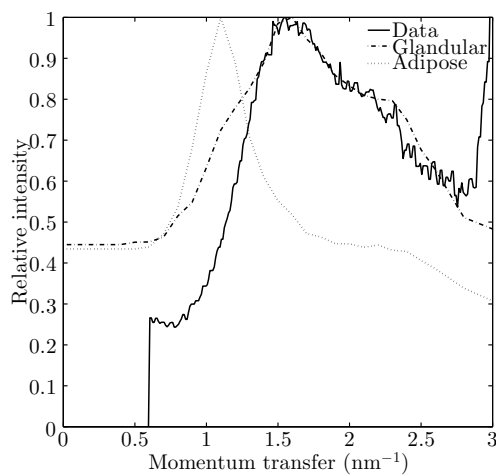
Figure 4.4.2: Obtained diffraction spectra for plastics and gels.



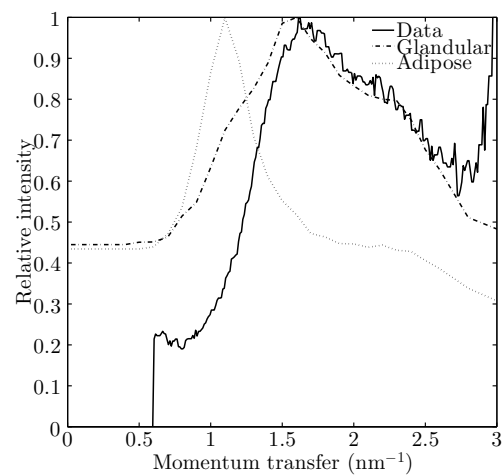
(a) Diffraction spectrum of Agar 5%



(b) Diffraction spectrum of Gelatine 10%.



(c) Diffraction spectrum of Gelatine 20%.



(d) Diffraction spectrum of Gelatine 5%.

Figure 4.4.3: Diffraction spectra obtained from the gel samples.

For each diffraction peak for each spectrum, the momentum transfer values corresponding to a diffraction peak and the corresponding momentum transfer value was found. In addition, a curve fitting function was utilised to find the FWHM of the diffraction peaks. This was conducted using a Gaussian curve fitting function in MATLAB. The FWHM of the curve was calculated using the

standard deviation of the Gaussian fit. The FWHM is commonly used within the literature to describe the width of the diffraction peaks, and therefore this value is used here, even though not all peaks appear Gaussian. The attenuation coefficient of each material in Table 4.4.1 is found for the energy of 17.44 keV, as this is the energy utilised by Poletti et al. (2002a) and can therefore be used as a reference value.

| Sample name      | Peak 1 position | Peak 2 position | FWHM 1     | FWHM 2     | Linear Att. |
|------------------|-----------------|-----------------|------------|------------|-------------|
| Caffeine         | 0.64±0.1        | 1.34±0.2        | 0.13± 0.01 | 0.36± 0.01 | 0.73        |
| Delrin           | 1.23±0.2        | -               | 0.36± 0.02 | -          | 0.81        |
| Ertralyte        | 0.96±0.2        | 1.32±0.1        | 0.43±0.03  | 0.60±0.01  | 0.77        |
| Lexan 9030       | 0.93±0.2        | -               | 0.49±0.02  | -          | 0.77        |
| Nylatron         | 1.18±0.2        | -               | 0.45± 0.03 | -          | 1.02        |
| Nylon GF30       | 1.25±0.2        | -               | 0.52±0.02  | -          | 0.9         |
| Nylon Oil filled | 1.14±0.2        | -               | 0.48±0.03  | -          | 0.68        |
| Polymorph        | 1.20±0.2        | -               | 0.45±0.03  | -          | 0.73        |
| PTFE             | 0.96±0.2        | 2.11±0.2        | 0.42±0.01  | 0.48±0.03  | 1.25        |
| Polyester resin  | 0.98±0.2        | -               | 0.63±0.03  | -          | 0.53        |
| Agar 5%          | 1.61±0.2        | -               | 1.04±0.02  | -          | 1.14        |
| Agar 9%          | 1.62 ±0.2       | -               | 1.00±0.02  | -          | 1.14        |
| Gelatine 5%      | 1.64±0.2        | -               | 1.02 ±0.03 | -          | 1.14        |
| Gelatine 9%      | 1.68±0.2        | -               | 0.91±0.03  | -          | 1.14        |
| Gelatine 17%     | 1.60±0.2        | -               | 1.08±0.03  | -          | 1.14        |

Table 4.4.1: Summary of peak positions and FWHM values.

The fitting errors have been taken into consideration in Table 4.4.1. This is based on the uncertainty in the curve fitting function, as provided by MATLAB. For samples with more than one diffraction peak, Peak 1 corresponds to the most intense peak, and Peak 2 corresponds to the second most intense peak observed in the spectra.

The gel type materials demonstrate a diffraction peak at approximately  $1.6 \text{ nm}^{-1}$ .

This is the case for Agar 1, Agar 2, and Gelatine samples 1-3, although there are variations seen in the measured values of less than the error in the fitting, therefore these can be approximated as the same values. A diffraction signal at  $1.6 \text{ nm}^{-1}$  is associated with glandular tissue and water. The gel is made with water which forms a semi-solid structure caused by aggregation of the gelatine. It is therefore not surprising that the diffraction pattern has a similar peak to water. The agar and gelatine are therefore possible materials to consider diffraction signals at  $1.6 \text{ nm}^{-1}$ , due to their water holding ability.

Table 4.4.2 shows the calculated properties for adipose and glandular tissue, to which the materials present here can be compared.

| Tissue                             | Adipose         | Glandular       |
|------------------------------------|-----------------|-----------------|
| Linear attenuation at 17.44 keV    | $0.66 \pm 0.2$  | $1.08 \pm 0.2$  |
| Peak position ( $\text{nm}^{-1}$ ) | $1.12 \pm 0.03$ | $1.59 \pm 0.03$ |
| FWHM                               | $0.39 \pm 0.05$ | $1.02 \pm 0.06$ |

Table 4.4.2: Data from Poletti et al. (2002a)

According to Joint Committee on Powder Diffraction Studies (JCPDS), caffeine has a diffraction signal corresponding to momentum transfer value of  $0.66 \text{ nm}^{-1}$ , which corresponds to a d-spacing of  $7.52 \text{ \AA}$  (JCPDS (1980)). There is also a diffraction peak expected at  $1.5 \text{ nm}^{-1}$ . Within experimental and fitting errors, the diffraction signal measured here is in agreement with that of JCPDS. In addition to this, the diffraction peak of PTFE is given as  $1.0 \text{ nm}^{-1}$ , which has been measured to be  $0.98 \text{ nm}^{-1}$  in this case, and is again in good agreement with JCPDS. For the plastics, the nylon type materials, including Nylatron, oil filled nylon and the glass filled nylon (Nylon GF30), all have similar peaks to pure nylon, which has been documented previously to be at  $1.2 \text{ nm}^{-1}$ . This is in agreement with the works of Poletti et al. (2002a), Alkhateeb et al. (2012) and

Kozorezov et al. (2005). Nylon is used as an equivalent material for adipose tissue and also has similar attenuation properties. Polyester resin, useful for moulding and shaping potential phantoms, has a diffraction peak at  $0.98 \text{ nm}^{-1}$ , which could be similar to that of adipose tissue.

The closest linear attenuation coefficient values to glandular tissue are the gel samples. This is not surprising as the gel samples have essentially been considered as water, although the samples themselves have different densities due to the variations in percentage weights of the components. In the case of adipose tissue, where the linear attenuation coefficient is quoted as  $0.66 \pm 0.2$ , the closest materials is the oil filled nylon (Errtalon LFX). The first peak of oil filled nylon has a quoted diffraction peak of  $1.14 \pm 0.2 \text{ nm}^{-1}$ , which is of great interest for the adipose signal. Therefore, based on the diffraction peak and the linear attenuation coefficient, this is of great consideration. However, the density of the adipose tissue is quoted as  $0.92 \pm 0.02 \text{ gcm}^{-3}$  in the study by Poletti et al. (2002a) and is given as  $0.95 \pm 0.02 \text{ gcm}^{-3}$  by the ICRU (ICRU (1989)). The density of oil filled nylon is approximately 20% greater.

The FWHM is presented here for reference should the same or similar system be used again with samples of this thickness. Due to the differences between the systems, no direct comparison is made with that of other works. However, in general terms the first peak of the adipose type tissues have a more definitive diffraction peak i.e. the FWHM is smaller. This is shown with samples including oil filled nylon, polyester resin and Delrin. Samples that have a broader diffraction peak more similar to that of glandular tissue also have a wider diffraction peak, which is in keeping with previously obtained observations between adipose and glandular tissue, including the works of Kidane et al. (1999).

## 4.5 Discussion

Polymorph resin is user friendly as it is designed for melting with water at temperatures of approximately 60 °C. It has demonstrated a diffraction peak at  $1.2 \text{ nm}^{-1}$ , similar to that of nylon as given within the literature. It is therefore a possibility for use in diffraction phantoms for equivalence to adipose tissue based on the diffraction peak position. Practically, polymorph resin is designed to be moulded and set into a desired shape by the user, therefore it would be of interest for use in diffraction phantoms.

Generally speaking the melting point of the thermoplastics is approximately 200 °C, making them practically difficult to use without the correct equipment and formation techniques if the plastics were to be reshaped into a shaped phantom, such as drape forming or vacuum forming, described in the Lexan datasheet (General Electric Company (1997)). This is practically difficult to perform and would have to be carefully done by any user, using industrial style equipment, which could be an expensive investment for phantom making.

Although the thermoplastics are designed to be melted and reset, such that their original state is the same, it would be necessary to consider the effects of heating and resetting the material with respect to their diffraction patterns and properties.

Agar and gelatine have both shown a broad diffraction peak at  $1.6 \text{ nm}^{-1}$ , which is considered to be due to the water content of the hydrophilic colloid. In terms of practical considerations, the formed semi-solid gels are not permanent. Due to gradual loss of water, the semi-solid structure loses its structure, becomes dry and can fracture. The grade of agar and gelatine utilised in this research is a culinary grade type. There are several types of agar that are utilised for cell cultures, as an example, which require that they remain in a solidified state for longer periods of time. It would therefore be possible to investigate other types

of agar for potential use in phantoms, as well as to explore the lifetimes of these different types of agar and gelatines. However, this does not limit these materials' usage in phantoms. The requirements of a phantom can vary depending on the study being considered and the reproducibility that is required. If the purpose of the study is to demonstrate a proof of concept for an imaging analysis method, or to test a system performance, then a temporary phantom might be sufficient. If the phantom is to be used repeatedly, then utilising a material with limited lifespan would not be sufficient. This would be for example, phantoms that are used for quality control purposes of an imaging system. For lab based research, it would be possible to set agar and gelatine in specific shape for a phantom design, especially in the circumstances where liquid water is not suitable.

The linear attenuation coefficient of the fixed agar or gelatine gels were assumed to be that of water, due to the dominant component being water, and that the constituents of the agar and gelatine were unknown. The transmission information could be measured using a monochromator system similarly to that performed by Poletti et al. (2002a). Other studies have used transmission imaging to correct diffraction data for attenuation effects, such as Cook (2008) and Griffiths et al. (2004). However it was not possible to do this with the system used, as it was not possible to adjust the system for transmission due to the fact the system was also used by other group members and would have to be realigned for diffraction, which would be time consuming and also interrupt the research of other group members. For the purpose of this research, as an initial investigation of agar and gelatine for diffraction studies, considering the samples as 100% water was considered as acceptable.

Relatively the cost of the materials is low. The plastics used were cheap for these investigations as they were samples, with three samples provided for £5. Larger amounts would cost more, and the amount required would depend on the size and shape of the desired phantom. For a biopsy sample phantom, where

the thickness of the samples is thin, the thicknesses of 3-5 mm obtained from the samples plastics obtained would be suitable.

Both the agar and the gelatine are cooking grade gelatine. Other suppliers such as Sigma Aldrich ([www.sigmaaldrich.com](http://www.sigmaaldrich.com)) also provide gelatine and agar, however these are standardised grades used for microbiology, for example. Procuring and obtaining materials where the constituents and components can be standardised would be useful to the reproduction and future testing of materials and use in any phantoms. Currently the cooking grade materials have helped to provide the evidence that the gelatine and agar can indeed be used in this way, but further work would have to be performed to formalise this further and to establish the best material for phantoms.

This study shows the possibility of using oil filled nylon as an equivalent material to adipose tissue, based on the peak position and the linear attenuation coefficient. Practically speaking, however, the melting point is 220 °C, making it potentially a difficult material to use without the aforementioned techniques such as drape forming and any required equipment.

## 4.6 Conclusions

The work in this Chapter has considered materials that have previously been investigated in the literature for tissue equivalence in diffraction studies for breast tissue, but in particular for phantom creation, discussing both their x-ray properties, such as their linear attenuation coefficient at the reference value of 17.44 keV, their chemical composition and their density values, as well as measuring diffraction profiles in an EDXRD system. The melting point was also considered in order to discuss their practical properties and possibilities for phantom creation. Nylon is a commonly used equivalent material, however there are variations of nylon materials, including glass-filled and oil filled types, which leads to some

variation in the melting point of the samples. When compared to adipose tissue, oil filled nylon in particular shows good promise in terms of the diffraction peak measured and the linear attenuation coefficient.

Other materials such as gels were also considered. Gels have not been considered in studies by Evans et al. (1991), Alkhateeb et al. (2012), Poletti et al. (2002b), and are the first to be performed, to the author's knowledge, in this context. Previous studies have been performed on gelatine to consider the collagen content, however the application of gelatine and agar in the context of breast tissue equivalent materials for x-ray diffraction phantoms has not been made previously. Here it has been shown that agar and gelatine diffraction profiles are similar to that of glandular tissue, and could therefore be a potential way to incorporate water within a phantom.

The work here begins the collation of a materials library that begins not only the discussion of the diffraction signatures of the materials, but also the practical properties for the development of future phantoms for breast tissue diffraction studies.

# Chapter 5

## Laser etched phantoms for EDXRD studies

### 5.1 Introduction

A phantom is a specifically defined object that can be use in an imaging system to evaluate a system, for development of analysis techniques, performance testing of a system and quality assurance. Phantoms can also be developed to represent a test object, such as an organ, that cannot be acquired easily, or such that tests can be performed before using real tissue. It is important that the phantom material behaves with equivalent attenuation, absorption and scattering properties

of the tissue of interest. When imaging real tissue, the true composition is not necessarily known unless a histopathological analysis has been conducted, as is performed in studies including Castro et al. (2004), Castro et al. (2005b), and Kidane et al. (1999). This requires the time and expertise of clinicians. For x-ray diffraction studies, it is necessary to know the origin of the signal to relate the analysis of diffraction to the true state of the tissue. In the case of phantoms, the input state to the system can be specifically created and known by the user.

Griffiths et al. (2004) utilised two phantoms for their study, one combining both thin tissues and PMMA, and the other utilising just PMMA. The first phantom was a PMMA phantom used to test the spatial resolution of the system. The phantom was formed of a 3 cm block of PMMA composed of three 1 cm slabs. Within these slabs holes of range 1 mm to 8 mm were drilled. This phantom is not designed to be anthropomorphic, but was used in the study to create images as a means of testing the spatial resolution of the system in a methodical way. The researchers used drilling bits and a drill stand to create the phantom. The tissues used in this study were unfixed and needed to be contained for imaging purposes. The materials used include PMMA, an easily procured and cheap material commonly used in diffraction studies. The real tissues were of the order 1.5 cm thick. These were then packed within slabs of 1 cm of PMMA and 1.5 cm of low density packing. This 4 cm thick phantom was itself contained in a thin walled air-tight PMMA container. This phantom was then used in the system to represent a tumour within healthy breast tissue.

Other phantoms used in diffraction studies include in the work of Bohndiek et al. (2009). Two test objects of 6 mm thick were created to match the thickness of the samples being investigated in the study, one to investigate the resolution of the system and one to investigate the contrast of the system. For the 'resolution' phantom, the test object was created using a polyethylene background material, with inserts of PMMA discs and blocks of varying sizes. The 'contrast' object

used PMMA as a background material and had inserts of other materials, such as polytetrafluoroethylene (PTFE), polyethylene (PE), polypropylene (PP), and polyvinylchloride (PVC). In addition, test samples were made from mixtures of pork fat (lard) and chicken, to simulate adipose and fibrous tissue.

Although not strictly phantoms, Alkhateeb et al. (2012) combined different materials in order to investigate which materials can be used to recreate the contrast measured from previous studies using breast tissue. The combination of materials could be used in the future for phantom development to find the combination of materials desired for the phantom in terms of contrast e.g. between malignant and benign tissues.

As previously stated, there is not currently a defined and accepted method of analysis for x-ray diffraction studies and breast tissue. This is demonstrated by the fact that several papers utilise differing analysis methods for their studies, and within each study these vary. There is no standardised method of post-analysis although utilising the intensity of the momentum transfer values of interest is typically used. Previous works on diffraction systems have shown a series of successful results utilising different analysis methods, both in ADXRD and EDXRD systems when applied to breast tissue imaging. Multivariate Analysis of Variance (MANOVA) statistics has been used to characterise breast tissue as normal (adipose and fibroglandular), benign and malignant for 106 samples by Conceição et al. (2011). When compared to histopathological classification, it was possible to classify correctly 91.5% of the samples with 98.5% sensitivity, and 89% specificity. Ryan and Farquharson (2007a) used both EDXRD measurements of breast tissue and electron density measurements using the  $K_{\alpha_2}$  line of tungsten at 57.96 keV and the detector at  $30^\circ$ , to be able to resolve both Compton and coherent scatter peaks, using an acquisition time of four hours. The attenuation of the samples were based on the transmission signal of the samples, with the HpGe detector used in their study placed at 0 degrees. Within their study they

perform analysis using soft independent modelling of class analogies (SIMCA) (Esbensen et al. (2002)). As described by the authors, this technique creates a principle component analysis (PCA) model for each tissue type using a training set of tissues. SIMCA is then used to combine each of these PCA models into one classification model. Their best MVA model is able to correctly classify 6 out of 11 malignant samples correctly, with 54% sensitivity and 100% specificity.

Work conducted by Emily Cook in her Phd thesis (Cook (2008)) performed breast imaging of 6 samples in a lab based environment using a HPGE detector. During post analysis, windows of momentum transfer were considered and explored to establish the greatest contrast between the tumorous and healthy tissues. These were found to be  $1.04\text{--}1.10\text{ nm}^{-1}$  and  $1.84\text{--}1.90\text{ nm}^{-1}$ . However, performed on such a small number of samples more would need to be investigated further to provide a realistic lab based system that has high sensitivity and specificity when identifying cancerous cells in breast biopsy samples.

In addition to the peak positions utilised by works such as Griffiths et al. (2008), Castro et al. (2004), Kidane et al. (1999), and Evans et al. (1991), the peak area was used in works by Ryan and Farquharson (2007a) and Theodorakou and Farquharson (2009), the full width half maximum of the peak was used by Poletti et al. (2004) and Elshemey et al. (2010), and the ratio of peaks heights, was utilised by Royle and Speller (1995) and Elshemey et al. (2010). There are several different parameters that can be used to quantify the diffraction signals obtained, and these vary from study to study.

Research conducted by several workers investigate the use of 3D printers for breast imaging phantoms using x-ray imaging modalities, including mammography and CT. Carton (2010) were able to simulate patient anatomy using an existing computer model of the breast to generate breast voxel phantoms. They are able to vary the size, shape, amount of glandular tissue, and skin in their model. In order to create the phantom they used a single tissue equivalent ma-

terial suitable for each part of the virtual phantom and then stacked the created sections to create the full 3D phantom. This technique is therefore in parts, as it requires multiple printing sessions, and also various printing materials. However, the final structures are still related to the virtual model. The final phantom was used in digital mammography and digital breast tomosynthesis systems. Kiarashi et al. (2013) discusses the importance of having a ground truth phantom for works such as virtual clinical trials and highlights the lack of anthropomorphic 3D physical phantoms commercially available for such purposes. Using real breast tissue data from segmented patient dedicated breast computed tomography data, they were able to import the data into their 3D printer software. In their study they use a high resolution printer, capable of printing with multiple materials. This is relevant for being able to utilise more than one material and obtaining contrast within an image using the phantom. As stated in their study, glandular tissue and skin were presented by the most radiographically dense photopolymer available to the printer, mimicking a 75% glandular tissue. Adipose tissue was presented by the least radiographically dense photopolymer. In order to establish equivalence, they compared x-ray images of samples of the available polymers available for use in the printer with those of breast tissue-equivalent materials. In both pieces of work, the process for creating the 3D printed phantom is not continuous, and multiple polymer materials suitable for 3D printing have to be found to suitably recreate the virtual phantom in physical form.

Nolte et al. (2014) is a study which continues from the previous works of Kiarashi et al. (2013). The principle of these phantoms is to 3D print the glandular tissue and infill the adipose tissue with a tissue equivalent material. They define two phantoms, namely the singlet and the doublet. The singlet phantom contains one material to mimic a 4.5 cm compressed 28% dense breast and is printed in a 75% glandular equivalent material, into 3 slabs of 1.5 cm each. The doublet phantom uses two photopolymers to represent glandular and adi-

pose tissues with the greatest physical contrast available, mimicking 75% and 35% glandular tissue. Within the study they modify the filler material of the singlet phantom, which represents adipose tissue. Previously vegetable oil had been used as the adipose equivalent material, but taking into account the practical handling of the material and to achieve better contrast, they investigate other possible materials including beeswax. The vegetable oil was considered to be user unfriendly when used in the phantom.

These phantoms, although 3D printed require an element of ingenuity to combine both the glandular tissue and the adipose tissue. The practicalities of the chosen infilling material also have to be considered in addition to their suitability of imaging in terms of the image contrast, attenuation coefficients and density in comparison to adipose tissue.

Laser cutters have previously been used for phantom creation, although not in the context of x-ray diffraction and breast tissue biopsy samples, to the author's knowledge. They are also geometric phantoms, focussing on the geometrical considerations of radiography systems rather than being used for testing images for x-ray diffraction systems. Laser cutting is not a new nor novel technique, as the systems are commonly used for creating displays in the graphics industry.

The works of Mango (2011) utilise a laser cut phantom as part of the investigation in non-destructive technology, particularly in the military and government defence fields where radiography techniques are used. This paper describes a phantom and an automated method for the quality assurance (QA) of digital imaging systems, providing a simple and quick way to quantitatively measure the key characteristics of storage phosphor-based computed radiography (CR) imaging systems and direct-digital, flat-panel, detector-based direct radiography (DR) imaging systems. The phantom itself is created using a patented method using a combination of stamped and laser-cut apertures in a metal absorber. The phantom can be used to measure a Module Transfer Function (MTF) of an

imaging system due to the sharp edges and the design of the phantom, which is created using graphics software translated into the metal. This is an example of a geometric phantom used for characterising imaging properties of radiography systems. However, their technique requires metal, which is not used as a breast tissue equivalent material, and is generic in its application.

A second paper that utilises a laser cutter system in a phantom is the work of Cardoso de Moura et al. (2008). In this case the phantom is made of stainless steel, and small squares of 20 mm×20 mm are laser cut into the phantom. The laser cutter is used to obtain sharp geometrical edges on the test object. Both works use the laser cutter as a tool to create geometric phantoms for imaging evaluation. No characterisation of the laser cutter performance, the settings used and a discussion of depth is provided in these papers.

Patents also exist for the use of lasers to create cut lines within phantoms. This is part of a wider phantom creation technique or general system. Such patents include the those of Goodenough and Levy (1992) and Moore and Smith (1991). In the case of Moore and Smith (1991), the patent includes details of a generic 'simulation/generation/verification' system for blocker patterns and blockers for use in radiotherapy. The principle invention of the patent is 'A system for generating radiation blockers, said system including a fluoroscopic simulator for generating a fluoroscopic image of a patient and comprising: cutter means; computer means for digitized processing of said image and control of said system, said computer means including image grabbing means for grabbing and processing said fluoroscopic image to convert said fluoroscopic image to a computer-handleable image to further process said image and, to generate cutter control signals means for delivering said cutter control'. Part of the patent is to utilise the laser cutter to achieve this.

Within Goodenough and Levy (1992) the principle invention is to create 'A test body for determining an operating characteristic of an image reconstructing

apparatus, wherein said test body includes at least one test element for testing the resolution of the apparatus, the test element comprising direction of scoring line pairs, said line pairs being of predetermined width, wherein the number of line pairs per unit length varies in the direction of scoring from about twelve line pairs per centimeter to about twenty line pairs per centimeter.’ As part of their proposal, ‘laser technology’ is to be used as a means of creating the line pairs within the a plastic test object. No specific application or reconstruction apparatus is stated, although Magnetic Resonance Imaging (MRI) and CT are mentioned in the description.

## 5.2 Objectives

In order to be able to help develop a diffraction system for future investigations and for future potential clinical system development, this Chapter aims to propose a method for developing a diffraction breast tissue biopsy phantom. The aim of this is to provide a means of creating a ‘ground truth’ phantom for use in a diffraction study. A ground truth phantom would enable EDXRD researchers to have a sample that would always act as a reference for post-analysis investigations. Establishing an ideal post analysis technique, or creating a test object that could be used in different systems, allows for some standardisation between different research works. However, this work also seeks to provide a technique that can be tailored to an individual study. A phantom that relates an input image to the created hardware would allow for the tailoring of features to be explored in a diffraction system, for example different images of different features, e.g. infiltrating ductal carcinoma or benign. Such a phantom could provide the flexibility for individuals to optimise and explore the parameters of their systems (detector, geometry, post-analysis technique), that would be ideal for the system they are investigating.

To this end, a phantom designed to replicate a biopsy sample will be developed, using an already established material used for tissue equivalence in EDXRD and ADXRD. The laser system used in this Chapter was available due to its presence in the Makespace in UCL. PMMA is an equivalent material for EDXRD and ADXRD studies and is also a recommended material for use in the laser system and features in the materials library of the laser system as a standard material. In order to use the laser system, one hour slots had to be booked. Other methods were available, such as 3D printing and mould making e.g. using silicon. Mould making was not considered due to time constraints. Access to the 3D printers was more difficult than the laser system due to the fact that users could set printing works that could take several hours at least, whereas with the laser system all users were limited to hourly slots only, thereby making it necessary to finish ones project during the allocated time slot of one hour. Prior to use, the plastics in the 3D printers would have to be tested to check their suitability for their use in diffraction. The plastic filaments used in the available 3D printers at the time were acrylonitrile butadiene styrene (ABS) and polylactic acid (PLA) which are both thermal plastics

In order to achieve a relationship between the input image, the created phantom and the laser system settings, a method to characterise the phantoms based on the laser system needs to be developed and the effects of using different settings on the created physical phantoms considered. The phantoms need to be evaluated in a diffraction system both with and without a contrasting material to PMMA to act as a secondary tissue type. This would allow for the exploration of the phantom's use for diffraction studies using post-analysis techniques used by previous researchers, such as contrast analysis, creating images using intensity values at momentum transfer values of interest, and creating images using relative intensity values.

The work in this Chapter will be separated into two parts: creating the phan-

toms and the use of the phantoms in the diffraction system.

## 5.3 Laser system

### 5.3.1 Details of the VLS CO<sub>2</sub> Laser system

The laser system used for this research is the VLS 4.60 Universal Laser System (Universal Laser Systems Inc, Arizona, USA). It utilises an OEM (original equipment manufacturer) ULR CO<sub>2</sub> Laser with wavelength of 10.6  $\mu\text{m}$ , with gain medium of carbon dioxide (CO<sub>2</sub>). The stimulated emission is caused by radio frequency (RF) electromagnetic radiation. The information presented here is based on the information provided by the VLS platform user guide, revised in August 2012 (Universal Laser Systems Inc (2012)), as well as the integration manual of the OEM ULR CO<sub>2</sub> LASER used in the system itself (Universal Laser Systems Inc (2010)).

The laser system utilises a laser in a manner similar to how a conventional computer printer would use ink. In conventional computer printers the input images, which can contain continuous tonality, are converted to a series of dots. Mechanically these dots are translated to the order of 50 to 60  $\mu\text{m}$  and are applied onto the paper to build up the printed image. In terms of the laser system, dithering is the process in which the image (colour or greyscale) is converted to a black and white image using a filter, while preserving the illusion of shades of grey by varying the distribution of the dots (pixels) in the image, as shown in Figure 5.3.1. The denser the dots, the darker the image, and conversely the sparser the dots, the lighter the image. The user interface allows for the dither pattern to be selected; half-toning, error diffusion and black and white mode. Only half-toning is used in this work and other options were not considered. The halftone dither pattern applies a 45 degree line screen using a line-type filter to

a colour or greyscale image and converts it to black and white. For low density images, the line screen is coarser when compared to high density images which are finer.

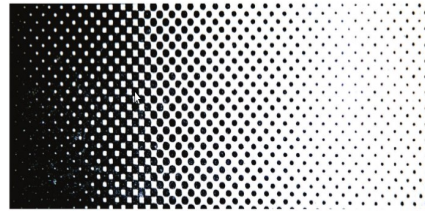


Figure 5.3.1: Demonstration of the halftone dithering.

For a laser system, the laser is designed to pulse at a certain rate, often expressed in pulses per inch. As the laser is scanned across the material it locally vaporises the material with each pulse, effectively printing the image into the material using the previously described image conversion methods. This achieves different depths within the material. The dithering process in this case translates the input image to the laser such that different depths within the material are created, giving the image etched into the material depth and tone.

To translate the image from the software to the material, the laser system can operate in two modes; raster mode or vector mode. The laser system is able to perform three functions; to score, to etch, or to cut into the material. The system interprets what is required by relating the colours of the image to the required functions, which is predefined in the software of the system. These modes are summarised in Table 5.3.1. For the system used for this work, pure red was interpreted as cutting the material, pure blue was interpreted as scoring the material, and black was interpreted as etching the material. All colours are represented by the RGB colour system.

In the raster mode, 2D images are etched into the material using a pattern

| Function | Colour | Mode   |
|----------|--------|--------|
| Cut      | Red    | Vector |
| Score    | Blue   | Vector |
| Etch     | Black  | Raster |

Table 5.3.1: Colour functionality in the laser system software.

of dots. When in vector mode the laser follows a two-dimensional path to cut the shape into the material. If all colours, red, blue and black are present in the image, the laser system will perform both by switching between the two. If no vector lines are present, all elements of the graphic are instead interpreted as raster objects which will utilise the vast job settings with a greyscale dithering pattern. When greyscale images are used in the system, the dithering pattern is applied such that it is mapped to the settings associated with black power and speed settings. These power and speed setting variations help to achieve the variations in depths within the material. The dithering process affects the way the image is translated to the material and it is the mapping of the greyscales to speed and power settings that achieve the variation in depth within the phantom.

### 5.3.2 Laser system settings

The laser cutting system has a laser cartridge mounted on a motorised translation system that is able to move the laser across the scanning area. The motion of the laser is determined by settings that are defined by the system, using pre-settings optimised for materials in its material library (such as plastics and woods), or they can be manually adjusted by the user. The motion settings are different depending on the required function. The power setting can be varied from 0 to 100% and allows the user to select the laser power level. This power percentage determines the duty cycle of each laser pulse in the job. Adjusting the power

setting is completed by pulse width modulation which modifies the width (and therefore the duration) of the RF signal. The duty cycle during the pulsing of the laser is the proportion of time that the laser is on, as opposed to off. For a 100% cycle, the duty cycle is 100% and is obtained by modulating the pulse width. As given in Eqn. 5.3.1, the duty cycle  $D_c$  is the ratio of the time  $T_l$  the laser is on compared to the total period,  $P$  of the signal.

$$D_c = \frac{T_l}{P} \quad (5.3.1)$$

The speed setting allows the user to choose values between 0 to 100% and is associated with the maximum rate of travel of the motion system. For vector motion this setting determines the maximum rate of travel of the motion system. If the speed setting for the system is not appropriate, based on the other variables that influence the engraving time, the speed setting is adjusted automatically by the system. The maximum speed setting for the vector motion is that of the raster motion. The scanning is driven by two motion carriages, for both the horizontal ( $x$ -axis) and vertical ( $y$ -axis) directions of the image plane. The rastering is done with the  $x$ -axis focus carriage of the laser system. It has a higher acceleration and top speed compared to the  $y$ -axis due to its lighter weight. In absolute terms, this leads to the maximum speed for vector processing equalling one third to one half of the raster speed, which utilises both motion carriages. The pulses per inch of the pulse frequency for the laser stream, corresponds to the laser pulses per linear inch (PPI). The PPI is electronically linked to the motion and the laser will always pulse in equal spacings regardless of the changes in the motion speed. For this work, a PPI value of 500 was used as it was the recommended value from the materials database. However, the manual settings for the speed and power were changed. The actual engraving time is dependent on this speed setting input by the user but is also dependent on the image being placed and the intricacy of the image detail. The speed and power settings determine the

time and energy deposited at a location on the object and therefore how much material is removed.

## 5.4 Classification of the laser system

The laser system in this research is used in raster mode and with greyscale images to represent the intensity values in a mammography image. The laser is able to etch into the material, but the total etch depth associated with a greyscale value is unknown.

This work investigates the relationship between the greyscale values to be sent to the laser system and the output etch depths (thickness of material removed) of the physical phantom. The following experiment aims to characterise the settings of the laser system used for PMMA, and relate the greyscale values to the total thickness of the remaining material. This would not only detail the relationship between the greyscale values and the etch depth, but can relate the software input to the physical phantom developed.

The greyscale values used fall within the range of 0–255, corresponding in scale from pure white (255) to pure black (0), using 8-bit representation. Areas of pure white are not etched, but all other greyscale areas are, but never exceeding the material thickness, as shown in Figure 5.4.1



Figure 5.4.1: Etching scale. The etch depth depends on several variables including the speed and power settings of the laser system.

Transmission imaging is based on the transmission properties of the sample, with the intensity image obtained being sensitive to the changes in the material thickness. Based on the Beer–Lambert law, the number of transmitted photons is dependent on the attenuation of the sample, which is itself dependent on the energy of the photons. It should therefore be possible to recreate the original image used to create the phantom using transmission. Although primarily designed for diffraction purposes, it is simple to characterise the phantom using transmission, as only the attenuation properties are being considered. Several studies also use transmission images to provide attenuation correction to their diffraction data, and also to establish regions of interest for which a diffraction scan is performed, such is the case for works including Griffiths et al. (2004), Darambara (2004), Ryan and Farquharson (2007a), Griffiths et al. (2008), Bohndiek et al. (2009) and Pani et al. (2010). Transmission information is useful information to obtain in diffraction studies and is commonly used.

## 5.5 Method for the calibration of the phantoms

For this experiment, the laser system settings were set such that the power used was 100%. The PMMA material was 6.5 mm thick and the thickness setting for the laser system GUI was always set to this value. The image density was kept at the default value of 500 pixels per inch to reduce any risk of melting or burning of the materials. The dithering pattern for the laser system was set to half-toning and the maximum speed setting for raster scanning is a variable.

Table 5.5.1 details the speed settings combinations used for the experiment. Those that have two speed settings had the laser system etch once at the first setting, the material left in place on the laser cutting bed, and then the laser system set to etch at the second speed. For example, etching with 10% and then 20% means that the first laser etching is conducted at speed setting of 10% and the second at 20% with all other settings kept the same.

| Setting | First etch speed % | Second etch speed % |
|---------|--------------------|---------------------|
| 1       | 20                 | 20                  |
| 2       | 10                 | 20                  |
| 3       | 15                 | 15                  |
| 4       | 5                  | -                   |
| 5       | 10                 | -                   |

Table 5.5.1: Speed combinations used for etching into 6.5 mm thick PMMA

To demonstrate and calibrate the etch depth variation with greyscale value, and to establish the speed setting response of the laser, a speed-calibration phantom was designed, as shown in Figure 5.5.1. Blocks of greyscale values were varied from 0 to 240 in steps of 16 (0,16,32,64...) with pure white spacings in-between. These were then etched into the 6.5 mm thick PMMA piece, creating 16 unique greyscale valued blocks. Etching was completed using all of the speed settings

previously described in Table 5.5.1.



Figure 5.5.1: The input vectorised image (l) consisting of varying greyscale blocks and the resulting etched PMMA piece with different speed settings (r).

The phantoms were imaged in a research transmission system comprising of a molybdenum micro focal source (X-tek, Tring, U.K.) with external filtration of  $30\mu\text{m}$  Molybdenum and using a wafer scale Complementary Metal–Oxide–Semiconductor (CMOS) Active Pixel Sensors (APS) detector consisting of Dynamically range Adjustable Medical Imaging Technology (DynaMITe)(Esposito et al. (2011)). Recently developed in the U.K, the detector has been specifically designed for ADXRD and conventional x-ray images in one image system (Konstantinidis et al. (2012)). For the purpose of establishing a relationship between the speed of the laser system and the etch depth of the phantoms, the system is used as a transmission imaging system only. The pixel size of the system is  $50\mu\text{m}$ . The system is ideal for characterisation of the phantoms, as the molybdenum target is used often in transmission imaging systems and the sensor area allows for images of the whole phantom to be acquired in one acquisition. Figure 5.5.2 demonstrates a schematic of the experiment set-up.

The phantom was placed at a distance of 1.6 cm from the sensor, which was itself placed 25 cm away from the x-ray source. For an integration time of 1 s for each image acquired, 100 dark corrected images were taken at 18, 20, 22,

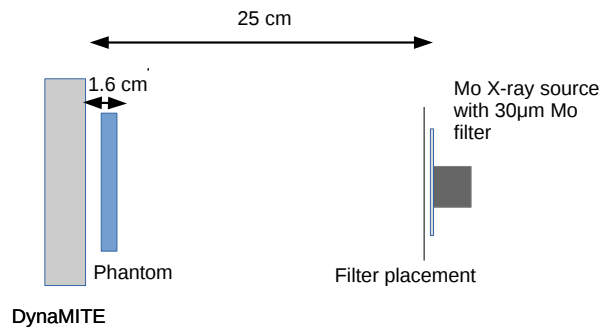


Figure 5.5.2: Schematic of the system used for establishing response functions for the laser system.

24 and 26 kVp tube setting and a fixed tube current of 0.18 mA. A total of 100 dark corrected flat images were also obtained at all energies and the calibration phantom was imaged at the same energies.

Based on the molybdenum target, the filtration and the mean energies of the x-ray source, it is possible to use prediction software to predict the molybdenum spectrum and the mean energy of the target. Using the prediction software from Siemens (Siemens AG, Germany) for molybdenum targets, the mean energies, summarised in Table 5.5.2 for the system were calculated.

| kVp | Mean photon energy (keV) |
|-----|--------------------------|
| 18  | 13.34                    |
| 20  | 14.38                    |
| 22  | 15.18                    |
| 24  | 15.76                    |
| 26  | 16.28                    |

Table 5.5.2: Mean energy values of the spectra using a Mo target

## 5.6 Method for establishing the intensity–PMMA thickness relationship

Utilising the same experimental set-up as Figure 5.5.2, images with no phantom present were obtained with incrementally increasing external filtration of PMMA applied to the system, in values of 1.2 mm from 0–7.2 mm, to cover the range of thickness of PMMA used for the phantoms. A total of 100 dark corrected images were obtained for each filter using 0–7.2 mm thickness of external PMMA filtration to determine the intensity associated with thickness of PMMA. This was repeated for maximum tube settings of 18 kVp to 26 kVp and with 0.18 mA current.

## 5.7 Analysis

All 100 images for each acquisition were averaged to remove statistical noise from the data, and were flat and dark field corrected to take into consideration the x-ray source variation and detector gain. All code for data processing was developed by the author.

An example of the average flat field image (0 mm PMMA filtration) at 22 kVp tube setting is shown in Figure 5.7.1. The image was processed to reduce the temporal noise and was dark field corrected.

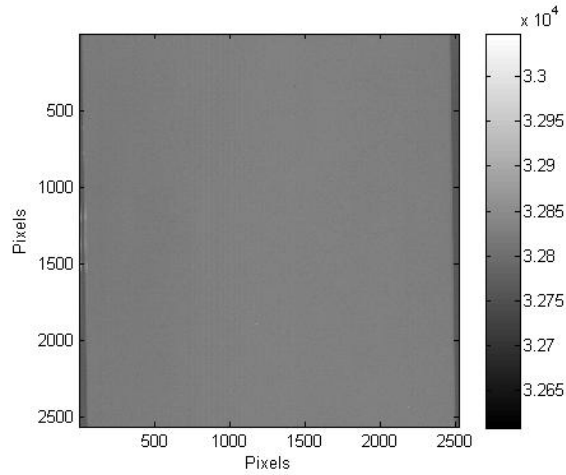


Figure 5.7.1: Flat field image at 22 kVp tube setting and no external PMMA filtration. The intensity values are shown in the colourbar.

From the filtered images a region of interest measuring 2000 pixels by 1400 pixels (equivalent to 10 cm by 7 cm) was defined and the average normalised intensity values were obtained for each combination of filters and energy. Normalised intensity was then plotted against the thickness of PMMA for each tube setting (kvp) utilised in each experiment. The mean energy of the x-ray source for each kvp setting used changes, depending on the kvp value. This has been demonstrated in Table 5.5.2. Therefore, based on the change of distribution of the spectrum, it would be expected that the attenuation of the beam through varying filters of PMMA would change, as the photon energies also vary. For multiple energies, the total number of photons,  $I_N$ , transmitted through the PMMA filters with thickness  $t$  depends on the number of photons incident with energy  $E_\gamma$  and the attenuation  $\mu(E_\gamma)$  such that

$$I_N = \sum I(E_\gamma)e^{-\mu(E_\gamma)t} \quad (5.7.1)$$

Figure 5.7.2 shows the different response functions for the different maximum x-ray source potential settings. These response functions relate the photon energies within the utilised spectrum and the attenuation due to the PMMA filters.

For each tube setting, i.e. spectrum used in the experiment, a curve of best fit was found for each relationship. This was found to be a sum of two exponentials for each case. Therefore a relationship between the normalised intensity and the filtration of PMMA has been obtained for each tube setting used in the experiment.

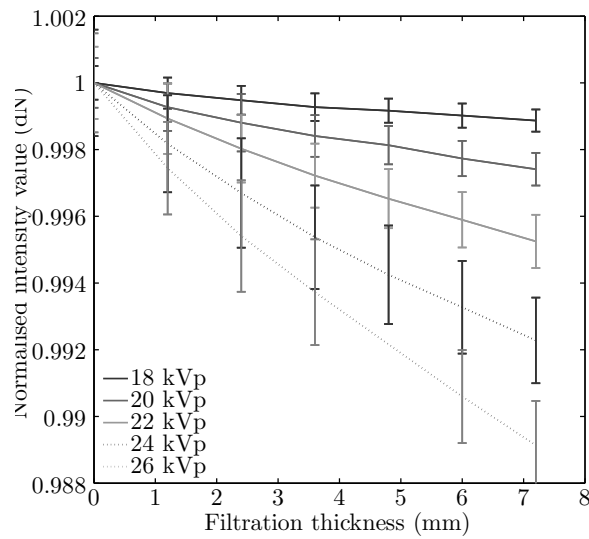


Figure 5.7.2: Normalised intensity (digital number (dN)) filter response functions at different maximum tube settings.

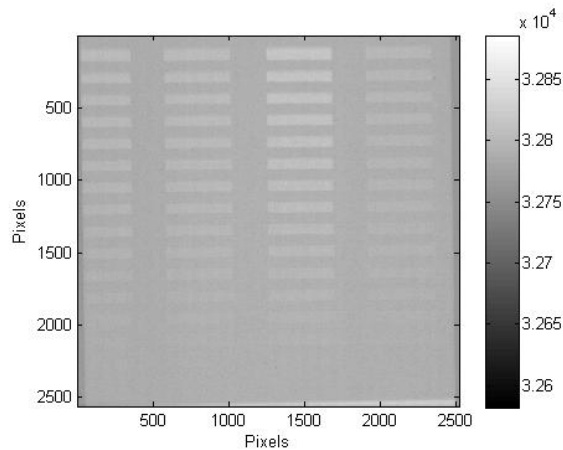


Figure 5.7.3: Speed calibration phantom. Image obtained at 18 kVp tube setting. The colourbar shows the intensity values.

For the depth speed phantoms, an example of which is shown in Figure 5.7.3, a region of interest was defined for all greyscale value blocks with size 200 pixels by 40 pixels (10 mm by 2 mm). The average intensity was found for each greyscale block and then normalised to the maximum. This process was repeated for all of the maximum tube settings that were used, and a curve of best fit for each was obtained using the MATLAB curve fitting toolbox. This then provided a relationship between the normalised intensity of the transmission images with the greyscale value used in the calibration phantom and for each of the tube settings used in the experiments. It is now possible to establish a relationship between the PMMA thickness, the normalised intensity and therefore the greyscale value used in the laser system. The curves of best fit found for the intensity–filter data, having been previously found, were then interpolated using the `interp1` function in MATLAB to find, for a depth of choice, the expected normalised intensity. The corresponding greyscale value associated with the intensity was then found from the calibration data. Using the interpolated response function of the intensity–filters data, the intensities of the greyscale phantoms were obtained and the associated thickness of PMMA recorded.

The speed–greyscale value response function for the laser system is independent of the tube kilovolt potential used, and therefore the average response function was found from all energies, as shown in Figure 5.7.4. The average response curve is obtained by averaging the response curves found for the 18 kVp–26 kVp beam settings. These will be referred to as the speed setting response curves  $F_{sp}(g)$ ,  $F_{sp}$  is the response curve for a speed setting, sp, and  $g$  is the greyscale value. The speed settings response curves are therefore a function of the greyscale value, as has been shown in these results.

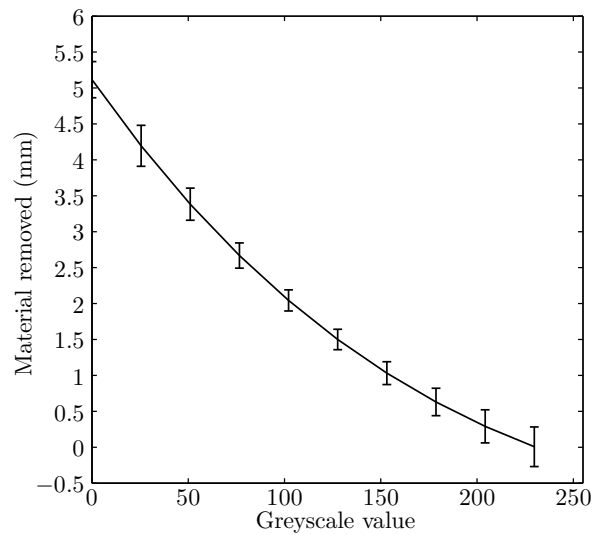


Figure 5.7.4: The final averaged response curve obtained for etching speed of 5%.

For each laser speed combination the process was repeated with the final obtained etch depth greyscale response curves determined for each speed setting combination, as shown in Figure 5.7.5.

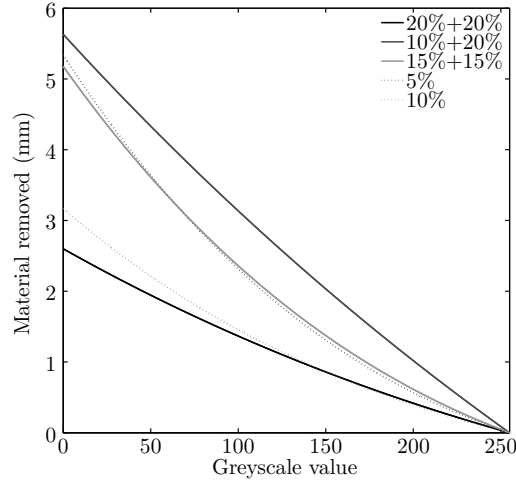


Figure 5.7.5: Speed setting response of the laser system to the input greyscale values. The speed settings combinations are tabulated in Table 5.5.1

As a reference, the maximum etch depth for each setting is summarised in Table 5.7.1. It can be seen that the maximum etch depth is obtained with the 5% speed setting. This is to be expected as the laser will pulse in the localised area more due to the slow motion of the laser system. Therefore there is more vaporisation of the PMMA material in this area.

| Speed settings (%) | Maximum etch (mm) |
|--------------------|-------------------|
| 20 and 20          | $3.2 \pm 0.2$     |
| 10 and 20          | $5.4 \pm 0.2$     |
| 15 and 15          | $5.1 \pm 0.2$     |
| 5                  | $5.6 \pm 0.2$     |
| 10                 | $2.6 \pm 0.2$     |

Table 5.7.1: Details of the speed settings used and the corresponding maximum etch depth.

For each speed setting the function,  $F_{sp}(g)$ , between the etch depth and the

greyscale has been found analytically using the curve fitting tool box in MATLAB. The change of etch depth with respect to the greyscale value can be calculated analytically from the function  $F_{sp}(g)$ , as in Equation 5.7.2

$$\frac{dF_{sp}(g)}{dg} \quad (5.7.2)$$

The analytical gradient curves of the greyscale–depth response functions were obtained to show the change in etch depth per greyscale value, as shown in Figure 5.7.6 for each of the speed settings.

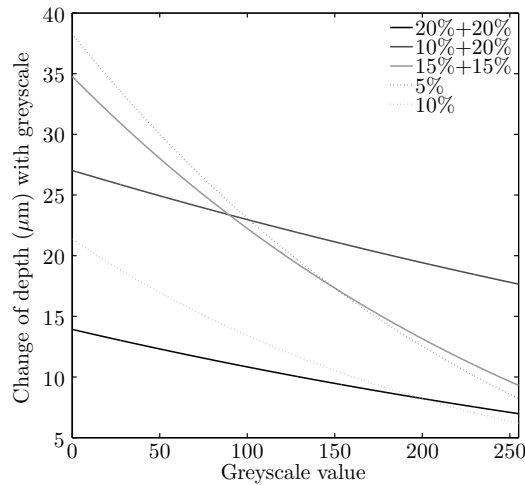


Figure 5.7.6: Change in the etch depth of the phantom with greyscale values. The changes can represent the changes in the presence of healthy and non-healthy tissues.

## 5.8 Discussion

The presented laser etched phantoms offer the opportunity to quantify the depth variations of the input image based on a greyscale image, such that there is a direct relationship between the input image of the phantom and the physical phantom. The calibration laser etched phantom was designed by the author,

and in itself is essentially a geometric phantom that can be used to characterise other laser etched phantoms from different laser etched systems, or laser etched phantoms that use different speed settings for creation of the phantom. Also developed within this Chapter is a method for quantifying and characterising the produced phantoms has been presented using transmission imaging, a commonly used modality in addition to x-ray scatter. The transmission information utilised in diffraction studies includes determining attenuation correction factors of the diffraction data, identifying regions of interest, as well as comparing the contrast between the two types of information obtained, coherent scatter and transmission. Utilising the input greyscale image enables the recreation of the input image in a transmission system. This is significant as it shows that the phantom is capable of being used to reproduce realistic images, based on patient data. This is a desirable feature for a phantom being used in x-ray diffraction studies.

The results have shown that varying the laser system speed setting when in etching mode leads to different achievable etch depths with various intensity–etch depth speed responses for different speed settings. Ultimately a function between the intensity images and the greyscale values were found for each speed setting, referred to as  $F_{sp}(g)$ . The power setting of the laser was always set to 100% so that the speed setting was the variable within the experiment. The speed settings of 5%, 10% and combinations of 10%, 15% and 20% lead to different etch depths. The minimum etch depth achieved by the speed settings utilised in this study was  $2.6 \pm 0.2$  mm, corresponding to a speed setting of 10%. The greatest etch depth achieved was  $5.6 \pm 0.2$  mm, corresponding to the speed setting of 5%. As expected, the slower the speed of the laser carriage, the greater the etching. This is based on the fact that the laser remains in one location for longer, and therefore pulse in the same position, ablating more material.

This work has shown it would be possible to tailor a phantom by utilising different laser speed settings and greyscale values during the etching process,

based on the image intensities. The testing of sensitivity of a system would depend on the thickness range of interest and also the changes in the tumour shape. The differential of  $F_{sp}(g)$  determines the changes in etch depth with greyscale value. Within a diffraction study, it would therefore be possible to quantify and relate the amount of PMMA to the diffraction signal, but also with knowledge of how the tumour depth within healthy tissue (the PMMA) changes. The current change of depth with greyscale are of the order of micrometers. Diffraction system sensitivity could be explored using such a phantom. The phantoms can therefore be characterised prior to use in a diffraction based investigation.

## 5.9 Creation of a diffraction test phantom

With knowledge of the response function between the speed setting of the phantom and the greyscale values of an image, as presented in Section 5.7, it is possible to quantify the height values corresponding to a real spiculated region of interest (ROI), as the depth variation for all greyscale values of 0–255 are known. However, this does require that an image using only 8-bit data is used. An example 8-bit image of infiltrating ductal carcinoma is shown in Figure 5.9.1 (Strith Medical School, 2013). For use in the laser system, the image is inverted such that the background is white and the tumour is black. This would therefore mean the tumour is etched into the PMMA.

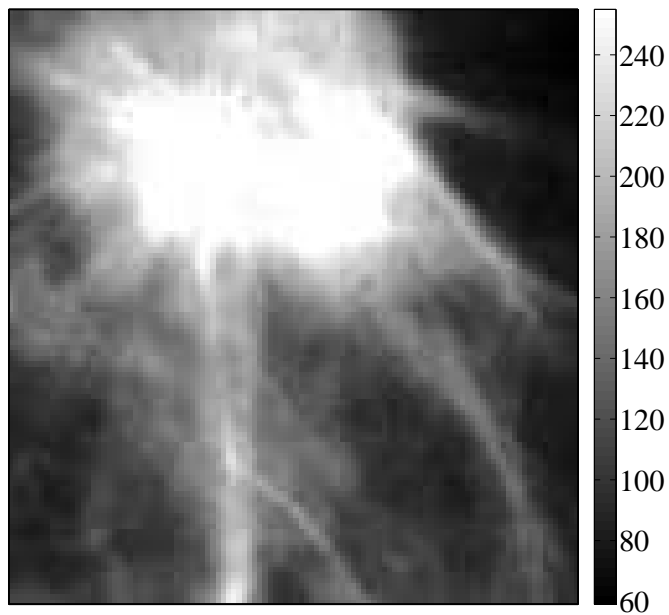


Figure 5.9.1: Original spiculated tumour ROI. The colourbar shows the corresponding greyscale values.

Each speed setting response curve  $F_{sp}(g)$  has a dependency on greyscale value. From these relationships it is possible to find the unknown etch depth of a known greyscale value of an image.

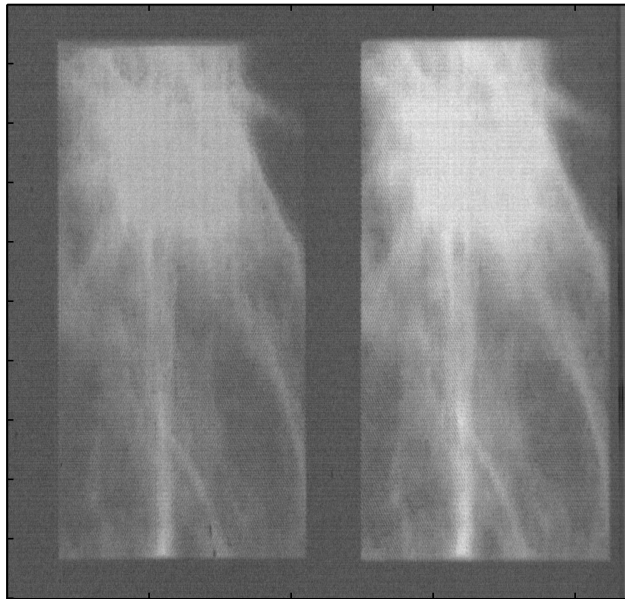


Figure 5.9.2: Example transmission images for 15% then 15% (left) and 5% (right)

Figure 5.9.2 shows example transmission images using the 15% and then 15% speed setting combination and 5%. From these transmission images and using the speed setting response functions for etch depth with greyscale value for each pixel in the 8-bit tumour image, a 3D presentation can also be developed. The example 3D depth representation of the phantom calculated by the response curves is shown in Figure 5.9.3. The etched phantoms were of dimensions  $4\text{ cm} \times 4\text{ cm}$  using 6.5 mm thick PMMA as an etching material. The phantom area was selected to ensure that scanning could be performed within the diffraction system.

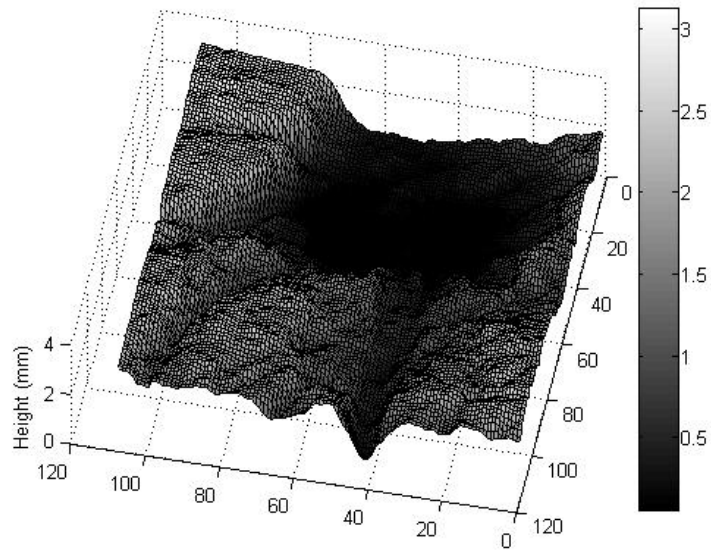


Figure 5.9.3: 3D representation of an etched tumour.

Figure 5.9.4 shows a photograph of the created laser etched phantom of a spiculated tumour. The speed settings from left to right are 20% followed by 20%, 15% followed by 15% , 10% and 5%.



Figure 5.9.4: A photo of the 6.5 cm thick PMMA and the spiculated tumour etched into the material using different speed settings.

The phantoms are essentially 2D, but the removal of the PMMA material can allow for another material of interest to be used by in-filling the removed PMMA material with another material of interest for the diffraction study.

### 5.9.1 Context of this section

The diffraction system previously described in Chapter 3 is used to create 2D images of the phantom corresponding to the 5% speed setting. This phantom had the maximum thickness etched out from the PMMA.

In order to investigate the usage of the phantom, the phantom is first left unfilled and then filled with water. The signals from PMMA and water can be considered as adipose and glandular tissue.

This work seeks to explore the use of the phantom in a diffraction system, how to create images, and to present different analysis methods, as well as to compare the obtained images to the original images used to create the phantoms.

### 5.9.2 Experimental method for diffraction test phantom imaging

The system previously used in Chapter 3 is used to scan the phantoms. The scanning code previously developed in MATLAB was used to automate the sample scan, as well as to ensure that data was only acquired when the bias voltage of  $-400\text{ V}$  was applied, and such that the motion of scans occurred while the bias was set to  $0\text{ V}$ . A schematic of the system is shown in Figure 5.9.5.

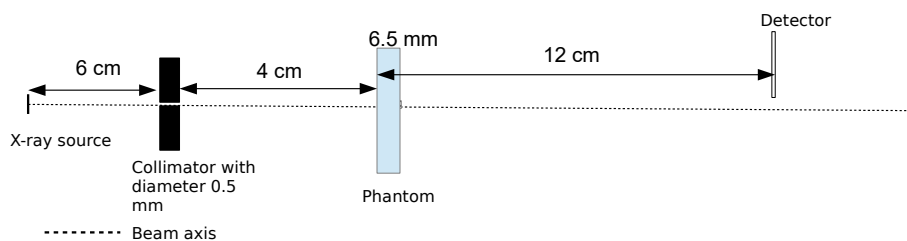


Figure 5.9.5: Schematic of phantom placement in the diffraction system.

Due to time constraints rather than scan the entire  $16\text{ cm}^2$  at a lower resolution, it was decided to scan a smaller ROI which had more interesting structure in terms of the tumour fibrils. The region of interest was chosen due to the differing structures, and is shown in Figure 5.9.6

Instead of the tumour mass being considered, the thinner fibrils of the phantom were preferred for investigation, as these are more relevant when considering the expanse of the tumour and the margins of the tumour. The smaller ROI would also allow for a reduced scan time. A step size of  $0.5\text{ mm}$  was used, which is approximately the same size as the collimated beam at the sample. The acquisition time for the scan step was  $30\text{ s}$ , and the total number of steps was  $20\times 20$ , equivalent to  $1\text{ cm}\times 1\text{ cm}$ . The phantom was always placed at  $12\text{ cm}$  away from the detector.

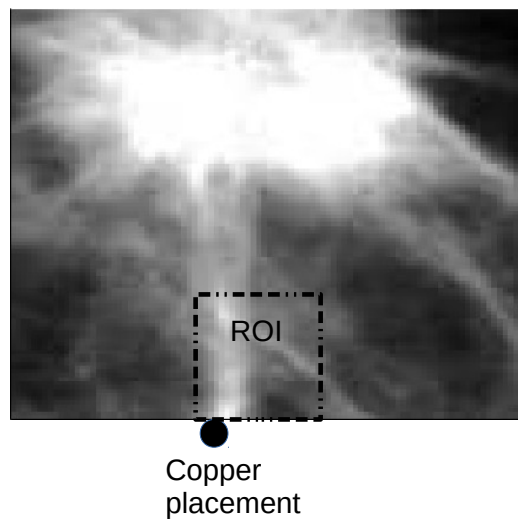


Figure 5.9.6: Primary region of interest and the copper marker placement.

In the first instance the phantom was left unfilled, i.e. with only PMMA present in the phantom. A piece of copper marker ( $0.4\text{ mm}\times 0.4\text{ mm}$ ) was used to mark the edge of the region of interest, as demonstrated in Figure 5.9.6. The translation stages were used to find the edge of the copper marker by detecting

the diffraction signal of copper until this was no longer recorded. There is some uncertainty to the exact position of the region of interest due to both the placement of the copper marker as well as the resolution of the step size taken to find the edge of the copper marker.

In the second case the phantom was laid flat on a worktop, similarly to Figure 5.9.4, and filled with water and then covered with a waterproof covering to reduce the loss of water during the scan. During the scan the phantom is placed upright, rather than flat on a surface, and therefore if not contained, water would spill out of the phantoms. Once the phantoms were filled and sealed while horizontal, they were placed vertically and checks for leaks were performed, and in the case of leaks, the process was repeated until no water leaks were observed.

For the case of the water filled phantom, once again a copper marker was used as a means of detecting the edge of the ROI.

### **5.9.3 Results: Production of diffraction images of the unfilled phantom.**

The data were processed using the previously described method in Section 3.9.6, utilising the selected energies of 15 keV–20 keV. The choice was made to use a limited energy range to obtain a defined relationship between the thickness of PMMA and the diffraction signal, as shown in Figure 5.9.7. The relationship between the normalised intensity signal and the depth can be used to recreate the depth of the phantom, based on the obtained data. It should be possible to determine the thickness of PMMA based on the intensity of the diffraction signal at  $0.78 \text{ nm}^{-1}$  for each scan point.

A diffraction image was created by finding the intensity value of the diffraction peak at  $0.78 \text{ nm}^{-1}$  and recording an intensity value for each scan position.

Utilising the intensity–thickness data obtained in Section 3.9.6, a relationship

was found by applying a best fit suited to the data. Only the positive signals were taken into account, which is up to 7 mm thickness, which is greater than the thickness of the PMMA phantom at its maximum, as shown in Figure 5.9.7. The final relationship was scaled with respect to the maximum signal to take into account variation between scans. Figure 5.9.7 shows that there exists a relationship where the diffraction intensity,  $I_d$ , is a function of PMMA thickness,  $\text{PMMA}_t$ , and therefore can be written as  $I_d(\text{PMMA}_t)$

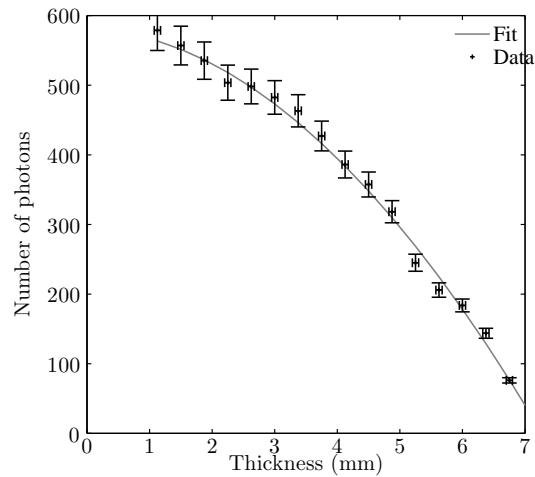


Figure 5.9.7: Relationship  $\text{PMMA}_t(I_d)$  between the signal of diffraction of PMMA at  $0.78 \text{ nm}^{-1}$  and the sample thickness.

By inverting this relationship i.e. rather than finding the signal when the thickness is known, to finding the thickness when the signal is known, it should be possible to relate the detected signal to the thickness of the sample. This can be performed by interpolating the relationship  $\text{PMMA}_t(I_d)$  using the MATLAB function `interp1`, such that `interp1` and for each point of the diffraction scan for the 5% phantom, find the corresponding PMMA thickness for the corresponding normalised intensity, using the `find` function in MATLAB. This was repeated for each point in the scan and a diffraction image with the intensity representing the

predicted thickness  $PMMA_t$  was found at each scan position.

Figure 5.9.8 shows an example of the diffraction image obtained with the scanned 5% laser cut phantom of PMMA. This example demonstrates that utilizing the signal variation due to the change in thickness of the sample can be used to recreate diffraction images of the original phantom. The uncertainty in the region of interest positioning is indicated by the dashed line in the top left image of Figure 5.9.8. These images were obtained only using the PMMA phantom. In this case it was observed that the copper marker was placed higher than was originally intended by the author.

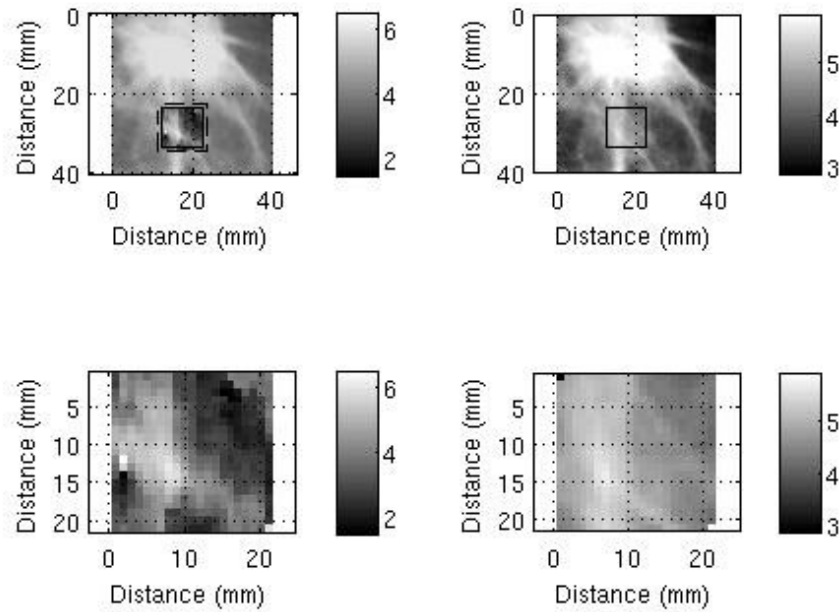


Figure 5.9.8: Top left: The original transmission image of the infiltrating ductal carcinoma. The position of the scanned ROI is indicated by the black box. Top right: The original transmission image of the tumour re-binned such that the pixel size corresponds to the steps used in the scan, i.e.  $0.5\text{ mm} \times 0.5\text{ mm}$ . Bottom left: The intensity of the diffraction data at  $0.78\text{ nm}^{-1}$ . Bottom right: The thickness variation of the phantom in the region of interest. All images have the same contrast and the greyscale values correspond to the average thickness found at the corresponding scan position.

#### 5.9.4 Results: Production of diffraction images of the in-filled phantom.

For the in-filled PMMA and water scan, the data were processed in the same way as Section 5.9.3. Due to the increased attenuation through a thicker sample and to explore post analysis techniques, the intensity image was found by summing the intensity at a chosen momentum transfer value of interest  $\chi_c$  within a window of  $d\chi$ , such that the total signal is a sum of the signal in  $\chi_c \pm d\chi$ . The following images in Figures 5.9.9 and 5.9.10, show the data obtained for the signal at  $0.78 \text{ nm}^{-1}$ , corresponding to a peak of PMMA, and also at  $1.6 \text{ nm}^{-1}$ , corresponding to the peak of water. The diffraction window  $d\chi$  was  $0.1 \text{ nm}^{-1}$  for both cases.

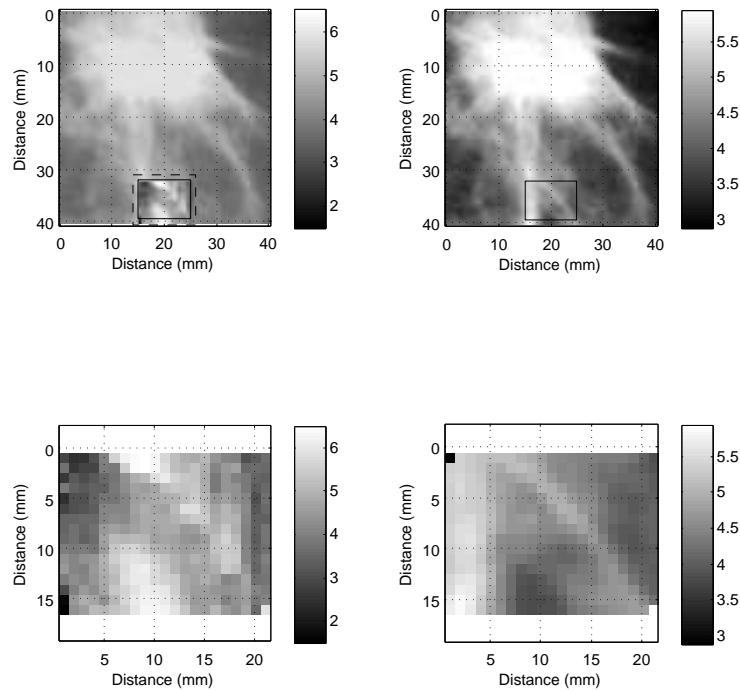


Figure 5.9.9: Images from the PMMA and water scan. Top left: The original transmission image of the infiltrating ductal carcinoma. The position of the scanned ROI is indicated by the black box. Top right: The original transmission image of the tumour re-binned such that the pixel size corresponds to the steps used in the scan, i.e.  $0.5\text{ mm}\times 0.5\text{ mm}$ . Bottom left: The intensity of the diffraction data at  $0.78\text{ nm}^{-1}$ . Bottom right: The thickness variation of the phantom in the region of interest. All images have the same contrast and the greyscale values correspond to the average thickness found at the corresponding scan position.

Figure 5.9.9 shows the scan images which include clockwise from top left; the original image of the phantom and the ROI indicated by the black box, the corresponding thickness obtained from the diffraction data, and the region of interest from the phantom thickness data. All images have the same contrast and the greyscale values correspond to the average thickness found at the corresponding scan position. Data correspond to the  $0.78 \text{ nm}^{-1}$  of PMMA with a window of  $0.1 \text{ nm}^{-1}$ .

The same sequence of images are shown in Figure 5.9.10, but this time the data correspond to the  $1.6 \text{ nm}^{-1}$  of water with a window of  $0.1 \text{ nm}^{-1}$ .

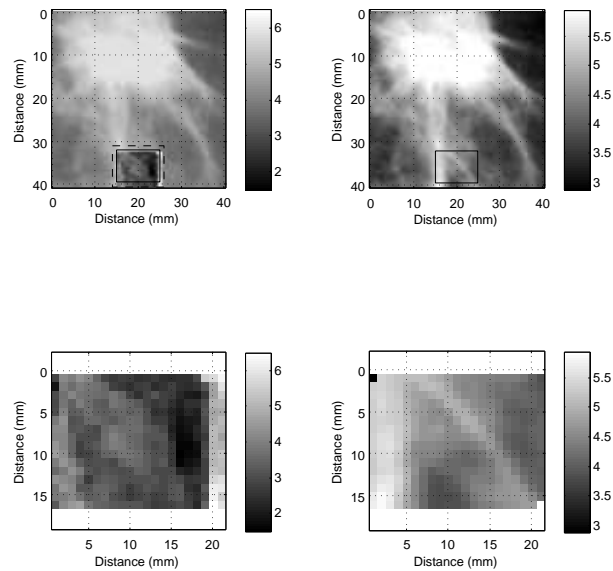


Figure 5.9.10: Top left: The original transmission image of the infiltrating ductal carcinoma. The position of the scanned ROI is indicated by the black box. Top right: The original transmission image of the tumour re-binned such that the pixel size corresponds to the steps used in the scan, i.e.  $0.5\text{ mm} \times 0.5\text{ mm}$ . Bottom left: The intensity of the diffraction data at  $1.6\text{ nm}^{-1}$ . Bottom right: The thickness variation of the phantom in the region of interest. All images have the same contrast and the greyscale values correspond to the average thickness found at the corresponding scan position.

Observation of Figures 5.9.9 and 5.9.10 shows the overall structure of the ROI

when comparing to the original transmission image used to create the phantom. The original image is shown in the bottom left of the image and is re-binned to the dimensions of the scan. The fibril extending from the top left to the bottom right of the ROI can also be seen in the images. However, this is not as clear in the  $1.6 \text{ nm}^{-1}$  image, where contrast appears to be not as high as when the signal at  $0.8 \text{ nm}^{-1}$  is used. To quantify this further, the contrast of the image is defined in Eqn 5.9.1

$$C = \left( \frac{\chi_f - \chi_b}{\chi_f + \chi_b} \right) \times 100 \quad (5.9.1)$$

where  $\chi_f$  is the diffraction signal from within the fibril region,  $\chi_b$  is the background region (or region where no clear structure is seen), and C is the contrast in percentage. Two sub regions of interest were defined from the ROI to consider the differences in the contrast between the fibril region, based on visual inspection, and from a background region where no clear structure can be seen. These sub ROIs are shown in Figure 5.9.11. The diffraction signal of the sub regions is taken as the mean signal of the ROI.

The diffraction intensity at a momentum transfer value of choice is the most commonly used representation of the diffraction signal. Unlike transmission, multiple signals can be obtained when using EDXRD. For the example used in this research, where up to 400 momentum transfer bins are obtained, this can consequently lead to up to 400 intensity images obtained in one scan, compared to one transmission image. The transmission image presents the same contrast, however when using the diffraction data, it is possible to vary contrast depending on the chosen momentum transfer value of interest, as well as the window of momentum transfer in which the data is summed.

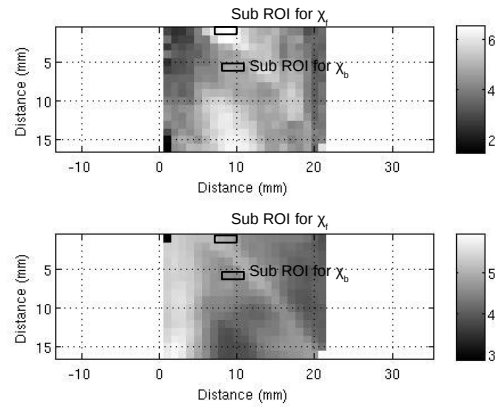


Figure 5.9.11: Top image: The intensity of the diffraction at  $0.78 \text{ nm}^{-1}$  and the positioning of the corresponding sub ROIs. Bottom image: The original transmission image of the phantom with pixel size corresponding to that of the scan, i.e.  $0.5 \text{ mm} \times 0.5 \text{ mm}$

For momentum transfer values of  $0.78 \text{ nm}^{-1}$  and  $1.6 \text{ nm}^{-1}$ , the momentum transfer window was varied between  $0.01 \text{ nm}^{-1}$  and  $0.5 \text{ nm}^{-1}$ . Figure 5.9.12 and Figure 5.9.13 show the diffraction variation in the contrast of the images for the signal at  $0.8 \text{ nm}^{-1}$  and  $1.6 \text{ nm}^{-1}$ , respectively. The contrast of the original image used to create the phantom is 1.78%, when considering the two sub ROIs.

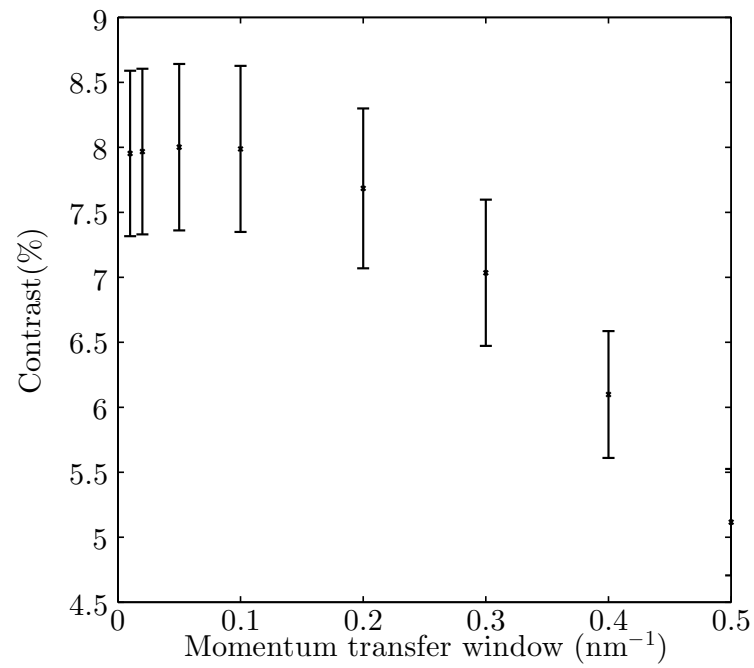


Figure 5.9.12: Variation in the diffraction intensity contrast with varying diffraction window.

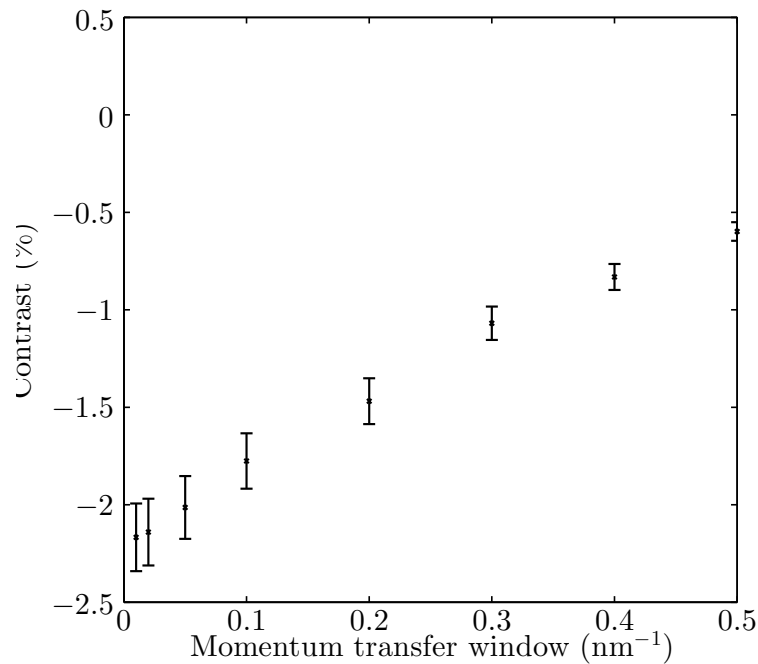


Figure 5.9.13: Variation in the diffraction intensity contrast with varying diffraction window.

For the PMMA signal, the contrast is higher than the original image, even with a window of  $0.5 \text{ nm}^{-1}$ , and therefore helps to provide greater visualisation of the structure in the phantom. Although the signal from water shows improved contrast, beyond a window of  $0.1 \text{ nm}^{-1}$  the contrast becomes poorer than the original image.

#### 5.9.4.1 Relative intensity image

To make use of the multiple signals obtained in the diffraction data, i.e. multiple intensity values at different momentum transfer values, the relative intensity of the diffraction signal at  $0.78 \text{ nm}^{-1}$  and  $1.6 \text{ nm}^{-1}$  were compared within varying momentum transfer windows. The relative signal is defined in Eqn 5.9.2.

$$I_{rel} = \frac{I_{pmma}(\chi_w)}{I_{water}(\chi_w)} \quad (5.9.2)$$

where  $I_{pmma}$  and  $I_{water}$  are the total intensities measured within the momentum transfer window  $\chi_w$ . Figure 5.9.14 shows the obtained intensity images when considering the relative intensity of the data.

The features of the phantom can clearly be seen from the images, as shown in Figure 5.9.14, however the contrast varies when using the relatively intensities. As the PMMA thickness increases the signal of the PMMA decreases. Areas where the etch depth is low correspond to areas where PMMA is thicker and therefore the diffraction signal from the PMMA is low.

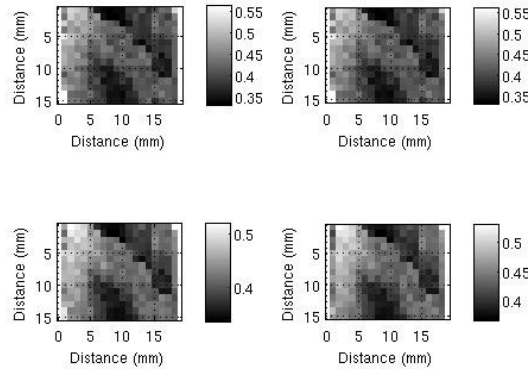


Figure 5.9.14: Relative intensity images of the scanned phantom. From top left clockwise, the momentum transfer windows are  $0.01 \text{ nm}^{-1}$ ,  $0.02 \text{ nm}^{-1}$ ,  $0.2 \text{ nm}^{-1}$  and  $0.4 \text{ nm}^{-1}$ . The colorbar indicates the relative intensity.

The value of  $\chi_w$  was varied and the contrast between the two previously defined sub ROIs was considered. The value of  $\chi$  was varied within the range of  $0.01 \text{ nm}^{-1}$  to  $0.5 \text{ nm}^{-1}$ .

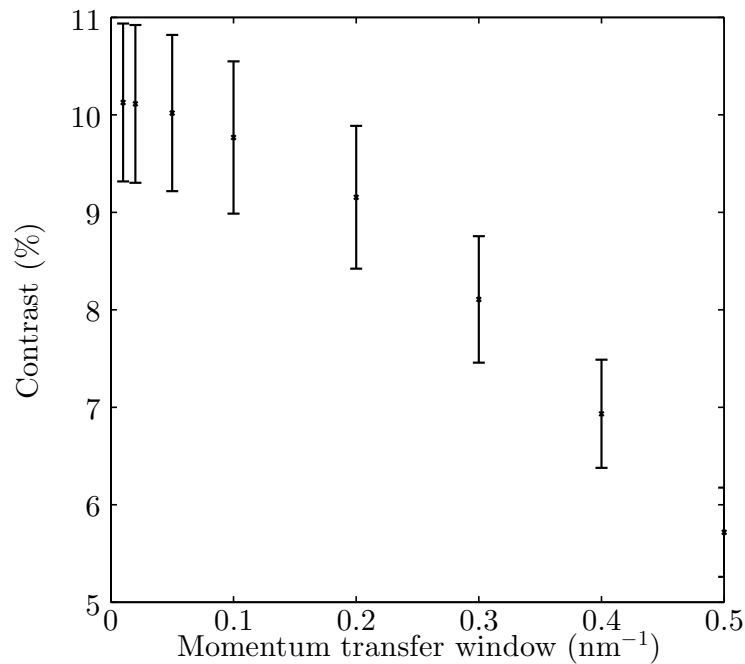


Figure 5.9.15: Relationship between the contrast of the sub ROIs with respect to the momentum transfer window.

It can be seen from Figure 5.9.15 that when defining the two sub ROIs, that the contrast, when using the relative intensity of the diffraction signal, decreases from 10% to 6%, when a diffraction window of  $0.5 \text{ nm}^{-1}$  is used. These values are consistently better than the original image used to create the phantom.

### 5.9.5 Discussion: Creation of a diffraction test phantom

The phantoms have the potential to be filled with a material chosen for a particular investigative study. In this case, the phantom at 5% speed setting was imaged both unfilled and in-filled with water, a commonly used equivalent material for x-ray diffraction. The thickness of the filled material is known, as in this case it is assumed that the infilling material replaces the volume of PMMA removed by the laser system. This would produce a direct relationship between the input

software image and the created physical phantom for both the etching material, in this case the PMMA, and for the in-filling material, in this case water. In order to seal in the water, water proof tape had to be used to prevent leakages and spillages. Practically speaking this is not a user friendly option. Ideally the phantom could be sealed in a non-restrictive manner, i.e. that there is a design or feature that would securely allow the use of water. The phantom was placed in a vertical position which also made it practically difficult to use at times. In order to find the ROI, a copper marker was used and the diffraction peak of the copper found. This meant there was uncertainty in the placed of the copper and can lead to misplacement if not performed with caution. Ideally a fixed reference point on the phantom could be used to align the system. Once this reference point is aligned to the beam a map of the phantom can be used to find specific ROIs. This would aid alignment time and user friendliness of the phantom for other systems.

Utilising different speed settings would allow for the user to use a phantom with varying thickness and change of thickness with greyscale value, which would be equivalent to the variation in tissue matter within a tissue sample. However, the thickness of the phantom would ultimately remain at 6.5 mm, as the total thickness is the sum of the PMMA removed, corresponding to the volume of in-filling material, and the PMMA that remains from the original block 6.5 mm PMMA. The phantom therefore offers the ability to essentially combine tissue equivalent materials with varying contours, based on the intensity of the original transmission image, but remaining at constant overall thickness. This would represent the fact that the growth of a tumour is not uniform within surrounding healthy tissue. This makes the combination of materials for x-ray diffraction more realistic than, for example, only combining two sheets of materials, or using geometric phantoms for imaging.

The thickness of PMMA utilised in this study matches the thickness of the

biopsy samples, e.g. that of 6 mm used by Pani et al. (2010) and Bohndiek et al. (2009) but doesn't necessarily match the equivalent breast tissue thickness, which in this case is 8 mm of breast tissue. However, this is not to be seen as a limitation of the technique. As part of the laser etching system it is necessary to input the thickness of the material utilised, so that the greyscale values would not exceed the maximum thickness and therefore cut through the material. It would therefore be possible to use thinner PMMA if it was desired for the study. The technique would allow for the development of different biopsy sample thickness, as demonstrated by the fact that the maximum etch depth varies depending on the speed setting used, as well as the fact the parameter used for the laser etching software for the thickness of the sample can be input by the user. This parameter then could limit the ablation depth of the PMMA and would act as an etching limit for the system. No speed combination reaches the limit of 6.5 mm as this would be equivalent to cutting through the material, which is not possible within the greyscale interpretation. This is due to the fact that the laser system is designed to interpret colours as vectors or raster scanning in which greyscale does not correspond to cutting.

The method allows for the customisation of phantoms based on the study of interest by the users and are aimed primarily for diffraction studies, utilising the fact that PMMA is a commonly used equivalent material. It is however only a single slice view, so would not be useful for example in diffraction CT imaging. The benefit for diffraction is that the shape of the phantom is realistic to a tumour as it is based on an image of a real tumour. An image of choice could be etched into the material, depending on the requirements of a diffraction study.

The phantom created using the 5% speed setting was scanned in the diffraction system over a ROI of  $1\text{ cm} \times 1\text{ cm}$ . In the first example of using the phantom in the diffraction imaging system, only one material type is used. It is possible to show the relationship between the depth of the phantom material (or etch

depth) and the diffraction signal obtained. This work showed that the system is sensitive to changes in the diffraction signal over the thickness range, therefore the thickness of the phantom was limited to a range at which the system was sensitive to variations in the PMMA thickness. This will only work if the system is sensitive to thickness changes. Therefore, each researcher wishing to recreate diffraction images in a similar way would need to perform an experiment to establish the relationship between the obtained diffraction signal for their system and the sample thickness.

An example of the filled phantom is also shown, with water as the in-filling material. Water behaves more like glandular tissue and PMMA can be considered to have more adipose tissue qualities, based on the diffraction peak at  $0.78 \text{ nm}^{-1}$ . The intensity of the signal at momentum transfer values of interest were used, similarly to several previous works. The contrast of the data was explored by varying the momentum transfer signal over which the intensity signal is summed, which is then averaged over pre-defined sub ROIs. The data have shown, that when comparing to the original image used to create the phantom, there is a benefit of using the PMMA signal, as the contrast increased from 1.85% to almost 8% for the same sub ROIs. In the case of the signal at  $1.6 \text{ nm}^{-1}$  limited improvements to the diffraction signal contrast are shown, with the best achieved contrast of 2.15%, using a diffraction window of  $0.01 \text{ nm}^{-1}$ .

It has also be shown that it is possible to process the diffraction data in different ways from data obtained from one scan. Utilising different diffraction windows meant it was possible to explore the effects of the diffraction windows on the biopsy phantom and for the best contrast to be found. From the diffraction data it is possible to reconstruct the phantom depth utilising the signal intensity used. However, it has been shown in Section 3.9, that the relationship of signal intensity to sample thickness depends on the method of post-processing used for the 3D data acquired. It would be possible to optimise such a system and post-

analysis depending on the signal of interest. The phantoms created, although a single slice of a breast tumour image, could be used for further diffraction studies to explore the use of variation in diffraction signal and reconstruction of images based on the amount of sample present, which is in this case characterised by the thickness. Therefore, this phantom could indeed be used to explore the post-analysis methods.

Using the relative intensity of the diffraction signal at  $0.78 \text{ nm}^{-1}$  and  $1.6 \text{ nm}^{-1}$  has shown the features of the phantom such that the contrast of the two sub ROIs were improved. The combination of PMMA and water lead to differences in the detected diffraction signal as well as variations in the attenuation of the signal, as the attenuation properties of PMMA and water are different and would therefore cause the attenuation of the diffraction signal to vary, depending on the thicknesses of materials in the phantom voxels (based on the diffraction system).

## 5.10 Conclusions

A laser etched phantom has been developed for use as a biopsy sample phantom for EDXRD studies. The speed setting of the laser system was used as a variable to create different etch depths within a 6.5 mm piece of PMMA from an input virtual model, namely a transmission image of a spiculated tumour.

The author presents a method of characterising and obtaining relationships between the etch depths, the greyscale values and the speed settings, using a transmission system. This is a method that could be used in future versions of the phantom. There is a direct relationship between the original image of the tumour, the parameters used to create the phantom, the hardware version of the phantom and the transmission images of the phantom. There is therefore a 'ground truth' version of the phantom that can be used for diffraction studies.

Use of the phantom was demonstrated both unfilled i.e. only the PMMA

material is present, and in-filled, i.e where another material is used to replace the PMMA removed. In the case of the unfilled phantom, a  $1\text{ cm}\times 1\text{ cm}$  region of interest was scanned in  $0.5\text{ mm}$  steps, and a diffraction intensity image was created using the diffraction peak of PMMA at  $0.78\text{ nm}^{-1}$ .

The material used to in-fill the phantom was water. Combining the two materials, the 5% speed setting phantom was investigated. Once again, a  $1\text{ cm}\times 1\text{ cm}$  region of interest of the phantom was scanned in the automated diffraction system presented in Chapter 3, in steps of  $0.5\text{ mm}$ . In this case, two signals of diffraction were analysed; the intensity at  $1.6\text{ nm}^{-1}$  and the signal at  $0.78\text{ nm}^{-1}$ . The contrast of the images were investigated using sub ROIs, demonstrating that the phantoms, combined with the EDXRD data, can be used to explore contrast within an image by varying the momentum transfer signal of interest, as well as the momentum transfer window used to generate the images. Compared to the original transmission image of the tumour, for which the contrast between two regions of interest remained at 1.85%, improvements in the contrast based on the diffraction signals of interest were found. The data have shown, that when comparing to the original image used to create the phantom, there is a benefit of using the PMMA signal, as the contrast increased from 1.85% to almost 8% for the same sub ROIs. In the case of the signal at  $1.6\text{ nm}^{-1}$  limited improvements to the diffraction signal contrast are shown, with the best achieved contrast of 2.15%, using a diffraction window of  $0.01\text{ nm}^{-1}$ . This therefore highlights that not only can diffraction provide additional information, as used in additional studies such as the works of Griffiths et al. (2004) and Griffiths et al. (2008), that post-analysis techniques can be explored using the phantoms for a specific system.

# Chapter 6

## Future work

In addition to comments made in the Discussion sections, this section details further work that can be conducted based on the research presented.

The work detailed in Chapter 2 considers the available pixellated 2D detector for use in EDXRD, by considering the energy resolution, the charge sharing effects, the efficiency at 60 keV, the Row-S<sub>1</sub> and also the system stability. As future improvements are made to the software and the system, including the inclusion of a charge sharing addition algorithm, these too would be explored in the context of EDXRD. At the time of this work, the charge addition algorithm was not implemented in the available software, so as software updates are available, further tests of the effects of the algorithm on the diffraction data would have to be made. Being able to include charge sharing events through charge addition would mean an expected greater number of photons included in the spectra, improving the measured efficiency and spectral statistics for a specific acquisition time.

The detector was used in an EDXRD system using the multi-angle technique. The potential future work for a diffraction system utilising the 2D system is to refine the diffraction angles to a limited number of angles-moving the detector along the beam-axis, i.e. by increasing the detector-sample distance would refine the angles. However two practical considerations need to be taken into account.

As the detector is moved further away from the source, the intensity of the beam would decrease based on the inverse square law. This would have an effect on the counting time and the integrated number of counts within a spectrum, which could therefore lead to low noise data. Low noise data could be used with MVA techniques, as have previously been shown by Christodoulou et al. (2011) and O’Flynn et al. (2012). These were both generally speaking for powdered materials, so future work investigating the use of the detector for multi-angle diffraction applied to amorphous materials using MVA would be an area of investigation. Reducing acquisition times and introducing MVA techniques that can classify e.g. healthy tissue from unhealthy tissue would make the detector more clinically relevant, where results are ideally available as soon as possible.

It is also necessary to consider the XRF and the removal of the signal. This again can be done by geometry and would have to be explored in any future system utilising the 2D pixellated ASIC with 1 mm CdTe. Now that the problems are known, these would have to be optimised for use in any clinical system investigating breast tissue biopsy samples. This would include the placement of the detector both along the beam axis and perpendicular to the beam axis, and visualisation of the data, which currently chooses to emphasise the diffraction rings so that it is obvious that diffraction is present. A narrower range of angles would remove this visualisation effect. However, creating a spectrum should highlight that diffraction is indeed being detected.

In addition to this it could be possible to adjust the beam spectrum used for the experiments, such that the mean energy of the beam is either higher or lower than the binding energies of the k-shells of the cadmium and tellerium, that cause the XRF peaks in the material. Reducing the kilovolt potential of the x-ray source would mean more photons with lower energies, which would mean that the self-attenuation of the sample could be worse. Or, alternatively, one might need to consider using higher energy photons that would be less likely to

be self-attenuated by the sample but would not necessarily interact with such an extent with the sample. This is dependent on the cross-section of interaction.

For future systems using a 2D array for breast tissue equivalent materials, it would be necessary to consider all of these effects. In order to establish if the system is able to obtain diffraction signals from samples similar to breast tissue biopsy sample types, it would be necessary in any future work using the detector to ensure that a diffraction signal can be obtained i.e. that the system is indeed sensitive to the sample type and to what thickness. It has been shown in Chapter 3 that processing the data in different ways led to different relationships between imaging parameters such as the intensity of the diffraction signal at a chosen momentum transfer, as well as for other parameters including the FWHM. This also depended on the sample type. Future work would be required to fully understand these effects, through a combination of modelling, such as Monte Carlo modelling of the interaction of photons within the sample, as well as further experimental investigations. This work would then contribute to understanding the relationship between the geometry of the system, the sample thickness (and therefore the thickness limitations of the system), and the post-analysis techniques.

Chapter 4 considered materials that could be used for phantom development work in the future by extending the list of known equivalent materials, as well as considering their practical properties, in this case the melting point for potentially moulding and shaping the plastics into an anthropomorphic phantom. Other materials such as variations of nylon were considered, as well as the gel type materials of gelatine and agar. The gel type materials were included primarily due to the fact that they can hold water in a semi-solid state making water, a known tissue equivalent substance, more tissue like and also more containable for use in a phantom. However, practically speaking the gels used in this work can not be used in the long term and is a limitation of their application in diffraction

phantoms. It would be possible and necessary to investigate the lifetimes of the gels, as well as to investigate different grades of the gels based on, for example, the Bloom strength. This is a measure typically for gelatine gels which quantify the strength by the weight in grams needed to deflect the surface of the gel 4 mm. Under the condition of the test, the gel must not break.

Future work for phantom equivalent work would be to expand the materials library, considering the practical elements of the materials including melting point, setting point, and lifetime of the materials. This could include gels such as the G9391 Gelatin, available from Sigma Alrich ([www.sigmaaldrich.com](http://www.sigmaaldrich.com)). The gelatine is created from bovine skin Type B (derived from lime-cured tissue). Other gelatine available include G1890 which is made from porcine skin powder and is of Type A, which is derived from acid cured tissue. Both types, for example, are suitable for cell culture and are formerly produced to set standards.

Chapter 5 includes the development of laser etched phantoms for breast tissue biopsy samples. The phantoms were characterised in a transmission image, demonstrating that it was possible to relate the settings of the laser system, the input intensity image used, the greyscale values and the etch depth of the phantom. This was demonstrated using PMMA of 6.5 mm. To explore the technique further, testing the technique on thinner and thicker PMMA pieces would test the creation limits of such phantoms. This would also mean that a range of phantoms would be available for researchers to test in their diffraction systems.

The work presented here utilised water as an in-filling material. Alternative materials, such as gels, oil, and nylon type plastics would also need to be investigated to explore the practicality of using alternative materials to infill the phantom. Keeping the materials in place would also need to be considered in order to make the phantoms more user friendly. Currently, water was used due to its easy of use in terms of replacing the removed materials, as well as its diffraction signal for glandular tissue equivalence. In order to be diverse for system tests

and researchers, the phantom would need to be tested with other materials.

# Bibliography

S.N. Ahmed. *Physics and engineering of radiation detection*. Academic Press, 1997.

Y.A. Akovali. Table of radioactive isotopes, March 1994. URL <http://www.test.org/doe/>.

Alec Tiranti Ltd. General purpose resin technical data sheet.

S.M. Alkhateeb, M.H. Abdelkader, D.A. Bradley, and S. Pani. Breast tissue contrast-simulating materials using energy-dispersive x-ray diffraction. *Applied Radiation and Isotopes*, 70(7):1446–1450, 2012.

G. M. Ardran and H. E. Crooks. Some technical problems with diagnostic radiography at 20 to 40 kvp. *British Journal of Radiology*, 44(524):625–630, 1971.

R. Ballabriga, M. Campbell, E. Heijne, X. Llopart, L. Tlustos, and W. Wong. Medipix3: A 64k pixel detector readout chip working in single photon counting mode with improved spectrometric performance. *Nuclear Instruments and Methods in Physics Research Section A: Accelerators, Spectrometers, Detectors and Associated Equipment*, 633:S15–S18, 2011.

G. Beldjoudi, V. Rebuffel, L. Verger, V. Kaftandjian, and J. Rinkel. An optimised method for material identification using a photon counting detector.

- Nuclear Instruments and Methods in Physics Research Section A: Accelerators, Spectrometers, Detectors and Associated Equipment*, 663:26–36, 2012.
- R.O. Bell, G. Entine, and H.B Serreze. Time dependent polarization of CdTe gamma-ray detectors. *Nuclear Instruments and Methods*, 117, 1974.
- A. Bergamashi, A. Cervellino, R. Dinapoli, F. Gozzo, B. Henrich, P. Kraft, A. Mozzanica, B. Schmitt, and X. Shi. The MYTHEN detector for x-ray powder diffraction experiments at the Swiss Light Source. *Journal of Synchrotron Radiation.*, 17, 2010.
- M.J. Berger, J.H Hubbell, S.M. Seltzer, J. Chang, J.S. Coursey, R. Sukumar, D.S. Zucker, and K. Olsen. Xcom: Photon cross sections database, 2010.
- S. E. Bohndiek, G. J. Royle, and R. D. Speller. An active pixel sensor x-ray diffraction (APXRD) system for breast cancer diagnosis. *Physics in medicine and biology*, 54(11):3513–27, 2009.
- J.T. Bushberg. *The Essential Physics of Medical Imaging*. Lippincott Williams & Wilkins, 2002. ISBN 9780683301182.
- M. Campbell. 10 years of the medipix2 collaboration. *Nuclear Instruments and Methods in Physics Research Section A: Accelerators, Spectrometers, Detectors and Associated Equipment*, 633, Supplement 1(0):S1–S10, 2011.
- D. Cardoso de Moura, J.M.G. Barobsa, J.M.R.d.S Tavares, and A. Reis. Calibration of bi-planar radiography with minimal phantoms. 2008.
- Bakic P. Carton, A-K. and. Development of a 3D high-resolution physical anthropomorphic breast phantom. volume 7622. *Medical Imaging 2010: Physics of Medical Imaging*, 2010.
- C. Castro, R. Barroso, L. Deoliveira, and R. Lopes. Coherent scattering X-ray imaging at the Brazilian National Synchrotron Laboratory: Preliminary

- breast images. *Nuclear Instruments and Methods in Physics Research Section A: Accelerators, Spectrometers, Detectors and Associated Equipment*, 548(1-2): 116–122, 2005a.
- C. R. F. Castro, R. C. Barroso, and R. T. Lopes. Coherent scattering characteristics of normal and pathological breast human tissues. *Radiation Physics and Chemistry*, 71(3-4):649–651, 2004.
- C. R. F. Castro, R. C. Barroso, and R. T. Lopes. Scattering signatures for some human tissues using synchrotron radiation. *X-Ray Spectrometry*, 34(6): 477–480, 2005b.
- C. Christodoulou, C.B. Reid, D. OFlynn, M. Wilson, M. Veale, R.J. Cernik, P Seller, and R.D Speller. Multivariate analysis of pixelated diffraction data. *Journal of Instrumentation*, 6(C12027), 2011.
- C. Christodoulou, M. Wilson, D. Veale, M.and OFlynn, P Seller, and R.D Speller. Energy resolution and efficiency comparisons of two ASICs of Cadmium Telluride suitable for room temperature diffraction medical imaging. volume 6, 2013.
- J.H Clark. A study of tendons, bones, and other forms of connective tissue by means of x-ray diffraction patterns. *American Journal of Physiology*, 1931.
- A. Cola and I. Farella. The polarization mechanism in CdTe Schottky detectors. *Applied Physics Letters*, 94(10), 2009.
- A. L. C. Conceição, M. Antoniassi, and M. E. Poletti. Analysis of breast cancer by small angle X-ray scattering (SAXS). *The Analyst*, 134(6):1077–1082, 2009.
- A.L.C. Conceição, M. Antoniassi, D.M. Cunha, A. Ribeiro-Silva, and M.E. Poletti. Multivariate analysis of the scattering profiles of healthy and pathological

- human breast tissues. *Nuclear Instruments and Methods in Physics Research A*, 652:870–873, 2011.
- E.J. Cook. *Analysis of energy dispersive X-ray diffraction profiles for material identification, imaging and system control*. PhD thesis, University College London, 2008.
- E.J. Cook, S. Pani, L. George, S. Hardwick, J. Horrocks, and R.D. Speller. Multivariate Data Analysis for Drug Identification Using Energy-Dispersive X-Ray Diffraction. *IEEE Transactions on Nuclear Science*, 56(3):1459–1464, 2009.
- C. Crespy, P. Duvauchelle, V. Kaftandjian, F. Soulez, and P. Ponard. Energy dispersive X-ray diffraction to identify explosive substances: Spectra analysis procedure optimization. *Nuclear Instruments and Methods in Physics Research Section A: Accelerators, Spectrometers, Detectors and Associated Equipment*, 623(3):1050–1060, 2010.
- D. Darambara. A low-angle X-ray scatter breast-imaging system based on a novel multi-element Si-pad array operated in spectroscopic mode. *Nuclear Instruments and Methods in Physics Research Section A: Accelerators, Spectrometers, Detectors and Associated Equipment*, 525(1-2):253–257, 2004.
- G. De Geronimo, P. OConnor, V. Radeka, and B. Yu. Front-end electronics for imaging detectors. *Nuclear Instruments and Methods in Physics Research Section A*, 471:192–199, 2001.
- G. De Geronimo, P. OConnor, and A. Kandasamy. Analog CMOS peak detect and hold circuits. Part 1. Analysis of the classical configuration. *Nuclear Instruments and Methods in Physics Research Section A*, 484:533–543, 2002.
- Dectris AG. PILATUS3 X CdTe Series. Online, 2015. URL <https://www.dectris.com>.

- N. Dedek, R. D. Speller, P. Spendley, and J. A. Horrocks. Performance evaluation of 98 CZT sensors for their use in gamma-ray imaging. *2007 IEEE Nuclear Science Symposium Conference Record*, 2007.
- S. Del Sordo, L. Abbene, E. Caroli, A.M. Mancini, A. Zappettini, and P. Ubertini. Progress in the development of CdTe and CdZnTe semiconductor radiation detectors for astrophysical and medical applications. *Sensors*, 19:3491–3526, 2010.
- O. S. Desouky, W. M. Elshemey, and N. S. Selim. X-ray scattering signatures of  $\beta$ -thalassemia. *Nuclear Instruments and Methods in Physics Research Section A: Accelerators, Spectrometers, Detectors and Associated Equipment*, 607(2):463–469, 2009.
- W. M. Elshemey, O. S. Desouky, M. M. Fekry, S. M. Talaat, and A. a. Elsayed. The diagnostic capability of x-ray scattering parameters for the characterization of breast cancer. *Medical Physics*, 37(8):4257, 2010.
- W.M. Elshemey, F.S Mohamed, and I.M. Khater. X-ray scattering for the characterization of lyophilized breast tissue samples. *Radiation Physics and Chemistry*, 90(0):67–72, 2013. ISSN 0969-806X.
- T. Enomoto, E. Sato, P. Abderyim, A. Abudurexiti, O. Hagiwara, H. Matsukiyo, A. Osawa, M. Watanabe, J. Nagao, S. Sato, A. Ogawa, and J. Onagawa. Conventional X-ray fluorescence camera with a cadmium-telluride detector and its application to cancer diagnosis. *Nuclear Instruments and Methods in Physics Research Section A: Accelerators, Spectrometers, Detectors and Associated Equipment*, 635:108–115, 2011.
- K.H. Esbensen, D. Guyot, F. Westad, and L.P. Houmoller. *Multivariate Data Analysis in Practice : An Introduction to Multivariate Data Analysis and Experimental Design*. Camo Process AS; 5th edition, 2002.

- M. Esposito, T. Anaxagoras, A Fant, K. Wells, A. Konstantinidis, J.P.F. Osmond, P.M. Evans, R.D. Speller, and N.M. Allinson. Dynamite: a wafer scale sensor for biomedical applications. *Journal of Instrumentation*, 6(12):C12064, 2011.
- S.H Evans, D.A. Bradley, D.R. Dance, J.E Bateman, and C.H. Jones. Measurement of small-angle photon scattering for some breast tissues and tissue substitute materials. *Phys. Med. Biol.*, 36(1):7–18, 1991.
- G Falzon, S Pearson, R Murison, C Hall, K Siu, A Evans, K Rogers, and R Lewis. Wavelet-based feature extraction applied to small-angle x-ray scattering patterns from breast tissue: a tool for differentiating between tissue types. *Phys. Med. Biol.*, 51:246577, 2006.
- M.J. Farquarson and R.D. Speller. Trabecular bone mineral density measurements using energy dispersive X-ray diffraction (EDXRD). *Radiation Physics and Chemistry*, 51:607–608, 1998.
- M.J. Farquarson, R.D. Luggar, and R.D. Speller. Multivariate calibration for quantitative analysis of EDXRD spectra from a bone phantom. *Applied Radiation and Isotopes*, 48:1075–1082, 1997.
- M. J. Farquharson, A. Al-Ebraheem, S. Cornacchi, G. Gohla, and P. Lovrics. The use of x-ray interaction data to differentiate malignant from normal breast tissue at surgical margins and biopsy analysis. *X-Ray Spectrometry*, 42(5): 349–358, 2013. ISSN 1097-4539. doi: 10.1002/xrs.2455.
- M. Fernández, J. Keyriläinen, R. Serimaa, M. Torkkeli, M. L. Karjalainen-Lindsberg, M. Tenhunen, W. Thomlinson, V. Urban, and P. Suortti. Small-angle x-ray scattering studies of human breast tissue samples. *Physics in medicine and biology*, 47(4):577–92, 2002.
- M. Fernández, H. Suhonen, J. Keyriläinen, A. Bravin, S. Fiedler, M.-L.

- Karjalainen-Lindsberg, M. Leidenius, K. von Smitten, and P. Suortti. US-AXS and SAXS from cancer-bearing breast tissue samples. *European journal of radiology*, 68(3):S89–S94, 2008.
- P. Fischer, M. M. Kouda, H. Krüger, M. Lindner, G. Sato, T. Takahashi, S. Watanabe, and N. Wermes. A Counting CdTe Pixel Detector for Hard X-Ray and  $\gamma$ -Ray Imaging. *IEEE Transactions on Science*, 48(6), 2001.
- General Electric Company. Lexan 9030 sheet. 1997.
- K. Geraki, M. Farquharson, and M. Bradley. X-ray fluorescence and energy dispersive x-ray diffraction for the characterisation of breast tissue. *Radiation Physics and Chemistry*, 71(3-4):969 – 970, 2004a.
- K. Geraki, M.J. Farquharson, and D.A. Bradley. X-ray fluorescence and energy dispersive x-ray diffraction for the quantification of elemental concentrations in breast tissue. *Physics in Medicine and Biology*, 49, 2004b.
- K. Geraki, M.J. Farquharson, D.A. Bradley, and R.P. Hugtenburg. A synchrotron xrf study on trace elements and potassium in breast tissue. *Nuclear Instruments and Methods in Physics Research Section B: Beam Interactions with Materials and Atoms*, 213:564–568, 2004c.
- O. D. Gonçalves, C. Cusatis, and I. Mazzaro. Solid-state effects on rayleigh-scattering experiments: Limits for the free-atom approximation. *Phys. Rev. A*, 48:4405–4410, Dec 1993.
- D.J. Goodenough and J.R. Levy. Test body and element for a scanning image reconstructing apparatus, November 17 1992. URL <https://www.google.com/patents/US5164978>. US Patent 5,164,978.
- D. Greiffenberg, A. Fauler, A. Zwerger, and M. Fiederle. Energy resolution and

- transport properties of CdTe-Timepix-Assemblies. *Journal of Instrumentation*, 6:533–543, 2011.
- J. A. Griffiths, G. J. Royle, R. D. Speller, J. A. Horrocks, A. Olivo, S. Pani, R. Longo, S. H. Spencer, M. S. Robbins, D. P. Clifford, and Hanby A. M. Diffraction enhanced breast imaging: assessment of realistic system requirements to improve the diagnostic capabilities of mammography. In *IEEE Nuclear Science Symposium. Conference Record*, 2004.
- J. A. Griffiths, G. J. Royle, J. A. Horrocks, A. M. Hanby, S. Pani, and R.D. Speller. Angular dispersive diffraction microCT of small breast tissue samples. *Radiation Physics and Chemistry*, 77(4):373–380, 2008.
- J. Grindlay, J. Hong, B. Allen, S. Barthelmy, and R. Baker. Development of tiled imaging CZT detectors for sensitive wide-field hard X-ray surveys to EXIST. *Nuclear Instruments and Methods in Physics Research A*, check:check, 2010.
- G. Harding. X-ray scatter tomography for explosives detection. *Radiation Physics and Chemistry*, 71, 2004.
- G. Harding, J. Kosanetsky, and U. Neitzel. X-ray diffraction computed tomography. *Medical Physics*, 14, 1987.
- W.M. Haynes. *Handbook of Chemistry and Physics*. CRC Press, 2014.
- B. Henrich, A. Bergamaschi, C. Broennimann, R. Dinapoli, E.F. Eikenberry, I. Johnson, M. Kobas, P. Kraft, A. Mozzanica, and B. Schmitt. Pilatus: A single photon counting pixel detector for x-ray applications. *Nuclear Instruments and Methods in Physics Research Section A: Accelerators, Spectrometers, Detectors and Associated Equipment*, 607(1):247–249, 2009.
- J. Hong, B. Allen, J. Grindlay, N. Chammas, S. Barthelemy, R. Baker, N. Gehrels, K. E. Nelson, S. Labov, J. Collins, W. R. Cook, R. Mclean, and F. Har-

- risson. Building large area CZT imaging detectors for a wide-field hard X-ray telescope-ProtoEXIST1. *Nuclear Instruments and Methods in Physics Research A*, 605:364–373, 2004.
- J.H. Hubbell, Wm.J. Veigele, E.A. Briggs, R.T. Brown, D.T. Cromer, and R.J. Howerton. Atomic form factors, incoherent scattering functions and photon scattering cross sections. *J. Phys. Chem. Ref. Data*, 4(3), 1975.
- ICRU. Tissue substitutes in radiation dosimetry and measurement, report 44 of the international commission on radiation units and measurements. Technical report, Bethesda, MD, 1989.
- IEC 62220-1. Medical electrical equipment - Characteristics of digital x-ray imaging devices - Part 1: Determination of the detective quantum efficiency, 2003.
- IEC 62220-1-2. Medical electrical equipment - Characteristics of digital x-ray imaging devices: Part 12. Determination of the detective quantum efficiency - detectors used in mammography, 2007.
- K. Iniewski, H. Chen, G. Bindley, I. Kuvvetli, and C. Budtz-Jorgensen. Modeling charge-sharing effects in pixellated CZT detectors. In *Nuclear Science Symposium Conference Record, 2007. NSS '07. IEEE*, pages 4608–4611, Oct 2007.
- C.K. Jae, S.E. Anderson, W. Kaye, S.J. Kaye, Z. Yuefeng, Z. Feng, and H. Zhong. Study on effect of charge sharing events in common-grid pixelated CdZnTe detectors. In *Nuclear Science Symposium Conference Record (NSS/MIC), 2009 IEEE*, pages 1640–1646, Oct 2009.
- JCPDS. Joint committee on powder diffraction studies, powder diffraction file., 1980.

- P.C. Johns and M.J Yaffe. X-ray characterisation of normal and neoplastic breast tissues. *Phys. Med. Biol.*, 32(6):675–695, 1987.
- P.C. Johns, R.J. LeClair, and M.P. Wismayer. Medical x-ray imaging with scattered photons. volume TD01, pages 355–357, 2002.
- L. Jones, P. Seller, M. Wilson, and A. Hardie. HEXITEC ASICa pixellated read-out chip for CZT detectors. *Nuclear Instruments and Methods in Physics Research Section A: Accelerators, Spectrometers, Detectors and Associated Equipment*, 604(1-2):34–37, 2009.
- N. Kiarashi, G.M. Sturgeon, L.W. Nolte, J.Y. Lo, W.P. and Samei E. Dobbins III, J.T. and Segars, and C.E. Ravin. A second generation of physical anthropomorphic 3d breast phantoms based on human subject data. volume 8668. *Medical Imaging 2013: Physics of Medical Imaging*, 2013.
- G. Kidane, R. D. Speller, G. J. Royle, and A. M. Hanby. X-ray scatter signatures for normal and neoplastic breast tissues. *Physics in medicine and biology*, 44(7):1791–802, 1999.
- A. Konstantinidis, T. Anaxagoras, M. Esposito, N. Allinson, and R. Speller. DynAMITe: a prototype large area CMOS APS for breast cancer diagnosis using x-ray diffraction measurements. In *Society of Photo-Optical Instrumentation Engineers (SPIE) Conference Series*, volume 8313, February 2012.
- A. Kozorezov, J. Wigmore, A. Owens, R. Denhartog, A. Peacock, and H. Aaljawhari. Resolution degradation of semiconductor detectors due to carrier trapping. *Nuclear Instruments and Methods in Physics Research Section A: Accelerators, Spectrometers, Detectors and Associated Equipment*, 546(1-2):209–212, 2005.
- P. Kraft, A. Bergamaschi, C. Broennimann, R. Dinapoli, E. F. Eikenberry,

- B. Henrich, I. Johnson, A. Mozzanica, C. M. Schleputz, P. R. Willmott, and B. Schmitt. Performance of single-photon-counting PILATUS detector modules. *Journal of Synchrotron Radiation*, 16:368–375, 2009.
- P. Latha, K.K. Abdullah, M.P Unnikrishnan, K.M. Varier, and B.R.S. Babu. Coherent and Incoherent Scattering cross sections for elements with  $13 \leq Z \leq 50$  using  $^{241}\text{Am}$  gamma rays. *World Academy of Science, Engineering and Technology*, 81, 2011.
- H. Q. Le, J. L. Ducote, and S. Molloy. Radiation dose reduction using a CdZnTe-based computed tomography system: Comparison to flat-panel detectors. *Medical Physics*, 37(3):1225, 2010.
- R.J. LeClair, M.M. Boileau, and Y. Wang. A semianalytic model to extract differential linear scattering coefficients of breast tissue from energy dispersive X-ray diffraction experiments. *Medical Physics*, 33:959–967, 2006.
- L. Li, M. Li, B. Sun, J.-h. Liu, and F. Zhang. Confirm of the optimum detection angles of several substances using energy dispersive X-ray diffraction. *Procedia Engineering*, 7:147–150, 2010.
- W. Li, D. Yu, F. Zhang, B. Sun, J. Liu, M. Li, and J. Liu. Detection of heroin covered by skin by using robust principal components analysis. *Measurement*, 44:267–273, 2011.
- M. Löcker, P. Fischer, S. Krimmel, H. Krüger, M. Lindner, K. Nakazawa, T Takahashi, and N. Wermes. Single photon counting x-ray imaging with Si and CdTe [single chip pixel detectors and multichip pixel modules]. *IEEE Transactions on Nuclear Science*, 51(4), 2004.
- R.D. Luggar, M.J. Farquharson, J.A. Horrocks, and R.J. Lacey. Multivariate

- analysis of statistically poor EDXRD spectra for the detection of concealed explosives. *X-Ray Spectrometry*, 27(2):87–94, 1998.
- C. Malden and R. Speller. A CdZnTe array for the detection of explosives in baggage by energy-dispersive X-ray diffraction signatures at multiple scatter angles. *Nuclear Instruments and Methods in Physics Research Section A: Accelerators, Spectrometers, Detectors and Associated Equipment*, 449(1-2):408–415, July 2000.
- H. L. Malm and M. Martini. Polarization phenomena in cdte nuclear radiation detectors. *IEEE Transactions on Nuclear Science*, 21(1):322–330, 1974.
- S.A. Mango. Automated and quantitative method for quality assurance of digital radiography imaging systems. International Workshop SMART MATERIALS, STRUCTURES AND NDT in AEROSPACE, 2011.
- I. Matsumoto, Y. Imura, H. Morii, A. Miyake, and T Aoki. Development of a thick CdTe detector for BNCTSPECT. *Nuclear Instruments and Methods in Physics Research Section A: Accelerators, Spectrometers, Detectors and Associated Equipment*, 621:292–294, 2010.
- A. Mersov, Mersov. G., Al-Ebraheem. A., Cornacchi. S., Gohla. G., P. Lovrics, and M.J.” Farquharson. The differentiation of malignant and benign human breast tissue at surgical margins and biopsy using x-ray interaction data and bayesian classification. *Radiation Physics and Chemistry*, 95(0):210 – 213, 2014.
- R.M. Moore and R.L. Smith. Method and apparatus for generating radiation blockers, May 7 1991. URL <https://www.google.com/patents/US5014290>. US Patent 5,014,290.
- L.R.M Morin. Molecular form factors and photon coherent scattering cross sections of water. *J. Phys. Chem. Ref. Data*, 11, 1982.

- L.R.M Morin and A. Berroir. Calculation of X-ray scattering in diagnostic radiology. *Physics in Medicine and Biology*, 28:789–797, 1983.
- M. Nakhostin, Y. Kikuchi, K. Ishii, S. Matsuyama, and H. Yamazaki. Development of a digital front-end electronics for the CdTe PET systems. *Nuclear Instruments and Methods in Physics Research Section A: Accelerators, Spectrometers, Detectors and Associated Equipment*, 614:308–312, 2010.
- A.H. Narten and H.A. Levy. Liquid water: molecular correlation function from X-ray diffraction. . *J. Chem. Phys.*, 55:2263–2269, 1971.
- NHS Cancer Screening Programmes. NHS Breast cancer screening programme Annual Review 2012. Online, 2012.
- H. Nilsson, B. Norlin, C. Frojdh, and L. Tlustos. Charge sharing suppression using pixel-to-pixel communication in photon counting X-ray imaging systems. *Nuclear Instruments and Methods in Physics Research Section A: Accelerators, Spectrometers, Detectors and Associated Equipment*, 576(1):243–247, 2007.
- A. Nolte, N. Kiarashi, W.P. Samei, E. Segars, and J.Y. Lo. A second generation of physical anthropomorphic 3d breast phantoms based on human subject data. volume 9033. *Medical Imaging 2014: Physics of Medical Imaging*, 2014.
- J.N. O’Dwyer and J.R. Tickner. Quantitative mineral phase analysis of dry powders using energy-dispersive X-ray diffraction. *Applied radiation and isotopes : including data, instrumentation and methods for use in agriculture, industry and medicine*, 66(10):1359–1362, 2008.
- D. O’Flynn, C. Reid, C. Christodoulou, M. Wilson, M.C. Veale, P. Seller, and R. Speller. Pixelated diffraction signatures for explosive detection. *Proc. SPIE 8357, Detection and Sensing of Mines, Explosive Objects, and Obscured Targets XVII*, page 83570X, 2012.

- D. O'Flynn, C. Reid, C. Christodoulou, M. Wilson, M.C. Veale, P. Seller, D. Hills, H. Desai, B. Wong, and R. Speller. Explosive detection using pixellated x-ray diffraction (pixd). *Journal of Instrumentation*, 8:P03007, 2013.
- S. Pani, E. Cook, J. Horrocks, L. George, S. Hardwick, and R. Speller. Modelling an Energy-Dispersive X-Ray Diffraction System for Drug Detection. *IEEE Transactions on Nuclear Science*, 56:1238–1241, 2009.
- S. Pani, J.A Cook, E.J. and, J.L Jones, and R.D. Speller. Characterization of breast tissue using energy-dispersive x-ray diffraction computed tomography. *Applied Radiation and Isotopes*, 68(10):1980–1987, 2010.
- S. Pani, S.C. Saifuddin, C. Christodoulou, M. Veale, P. Seller, R.D. Speller, and M. Wilson. K-edge subtraction imaging using an energy-resolving detector. 2011.
- D. Pennicard and H. Graafsma. Simulated performance of high-Z detectors with Medipix3 readout. IOP, 2011.
- D.E. Peplow and K. Verghese. Measured molecular coherent scattering form factors of animal tissues, plastics and human breast tissue. *Physics in Medicine and Biology*, 43(9):2431, 1998.
- K. Pepper, C. Christodoulou, C. Guazzoni, A. Castoldi, C. Ozkan, N. Sodini, D. Dreossi, J.A. Griffiths, A.P. Gibson, and G.J. Royle. A system for x-ray diffraction and fluorescence imaging of nanoparticle biomarkers. In *Nuclear Science Symposium Conference Record (NSS/MIC), 2010 IEEE*, pages 2718 – 2721, 2010.
- K. Pepper, A. Castoldi, C. Guazzoni, C. Ozkan, Christodoulou C., A.P. Gibson, and Royle G.J. A quantitative x-ray imaging system for gold nanoparticle tumour biomarkers. *Physics in Medicine and Biology*, 57:55435555, 2012.

- I Perzon and M Djabourov. X-ray diffraction of gelatin fibers in the dry and swollen states. *Journal of Polymer Science: Part B: Polymer Physics*, 28, 1990.
- M. Poletti, O. Goncalves, and I. Mazzaro. Measurements of X-ray scatter signatures for some tissue-equivalent materials. *Nuclear Instruments and Methods in Physics Research Section B: Beam Interactions with Materials and Atoms*, 213:595–598, 2004.
- M.E. Poletti, O.D. Goncalves, and I. Mazzaro. X-ray scattering from human breast tissues and breast-equivalent materials. *Physics in Medicine and Biology*, 47 (1):47, 2002a.
- M.E. Poletti, O.D. Goncalves, H. Schechter, and I. Mazzaro. Precise evaluation of elastic differential scattering cross-sections and their uncertainties in x-ray scattering experiments. *Nuclear Instruments and Methods in Physics Research Section B: Beam Interactions with Materials and Atoms*, 187(4):437–446, 2002b. ISSN 0168-583X.
- G.G. Poludniowski. Calculation of x-ray spectra emerging from an x-ray tube. Part II. X-ray production and filtration in x-ray targets. *Medical Physics*, 34 (6), 2007.
- G.G. Poludniowski and P.M. Evans. Calculation of x-ray spectra emerging from an x-ray tube. Part I. Electron penetration characteristics in x-ray targets. *Medical Physics*, 34(6):2164–2174, 2007.
- G.G. Poludniowski, G. Landry, F. DeBlois, P.M. Evans, and F. Verhaegen. Spekcalc : a program to calculate photon spectra from tungsten anode x-ray tubes. *Physics in Medicine and Biology*, 54(19):N433, 2009.
- B. D. Price, C. J. Esbrand, A. Olivo, A. P. Gibson, J. C. Hebden, R. D. Speller,

- and G. J. Royle. Assessing the validity of modulation transfer function evaluation techniques with application to small area and scanned digital detectors. *Rev. Sc. Instr.*, 79, 2008.
- R.H. Redus, J.A. Pantazis, T.J. Pantazis, A.C. Huber, and B.J. Cross. Characterization of cdte detectors for quantitative x-ray spectroscopy. *IEEE Transactions on Nuclear Science*, 56(4):2524–2532, 2009.
- N. Remoue. Selection of CdTe detectors for the detection plane of the ECLAIRs gamma-ray burst detector. *Nuclear Instruments and Methods in Physics Research Section A: Accelerators, Spectrometers, Detectors and Associated Equipment*, 610(1):287–290, 2009.
- N. Remoue, D. Barret, O. Godet, and P. Mandrou. Extensive testing of Schottky CdTe detectors for the ECLAIRs X-/gamma-ray camera on board the SVOM mission. *Nuclear Instruments and Methods in Physics Research Section A: Accelerators, Spectrometers, Detectors and Associated Equipment*, 618:199–208, 2010.
- G. J. Royle and R. D. Speller. Quantitative x-ray diffraction analysis of bone and marrow volumes in excised femoral head samples. *Physics in medicine and biology*, 40(9), 1995.
- G. J. Royle, M. Farquharson, R. D. Speller, and G. Kidane. Applications of X-ray diffraction analysis in crystalline and amorphous body tissues. *Radiation Physics and Chemistry*, 56:247–258, 1999.
- E.A. Ryan and M.J Farquharson. Breast tissue classification using x-ray scattering measurements and multivariate data analysis. *Physics in Medicine and Biology*, 52:6679–6696, 2007a.
- Elaine A Ryan and Michael J Farquharson. Breast tissue classification using x-ray

- scattering measurements and multivariate data analysis. *Physics in Medicine and Biology*, 52(22):6679, 2007b.
- E. Samei, M. J. Flynn, and D. A. Reimann. A method for measuring the presampled MTF of digital radiographic systems using an edge test device. *Medical Physics*, 25(1):102–113, 1998.
- E. Samei, N. T. Ranger, J. T. Dobbins, and Y. Chen. Intercomparison of methods for image quality characterization. I. Modulation transfer functions. *Medical Physics*, 33(5):1454–1465, 2006.
- E. Sato, T. Abderyim, P. amd Enomoto, M. Watanabe, K. Hitomi, K. Takahasi, S. Sato, A. Ogawae, and J. Onagawa. Energy-discriminating X-ray computed tomography system utilizing a cadmium telluride detector. *Nuclear Instruments and Methods in Physics Research Section A: Accelerators, Spectrometers, Detectors and Associated Equipment*, 619:262–265, 2010.
- P. Seller, S. Bell, R.J. Cernik, C. Christodoulou, C.K. Egan, J.A. Gaskin, S. Jacques, S. Pani, B.D. Ramsey, C. Reid, P.J. Sellin, J.W. Scuffham, R.D. Speller, M.D. Wilson, and M.C. Veale. Pixellated Cd(Zn)Te high-energy X-ray instrument. In *Journal of Instrumentation 9th International Conference on Position Sensitive Detectors (PSD9)*, 2011.
- R. E. Shuping and P. F. Judy. Resolution and contrast reduction. *Medical Physics*, 5(6):491–496, 1978.
- S. Sidhu, K.K.W. Siu, G. Falzon, S. A. Hart, J. G. Fox, and R. A. Lewis. Mapping structural changes in breast tissue disease using x-ray scattering. *Medical Physics*, 36(7):3211, 2009.
- J.H. Siewerdsena, A.M. Waese, D.J. Moseley, S. Richard, and D.A. Jaffray.

- Spektr: A computational tool for x-ray spectral analysis and imaging system optimization. *Medical Physics*, 31, 2004.
- Taha Sochi. *High Throughput Software for Powder Diffraction and its Application to Heterogeneous Catalysis*. PhD thesis, Birkbeck College London, 2010.
- R. Speller. Tissue analysis using x-ray scattering. *X-Ray Spectrometry*, 28(4): 224–250, July 1999.
- R. D. Speller and J. A. Horrocks. Photon scattering—a 'new' source of information in medicine and biology? *Physics in Medicine and Biology*, 36(1):224–250, 1991.
- P Spiegler and A Norman. The total unsharpness in radiography. *Physics in Medicine and Biology*, 18(6):884, 1973.
- B. Sun, M. Li, F. Zhang, Y. Zhong, N. Kang, W. Lu, and J Liu. The performance of a fast testing system for illicit materials detection based on energy-dispersive X-ray diffraction technique. *Microchemical Journal*, 95(2):293–297, 2010.
- A. Taibi, G.J. Royle, and R.D. Speller. A monte carlo simulation study to investigate the potential of diffraction enhanced breast imaging. *IEEE. Transactions in Nuclear Science*, 47:1581–1586, 2000.
- C. Theodorakou and M. J. Farquharson. Human soft tissue analysis using x-ray or gamma-ray techniques. *Physics in medicine and biology*, 53(11):R111–49, 2008. ISSN 0031-9155.
- C. Theodorakou and M. J. Farquharson. The classification of secondary colorectal liver cancer in human biopsy samples using angular dispersive x-ray diffraction and multivariate analysis. *Physics in medicine and biology*, 54(16):4945–57, 2009.

- L. Tlustos, R. Ballabriga, M. Campbell, E. Heijne, K. Kincade, X. Llopart, and P. Stejskal. Imaging properties of the Medipix2 system exploiting single and dual energy thresholds. *Nuclear Science, IEEE Transactions on*, 53(1):367–372, 2006.
- Universal Laser Systems Inc. *OEM ULR CO<sub>2</sub> LASER Integration Manual*, 2010.
- Universal Laser Systems Inc. *VLS Platform User Guide VLS3.60, VLS4.60, VLS6.60*, 2012.
- M.C. Veale, J. Kalliopuska, H. Pohjonen, S. Nenonen, P. Seller, and M.D. Wilson. Characterization of m- n cdte pixel detectors coupled to hexitec readout chip. In *Radiation imaging detectors 13th International workshop*, 2011.
- M.C. Veale, S.J. Bell, P. Seller, M.D. Wilson, and V. Kachkanov. X-ray micro-beam characterization of a small spectroscopic CdTe detector. *Journal of Instrumentation*, 7, 2012.
- R.F. Wagner. Toward a unified view of radiological imaging systems. Part II: Noisy images. *Medical Physics*, 4(4):279–296, 1977.
- S. Webb. *The Physics of Medical Imaging*. Number 578 in Medical science series. Taylor & Francis, 1988. ISBN 9781439822081.
- M. Wilson. HEXITEC Data corrections version 1.0, 2011.
- M.D. Wilson, P. Seller, M.C. Veale, and P.J. Sellin. Investigation of the small pixel effect in CdZnTe detectors. In *IEEE Nuclear Science Symposium Conference Record*, 2010.
- World Health Organisation. Causes of death database for years 2009-2010. March 2012.

M.J Yaffe and J.A Rowlands. X-ray detectors for digital radiography. *Phys, Med Biol.*, 42:1–39, 1997.

# Chapter 7

## Publications

The author has contributed and been involved with work resulting in the following publications and conference proceedings.

Pepper et al. (2010)- The author prepared a series of samples of gold nanoparticles suspended in ionized water, basing the required concentrations of experiments on the literature of previous works considering gold nanoparticles for enhanced radiotherapy and diagnosis. The author prepared for the experiments and was also involved in collection of synchrotron data in Trieste using the samples in diffraction and the florescence experiments, in collaboration with a group from Milan and UCL. Primary work was conducted on the diffraction data, considering the attenuation correction based on the solution of the samples and the diffraction signal obtained.

Christodoulou et al. (2011)-A prototype system was used to investigate the use of multi-angle diffraction signal for identifying the contents of powdered materials. Caffeine based samples were used to train a PLS model and using a 'leave-one-out' method, the caffeine content of samples was predicted.

Pani et al. (2011)-The system set up by the author was used for the experiments and the author was involved in data collection.

Seller et al. (2011)- Primary work conducted on the data and the multivariate analysis is incorporated into this paper which summaries the ASIC and the usages of the detector by collaborators.

Pepper et al. (2012)-The author wrote the MATLAB code for the L-edge subtraction data and processed the data ready for further analysis.

O’Flynn et al. (2012)- Helped set-up the detector in the initial stages of the PixD project with Post Doc Caroline Reid, as well as to provide initial already written code developed by to be used for initial processing for the first deliverable and as a guideline for future post-processing.

Christodoulou et al. (2013)- The energy resolution and efficiency of ASIC A and ASIC B were presented at PGBiomed at the University of Surrey in 2013.

The author has also been involved in further Synchrotron data collection at Diamond, Oxfordshire. Work was conducted with beamline scientist to obtain X-Ray Absorption Near Edge Subtraction (XANES), L-edge Imaging and L-line X-ray Fluorescence imaging at the I18 beamline, of gold nanoparticles attached to cancer cells in a healthy collagen matrix.